

City Research Online

City St George's, University of London

Citation: Fumarola, I. (2019). Effect of Freestream Turbulence on the Boundary Layer on a Swept Leading Edge. (Unpublished Doctoral thesis, City, University of London)

This is the accepted version of the paper.

This version of the publication may differ from the final published version. To cite this item please consult the publisher's version.

Permanent repository link: https://openaccess.city.ac.uk/id/eprint/22364/

Copyright and Reuse: Copyright and Moral Rights remain with the author(s) and/or copyright holders. Copies of full items can be used for personal research or study, educational, or not-for-profit purposes without prior permission or charge, unless otherwise indicated, provided that the authors, title and full bibliographic details are credited, a hyperlink and/or URL is given for the original metadata page and the content is not changed in any way. For full details of reuse please refer to City Research Online policy.

City Research Online: http://openaccess.city.ac.uk/ publications@citystgeorges.ac.uk

Effect of Freestream Turbulence on the Boundary Layer on a Swept Leading Edge

Isabella Fumarola

Supervised by

Prof. M. Gaster and Prof. C. J. Atkin

Thesis submitted as part of the requirement for the fulfilment of a degree of Doctor of Philosophy



City, University of London

School of Mathematics, Computer Science and Engineering

May, 2019

To my parents, to my brother and to Philip



Figure 1: Leonardo da Vinci, *Old Man with Water Studies* (1513).
Source: http://www.drawingsofleonardo.org/.

Contents

Contents v

List of Figures ix

List of Tables xix

Acknowledgements xxi

Declaration xxiii

Abstract xxv

Nomenclature xxvii

1 Background and motivation 1

1.1 Introduction 1

1.2 Brief history of transition 4

1.3 Transition mechanisms 6

1.4 Hydrodynamic stability theory 8

1.5 Primary modes 13

1.5.1 Tollmien-Schlichting 14

1.5.2 Görtler vortices 14

1.5.3 Attachment-line mechanisms 16

1.5.4 Cross-flow 17

1.6 Influence of freestream turbulence 19

1.7 Motivation of the thesis 22

1.8 Outline of the thesis 23

2 Flow in front of a leading edge **25**

2.1 Stagnation point flow 25

2.1.1 The Hiemenz flow 25

2.1.2 Hiemenz flow and enhancement of turbulence 28

2.1.3 Discussion 40

2.2 Attachment-line flow 42

2.2.1 Falkner-Skan-Cooke equations 43

2.2.2 Attachment-line contamination 46

2.2.3 Attachment-line instability 48

2.2.4 Discussion 51

3 A first experiment **53**

3.1 Design of the model 53

3.1.1 Vertical flat plate 56

3.2 Wind tunnel facilities 62

3.3 Preliminary experiments 66

3.3.1 Attachment-line contamination 66

3.3.2 Pressure measurements 70

3.4 Flow approaching the leading edge 71

3.4.1 Boundary layer along the attachment-line 75

3.5 Cross-flow instability and development of the flow along the flat plate 76

3.6 Experiments with freestream disturbances 82

3.6.1 The string 82

3.6.2 The grid 89

3.7 Summary 97

4 Experiments on a circular cylinder **99**

4.1 The model and the wind tunnel 99

4.2 Methodology 102

4.3 Results on the unswept cylinder 105

4.3.1 Pressure distribution 105

4.3.2 Potential flow 106

4.3.3 Viscous effect . . . 108
4.3.4 Frequency domain . . . 112
4.3.5 YZ Scan . . . 116
4.4 Results on the swept cylinders . . . 118
4.4.1 Pressure distribution . . . 118
4.4.2 Potential flow . . . 120
4.4.3 Viscous effect . . . 121
4.4.4 Frequency domain . . . 124
4.4.5 YZ scan . . . 130
4.5 Other results and observations . . . 130
4.5.1 Characterisation of freestream disturbances . . . 130
4.5.2 Velocity dependence . . . 132
4.5.3 Re_Θ dependence . . . 134
4.5.4 Effect of separation on the observed phenomenon . . . 135
4.6 Summary . . . 137

5 Some theoretical considerations 139
5.1 The vorticity amplification theory . . . 139
5.2 Influence of the sweep angle on the vorticity transport (far field) 142
5.2.1 The full solutions . . . 145

6 Discussion and conclusion 147
6.1 Main objective . . . 147
6.2 Experimental methods and apparatus . . . 147
6.3 Experiments on a vertical swept flat plate . . . 148
6.4 Experiments on the circular cylinder . . . 150
6.5 Conclusion . . . 151
6.5.1 Suggestions for further work . . . 152

Appendices 155

A Cross-flow Reynolds number 157

B Hot-wire anemometer **159**

B.1 Working principle . . . 159

B.2 Hot-wire setup . . . 160

B.3 Calibration . . . 162

B.4 Data acquisition . . . 163

B.5 Data analysis . . . 164

C Laser Doppler anemometer **167**

C.1 Working principle . . . 167

C.2 Multi-component velocity measurements . . . 168

C.3 Laser beams setup . . . 170

C.3.1 Data acquisition . . . 175

C.4 Data analysis . . . 176

C.4.1 Time domain analysis . . . 177

C.4.2 Spectral analysis . . . 182

D Uncertainty analysis **187**

D.1 Experimental errors . . . 187

D.2 Uncertainty analysis . . . 188

D.3 Density of the air . . . 189

D.4 Freestream velocity . . . 190

D.5 Pressure distribution . . . 190

D.5.1 Gaster wind tunnel . . . 190

D.5.2 T2 wind tunnel . . . 190

D.6 Hot-wire measurements . . . 192

D.7 LDA measurements . . . 194

List of Figures

1 Leonardo da Vinci, *Old Man with Water Studies* (1513). Source: http://www.drawingsofleonardo.org/ iii

1.1 a) A sketch of a laminar and turbulent flow b) a comparison of the boundary layer velocity (U) profile as function of the wall normal direction (y) for the laminar and the turbulent conditions in the dimensionless coordinate (δ is the boundary layer thickness and U_∞ the velocity of the freestream). 2

1.2 North American Aviation P-51 Mustang. Source: https://nationalinterest.org/blog/buzz/why-nothing-could-stop-p-51-mustang-30287. . . 4

1.3 Reynolds (1883) experiment, evolution in a pipe flow: a) laminar b) turbulent. 5

1.4 Transition path, modified from Morkovin (1994). 7

1.5 An example of wave growing in time and space ($\alpha_i, \beta_i, \omega_i$ positive). 11

1.6 For the Rayleigh circulation criterion the flow in b) and c) is stable, while in a) and d) is unstable (modified from Saric (1994)). 15

1.7 The Görtler instability, the boundary layer on concave walls produces unstable vortices. Figure from Saric (1994). 16

1.8 a) Inviscid streamline on a swept wing, b)generation of the cross-flow (Arnal and Casalis (2000)). 17

1.9 Schematic of co-rotating cross-flow vortices. 18

2.1 The flow against a vertical flat plate (Hiemenz flow). SP is the stagnation point from which the δ boundary layer grows. 26

2.2 Viscous Hiemenz flow solution (continous curves) and the linear interpolation of the outer flow (dashed line). 27
2.3 Contours of velocity fluctuations, measured through a vibration galvanometer around a cylinder immersed in a flow (left to right) by Piercy and Richardson (1928). 29
2.4 Stretching of vorticity approaching a flat plate (modified from Sadeh et al. (1977)). 31
2.5 Sketch of the counter-rotating vortices developing at the stagnation point of a cylinder (Kestin and Wood, 1970). 33
2.6 Flow visualisation at the stagnation point of a flat plate (flow left to right) Sadeh et al. (1970). 36
2.7 Sadeh and Brauer (1981) experiment on the flow approaching a stagnation point of a cylinder ($R = 80\ mm$, $Re_D = 1.2 \cdot 10^5$) with a turbulence generating grids. The plot shows the turbulence energy ($\overline{u_2^2}$) for difference scales (λ) normalised by its minimum value ($\overline{u_{2,0}^2}$) as function of the distance from the cylinder. Legend: • $\lambda/\lambda_0 = 5.52$,• $\lambda/\lambda_0 = 6.90$, • $\lambda/\lambda_0 = 13.80$. 37
2.8 Flow against a swept flat plate. 42
2.9 Wedge flow. 43
2.10 Falkner-Skan-Cooke solution with $\beta = 1$, swept Hiemenz flow. . 45
2.11 Attachment-line contamination: a) the disturbances coming from the fuselage decay and the flow is laminar $Re_\Theta < 100$, b) the disturbances grow along the attachment-line and the boundary layer is turbulent. 47
2.12 Devices decontaminate the turbulent attachment-line flow a) flow visualisation on the Gaster bump (Gaster, 1965), b) the Gaster slot, the red arrows indicate turbulent flow and the green arrows laminar flow (Alderman et al., 2016). 48
2.13 Attachment-line instability over a swept wing. 48
2.14 Neutral curve for attachment-line flow by Hall et al. (1984), compared to experiments by Pfenninger and Bacon (1969) and Poll (1978). 50

2.15 Wavelength of streaky pattern as function of sweep angle (Gostelow et al., 2013). 52

3.1 Gaster wind tunnel at City, University of London 54

3.2 Models considered during the design: a) swept double wedge b) horizontal flat plate with displacement bodies c) vertical swept flat plate mounted on a wing body. The arrows indicate the flow direction. 55

3.3 a) Cross-flow Reynolds number (χ) at $x = t$ normalised to be function only of the sweep angle (Λ); b) Re_Θ at the attachment-line for $Q_\infty = 25\ m/s$ (red) and for $Q_\infty = 18\ m/s$ (blue) as function of the sweep angle Λ for $t = 0.09m$. The black dashed line represents the limit to avoid attachment-line contamination. 59

3.4 Overview of the model design: a) cross section of the model, b) design for manufacturing. 60

3.5 The model mounted in the Gaster wind tunnel (flow from right to left). 61

3.6 Overview of the wind tunnel facilities. 62

3.7 Top view of the wind tunnel with the coordinate system adopted. The hot-wire traverse, mounted perpendicular to the leading edge, approaches the model from a side. 63

3.8 Boundary layer at the attachment-line; $\Delta\eta$ is the shift from the wall. 65

3.9 Device to prevent the attachment-line contamination from the circulation bubble at the corner between the model's root and the wind tunnel. 67

3.10 a) anti-contamination device installed on the model, b) flow visualisation. 68

3.11 Front view of the model mounted in the Gaster wind tunnel with the device to prevent contamination. 68

3.12 Spike appearing in the hot-wire filtered time signal. 69

3.13 Spectra of the hot-wire signal with (blue) and without (red) the spike. 69

3.14 Pressure distribution on the flat leading edge: • measured, - numerical. 71

3.15 Velocity profiles, mean and RMS, approaching the model at different freestream velocities: □ $Q_\infty = 8\,m/s$, * $Q_\infty = 10\,m/s$, × $Q_\infty = 15\,m/s$, • $Q_\infty = 18\,m/s$. 71

3.16 a) Boundary layer velocity profile compared to Falkner-Skan-Cooke solution (blue line) and b) RMS profiles at four freestream velocities:7 □ $Q_\infty = 8\,m/s$, * $Q_\infty = 10\,m/s$, × $Q_\infty = 15\,m/s$, • $Q_\infty = 18\,m/s$. 72

3.17 Spectra at the edge of the boundary layer at different velocities:— $Q_\infty = 8m/s$, — $Q_\infty = 10m/s$, — $Q_\infty = 15m/s$, — $Q_\infty = 18m/s$. 73

3.18 Spectra inside the boundary layer (closest point to the wall) at different freestream velocities: — $Q_\infty = 8\,m/s$, — $Q_\infty = 10\,m/s$, — $Q_\infty = 15\,m/s$, — $Q_\infty = 18\,m/s$. 73

3.19 Boundary layer profile of the signal band passed respectively in the ranges a) $15\,Hz \leq f \leq 25\,Hz$ and b) $50\,Hz \leq f \leq 60\,Hz$, at different velocities:— $Q_\infty = 8\,m/s$,— $Q_\infty = 10\,m/s$,— $Q_\infty = 15\,m/s$,— $Q_\infty = 18\,m/s$. 74

3.20 PSD of the hot-wire signal at $Q_\infty = 18m/s$, $1mm$ from the wall (edge of the boundary layer) with (green) and without (red) the tape holding the sensor. 74

3.21 Contour plot inside the boundary layer along the attachment-line (z-direction) at $18\,m/s$: a) mean velocity b) RMS. 75

3.22 YZ scan along the boundary layer at x=60 mm. 76

3.23 Influence of the cross-flow instability on the mean chordwise velocity over a wing at different chordwise location (x/c) from Reibert (1996): a)$x/c = 0.1$ corresponding to the neutral stability point, N-factor=0 b)$x/c = 0.2$, N-factor=1.8 c)$x/c = 0.3$ N-factor=3 77

3.24 The spanwise fluctuation of the mean velocity in the presence of cross-flow instability by Reibert (1996). The plots a), b) and c) correspond to figure 3.23 d) evolution of the mode shape along the chord. 78

3.25 (a) Boundary layer profiles across z at $x = 60\ mm$, (b) spanwise variations from the average boundary layer profile at $x = 60mm$, (c) average spanwise variations (W^*) at x=0 mm (blue) and x=60 mm (red). 79

3.26 Spectra of a single boundary layer profile at $x = 60\ mm$: a) spectra plot at different height in the boundary layer b) corresponding contour plot. 80

3.27 Contour plot of the velocity fluctuations band passed between 550 Hz and 650 Hz in a y-z plane. 80

3.28 YX scan along the entire plate: mean spanwise velocity and signal bandpassed between $550 - 650\ Hz$. 81

3.29 Spectra of a single boundary layer profile at $x = 60\,mm$ (brown) and $x = 0\,mm$ (green): a) Inside the boundary layer ($\eta = 1$) b) outside the boundary layer ($\eta = 6$). 82

3.30 Mechanism to tension the string. 83

3.31 String location with respect to the model for each test case. . . 84

3.32 Interaction of the horizontal string with the model. The turbulence coming from the string (red) may interact with the anti-contamination device and make the flow turbulent on the attachment-line of the device itself. 85

3.33 Mean and RMS velocity profile, approaching the model with the vertical wire in position V1 at different velocities: ▫ $Q_\infty = 8m/s$, ∗ $Q_\infty = 10\ m/s$, • $Q_\infty = 18m/$. 86

3.34 a) Vertical string in the position V4 and b) an example of the corresponding velocity profile along the attachment-line downstream of the string ($Q_\infty = 18\ m/s$). 87

3.35 Contour plot of the mean and rms velocity along the attachment-line with the vertical string in position V4. 88

3.36 Overview of different types of grids: (a) square mesh, (b) parallel vertically rods, (c) parallel horizontal rods. 90

3.37 Rod diameter of the grid (d) as function of the amplification (Λ/λ_0) at different velocities: $Q_\infty = 8\,m/s$, $Q_\infty = 10\,m/s$, $Q_\infty = 15\,m/s$, $Q_\infty = 18\,m/s$. 91

3.38 Turbulence generating grid mounted vertically in the wind tunnel. 92

3.39 Boundary layer velocity profiles on the attachment-line at different velocities with turbulence generating grid installed horizontally (•) and vertically (×). 94

3.40 PSD inside the boundary layer at the maximum of the RMS with (a) an horizontal grid and (b) a vertical grid for each freestream speed: $Q_\infty = 8\,m/s$, $Q_\infty = 10\,m/s$, $Q_\infty = 15\,m/s$, $Q_\infty = 18\,m/s$. 95

3.41 Comparison of the effect of the grid with respect to the effect of the horizontal string in H1 at $Q_\infty = 18\,m/$: • grid horizontally oriented, × grid vertically oriented, □ string $d = 3\,mm$ in H1, ◊ string $d = 0.23\,mm$ in H1. 96

4.1 Unswept Perspex cylinder mounted in the wind tunnel. 100

4.2 Cylinder mounted on a sweep angle inside the wind tunnel. . . . 101

4.3 LDA setup outside the wind tunnel. 102

4.4 LDA during the alignemnt procedure usign the L-shaped metallic foil. 103

4.5 Example of the flow in front of the cylinder to align the laser with the stagnation point 103

4.6 Coordinate systems for the cylinder experiments: (X_T, Y_T, Z_T) is the coordinate system defined by the LDA traverse, (X, Y, Z) is the coordinate system adopted in the data analysis. 104

4.7 Pressure distribution on the unswept cylinder. 105

4.8 Mean and RMS of the three velocity components approaching the straight cylinder. 107

4.9 Potential flow approaching the cylinder: data points •, potential flow theory —, Hiemenz theory—. 108
4.10 Mean and RMS (•) of the velocity components in the boundary layer at the stagnation point. The V-component is compared to the Falkner-Skan (-) solution. 109
4.11 Method used to find the distance from the wall: • experiment — theory. 109
4.12 Velocity fluctuations ($\overline{u_2^2}$) from hot-wire measurements by Sadeh and Brauer (1981) on a straight cylinder: $Re_D = 12 \times 10^4$, $R = 80\,mm$. 111
4.13 Normalised RMS for the three velocity components. 111
4.14 Spectra at various η for a) V component and b) W component. . 113
4.15 Contour plot of the PSD for the V and the W velocity components in the boundary layer 114
4.16 Contour plot of the PSD for the V and the W velocity components in the boundary layer as function of the length scale. The dashed line represents - - is the neutral wavelength (λ_0) for Hiemenz flow. 115
4.17 Velocities and fluctuation on a YZ plane. 116
4.18 Velocity fluctuation after having subtracted the mean of RMS along Z. 117
4.19 Pressure distribution at different sweep angle: theoretical laminar (dashed line) and experimental data (dots). The colours indicate the sweep angles:• $\Lambda = 0°$, ▲ $\Lambda = 5°$, ◇ $\Lambda = 10°$, ■ $\Lambda = 20°$, ∗$\Lambda = 30°$ 119
4.20 Potential flow approaching the sweep cylinder in two configurations, ■ $\Lambda = 20°$, ◀ $\Lambda = 30°$, compared to potential flow theory (black line). 120
4.21 Mean and fluctuating velocity for different sweep angle: • $\Lambda = 0°$, ▲ $\Lambda = 5°$, ⋆ $\Lambda = 10°$, ■ $\Lambda = 20°$, ◀ $\Lambda = 30°$. W/W_e for $\Lambda = 0°$ is not plotted. The mean velocity are compared to Falkner-Skan-Cooke solution -. 122

4.22 Normalised coviariance for different sweep angles: ● $\Lambda = 0°$, ▲ $\Lambda = 10°$, ⋆ $\Lambda = 10°$, ■ $\Lambda = 20°$, ▶ $\Lambda = 30°$. 123

4.23 a) Normalised coviariance for $\Lambda = 20°$ and the w versus v scatter plots for the corresponding data at b) $\eta \approx 9$ and c) $\eta \approx 4$. The black lines indicate the linear regression. 123

4.24 Contour plot of the cross-product along the spanwise direction for $\Lambda = 20°$ 124

4.25 PSD contour plot $\Lambda = 5°$. 125

4.26 PSD contour plot $\Lambda = 10°$. 126

4.27 PSD contour plot $\Lambda = 20°$. 126

4.28 PSD contour plot $\Lambda = 30°$. 127

4.29 Contour plot $\Lambda = 5°$. 128

4.30 Contour plot $\Lambda = 10°$. 128

4.31 Contour plot $\Lambda = 20°$. 129

4.32 Contour plot $\Lambda = 30°$. 129

4.33 Freestream turbulence intensity at 200 mm from the leading edge of the cylinder for various sweep angle. Legend as in figure 4.34. 131

4.34 Freestream spectra for different sweep cylinder: - $\Lambda = 0°$, - $\Lambda = 5°$, - $\Lambda = 10°$, - $\Lambda = 20°$, - $\Lambda = 30°$. 131

4.35 Mean and fluctuation of the velocity at different freestream Reynolds number:$\Lambda = 20°$ ■ $Q_\infty = 6\ m/s$, □ $Q_\infty = 8\ m/s$, ● $Q_\infty = 10\ m/s$, ○ $Q_\infty = 15\ m/s$. 133

4.36 Mean and shear stress of the velocity at different freestream velocities:$\Lambda = 20°$ ■ $Q_\infty = 6\ m/s$, □ $Q_\infty = 8\ m/s$, ● $Q_\infty = 10\ m/s$, ○ $Q_\infty = 15\ m/s$. 133

4.37 Mean and fluctuation of the velocity at different Re_Θ and two sweep angles: $\Lambda = 20°$ ● $Re_\Theta = 29.1$, ○ $Re_\Theta = 35.6$ and ◀ $\Lambda = 30°$ $Re_\Theta = 31.5$. 134

4.38 PSD of LDA3 signal at $\eta = 7.5$ on the cylinder at $\Lambda = 10°$ with - and without - the roughness strips to trip the boundary layer. 135

4.39 Flow at the stagnation point on a cylinder at $\Lambda = 10°$ with ♦ and without • the roughness strips to trip the boundary layer. The mean velocity profiles are compared to Falkner Skan Cooke (black line). 136

5.1 Logarithmic oscillations. 145

A.1 Cross-flow velocity profile for $\epsilon = 0$. 158

B.1 Desired hot-wire voltage (E), as function of time (t), during the square wave test(Jørgensen, 2005). 162

B.2 Hot-wire calibration, example of King's law. 163

C.1 Overview of LDA setup in back scatter configuration. 168

C.2 Three-component LDA optic groups mounted on the three-axis traverse. 169

C.3 Three-component LDA optic groups mounted on the three-axis traverse: a) overall view, b) rails. 171

C.4 Sketch of LDA Alignment procedure, components not in scale. . 173

C.5 LDA velocity coordinate systems. Flow right to left. 175

C.6 Example of a LDA signal randomly distributed in time. 177

C.7 Two particles crossing the probe volume with different trajectory.179

C.8 Example of mean and RMS of the stagnation point flow on the unswept Cylinder: • arithmetical momentum, • weighted momentum (coordinate system according to figure 4.6). 179

C.9 Velocity distribution as function of the number of particles (N) and the transit time (TT) for the point in the boundary layer in table C.3. - weighted mean, - - weighted RMS, - arithmetical mean and - - atihmetical RMS. 181

C.10 Velocity distribution as function of the number of particles (N) and the transit time (TT) in the freestream. - weighted mean, - - weighted RMS, - arithmetical mean and - - atihmetical RMS.181

C.11 Example of PSD for the V and W velocities: - with and - without the weighting factor. 184

C.12 LDA data analysis: the slotting technique. 186

D.1 Two laser beam and a particle crossing the probe volume with velocity U_P. 195

D.2 Two laser beam crossing in the probe volume. 196

D.3 Four laser beams captured by the camera during alignment procedure. 198

List of Tables

3.1 Parameters in the final design of the flat face wing. 60

3.2 Test cases: H and V indicate the string orientation, respectively horizontal or vertical, d the diameter of the string, Q_∞ the freestream velocity, Re_d the Reynolds number of the string, y_g the distance from the leading edge. For each test case, the nature of the flow at the attachment-line is reported. 84

3.3 Turbulence intensity at $y = 30\,mm$ from the leading edge with the turbulence generating grid in the horizontal and vertical configuration compared to the turbulence intensity without the grid. 95

4.1 Freestream conditions for experiments at different sweep angles. 130

4.2 Freestream condition for experiments at different speeds and $\Lambda = 20°$. 132

C.1 Three-component LDA characteristics. 170

C.2 Example of wind tunnel coordinate to find the laser beams orientation 174

C.3 Arithmetical and weighted momentum for the fourth point of the scan in figure C.8. 180

C.4 Arithmetical and weighted momentum for a point at 200 mm from the cylinder stagnation point. 182

D.1 Uncertainties on measurements carried out in the Gaster wind tunnel. 191

D.2 Uncertainties on measurements carried out in T2 wind tunnel. . 192

D.3 Hot-wire uncertainties for a reference velocity of $10m/s$, corresponding to $E = 4.16V$ and calibration coefficients $A = 4.29$, $B = 7.74$ and $n = 0.35$. 194
D.4 LDA parameters 198
D.5 Example of wind tunnel coordinate to find the laser beams orientations with their absolute uncertainties. 199

Acknowledgements

I would like to express my gratitude to all the people who supported and encouraged me during the journey to my PhD.
First of all, I would like to thank my supervisors, Prof. Mike Gaster and Prof. Chris J. Atkin, for offering me the opportunity to do my PhD at City, University of London, for offering constant support, for sharing their knowledge and for providing guidance during the project.
I would like to express my special thanks to Dr. Oliver Kerr for his kind and valuable help and for all he has taught me and to Dr. Christian Thomas for running one of his codes in the context of the analysis of my model.
I would like to thank all the technicians in the workshop, in particular, Philip Beckwith who helped with the set up both experiments, and to Richard Leach and Keith Pamment for being always so supportive and helpful.
Many thanks to my entire research group: the postdocs Dr. Chetan Jagadeesh, Dr. Marco Placidi, Dr. Pradeepa Karnick and and fellow PhD students Evelien van Bockhorst, Barry Crowley, Dhamodaratan Veerasamy, Tobias Derek, Nick Brown. In particular, thanks to Barry for helping whenever I needed and thanks to Ricky and Chetan for offering guidance on more than one occasion. Sincere and deep thanks to my "*terrible twin*" Evelien, for learning together and for being a supportive and encouraging friend throughout the PhD. Together with Evelien, thanks to Judit and Weimiao for being part of all that and for being by my side through all the hard moments. The fun and the kindness I had experienced with them every day was the fuel for my work.
Thanks to all the other people of CG41, to all my other friends in London and to those friends who were far in distance but close in heart.

Many thanks to Philip – for being with me every day, for understanding my choices, for being so immensely supportive and patient.
Finally, I would like to express my gratitude to my parents and brother. Nothing would have been possible without their support, patience, advices. Thanks for being my comfort, my certainty and my strength.

Declaration

I, Isabella Fumarola, declare that this thesis, entitled *Effect of Freestream Turbulence on the Boundary Layer on a Swept Leading Edge*, has been composed solely by myself and that it has not been submitted, in whole or in part, in any previous application for a degree. Except where states otherwise by reference or acknowledgement, the work presented is entirely my own. I confirm that:

- this work was done wholly or mainly while in candidature for a research degree at this University;
- where I have consulted the published work of others, this is always clearly attributed;
- where I have quoted from the work of others, the source is always given. With the exception of such quotations, this thesis is entirely my own work;
- I have acknowledged all main sources of help;

Signed:.....

Date:.....

Abstract

An experimental study was carried out to understand the way the turbulence interacts with the boundary layer along the attachment-line of a swept wing, since it may have an important role in the receptivity process of cross-flow instability to freestream turbulence.

The work focused on the freestream turbulence amplification process approaching a leading edge, previously seen on two-dimensional bodies, but yet not investigated for swept models.

Two experimental investigations were carried out in two different wind tunnels using two different models. The first was carried out in the Gaster wind tunnel, characterised by very low turbulence intensity. The model consisted of a swept aluminium vertical flat plate inserted in a wooden fairing, similar to the unswept model used by Bearman (1972). The flow field was measured using a single hot-wire anemometer. In the low turbulent environment, no increase in the velocity fluctuations was observed as the wall was approached. Therefore, the freestream turbulence level was increased using, as a first attempt, a metallic string, crossing the entire wind tunnel section, placed at different orientations ahead of the model. It was found that the vertical string generated a localised freestream disturbance which was convected in the spanwise direction, following the streamlines, without influencing the level of fluctuations in the boundary layer. The horizontal string created a disturbance, distributed in the spanwise direction, that made the boundary layer turbulent at the attachment-line. A second attempt was carried out using a turbulent grid made of parallel rods, mounted either in a horizontal or vertical configuration. In both configurations, the grid had an effect similar to that of the

horizontal string creating a turbulent boundary layer on the attachment-line. This effect may have been due to a contamination of turbulence from the root of the wing. In all the cases, the turbulent boundary layer presented an increase of fluctuations approaching the wall.

A second experiment was carried out in the T2 wind tunnel, characterised by a level of turbulence higher than that of the Gaster wind tunnel, on a circular cylinder model. In this case, a multi-component Laser Doppler anemometer was used, enabling simultaneous measurements of the three velocity components. The experiment focused on the flow approaching the stagnation point of a cylinder mounted in the unswept configuration and then at four different sweep angles ($5°$, $10°$, $20°$, $30°$). The results achieved on the unswept configuration showed an amplification of the spanwise velocity fluctuations approaching the stagnation point with a maximum around the boundary layer edge, followed by decay as the wall was approached. The spanwise velocity fluctuation profiles were similar to those, based on hot-wire measurements, reported in the literature. In the swept configurations the increment of the spanwise velocity fluctuations was found to be still present and similar to the unswept case. At $30°$ sweep angle, the spanwise velocity fluctuations were observed to increasing right up to the measured point closest to wall. One of the effects of increasing sweep angle was to increase the frequency at which the turbulence was most amplified.

A number of new trends have been identified, confirming that, in general, the phenomena at the swept leading edge boundary layer cannot be explained using two-dimensional arguments.

Nomenclature

Latin Symbols

$\overline{Re}$	Attachment line Reynolds number based on velocity gradient	
$\overline{v'w'}$	Covariance of the v and w velocity fluctuations	m^2/s^2
Q_e	Total edge velocity components	m/s
U_e, V_e, W_e	Edge velocity components in the directions x, y, z	m/s
$\overrightarrow{q}$	Disturbances vector	
$\overrightarrow{U}$	Velocity vector	m/s
$\overrightarrow{u}$	Velocity perturbation	m/s
θ	Cylinder circumferential angle	$^\circ$
a	Hiemenz constant	s^{-1}
c	Complex wave speed (ω/α)	m/s
c_ϵ	Cross-flow velocity	m/s
c_f	Skin friction coefficient	
c_p	Dimensionless pressure coefficient	
c_{p2D}	Dimensionless pressure coefficient of the unswept model	
c_{p3D}	Dimensionless pressure coefficient of the swept model	
D	Characteristic length, diameter in the case of a cylinder	m
d	Diameter of the string	m
f	Frequency	Hz

$f(\eta)$	Falkner-Skan function	
f_{MAX}	Maximum frequency	Hz
f_{MIN}	Minimum frequency	Hz
f_{shed}	Shedding frequency	Hz
g	Gravity acceleration	m/s^2
$g(\eta)$	Cooke function	
H	Shape factor	
H_{AL}	Shape factor at the attachment-line	
H_w	Hann window	
M	Distance between the rods of the grid	m
N_{Λ_x}	Ratio between the integral scale and the natural wavelength	
P	Mean pressure	Pa
p	Pressure fluctuations	Pa
p_∞	Dynamic pressure of the Pitot tube	Pa
$p_{s\infty}$	Static pressure of the Pitot tube	Pa
$p_{t\infty}$	Total pressure of the Pitot tube	Pa
Q	Total velocity	m/s
Q_e	Edge total velocity	m/s
Q_∞	Total freestream velocity	m/s
R	Cylinder radius	m
R_u	Autocorrelation function	m^2/s^2
Pr	Prandtl number	
Re	Reynolds number	
Re_Θ	Reynolds number based on the attachment-line momentum thickness	
Re_D	Reynolds number based on the cylinder diameter	

Re_d	Reynolds number based on the diameter of the string	
s	Curvilinear coordinate	m
s_ϵ	Streamwise velocity	m/s
St	Strouhal number	
t	Half thickness of the plate	m
t	Time	s
TT_i	Transient time	s
Tu	Turbulence intensity	
$u(t), v(t), w(t)$	Time velocity signals	m/s
U, V, W	Mean velocity components in x, y, z directions respectively	m/s
U_1, U_2, U_3	Velocity components measured by the three laser	m/s
U_e, V_e, W_e	Edge velocity components	m/s
$U_\infty, V_\infty, W_\infty$	Freestream velocity components	m/s
U_X, U_Y, U_Z	Velocity components in the X_T, Y_T, Z_T coordinate system	m/s
U_{ku}, V_{ku}, W_{ku}	Kurtosis of the velocity components	
$U_{PSD}, V_{PSD}, W_{PSD}$	PSD of the velocity components	m^2/s^2Hz
$U_{RMS}, V_{RMS}, W_{RMS}$	RMS of the velocity components	m/s
x	Chordwise coordinate	m
x_g	Distance from the grid to the measurement region	m
X_T, Y_T, Z_T	Coordinate of the LDA traverse in T2 wind tunnel	m
y	Wall-normal coordinate	m
z	Spanwise coordinate	m

Greek Symbols

α	Chordwise wave number	m^{-1}
β	Spanwise wave number	m^{-1}

ω	Frequency	m^{-1}
$\overrightarrow{\omega}$	Dimensionless perturbation of the vorticity	
$\overrightarrow{\Omega}$	Dimensionless vorticity of the base flow	
χ	Cross-flow Reynolds number	
Δf	Frequency resolution	Hz
Δh	Height of the fluid in the manometer	m
δ	Boundary layer thickness	m
δ_{AL}	Boundary layer thickness at the attachment-line	m
δ^*	Boundary layer displacement thickness	m
δ^*_{AL}	Boundary layer displacement thickness	m
ϵ	Orientation of the cross-flow	$^\circ$
η	Dimensionless wall-normal coordinate	
γ	Wedge angle	$^\circ$
γ_H	Window factor	
Λ	Sweep angle	$^\circ$
λ	Wavelength	m
λ_0	Natural wavelength	m
Λ_x	Integral scale	m
λ_y, λ_z	Wavelength in the x, z directions	m
μ	Air viscosity	Ns/m^2
ν	Kinematic viscosity	m/s^2
ϕ_m	Angle of inclination of the manometer	$^\circ$
ρ	Air density	kg/m^3
ρ_m	Density of the fluid in the manometer	kg/m^3
τ_w	Shear stress at the wall	Pa

Θ	Boundary layer momentum thickness	$^\circ$
Θ_{AL}	Boundary layer momentum thickness at the attachment-line	$^\circ$
ξ	Dimensionless chordwise coordinate	
ζ	Dimensionless spanwise coordinate	

Acronyms

AL	Attachment Line
CF	Cross Flow instability
HW	Hot-Wire anemometer
LDA	Laser Doppler Anemometer
LFC	Laminar Flow Control
PSD	Power Spectra Density
RMS	Root Mean Square
SP	Stagnation Point
TS	Tollmien-Schlichting waves

Chapter 1

Background and motivation

1.1 Introduction

On the 17^{th} December 1903, Orville and Wilbur Wright transformed the human dream of flying into reality. Just 30 metres of flying distance, only 12 seconds that have shaped the future of the world in an unbelievable way (Anderson Jr, 1999). Nowadays, after 115 years, the aviation industry counts 4.1 billion[1] civil passengers travelling on commercial aircraft in a year.

Beside the incredible technological improvements, the aviation industry is facing a new challenge in the 21^{st} Century. The concern for the global warming and the climate change is requiring a combined effort by all the industrial sectors in reducing the environmental impact. The aviation industry is particularly involved since its emissions account for 3% of the total European greenhouse gases and 2% of the global emissions[2]. The vision in a long-term scenario, in which the air traffic is expected to grow enormously, is even worse. According to the air traffic forecast by ICAO (2016), the number of revenue passengers per kilometre (RPK) is expected to grow at 4.4% annually reaching 20 trillion RPK in the 2040. The growth of passengers and fleets would be accompanied by a growth of fuel consumption and air pollution. The emissions are expected to rise more than 300% by 2050[3].

[1]The number is referred to the year 2017 according to the ICAO statistic. Source: https://www.icao.int/annual-report-2017/Documents.

[2]Source: https://ec.europa.eu/clima/policies/transport/aviation_en.

[3]See note 2

A review of the different techniques that can be employed to reduce the fuel consumption is given in Green (2008). One possibility is to reduce the aerodynamic force that opposes to the body motion in a fluid, which is the drag, by preventing or delaying the transition from laminar to turbulent flow. By definition, a laminar flow is a well organised flow where the streamlines move smoothly parallel each other; while, in a turbulent flow the streamlines move in chaotic paths (see figure 1.1a). The laminar state of the flow is always a natural condition, but the presence of disturbances in the environment or on the wall over which the fluid is flowing, induces a change in the flow state from laminar to turbulent through a transition process. In other words, a flow could be laminar, but in reality it is unstable and would transition to a turbulent state.

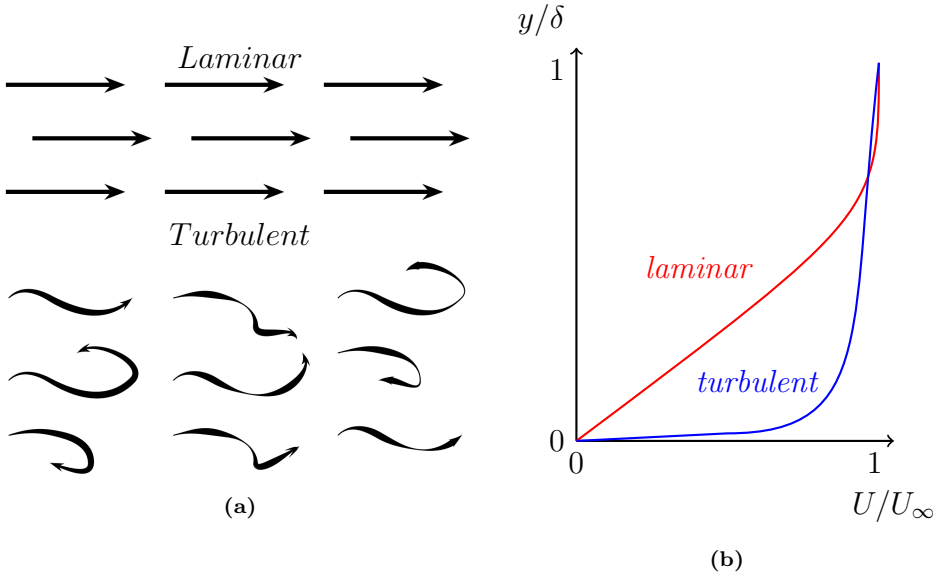


Figure 1.1: a) A sketch of a laminar and turbulent flow b) a comparison of the boundary layer velocity (U) profile as function of the wall normal direction (y) for the laminar and the turbulent conditions in the dimensionless coordinate (δ is the boundary layer thickness and U_∞ the velocity of the freestream).

One important difference between laminar and turbulent flows along the surface of a wing, or a generic solid body, is within the boundary layer, defined as the layer of fluid close to the wall where the viscous forces are not negligible (Prandtl, 1904). The boundary layer and the associated skin friction arises as the air flows over the surface. It is often quantified through the friction coefficient (c_f), a dimensionless quantity defined as the ratio between the shear

stress at the wall (τ_w) and the dynamic pressure:

$$c_f = \frac{\tau_w}{1/2\rho U_\infty^2}$$

where ρ is the density, U_∞ the freestream speed. On its turn, the wall shear stress is given by:

$$\tau_w = \mu \frac{dU}{dy}\bigg|_{y=0} \tag{1.1}$$

where μ is the viscosity, y is the wall-normal direction and U is the velocity that changes going towards the wall. A comparison of a typical laminar and turbulent boundary layer is shown in figure 1.1b. The velocity profile of a turbulent boundary layer is much fuller compared to the laminar flow and the derivative $\frac{dU}{dy}$, close to the wall, is clearly higher in the turbulent case, creating a larger shear stress τ_w.

Among all the contributions to the total drag on a commercial aircraft wings at cruise speed, the skin friction drag is approximately 50% (Goldhammer and Plendl, 2014). In particular, the laminar flow is limited to a narrow region close to the leading edge. It emerges that one possibility to reduce drag, which means less fuel consumption, and therefore less pollutants emitted, is to delay laminar to turbulent transition. A more detailed quantitative analysis of the benefit of laminar flow is reported in Green (2008).

Historically, the idea of Laminar Flow Control (LFC) was developed driven by a completely different aim. During the World War II, the British government appointed the North American Aviation to design and construct a new fighter aircraft for the Royal Air Force, the P-51 Mustang shown in figure 1.2 (Green, 2008). The aircraft is still remembered as one of the most successful project of that period thanks to the natural laminar flow wings. In the following decades, the interest for the laminar flow has been always oscillating with the price of oil. Many works have demonstrated the feasibility of the different solutions, such as laminar flow control through suction, but the aviation companies have never been persuaded to manufacture laminar flow aircraft.



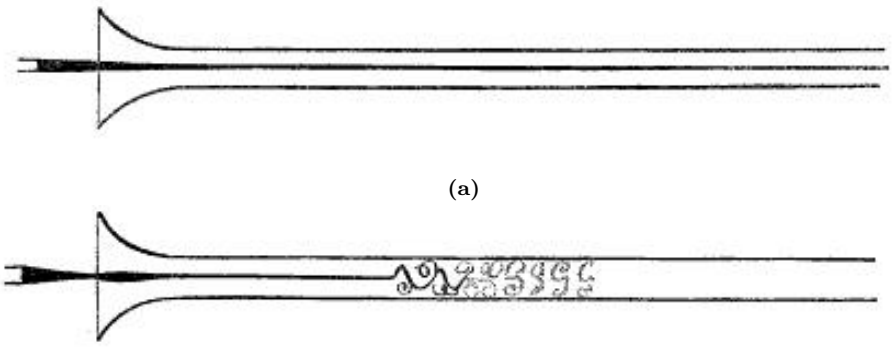
Figure 1.2: North American Aviation P-51 Mustang. Source: https://nationalinterest.org/blog/buzz/why-nothing-could-stop-p-51-mustang-30287.

Nowadays, due to the mentioned concern for CO_2 emissions and air pollution, the interest in the laminar flow technologies has raised again. The researchers are focused on two different ways to deal with transition. On one side, the optimisation of the wing design in order to obtain the laminar flow as much as possible. On the other side, the companies are looking for simple technical solutions to delay transition with either passive systems, such as roughness, or active systems, such as suction or blowing. Some of them have resulted promising, but the key point to be able to develop a system to prevent transition is the understanding of the physical processes involved. The topic is particularly challenging for research since the mechanisms that trigger transition are several, depending on the flow conditions and the environmental conditions which are often difficult to control.

1.2 Brief history of transition

Reynolds (1883) studied the flow into a long straight pipe with constant cross-section and smooth walls at different velocities using colour filaments. He observed that at low velocities every particle moves with constant velocity and the injected colour appear as straight lines (figure 1.3a). As soon as the velocity increases, the colour mix up with the surrounding water. By using a light of an electric spark, Reynolds observed distinct curls, indicating that the

flow was organised in eddies.



(a)

(b)

Figure 1.3: Reynolds (1883) experiment, evolution in a pipe flow: a) laminar b) turbulent.

Reynolds was able to demonstrate the existence of a critical velocity causing the laminar to turbulent transition. In addition, he was able to describe the phenomenon through few dimensional parameters combined in a non-dimensional group:

$$Re = \frac{\rho U_\infty D}{\mu} \tag{1.2}$$

where ρ and μ are respectively the density and the viscosity of the fluid, U_∞ its speed and D a characteristic length, i.e. the diameter in the case of the pipe. The Reynolds number (Re) represents the ratio between the inertial and the viscous forces.

Later, it was demonstrated that the Reynolds number gives a reliable criterion to determine whether the flow is laminar or turbulent in many cases, such as flows in a pipe or on a flat plate, but often it is not sufficient. In the years after Reynolds' experiment the transition mechanism has been widely studied. In 1914 Prandtl was able to show experimentally that the boundary layer itself can be either laminar or turbulent. He assumed that the viscous boundary layer can be unstable. But only years later, with the works by Tollmien (1923) and Schlichting (1933), a theoretical model of flow instability was proposed. Furthermore, only after the experiments by Dryden (1946) and Schubauer and Skramstad (1947) the theoretical model was actually confirmed and accepted (Schlichting, 1960).

After the second world war up to the nowadays, enormous progress has been made in the field, but the complicated nature of the topic has led to more advanced mathematical models accompanied by more elaborate experimental setups. It has been found that several mechanisms can establish the condition for transition. Furthermore, the processes are trigged by different disturbance sources (roughness, sound, turbulence, etc.) interacting with the boundary layer differently, and often not easy to control. A reliable model able to predict the transition from laminar to turbulent in all the situations has not been found yet.

1.3 Transition mechanisms

As mentioned, the transition mechanisms are usually trigged by *disturbances* interacting with the boundary layer making the flow unstable, as it was observed by Schubauer and Skramstad (1947). The authors classified the disturbances in two groups, the internals, such as vibrations, geometry and roughness, and the externals, disturbances coming from outside, such as turbulence or sound. In addition, the disturbances can naturally occur (i.e. freestream turbulence, sound) or be artificially generated (i.e. vibrating ribbon, localised suction/blowing).

The process by which the disturbances are fed into the boundary layer is called *receptivity*. It is considered the first stage of the transition process.

A schematic view of the transition process stages was proposed by Morkovin (1994) as shown in figure 1.4.

When the level of disturbances is particularly high, turbulent flow seems to occur immediately, almost naturally. This mechanism, called *bypass* (path C in figure 1.4), is still not fully understood. The name indicates that the flow bypasses the linear process, since, experimentally, the flow becomes turbulent in a very short time making the process very difficult to be observed.

With reference to figure 1.4, following paths B the second possible stage is the *transient growth*. This process is related to the eigenfunctions, which are part of the solutions of the stability equations, not being orthogonal. This means

that two eigenmodes, having different time rates, may still interact and generate an algebraic growth over a short time (Schmid and Henningson, 2012). Experimentally, the transient growth has been observed in environments with high levels of freestream turbulence and it manifests as streamwise vortical structures (Fransson et al., 2004). It is hypothesised that transient growth and by-pass transition are somehow related, but again this is an open field of research.

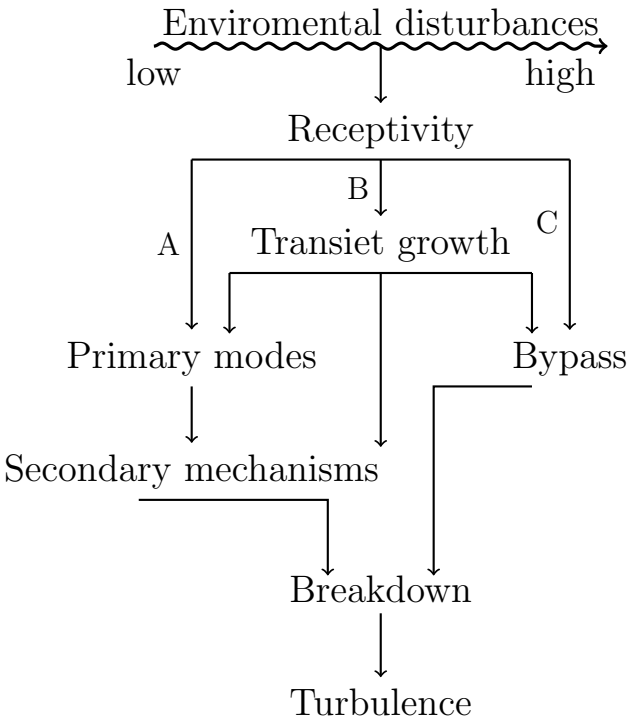


Figure 1.4: Transition path, modified from Morkovin (1994).

For small amplitude of the environmental disturbances, the transition mechanism follows the most common and validated path, A in figure. The receptivity is followed by the linear growth stage, where small disturbances are amplified exponentially (*primary modes*). Once the disturbances are grown to a finite amplitude, with the boundary layer being saturated, the process goes to the non-linear stage, where *secondary instability mechanisms* are present. The last stage is the breakdown, in which structures of different scales and frequencies are excited by the non-linear mechanisms and the flow becomes completely turbulent.

1.4 Hydrodynamic stability theory

A dynamic system is considered *stable* if, when perturbed by a disturbance, returns in its original state, whereas it is considered *unstable* if the disturbance grows. In a flow field, the latter case would correspond to the laminar to turbulent transition. Generally it is described by the *hydrodynamic stability theory*.

The basic assumption was conjectured by Reynolds (1894): the laminar flow is always a possible solution of the equations of motion (Schlichting, 1960). The hydrodynamics stability theory, in fact, analyses the response of the laminar boundary layer to disturbances of small or moderate amplitude (Schmid and Henningson, 2012).

A wide review of the hydrodynamic stability theory may be found in many well-known books, as those by Drazin and Reid (1981), Schlichting (1960), Schmid and Henningson (2012).

Linear stability theory

The motion of a viscous fluid flow is described by the *Navier-Stokes equations*, which include the conservation of mass and the conservation of the momentum. For an incompressible flow in dimensionless units it is:

$$\nabla \cdot \overrightarrow{U} = 0 \tag{1.3}$$

$$\frac{\partial \overrightarrow{U}}{\partial t} + (\overrightarrow{U} \cdot \nabla)\overrightarrow{U} = -\nabla P + \frac{1}{Re}\nabla^2 \overrightarrow{U} \tag{1.4}$$

where $\overrightarrow{U}$ is the velocity field, P the pressure and Re the Reynolds number. With appropriate boundary conditions, this set of equations describes the fluid motion in any circumstance[4]. However, since a general solution of the equations has not been found yet various assumptions need often to be adopted to simplify the problem.

Let define the base state flow in motion over a body (where x is the chordwise coordinate, y is the wall normal and z the spanwise), with the velocity

[4] In the presence of external forces an extra term needs to be added.

$\overrightarrow{U}(x,y,z)$ and the pressure $P(x,y,z)$, which is a solution of the Navier-Stokes equations and whose stability is the object of the investigation. The linear stability analysis superimposes to the stationary basic state flow a perturbation $\overrightarrow{u}(x,y,z,t)$, $p(x,y,z,t)$. The total flow field, sum of the basic flow and the fluctuation has to be, on its turn, solution of the Navier-Stokes equations:

$$\nabla \cdot \overrightarrow{u} = 0 \tag{1.5}$$

$$\frac{\partial \overrightarrow{u}}{\partial t} + (\overrightarrow{u} \cdot \nabla)\overrightarrow{U} + (\overrightarrow{U} \cdot \nabla)\overrightarrow{u} + (\overrightarrow{u} \cdot \nabla)\overrightarrow{u} = -\nabla p + \frac{1}{Re}\nabla^2 \overrightarrow{u} \tag{1.6}$$

The analysis seeks solutions of these unsteady, non-linear equations, which describe the evolution of the perturbed flow. In this form the equations are quite complicated to be solved and also to get a numerical solution they would require a high powered computer (Saric, 2008). For these reasons, often some simplifications are assumed. The first assumption is that the disturbances are infinitesimal, therefore the second-order term $(\overrightarrow{u} \cdot \nabla)\overrightarrow{u}$ can be neglected since u is much smaller than U (linear disturbance equations).

A second assumption is that the basic flow does not have a wall normal velocity component (V), and the spanwise (W) and streamwise (U) are only function of the y coordinate, that is $\overrightarrow{U} = (U(y), 0, W(y))$. This *parallel flow assumption* is clearly an idealisation, since the streamwise velocity depends also on the streamwise coordinate x; but in some cases the dependence on the x coordinate is much smaller compared to y, therefore the assumption gives results well comparable to the experiments (i.e. flat plate flow). For the pressure the dependence on both coordinates must still be considered ($P(x,y)$).

The linear disturbance equations, considering the parallel flow assumption, projected on the (x,y,z) axis become:

$$\frac{\partial u}{\partial x} + \frac{\partial v}{\partial y} + \frac{\partial w}{\partial z} = 0 \tag{1.7}$$

$$\frac{\partial u}{\partial t} + U\frac{\partial u}{\partial x} + W\frac{\partial u}{\partial y} + v\frac{dU}{dy} = -\frac{\partial p}{\partial x} + \frac{1}{Re}\nabla^2 u \tag{1.8}$$

$$\frac{\partial v}{\partial t} + U\frac{\partial v}{\partial x} + W\frac{\partial v}{\partial z} = -\frac{\partial p}{\partial y} + \frac{1}{Re}\nabla^2 v \tag{1.9}$$

$$\frac{\partial w}{\partial t} + U\frac{\partial w}{\partial x} + W\frac{\partial w}{\partial z} + v\frac{dW}{dy} = -\frac{\partial p}{\partial z} + \frac{1}{Re}\nabla^2 w. \tag{1.10}$$

The solution of this linear system of equations can be found considering a wave-like disturbance:

$$\overrightarrow{q'}(x, y, z, t) = \overrightarrow{q}(y)e^{i(\alpha x + \beta z - \omega t)} \tag{1.11}$$

where $\overrightarrow{q'}$ represents any of the disturbance quantities, for instance $\overrightarrow{q'} = [u, v, w, p]$. In equation 1.11, α, β and ω are complex quantities representing respectively the chordwise wave number, the spanwise wave number and the frequency. In the same way, $\overrightarrow{q}(y)$ is a complex quantity, while $\overrightarrow{q'}(x, y, z, t)$ has to be real, since the Navier-Stokes equations are real.

By substituting the disturbances in the equations 1.4 and after some manipulations, the well-known *Orr-Sommerfeld equation* can be derived:

$$\frac{d^4v}{dy^4} - 2k^2\frac{d^2v}{dy^2} + k^4v - iRe\Big[(\alpha U + \beta W - \omega)\Big(\frac{d^2v}{dy^2} - k^2v\Big) - \Big(\alpha\frac{d^2U}{dy^2} + \beta\frac{d^2w}{dy^2}\Big)\Big] = 0 \tag{1.12}$$

where $k^2 = \alpha^2 + \beta^2$. The Orr-Sommerfeld equation is a complex 4th-order linear differential equation Schlichting (1960). The stability analysis is, now, an eigenvalue problem of the perturbation equation that can be solved with appropriate boundary conditions. For a given basic flow $(U(y), 0, W(y))$, it exists only a specific combination of the parameters (α, β, ω, Re) who satisfy the equation 1.12. In the linear stability analysis, usually, the equations are solved for different Re numbers varying the other parameters. In particular, the analysis seeks for the limit of stability to obtain the *neutral stability curve*. This curve identifies, for each Re, which wave number makes the flow unstable. The lowest Re at which an instability is possible is called indifferent Reynolds number (Re_{ind}). An example is reported in Chapter 2, figure 2.14.

The imaginary part of α, β and ω (denoted by α_i, β_i and ω_i) determines if the solution is stable or unstable (see figure 1.5).

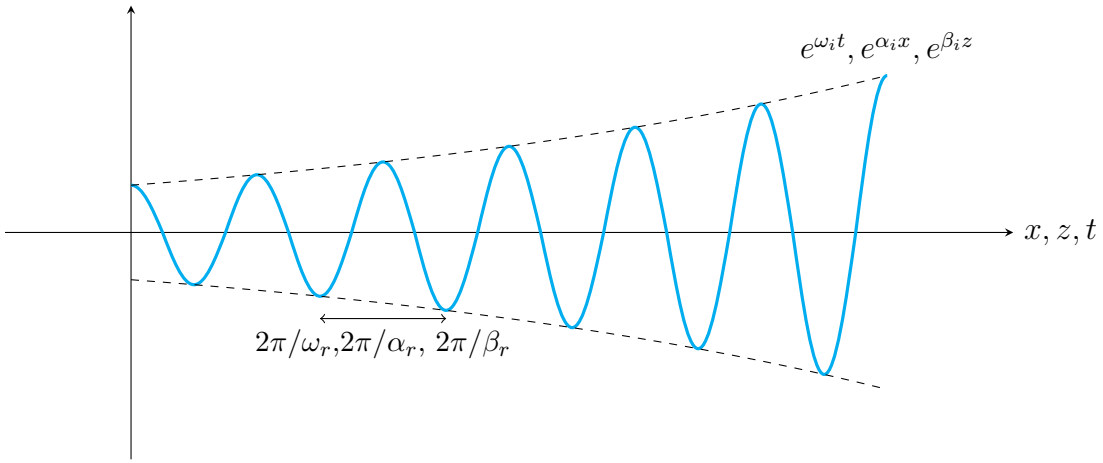


Figure 1.5: An example of wave growing in time and space ($\alpha_i, \beta_i, \omega_i$ positive).

Generally, the disturbances can be amplified spatially, temporally or both spatially and temporally:

- for a temporal stability analysis ω is complex, while α and β are real. If ω_i is positive, the disturbance grows in time and the flow is unstable;
- for the spatial analysis ω and β are assumed to be real, while streamwise wave number α is complex. If α_i is positive, the disturbance grows in space.

Clearly, the spatial analysis is more laborious. For small temporal or spatial growth and values of the parameters close to the neutral curve, the temporal stability can be converted in the spatial one through the *Gaster's transformation* (Gaster, 1962).

Rayleigh's inflection point criterion

If the instability under investigation is inviscid, in the limit of large Reynolds numbers, the Orr-Sommerfeld equation (eq. 1.12) becomes the Rayleigh equation:

$$(U-c)\left(\frac{d^2v}{dy^2}-\alpha^2 v\right)-\frac{d^2U}{dy^2}v=0 \tag{1.13}$$

where the spanwise component is omitted and $c=\omega/\alpha$ is the complex wave speed. In earlier works on instability this was the equation mostly used. Lord Rayleigh was already able to determine some very important theorems about

instability. In particular, he demonstrated the *inflection point criterion* which affirms that an inflection point in the velocity profile is a necessary condition for the flow to be unstable. It can be shown that multiplying the equation 1.13 by its complex conjugate and integrating with respect to y, the imaginary part of the equation becomes:

$$c_i \int_{y_1}^{y2} \frac{1}{(U-c_r)^2 + c_i^2} \frac{d^2U}{dy^2} |\hat{v}|^2 dy = 0, \tag{1.14}$$

where c_i is the imaginary part of c. If $c_i > 0$, then $\frac{d^2U}{dy^2}$ has to be zero between y_1 and y_2, which means that the base flow velocity has an inflection point.

e^N-method

As mentioned, the numerical methods to solve the stability analysis require a lot of computational time even with the modern computers. On the other hand, experimental investigations are also expensive and time consuming and can only provide a limited amount of test cases. For these reasons, the aviation industry has been looking for simple and quick criteria to predict the transition location in support of the wing design. In particular, the e^n-method, or N-factor method, is a well-established, and probably the most popular, methodology used to predict transition location. The e^N-method is briefly described here since it has been used to design the model for the experiment reported in Chapter 5.

The e^N-method was developed independently by Van Ingen (1956) and Smith and Gamberoni (1956) for two-dimensional low speed flows and it was extended in the '90s to three-dimensional flows. The assumption is that there exists a critical amplification rate (N) at which the laminar to turbulence transition occurs (Saric, 2008).

Consider a disturbance, defined by equation 1.11, at a generic x-location with amplitude $A = e^{\alpha_i x}$. In a second location at distance dx downstream, the amplitude becomes $A + dA = e^{\alpha_i (x+dx)}$. The amplitude of the disturbance

increases or decreases according to the ratio:

$$\frac{A + dA}{A} = \frac{e^{-\alpha_i x}}{e^{-\alpha_i (x+dx)}} \tag{1.15}$$

which becomes:

$$ln(A + dA) - ln(A) = -\alpha_i dx. \tag{1.16}$$

To observe the behaviour of the disturbance from a certain location x_0, where the disturbance has amplitude A_0, the equation can be integrated as:

$$N = ln(A/A_0) = \int_{x_0}^{x} -\alpha_i dx. \tag{1.17}$$

The result of this integration is the N-factor, and it can be calculated for each wave number. The method works assuming a certain threshold for N at which the flow becomes unstable. The threshold usually comes from experimental observations.

The method was initially developed based on linear theory, although there have been attempts to extend the methodology to non-linear stability analyses. It works, within some error limits, only for small and well-specified disturbances (Saric, 2008).

1.5 Primary modes

Going back to path A of figure 1.4, for a three-dimensional boundary layer four types of primary modes are generally identified:

- *Tollmien-Schlichting* (TS waves), waves propagating in the streamwise direction;
- *Görtler vortices*, counter-rotating vortices on a concave surface;
- *Attachment-line mechanisms*, due to disturbances propagating in the spanwise direction at the attachment-line;
- *Cross-flow* (CF), co-rotating vortices on rotating disk and swept wings.

In the next sections a brief overview of those types of instability is presented.

1.5.1 Tollmien-Schlichting

The Tollmien-Schlichting instability is a viscous instability characterised by temporal unstable waves growing in the streamwise direction. It was postulated in the '30s by Tollmien (1929), and Schlichting (1933) for a Blasius boundary layer. At the beginning the theory did not received a wide acceptance since, at that time, it was really difficult to build a wind tunnel with a level of turbulence intensity low enough to allow the observation of the predicted unstable waves. Only in 1943 did Schubauer and Skarmstad demonstrate the existence of this viscous instability, with an experiment published a few years later due to the war (Schubauer and Skramstad, 1947).
Since then, many experimental and computational studies have been carried out. A further description of the TS evolution and breakdown together with an historical literature review can be found in Mack (1984) and Schlichting (1960).
This instability may appear on swept wings, although a favourable pressure gradient has a stabilising effect on the TS waves.

1.5.2 Görtler vortices

The basic idea behind the Görtler instability is that the shear flow over a concave wall can be subjected to centrifugal instability. The idea comes from the Rayleigh circulation criterion which states that for a circular geometry, described by the curvilinear coordinates (r, θ, z), and a basic flow $\overrightarrow{U} = (0, V(r), 0)$ (respectively the radial, tangential and axial velocity components), the necessary and sufficient condition for the existence of an inviscid axis-symmetric instability is $d(\Gamma^2)/dr < 0$ everywhere in the flow, with Γ being the circulation ($\Gamma = rV$). Figure1.6 shows some examples of the criterion.
If the viscosity is considered, the Rayleigh criterion is only a necessary condition. The criterion was applied to the instability analysis of different types of flow. For instance, Taylor investigated the Coette flow, and Dean the channel flows.

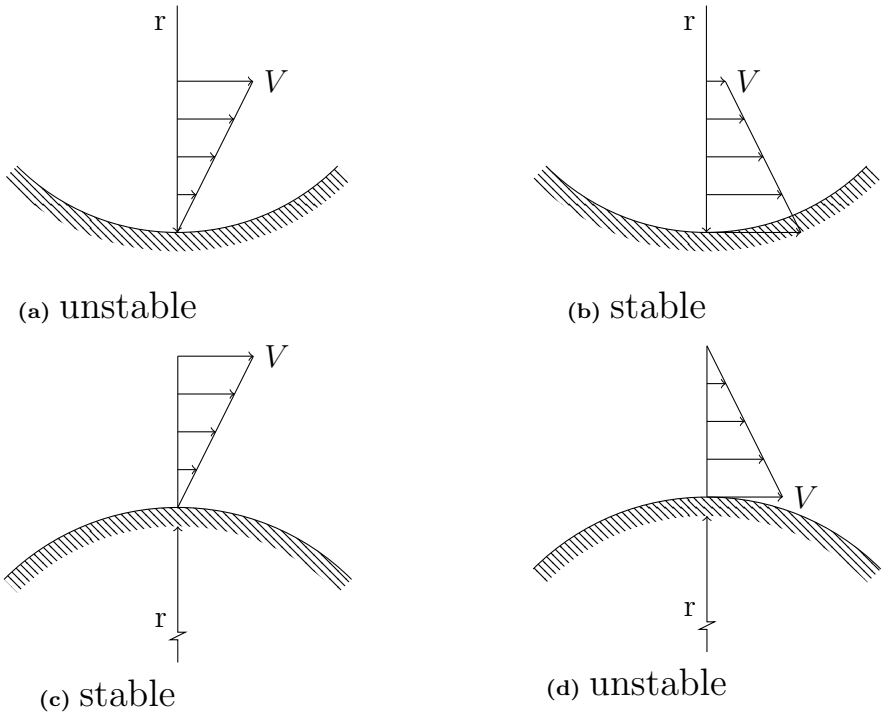


Figure 1.6: For the Rayleigh circulation criterion the flow in b) and c) is stable, while in a) and d) is unstable (modified from Saric (1994)).

The first application on boundary layer was presented by Görtler (1941), who considered the boundary layer travelling over a concave surface (figure 1.7). Görtler showed that for a boundary layer travelling on a concave wall, the instability forms streamwise counter-rotating vortices, which eventually become unstable. The fundamental consideration in Görtler's analysis is that the original wavelength of the vortices is preserved, therefore the instability is described by a single wavelength. Mathematically, the main difficulty is that the parallel flow assumption cannot be used on a curvilinear wall.

The Görtler instability causes transition on many common fluid systems, such as a supersonic nozzle and turbine-compressor blades, etc. A review of this type of instability has been given by Saric (1994). It has been demonstrated that the Görtler instability vortices can destabilise TS-waves on two-dimensional flat plate.

The linear instability in the case of a swept wall with variable curvature was studied by Hall (1985). In this case, the presence of a sweep angle, together with a pressure angle, create the condition for the cross-flow vortices, as it will be shown later. The cross-flow vortices are co-rotating, the opposite of the

counter-rotating vortices described by Görtler. If the swept body has a curvilinear surface and if the Rayleigh circulation criterion is verified, in principle there are the conditions for both the instabilities. Hall (1985) demonstrates that under moderate sweep angles, the Görtler vortices are suppressed by the presence of crossflow.

In addition, another region in which the Rayleigh criterion is verified is the stagnation region of bluff bodies. Therefore, in that region, the Görtler instability should be observable, but Stuart (1984) has demonstrated that such an instability does not occur.

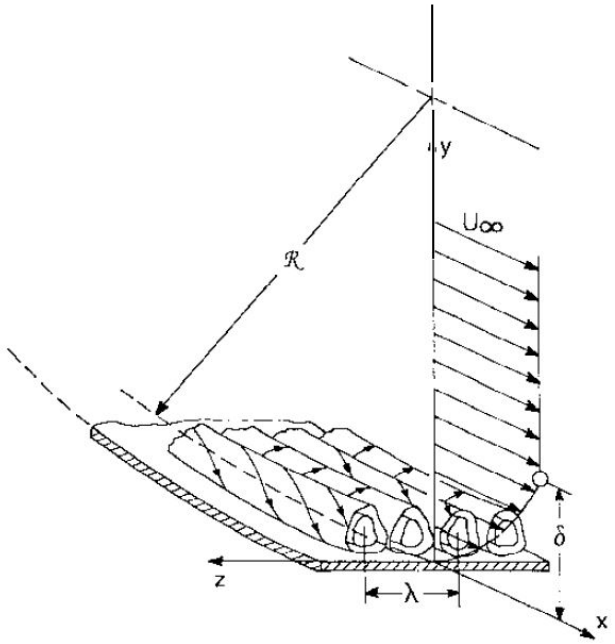


Figure 1.7: The Görtler instability, the boundary layer on concave walls produces unstable vortices. Figure from Saric (1994).

1.5.3 Attachment-line mechanisms

The attachment-line of a swept wing is the streamline at the leading edge where the flow impinges. The flow at the attachment-line is tangential to the leading edge uniquely in the spanwise direction. Since the flow has to be at rest at the wall, and since the spanwise velocity component is not zero, there exists a boundary layer along the attachment-line.

Two main mechanisms may affect the nature of the attachment-line boundary

layer: attachment-line contamination and attachment-line instability. Historically, these mechanisms and the cross-flow instability were discovered simultaneously.

The attachment-line contamination is not an instability, but it makes the attachment-line boundary layer turbulent. It is due to disturbances from the fuselage propagating along the spanwise attachment-line of a swept-back wing, which may render the flow turbulent. Instead, the attachment-line instability is a spatial instability that can occur at particularly high Reynolds numbers. The flow at the attachment-line of a swept wing will be described in detail in Chapter 2 together with a more comprehensive literature review about the two mechanisms just mentioned.

1.5.4 Cross-flow

The crossflow instability is an inviscid instability due to a combined effect of the pressure gradient and the streamlines curvature; for instance, it occurs on swept wings and on rotating disks.

The sketch in figure 1.8 shows the flow over a swept wing of a constant chord and infinite span. Two coordinates systems are usually defined: (X,Y,Z) based on the wing geometry and (x,y,z) following the external streamline, both with the y-direction being normal to the surface.

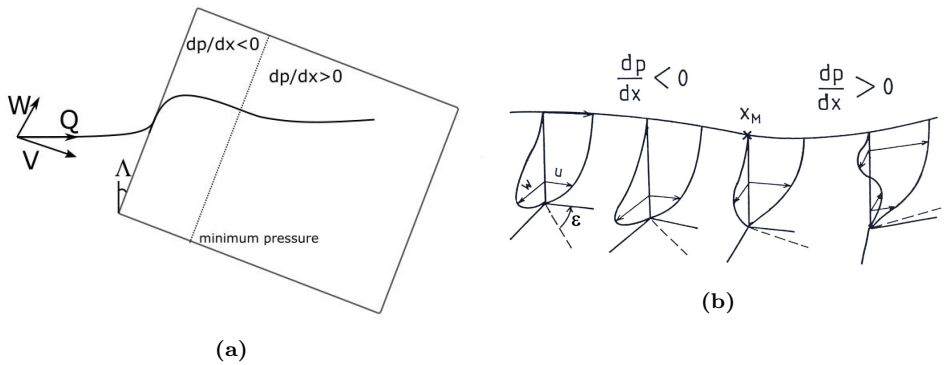


Figure 1.8: a) Inviscid streamline on a swept wing, b)generation of the cross-flow (Arnal and Casalis (2000)).

At the attachment line, the velocity is parallel to the spanwise direction. Over the wing, in the inviscid region, the streamwise velocity increases due to a favourable pressure gradient ($dp/dx < 0$) leading to a curvilinear inviscid streamline. The curvilinear streamline generates a centripetal velocity which is balanced by the pressure gradient in the inviscid region.

Inside the boundary layer, the streamwise velocity reduces, and so the centripetal force, while the pressure gradient remains unchanged since it depends only on the outer flow. Thus, the pressure gradient and the centripetal acceleration are not balanced (Saric et al., 2003). This imbalance creates a secondary flow in the boundary layer, perpendicular to the direction of the inviscid streamline. The velocity component in this direction is called the *cross-flow velocity*. Since the cross-flow velocity has to be zero on the wall and zero at the edge of the boundary layer, an inflection point must exist within the boundary layer (as shown in figure 1.8). According to the Rayleigh stability criterion, the inflection point is a sufficient condition for an inviscid instability. Although the cross-flow component is weak, about 5-10 % of the freestream velocity, its effect can destabilise the flow. Going back to figure 1.8, after point x_M,the pressure gradient decreases along the streamline and eventually becomes zero. In this region, the cross-flow velocity inside the boundary layer is weaker. In the last region, where the pressure gradient starts increasing ($dp/dx > 0$), the streamlines change the curvature and the cross-flow velocity close to the wall reverses, creating the characteristic s-shape profiles which generates the cross-flow spanwise vortices (see figure 1.9).

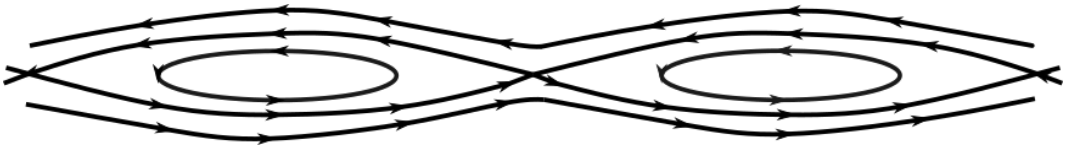


Figure 1.9: Schematic of co-rotating cross-flow vortices.

In this instability mechanism both stationary and travelling modes are present, although transition will be caused by one or the other, but not both of them. Whether the travelling or the stationary unstable modes dominate the instability, depends on the source of disturbances. In particular, Deyhle et al.

(1993) found that an increase in freestream disturbances lead to a travelling dominating scenario, while the presence of roughness triggers the stationary modes leading to a stationary modes dominated instability, although the two receptivity sources may interact.

The cross-flow instability was discovered by Gray (1952) during a flight test. Gray observed that the transition front on swept wings is moved much closer to the leading edge compared to unswept wings. The observation was followed by china clay flow visualisation that revealed a regular pattern of striations over the swept wing. These observations led to a series of further investigations, among which Gregory and Walker (1952) confirmed the existence of the phenomenon and observed the same three-dimensional instability in a rotating disk. In the latter case, the cross-flow velocity component in the radial direction is due to the centrifugal forces generated by the rotation of the disk.
Cross-flow instability has been subjected to many experimental and numerical studies. Reviews can be found in Bippes (1999), Arnal and Casalis (2000), Saric et al. (2003).

1.6 Influence of freestream turbulence

The generation of the unstable modes requires the presence of artificial or natural disturbances that interact with the boundary layer through a receptivity process. Among the natural disturbances, it has been highlighted that the freestream turbulence influences the nature of the cross-flow instability, determining whether it is stationary or travelling-wave dominated.
The freestream disturbances consists of two types: vortical (turbulence) and irrotational (sound) (Saric et al., 2003). The difference is that acoustic disturbances propagate at the speed of sound, while vortical disturbances are convected at the freestream speed. In contrast, the phase speed ($c = \omega/\alpha$) of the unstable wave is a fraction of the freestream speed. This means that the receptivity mechanism requires a wavelength conversion process.

The concept was introduced by Goldstein (1983, 1985) who studied the receptivity of TS waves on a Blasius flow, demonstrating that natural receptivity occurs in regions where the mean flow changes rapidly in the streamwise direction. Two regions were identified: (1) body leading edge region where the boundary layer grows rapidly; (2) downstream regions with localised surface non-uniformity, i.e humps or suction strips, were the mean flow has to adjust on a short streamwise length scale. He carried out an asymptotic analysis, showing that the freestream disturbances with large wavelength can trigger TS waves with smaller wavelength. For acoustic freestream disturbances it was found that the receptivity mechanism is effective only in the second region. Experimentally, the receptivity due to freestream disturbances on two-dimensional boundary layer has been widely studied in literature. A review of more recent works regarding receptivity of two-dimensional flows can be found in Saric et al. (2003).

The receptivity due to freestream turbulence of three-dimensional swept wings boundary layers is a relatively more recent field of investigation. The first experimental investigations were carried out on a swept flat plate with a displacement body placed at a certain height above the plate by Bippes and Mueller (1988), Deyhle et al. (1993), Bippes (1999). The displacement body was used to create the desired pressure distribution that would make the cross-flow instability grow. The experiments were performed in different wind tunnels with turbulence intensity in the range of $0.08\% \leq Tu \leq 0.57\%$. In the wind tunnels with lower turbulence intensity, a transition dominated by stationary cross-flow modes was observed, while in the wind tunnels with an higher turbulence intensity the transition was dominated by travelling cross-flow instability. The results have been confirmed by many authors. White et al. (2001) carried out an experimental investigation on a swept wing at different levels of turbulence intensity, finding that at $Tu \geq 0.2\%$ the instability was travelling-modes dominated. The work was followed by Downs and White (2013) who tested five turbulent generating grids varying the level of turbulence from 0.016% to 0.190%. Kurian et al. (2011) studied a swept flat plate with different turbulence generating grids, finding, as well, the threshold for the instability through

travelling modes at $Tu = 0.2\%$.

All the experiments mentioned involved the use of discrete roughness placed on the surface. It was demonstrated that the roughness establishes the initial condition for stationary cross-flow modes; while the freestream turbulence establishes the initial conditions for travelling cross-flow modes. In particular, when the freestream turbulence increases, the amplitude of the travelling cross-flow modes increases accordingly, while the stationary cross-flow modes are damped. It was observed that if the turbulence intensity is increased slightly ($Tu = 0.15\%$) the stationary modes are still predominant in the transition mechanism but their growth is reduced and the transition front delayed (Bippes, 1999). This means that the two types of disturbances, the roughness which is a stationary disturbance and the freestream turbulence which is a travelling disturbance, trigger two receptivity mechanisms that may interact. Schrader (2008) carried out a direct numerical simulation (DNS) on a swept flat plate with a pressure gradient. The receptivity study considered again two type of disturbances, a vortical freestream turbulence and the roughness finding the numerical limit for stationary dominated instability to be $Tu \leq 0.5\%$. The discrepancy between the DNS and the experimental works is influenced by the way the turbulence intensity is defined. In the DNS, the freestream disturbance was modelled by a single mode. In the experiments, the turbulence intensity is defined with respect to the band pass velocity fluctuations, generally from 2 Hz to 10 kHz. In addition, the signal is influenced by a series of electronic or environmental noises that vary with the wind tunnel conditions. In a more recent experimental work, Borodulin et al. (2017) investigated cross-flow instability in 39 different regimes using four turbulence generating grids ($0.054\% \leq Tu \leq 0.19\%$), and no grid installed, two types of distributed roughness and different freestream speeds. The model used was a 35° swept flat plate with a bump on the roof of the wind tunnel to create a desired pressure distribution. In agreement with previous investigations, the author described the following scenario:

- *low turbulence environment*, the instability is dominated by steady cross-

flow; the transition begins with appearance of local high-frequency secondary instability which appear at the apexes of the turbulent wedges;

- *high turbulence environment*, the instability is dominated by the travelling modes; the high frequencies, which determine the onset of the transition, appear intermittent in the time signal; the transition front does not present turbulence wedges and it is uniform in the spanwise direction.

The receptivity of cross-flow instability to the acoustic freestream disturbance was studied by Deyhle et al. (1993) in an experiment in which the sound wave was produced using a speaker. The sound produced large fluctuations in the freestream, but the boundary layer was unaffected and the transition front did not change. Similar results were found by Radeztsky et al. (1999), both the experiments were looking at stationary cross-flow dominated instabilities. Numerical study on Falkner-Skan-Cooke boundary layer by Crouch (1992) and Choudhari (1994) demonstrated that only the travelling waves are receptive to the acoustic disturbances.

1.7 Motivation of the thesis

The literature review reveals that the freestream turbulence interacts with the boundary layer and plays an important role in the receptivity mechanisms. The turbulence intensity in flight conditions is known to be much lower ($Tu = 0.05\%$ according to Riedel and Sitzmann (1998)) than that achieved in most of the wind tunnel facilities. It is, therefore, extremely important to understand the exact mechanisms behind the freestream turbulence and the boundary layer interaction to allow a correct interpretation of the experimental results. In addition, the boundary layer transition is a mechanism important also in applications where the level of the disturbances may be higher.
The idea of the present work has been to try to analyse the physical mechanism of freestream turbulence interacting with the boundary layer. In particular,

the work has focused on the flow approaching the leading edge of a swept body. As mentioned in the previous section, already Goldstein (1983, 1985) observed that the leading edge region plays a role in the receptivity problem of a Blasius boundary layer. For instance, Hanson et al. (2012) optimised the leading edge geometry for experiments on laminar to turbulent transition of unswept flat plate. The present work focuses on the freestream turbulence distortion in the region upstream of the swept leading edge and on the interaction with the attachment-line boundary layer. The main motivation is to provide a contribution to the understanding of the freestream turbulence and cross-flow interaction. Some authors have previously tried to address a similar problem, i.e. Seddougui (1990) suggested a connection between attachment-line and cross-flow instability, Bertolotti (2000) attempted a numerical analysis which turned out to be quite complicated.

1.8 Outline of the thesis

The thesis starts with a literature review on the two dimensional stagnation point flow; in particular the *vorticity amplification theory* is revisited. The theory predicts the amplification, due to the stretching, of freestream vorticity approaching a leading edge. It follows an examination of the flow at the attachment line, which reveals that the vorticity amplification theory has not been investigated on a swept body. This has given a new motivation to the current investigation, since the topic may be of interest also in several engineering fields, i.e. turbomachinery.

The investigation itself has been carried out through wind tunnel experiments. The first attempt was carried out on a vertical flat plate inserted in a faring body, or, in other words, a swept wing with a blunt leading edge. The aim of the model was to investigate simultaneously the vorticity amplification at the leading edge and the receptivity of cross-flow instability. The model has been investigated in a low turbulence wind tunnel using a single hot-wire anemometry. A leading edge disturbance amplification in the low turbulence

environment was not found. To create a controlled freestream turbulence disturbance, a tiny wire has been installed upstream of the model, vertically and horizontally oriented. The experimental investigation, carried out at different flow conditions, revealed that the use of the wire to convect a vortex towards the attachment-line is quite a complicated technique.

A second set of experiments has been carried out on a circular cylinder mounted initially straight and later at four different low sweep angles (5° to 30°) using multi-component laser Doppler anemometer in a wind tunnel with a relatively higher freestream turbulence level. The advantage of the latter wind tunnel is that a freestream disturbance was naturally present, although random and chaotic. The measurement technique has allowed to gather information on the three velocity components at the same time, which turned out to be useful to understand such three-dimensional flow. The different model configurations, unswept and swept, have allowed to identify how the sweep angle modifies the leading edge vorticity amplification.

In the last chapter on this thesis, the conclusions are accompanied by an analysis of suggested follow-up works.

Chapter 2

Flow in front of a leading edge

2.1 Stagnation point flow

2.1.1 The Hiemenz flow

A flow approaching a stationary solid two-dimensional surface decelerates until it encounters the wall and divides in two symmetrical streams about the so called attachment *stagnation point* (SP) to then becoming flow parallel to the surface (figure 2.1). The flow at the stagnation point is locally at rest and the velocity vanishes (SP in figure 2.1 at $x = y = 0$ where $V(0, 0) = 0$).

A stagnation point flow occurs in nature wherever a flow impinges on a solid surface. In many engineering applications the stagnation point assumes a critical role due to the establishment of a high rate of heat transfer, i.e. in gas turbine blade, turbulent combustion gas, micro-electronics cooling system or material processing.

The flow about this point is influenced by the streamlines rapidly curving to overcome the body, which is an obstacle for the flow.

The plane flow in the neighbourhood of the attachment stagnation point can be modelled as the flow impinging on an infinity vertical smooth flat plate. Following the Cartesian coordinate system in figure 2.1, the inviscid streamline

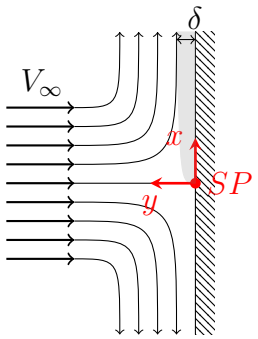


Figure 2.1: The flow against a vertical flat plate (Hiemenz flow). SP is the stagnation point from which the δ boundary layer grows.

function is $\Psi = axy$ and the velocity field is described by:

$$\overrightarrow{U} \begin{cases} U(x) = ax \\ V(y) = -ay \\ W = 0 \end{cases} \tag{2.1}$$

where a is a constant depending on the freestream velocity and dimension of the body. The pressure can be derived by applying the Bernoulli equation:

$$p = p_0 - \frac{\rho}{2}\, a^2(x^2 + y^2). \tag{2.2}$$

where ρ is the density and p_0 is the total pressure of the potential flow. At the stagnation point, the pressure reaches a maximum.

The viscous flow over a vertical flat plate was originally described by Hiemenz (1911), and it is often called after him *Hiemenz flow*. Hiemenz's intuition was to assume the streamfunction of the form $\Psi(x, y) = xF(y)$. Considering the dimensionless boundary layer coordinate $\eta = (a/\nu)^{1/2}y$, the streamfunction in the dimensionless coordinate system becomes $\Psi(x^*, \eta) = (\nu a)^{1/2}x^* f(\eta)$, where $x^* = (a/V_\infty)\, x$ and the velocity components are:

$$\overrightarrow{U} \begin{cases} U = axf'(\eta) \\ V = -\sqrt{a\nu} f(\eta) \\ W = 0. \end{cases} \tag{2.3}$$

Substituting in the dimensionless Navier-Stokes equations, and after some manipulations, Hiemenz found that the viscous flow is described by the third order differential equation:

$$f''' + f f'' - f'^2 + 1 = 0 \tag{2.4}$$

where the prime indicates the derivative respect to η.
The equation can be solved with the following boundary conditions at the wall and at the freestream:

$$\eta \to 0 \quad f = f' = 0; \quad \eta \to \infty \quad f' = 1 \tag{2.5}$$

In its turn, the pressure, considering the viscous solution, becomes:

$$p = p_0 - \frac{\rho}{2} \left(a^2 x^2 + \nu \, a \, f^2 + 2 \, \nu \, a \, f' \right) \tag{2.6}$$

Hiemenz (1911) calculated numerically the solution of equation 2.4, which is displayed in figure 2.2.

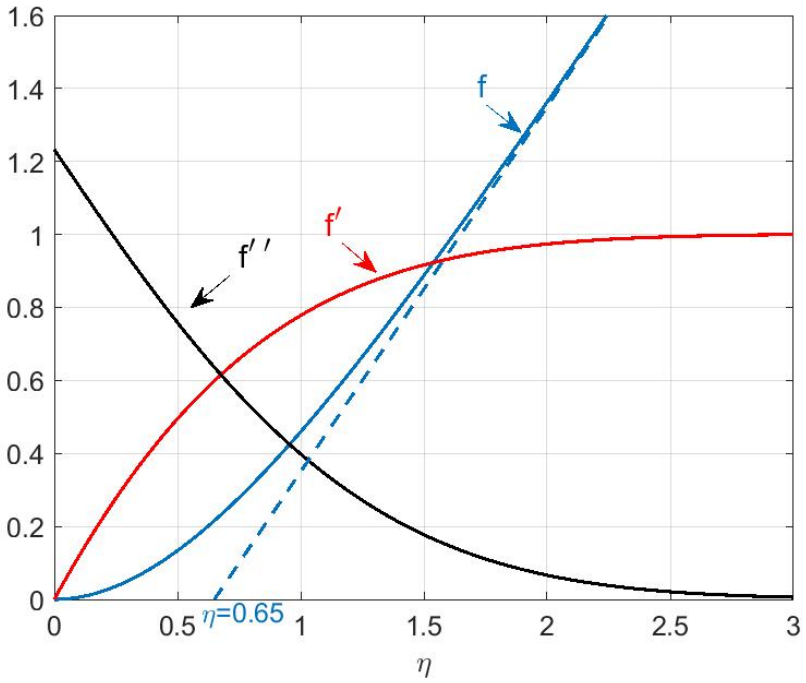


Figure 2.2: Viscous Hiemenz flow solution (continous curves) and the linear interpolation of the outer flow (dashed line).

The viscosity has a displacement effect on the inviscid velocity profile. The V-velocity profile (proportional to $f(\eta)$) tends to the inviscid straight line (dashed blue line in figure) at infinity, while the shape of the U-velocity profile is very similar to the classic boundary layer, i.e. Blasius flow, with the velocity approaching a constant value at infinity.
The boundary layer thickness, defined as the thickness at which the velocity is 99% of the freestream velocity ($u = 0.99\,U_\infty$), corresponds to:

$$\delta = \eta_{99}\sqrt{\frac{\nu}{a}} = 2.4\sqrt{\frac{\nu}{a}}.$$

To better characterise the shape, it is useful to refer to two integral quantities. In particular, the displacement thickness for the Hiemenz flow is:

$$\delta^* = \sqrt{\frac{\nu}{a}}\frac{1}{U}\int_0^\infty (U-u)d\eta \approx 0.65\sqrt{\frac{\nu}{a}}. \tag{2.7}$$

As shown in figure 2.2, the displacement thickness from equation 2.7 also corresponds to the displacement of the viscous solution:

$$\delta^* = \lim_{\eta\to\infty}[\eta - f(\eta)]. \tag{2.8}$$

A second integral quantity used to describe the boundary layer is the momentum thickness, that is a measure of the momentum loss in the friction layer:

$$\Theta = \int_0^\infty \frac{u}{U_e}\Big(1-\frac{u}{U_\infty}\Big)d\eta = 0.29\sqrt{\frac{\nu}{a}} \tag{2.9}$$

The ratio between the two integral parameters, the shape factor (H), characterises the boundary layer profile. For a Hiemenz flow it corresponds to $H = \delta^*/\Theta = 2.24$.

2.1.2 Hiemenz flow and enhancement of turbulence

The early observations

In 1928 Piercy and Richardson, while studying the generation of large-scale turbulence structures in the wake of a circular cylinder, measured the velocity

fluctuations in the entire flow field around the cylinder. The experiment reviled two main regions with higher turbulence intensity: the region where the flow develops in the wake and the area in front of the stagnation point (figure 2.3). The authors reported that the unsteadiness at the stagnation point attenuate around one third of the chord without being transported by the flow.

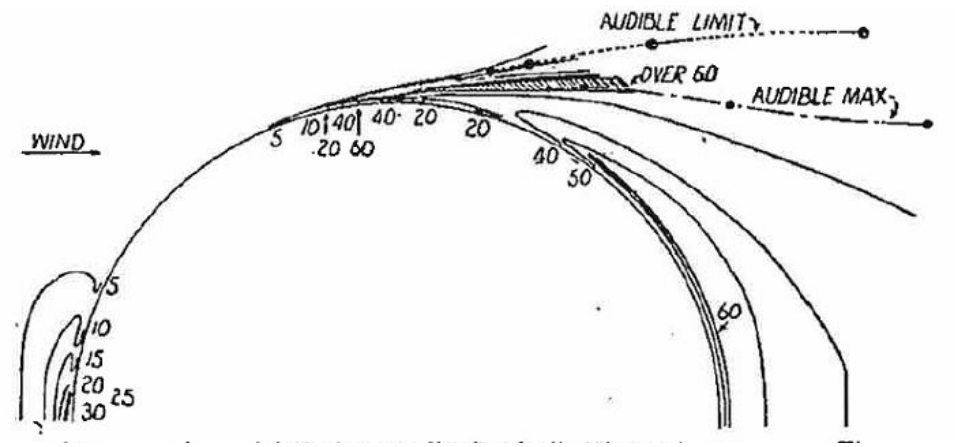


Figure 2.3: Contours of velocity fluctuations, measured through a vibration galvanometer around a cylinder immersed in a flow (left to right) by Piercy and Richardson (1928).

In 1930 the same authors repeated the experiment over an aerofoil, finding the same regions of unsteadiness (Piercy and Richardson, 1930). Also in this case, the fluctuations in front of the stagnation point were damped early downstream around one quarter of the chord length of the aerofoil.

The observations were confirmed by Kuethe et al. (1959) through a hot-wire investigation on a blunt-nosed body of revolution. In all cases, the region of unsteadiness extended over a distance of 30 to 50 boundary layer thickness in front of the leading edge.

The first conjecture

The physical mechanism that generates the unsteadiness in the flow approaching a solid body has been matter of investigations and discussions for years following the initial observations.

The first conjecture was proposed by Görtler (1955). He hypothesised that the

decelerating flow at the stagnation point would become unstable and develop counter-rotating vortices spaced at a fixed distance each other by a mechanism similar to the centrifugal instability on concave walls, *Görtler instability*[1], predicted by himself few years before (Kestin and Wood, 1970). Görtler idealised the undisturbed stagnation flow following the Hiemenz mathematical model and derived the disturbance equations for the stagnation flow against a flat plate assuming a disturbance proportional to $exp(\beta t + i\alpha z)$, where z is the direction normal to the plane of the flow, β is the time amplification exponent and α the spatial wavelength. The solution of those time-dependent equations was investigated by Hämmerlin (1955). He, firstly, analysed the time independent equations ($\beta = 0$) finding that the disturbances can exist for a continuous range of wavenumbers $\alpha = 2\pi(\nu/a)^{1/2}/\lambda$ for $0 \leq \alpha^2 \leq 1$. Then, he determined β for a given α, proving that the disturbances can amplify if $0 \leq \beta + \alpha^2 \leq 1$.

The vorticity amplification theory

Kestin and Maeder (1957) presented a NASA report with a comprehensive experimental investigation and some theoretical considerations of the influence of turbulence on heat transfer. They proved that the turbulence intensity and the Reynolds number have an influence on the heat transfer. The report concluded that it was necessary a study of the mechanism of *flow in, and heat transfer across, boundary layers at the outer edge of which exists a fluctuating velocity.*

Following the observations on the report, at the beginning of the '60s Kestin and Maeder, with the contribution of Sutera, developed the so called **vorticity amplification theory** to understand *the considerable discrepancies evident in the result of certain experiments in forced convective heat transfer* (Sutera et al., 1962). The first mathematical model was published in 1962 and a more general review in 1965 exclusively by Sutera (Sutera, 1965). The model superimposed a sinusoidal perturbation to the flow approaching the stagnation point and solved the time-independent vorticity-transport equation, together with the incompressible continuity equation, and the time-independent energy-

[1] see Chapter 1

transport equation, assuming no dissipation, and using the Hiemenz flow as a boundary condition. The theory found that the vorticity in the freestream is transported by the oncoming flow towards the body and, if properly oriented, may be stretched by the velocity field (see sketch in figure 2.4). The effect of the stretching is to amplify the vorticity intensity at the edge of the stagnation-point boundary layer. The parameter that determines whether the vorticity is amplified or attenuated is its wavelength; vorticity of scale smaller than a defined *natural wavelength* (λ_0) is indeed dissipated, while vorticity with larger scale ($\lambda > \lambda_0$) is amplified at the edge of the boundary layer. This concept is well represented in figure 2.4, where the freestream disturbance is sketched as a cross-vortex tube. When it approaches the stagnation point it is elongated by the stretching and consequently its scale, that is its diameter, decreases while increasing its vorticity (Sadeh et al., 1977).

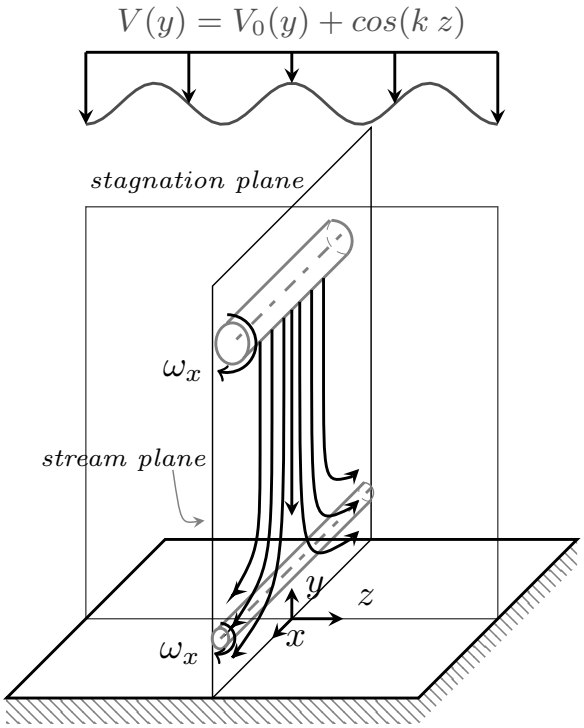


Figure 2.4: Stretching of vorticity approaching a flat plate (modified from Sadeh et al. (1977)).

The natural wavelength for the Hiemenz flow was found to be $\lambda_0 = 2\pi(\nu/a)^{1/2} \approx$

2.6δ, where a is the deceleration rate of Hiemenz flow, ν the cinematic viscosity and δ the boundary layer thickness for Hiemenz flow. In addition, Sutera et al. (1962) showed that the oncoming vorticity has also an effect on the thermal boundary layer and, actually, the latter was found to be even more sensitive compared to the velocity boundary layer. It was solved for various Prandtl number, finding that a wall-shear stress increment of 3% can correspond to a wall-heat-transfer increment of 40%.

A few years later, Sadeh et al. (1970) extended the theory to a circular cylinder considering the curvature effect. In the circular cylinder only in a narrow area in front the stagnation point the velocity behaves linearly as described by Hiemenz flow. The authors demonstrate that also in that case the stretching is the predominant mechanism within the linear range, with the vorticity, of scale larger than the neutral scale, that is preserved and eventually amplified as the linear velocity range is approached.

The instability

Kestin and Wood (1970) tried to refine the Görtler-Hämmerlin model considering a flow against a body with a curvature, as a cylinder. They argued that the continuous spectrum of eigenvalues found by Hämmerlin was due to an *idealisation* of the flow: Hiemenz flow solution goes to infinity really far from the surface, while for a generic body it should tend to the freestream velocity, as in the cylinder potential flow solution. The authors evaluated the stability analysis considering the flow on a circular cylinder, of radius R, in a wedged area around the stagnation point. They solved the problem with and without curvature ($R \to \infty$). The analysis was time-independent considering only a spanwise sinusoidal perturbation, forced to vanish in the freestream by the boundary conditions (i.e. $u(\eta \to \infty) = 0$). They concluded that the Hiemenz-type flow is inherently unstable for a continuous range of wavelengths, but in the presence of curvature it is unstable to only one wavelength:

$$\lambda = \frac{2\pi\, R}{Re^{1/2}} \frac{2^{4/3}}{\phi_0''^{1/3}} \frac{1}{\left(3 - \frac{2}{3}(2/\phi_0'')^{4/3}\right)^{1/2}} \tag{2.10}$$

where R the radius, ϕ_0 the stream function and the superscript $''$ indicates the second derivative with respect to the direction perpendicular to the wall. The authors have considered the power series approximation for the cylinder stagnation point flow at the wall which gives $\phi_0''(\eta \to 0) = 1.233$. Substituting the natural wavelength from the vorticity amplification theory (λ_0), they concluded that for a circular cylinder the unique unstable wavelength is:

$$\lambda = 1.79\,\lambda_0. \tag{2.11}$$

Physically, the flow becomes three-dimensional developing a series of spanwise counter-rotating vortices at the boundary layer edge (see figure 2.5). Instead, considering an infinite radius of curvature the solution gives a continuous spectrum, in agreement with Hämmerlin's solution.

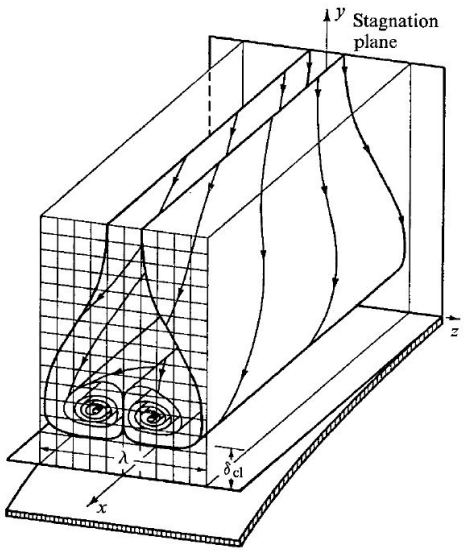


Figure 2.5: Sketch of the counter-rotating vortices developing at the stagnation point of a cylinder (Kestin and Wood, 1970).

In addition, Kestin and Wood compared their theory with available flow-visualisation experiments as function of Reynolds number and turbulence intensity. Those experiments have shown the presence of alternative streaks of higher and lower shear at a constant distance over circular cylinders. By plotting the experimental results and interpolating the data at the same turbulence level, the authors showed that their model predicts the distance between the

streaks at zero turbulence intensity, therefore they were probably the footprint of the stagnation point vortices developing on the cylinder.

Wilson and Gladwell (1978) revised the Görtler-Hämmerlin model and the Kestin approach questioning the boundary conditions and demonstrating that the flow at the leading edge, for high Reynolds number, is stable to infinitesimal periodic disturbances in the spanwise direction. On the other hand, they admitted that there are a lot of experiments which have proven the contrary and they indicated three main limitation of their model: a) it is valid only for infinite Reynolds numbers; b) it is valid only in the neighbourhood of the stagnation line, a wedge of about 0.5°; c) non-linear effect were not included even though they might play an important role with the appearance of secondary vortices. The authors agreed that the stretching is the cause of the amplification, but they disagreed on the possibility that such amplification causes secondary vortices.

Lyell and Huerre (1985) explained that the difference between Wilson-Gladwell and Görtler-Hämmerlin approaches is that the former was looking at disturbances originating in the viscous-stagnation-flow region, which turns to be always stable, while the latter was studying vortical disturbances forced from the outer potential mean flow, which would experience algebraic growth or decay as they approach the viscous layer. Lyell and Huerre progressed on the Hämmerlin approach by applying a Galerkin method[2] to the linear and non-linear stability analysis of the Hiemenz flow. The linear stability analysis revealed an infinite number of modes all attenuated in time, while the non-linear analysis showed that a disturbance exceeding a certain threshold can non-linearly destabilise the Hiemenz flow.

More recently, Xiong and Lele (2004) theoretically analysed the effect of length scale and intensity of turbulence of the impinging disturbances together with the effect associated with heat transfer; they gave a theoretical model that could be numerically solved and later Xiong and Lele (2007) tried to solve the problem using large eddy simulation (LES).

[2]The Galerkin methods are numerical techniques to solve partial differential equations.

The stagnation point flow in absence of solid boundary

Kerr and Dold (1994) considered a stagnation-point in absence of solid boundaries, i.e. four-roll mill, and studied the formation of vortices whose axes were parallel to the direction of the diverging flow. They were looking at mixing in a stagnation-point flow, but their founding was quite similar as in presence of solid boundaries. They analysed the solution of the Navier-Stokes equations for a decelerating Hiemenz flow with a periodic perturbation in the spanwise direction. As boundary conditions they assumed the flow at the leading-edge to be symmetrical with respect to the stagnation line and no wall at the stagnation point. They found that for certain wavelengths the perturbation amplified and created vortices at the stagnation point, similar to those observed by Sutera et al. (1962); Sutera (1965).

The experimental investigations

The discussion on the vorticity amplification and the instability of the stagnation point flow was accompanied by a great number of experimental investigations on different type of models and flow conditions.

Three important studies have been already mentioned: Piercy and Richardson (1928, 1930) and Kestin and Maeder (1957). The last is a NASA report focused on the effect of turbulence on the flow around a cylinder at subcritical Reynolds number in the range $5.2 \times 10^4 \leq Re_D \leq 20.9 \times 10^4$. The freestream turbulence was produced in a controlled manner by using different turbulence generating grids. Furthermore, flow visualisations of the separation line and dynamic pressure measurements were carried out. The results presented in the work revealed three main effects of the turbulence on the flow field: modification of the mean surface pressure distribution, delay in the separation point, reduction in the mean drag. The authors conclude that these modifications, function of both the Reynolds number and the freestream turbulence intensity, were due to the vorticity approaching the leading edge which reduces its scales to a value commensurate with the boundary layer thickness.

As previously mentioned, a strong motivation for studying the stagnation point flow was the interest in heat transfer. Smith and Kuethe (1966) carried out

measurements of heat transfer and skin friction on a flat plate and on a circular cylinder downstream a turbulence generating grid. They investigated how the heat transfer and the skin friction increases when the turbulence increases, in particular at the stagnation point of the cylinder. The existence of coherent structures at the stagnation point was revealed by flow visualisations published by Sadeh et al. (1970). The smoke visualisation was carried on a flat plate with adjustable flap and the oncoming turbulence was modified by inserting different turbulence generating grids. The flow visualisations show the smoke filament rolling up at the stagnation point and the response to different grids. The paper includes also a hot-wire investigation on the stagnation flow on the flat plate and on a circular cylinder at Reynolds number around 10^5.

The turbulence grid was realised by parallel rods oriented either horizontally or in parallel, the idea is that the grid orientation influences the preferential orientation of the eddies in the generated freestream turbulence. The vorticity oriented parallel to the cylinder axis was found to be the one that is amplified, in agreement with the vorticity amplification theory. The boundary layer at the leading edge was found to modify its shape when the turbulence is increased, showing that the higher freestream turbulence changes the nature of the boundary layer from laminar to turbulent. The measurements also demonstrated that the phenomenon is associated to a continuous shift of frequencies from high to low as the boundary layer is approached. In particular, for a scale smaller than the neutral wavelength, the energy decays as the boundary layer is approached. Inside the boundary layer the penetrated turbulence was observed to decay. The authors conclude that the eddies larger than the boundary layer cannot survive and therefore *a rapid transfer of energy to smaller scales* occurs.

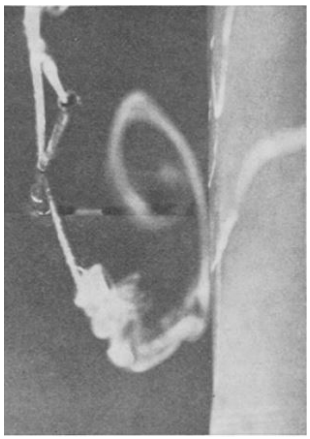


Figure 2.6: Flow visualisation at the stagnation point of a flat plate (flow left to right) Sadeh et al. (1970).

In addition, Sadeh et al. (1977) carried out an investigation on flow visualisation using white smoke of the flow at leading edge of a circular cylinder at

$Re_D = 8 \times 10^3$. They identified the coherent structures at the leading edge and captured their time evolution from three different views. The life cycle of a single vortex resulted between 700 ms and 800 ms which corresponds to a range between 1.2 Hz and 1.4 Hz. The same cylinder was further studied by Sadeh and Brauer (1980, 1981). The boundary layer investigation was conducted with a turbulence generating grid installed upstream of the model at different Reynolds number ($5 \times 10^4 \leq Re_D \leq 20 \times 10^4$) by using a single hot-wire anemometer. Only the measurements at $Re_D = 12 \times 10^4$ with the grid installed upstream have been published. The presence of the grid makes the boundary layer turbulent.

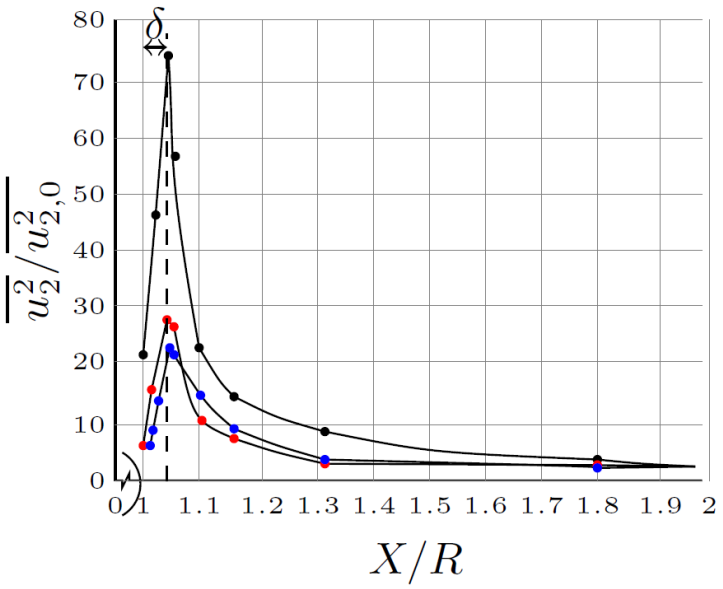


Figure 2.7: Sadeh and Brauer (1981) experiment on the flow approaching a stagnation point of a cylinder ($R = 80\,mm$, $Re_D = 1.2 \cdot 10^5$) with a turbulence generating grids. The plot shows the turbulence energy ($\overline{u_2^2}$) for difference scales (λ) normalised by its minimum value ($\overline{u_{2,0}^2}$) as function of the distance from the cylinder. Legend: • $\lambda/\lambda_0 = 5.52$,• $\lambda/\lambda_0 = 6.90$, • $\lambda/\lambda_0 = 13.80$.

The data were analysed applying the Taylor hypothesis to identify the energy corresponding to each wavelength and the most amplified wavelength. It was found that the energy amplifies outside the boundary layer and a continuous shift of frequency from high to low was found approaching leading edge. As shown in figure 2.7, the most amplified wavelength was found to be 5.52 times the neutral wavelength .

Most of the experimental vorticity amplification surveys were conducted on bluff body to achieve a relatively thick boundary layer at the stagnation point. Sadeh and Sullivan (1980) investigated the vorticity amplification on a NACA 65-010 aerofoil in a wind tunnel using turbulence generating grid made by vertical cylinders. The investigation consisted of a flow visualisation at Reynolds number of $2.5 \cdot 10^4$, based on the aerofoil chord at zero angle of attack, and of an hot-wire survey. The flow visualisation was able to capture the coherent structures at the leading edge. The hot-wire measurements were conducted at $Re = 1.5 \cdot 10^5$. With the turbulent grid installed the boundary layer was turbulent at the stagnation point. The turbulence approaching the model showed a gradual amplification with its maximum ahead of the boundary layer. By decomposing the turbulence at each wavelength, the authors showed that the results were in agreement with the ones from bluff body experiments. The amplification of the freestream turbulence occurred at scales larger than the neutral wavelength and the most amplified scale was comparable to the boundary layer thickness with its maximum amplification located at the edge of the boundary layer, while inside it the turbulence gradually decreased. Bearman (1972) studied the distortion of turbulence approaching a bluff body. The model used in the experiments was a vertical flat plate fitted with a fairing body. He carried out hot-wire and pressure measurements with different types of turbulence generating grids installed ahead of the model at $Re_D = 3 \cdot 10^4$. Each grid was characterised by a different longitudinal integral length scale Λ_x, all greater than or comparable to the model characteristic length D ($\Lambda_x/D = [1.2 \div 2.38]$)to analyse the effect of Λ_x/D on the distortion of the turbulence in the inviscid turbulent flow approaching the body stagnation point. The measurements were taken far from the turbulent boundary layer by using a cross hot-wire anemometer. In the discussion of the results, Bearman compares the experiments with the theoretical curves derived through the rapid distortion theory for Λ_x grater or less than D which distinguishes two different behaviours depending on the ratio Λ_x/D:

$\Lambda_x/D >> 1$: quasi-steady type approach can be used and $\overline{u^2}^{1/2}$ will be attenuated,

$\Lambda_x/D << 1$: the turbulence is distorted by the mean flow and $\overline{u^2}^{1/2}$ will be amplified due to vortex stretching.

In the experiment, Λ_x/D was $O(1)$ finding a combined situation was observed with attenuation of energy at low wavenumbers and amplification at high wave numbers in the streamwise fluctuations.

Following Bearman's experiment, Britter et al. carried out similar investigation on circular cylinders of radii from 3.18 mm up to 63.5 mm at variable Reynolds number $4.25 \times 10^4 \leq Re_D \leq 2.75 \times 10^4$ installing different types of turbulence generating grids with Λ_x/D from 0.025 up to 1.42.

Böttcher and Wedemeyer (1989) carried out a flow visualisation in a water tow tank on the flow downstream eight different turbulent screens. The aim of the study was to find evidence in support of the vorticity amplification theory. A wire controlled by a periodic voltage sent hydrogen bubbles which appeared as equally spaced lines travelling downstream from the grid. The first part of the work describes the flow downstream of a grid with no body behind it. Immediately behind the screen a periodic pattern of jets and wakes is shown, which coalesce downstream. Naturally the disturbances generated by a screen decrease with increasing distance from the screen while the wavelengths of the turbulence depend on the screen geometry. In the second part of the paper, a cylinder is mounted downstream of the screen to observe the stagnation point flow. With no screen no longitudinal vortices could be observed at Re_D up to 7×10^5, while in presence of the screen the vortical flow could clearly be observed. The authors conclude that this was a demonstration that vortices develop in the stagnation point flow when vortical disturbances approach from the freestream, and are not due to an instability as supposed by Görtler.

More experiments on turbulence generating grids influencing stagnation point flow can be found in reviews by Morkovin et al. and Zdravkovich (1997).

2.1.3 Discussion

From the previous review it can be concluded that, due to the complicated nature of the problem, both from the theoretical and the experimental point of view, despite the large number of investigations that have been carried out, a complete explanation of freestream turbulence amplification, able to predict all the experimental conditions, has not been found yet. The main reason, common to the theoretical and to the experimental approach, lies in the difficulties to mathematically model the freestream turbulence produced in the wind tunnel or, vice versa, to produce in the experiments the turbulence in a controlled manner able to reproduce the theoretical hypothesis. That represents still a big challenge for both experimentalist and theoretician.

It must also be stated that in many experimental investigations discussed in the previous section, the freestream turbulence conditions have not been reported in a systematic way. Moreover, in some cases the nature of the flow on the body under investigation, laminar or turbulent, has not been specified explicitly. The motivation of the cited investigations was to study the influence of freestream turbulence on heat transfer and not on the laminar to turbulence transition. A high level of freestream turbulence makes the turbulent boundary layer thicker with respect to the laminar, therefore easier to measure, and enhances the effect of the turbulence itself. It has been found that only Sadeh et al. (1970) have carried out single hot-wire measurements on the laminar stagnation point boundary layer, with no turbulence generating grid inserted. In addition, the theoretical models show that the phenomenon is three-dimensional, but the experimental investigations have used single hot-wire measurements, which allows to acquire only one velocity component. Bearman (1972) carried out experiments with cross hot-wire, measuring the three velocity components, but in a region far from the surface. It would have not been possible with that technique to measure the flow velocity inside the boundary layer.

Regarding the flow visualisations, two types of techniques have been used in literature: smoke and oil flow visualisation. The results with the smoke show clearly the formation of unsteady coherent structures at the leading edge

(Sadeh et al., 1977), but this technique can be applied only at low Reynolds number. Whereas, the oil coated technique, used by Kestin and Wood (1969), has revealed streaks developing downstream of the stagnation point of circular cylinder which wavelength is in the range of that predicted by Kestin and Wood (1970).

Despite some discrepancies between experimental and numerical works, a general overview of the phenomenon can be pictured:

- the flow approaching a leading edge shows an increment in the fluctuations of the velocity at the edge of the laminar boundary layer;

- the vorticity amplification theory has demonstrated that vorticity is amplified at the stagnation point flow, forming coherent structures aligned with the body axis. Flow visualisations have demonstrated the existence of these coherent structures observing their unsteadiness;

- the phenomenon is related to the freestream turbulence, either background or superimposed, which is not entirely dissipated, but is carried by the flow towards the wall. When the linear region is approached, the turbulence can either remain constant or decay, but at the edge of the boundary layer a substantial amplification was observed (Sadeh et al., 1970);

- the maximum of amplification depends on the characteristic of the external disturbance. Disturbances oriented parallel to the cylinder axis are mostly amplified according to the vorticity amplification theory (Sadeh et al., 1970);

- the turbulence-energy spectrum shows that simultaneously high frequencies are attenuated, while low frequencies are amplified as the turbulence is convected towards the wall. This corresponds to an amplification occurring for length scale greater than the theoretical neutral scale and an attenuation for smaller ones (Sadeh et al., 1970).

2.2 Attachment-line flow

Consider the flow impinging on a swept flat plate (figure 2.8), with sweep angle Λ.

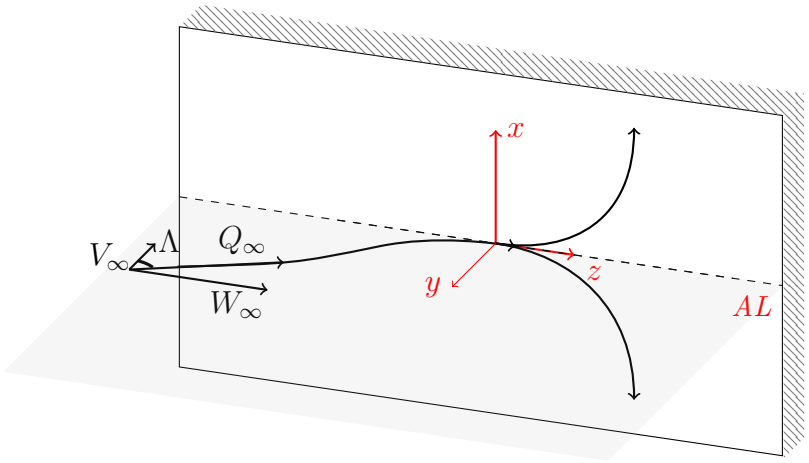


Figure 2.8: Flow against a swept flat plate.

This flow is similar to the one on the unswept case, described in the previous section, since it decelerates approaching the body and diverges symmetrically in two directions, but in this case the flow at the attachment-line has a velocity component parallel to the wall in the spanwise direction ($U = 0, V = 0, W \neq 0$). In the swept case, it is not possible to define an attachment stagnation point, but it is more appropriate to introduce an *attachment-line* (AL in figure 2.8), which is the streamline about which the flow diverges.

Also in the three-dimensional case, the flow on a swept attachment-line can be approximated by the flow against a vertical infinite flat plate. In addition, in this region the *independence principle* (Jones, 1947) can be applied, so that the solution for the U and V can be determined independently of the spanwise component W (Rosehead, 1963). Therefore, the inviscid flow can be described by superimposing the spanwise constant velocity on the two-dimensional inviscid solution:

$$\overrightarrow{U} \begin{cases} U(x) = ax \\ V(y) = -ay \\ W = W_\infty \end{cases} \tag{2.12}$$

a is the two dimensional Hiemenz flow constant and the $W_\infty = Q_\infty sin(\Lambda)$ is the spanwise component of the Q_∞ freestream velocity (as shown in figure 2.8).

For the inviscid solution the independence principle can be applied as well. Actually, the two-dimensional Hiemenz flow is part of a self-similar family of exact numerical solutions of Navier-Stokes equations, presented by Falkner and Skan (1931). Cooke (1950) extended the Falkner-Skan solution to swept body by applying the independent principle. Since this more general solution will be used in Chapter 2 of this thesis, in the next section the Falkner-Skan-Cooke equations are described, showing in which case they correspond to the swept Hiemenez flow.

2.2.1 Falkner-Skan-Cooke equations

The Falkner-Skan solution describes a family of flows in which the stream function has the form $\psi(\eta, \xi) = f(\eta, \xi)h(\xi)$, where $\eta = y/\delta$ is the dimensionless boundary layer coordinate perpendicular to the surface and $\xi = x/L$ is dimensionless the streamline coordinate. This stream function corresponds to the flow over a two dimensional wedge of angle γ (figure 2.9). For this case the edge velocity is described by $U_e = kx^m$, where m is a constant depending on the wedge angle $\left(\gamma = 2\pi\frac{m}{m+1}\right)$. The value $m = 0$ corresponds to an horizontal flat plate ($\gamma = 0$, Blasius flow), while $m = 1$ to a vertical flat plate ($\gamma = \pi$, Hiemenz flow). The dimensionless coordinate for a wedge flow can also be defined as $\eta = \sqrt{\frac{U(m+1)}{2\nu x}}y$.

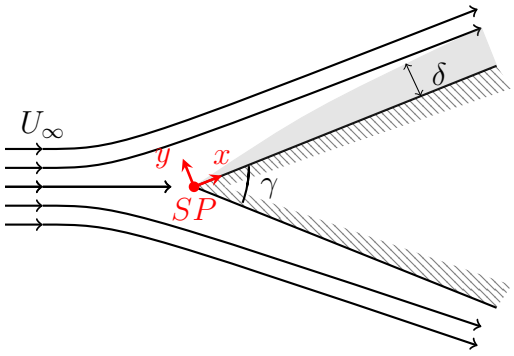


Figure 2.9: Wedge flow.

By substituting the stream function in the boundary layer equations for a steady incompressible flow, with negligible friction, and after some manipulations, the equations can be reduced to an ordinary differential equation (Schlichting, 1960):

$$f'''(\eta) + f f''(\eta) + \beta(1 - f'^2(\eta)) = 0 \tag{2.13}$$

where $\beta = 2m/(m+1)$, known as the Hartree parameter, depends on the geometry and on the flow accelerating ($m > 0$) or decelerating ($m < 0$). If $\beta = 0$ the equation describes the flow over an horizontal flat plate, well known as Blasius flow ($\gamma = 0$), while if $\beta = 1$ the equation becomes identical to the Hiemenz equation (2.4) and describes the flow impinging on a vertical flat plate. In the case of a swept wedge, Cooke (1950) demonstrated that the spanwise velocity component can be described by a function $g(\eta)$ defined by:

$$g''(\eta) + f g'(\eta) = 0. \tag{2.14}$$

The last equation is coupled with the Falkner-Skan equation. The system of equations 2.13 and 2.14 can be numerically resolved assuming the following boundary conditions:

$$\begin{cases} f = f' = g = 0 & \eta = 0 \\ f' \to 1, \quad g' \to 1 & \eta \to \infty \end{cases} \tag{2.15}$$

Boundary layer at the attachment-line

The solution of equations 2.13 and 2.14 with boundary conditions 2.15 and $m = 1$ gives the solution for the viscous flow on a vertical swept flat plate (swept Hiemenz flow):

$$\overrightarrow{U} \begin{cases} U = a f'(\eta) x \\ V = -\sqrt{\nu a} f(\eta) \\ W = W_\infty g(\eta). \end{cases} \tag{2.16}$$

The Falkner-Skan-Cooke equations have been solved numerically using FORTRAN, by applying a 4^{th} order Runge-Kutta integration scheme and a shooting method based on Newton-Raphson. The solution is shown in figure 2.10. The $f(\eta)$ and $f'(\eta)$ are identical to the two-dimensional solutions; while the spanwise component ($g(\eta)$) shows a typical boundary layer shape tending to a constant value at infinity. The shapes of $f'(\eta)$ and $g(\eta)$, both recalling a typical boundary layer, are indeed different since the constant freestream velocity is reached earlier by the $f'(\eta)$ function.

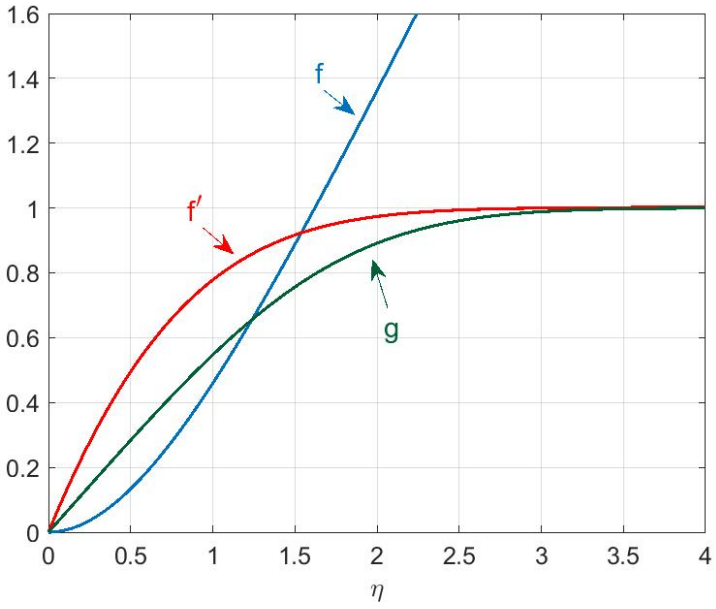


Figure 2.10: Falkner-Skan-Cooke solution with $\beta = 1$, swept Hiemenz flow.

At the attachment-line the U velocity component is zero, therefore the *attachment-line boundary layer* is referred using the W velocity component and the $g(\eta)$ function.

The boundary layer thickness at which $w(\eta_{99}) = 0.99W_\infty$ corresponds to $\delta_{AL} \approx 3.1\sqrt{\frac{\nu}{a}}$, which is greater than the one for u and v defined in the two-dimensional flow (as it can also be noticed in figure 2.10).

The boundary layer displacement thickness in this case is:

$$\delta^*_{AL} = \sqrt{\frac{\nu}{a}} \int_0^\infty \left(1 - \frac{w(\eta)}{W_\infty}\right) d\eta = 1.026\sqrt{\frac{\nu}{a}} \tag{2.17}$$

and the momentum thickness:

$$\Theta_{AL} = \sqrt{\frac{\nu}{a}} \int_0^\infty \frac{w(\eta)}{W_e}\Big(1 - \frac{w(\eta)}{W_\infty}\Big) d\eta = 0.404\sqrt{\frac{\nu}{a}}. \tag{2.18}$$

The shape factor is then $H_{AL} = \delta^*/\Theta = 2.539$.

When studying the attachment-line flow, in particular the instability, it is often useful to define the Reynolds number (Re_Θ) based on the attachment-line momentum thickness and the spanwise velocity component (W_∞):

$$Re_\Theta = \frac{W_\infty \Theta_{AL}}{\nu}. \tag{2.19}$$

In some cases, an equivalent Reynolds number $\overline{Re}$ is used:

$$\overline{Re} = \frac{W_\infty}{\nu}\left(\frac{\nu}{\frac{dU}{ds}|_{s=0}}\right)^{1/2} \tag{2.20}$$

where $\left(\nu\left(\frac{dU}{ds}|_{s=0}\right)^{-1}\right)^{1/2}$ represents the boundary layer length scale and s is the streamline curvilinear coordinate. It can be demonstrated that for the attachment-line flow $Re_\Theta = 0.404\,\overline{Re}$.

2.2.2 Attachment-line contamination

In a flight test, Gray (1952) demonstrated the difficulty of achieving laminar flow on swept wings. Initially, the cause was attributed to cross-flow instability (see Chapter 1). Both flight tests and wind tunnel experiments by Pfenninger and Bacon (1969), Anscombe and Illingworth (1956) and Gaster (1967) demonstrated that the flow on a swept back wing[3] may become turbulent already along the attachment-line. The disturbances coming from the fuselage are fed into the swept attachment-line and travel along the attachment-line itself (see figure 2.11), since the flow is dominated by a spanwise velocity. This phenomenon is called *attachment-line contamination*. As a result, also on moderate swept wings, $20° < \Lambda < 40°$ similar to those on commercial transonic

[3]A swept wing is considered *swept back* if the chord of the unswept section is reclined towards the rear of the fuselage. For the experiments the fuselage is represented by the wind tunnel wall. Otherwise, the wing is called in *swept forward* configuration.

aircraft, the flow is often turbulent already at the attachment-line.
Following Pfenninger and Bacon, Gaster (1967) proposed a criterion to predict attachment-line contamination based on Re_Θ. An equivalent criteria, based on $\overline{Re}$, was later proposed by Poll (1978). According to the experimental works by Gaster and Poll:

- for $Re_\Theta < 100$ the disturbances coming from the fuselage decay naturally and the attachment-line is laminar, figure 2.11a (Gaster, 1967).
- for $Re_\Theta \geq 100$ (Gaster, 1967) or $\overline{Re} \geq 250$ (Poll, 1978), the flow is transitioning from laminar to turbulent,
- for $\overline{Re} > 300$ the flow is fully turbulent, figure 2.11b (Poll, 1978).

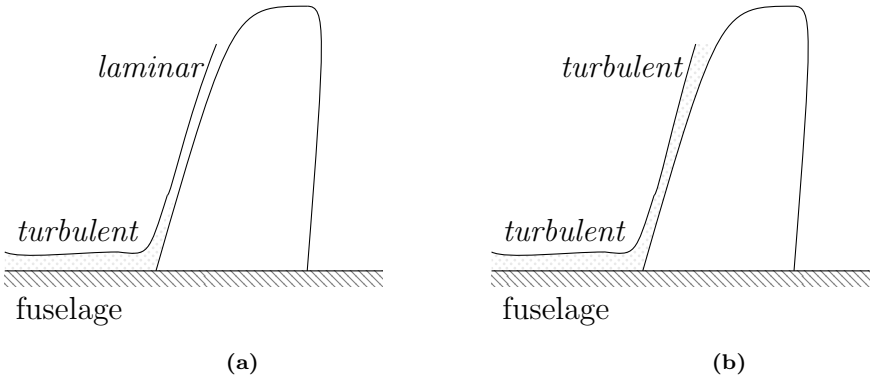
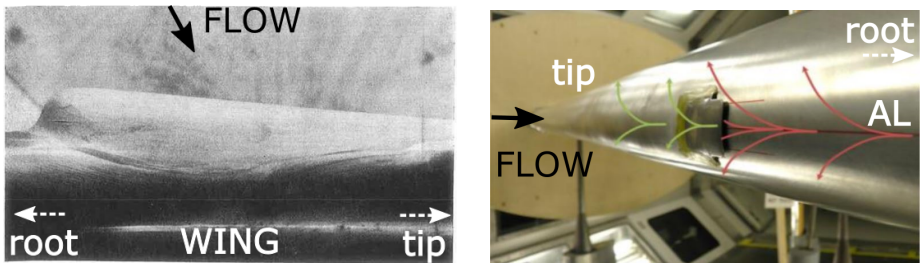


Figure 2.11: Attachment-line contamination: a) the disturbances coming from the fuselage decay and the flow is laminar $Re_\Theta < 100$, b) the disturbances grow along the attachment-line and the boundary layer is turbulent.

Gaster (1965) demonstrated that the attachment-line contamination can be stopped by preventing the disturbances to travel along the attachment-line. He proposed the use of a bump installed on the attachment-line of the wing (figure 2.12a). The device generates a new stagnation point from which a new laminar flow is established. Initially, the "Gaster bump" was simply hand-made by modelling some plasticine. Further studies led to an optimum shape. The bump was found to be effective up to $Re_\Theta = 160$.
Based on the same principle, the bump evolved in the "Gaster device" (Gaster, 2012), a bleeding slot that can be easily applied on the surface at the attachment-line (figure 2.12b). The device generates, as well, a new fresh stagnation point,

but the turbulent incoming flow can easily travel away from the attachment-line. It was also shown that the use of the device can reduce the drag(Alderman et al., 2016).



(a) (b)

Figure 2.12: Devices decontaminate the turbulent attachment-line flow a) flow visualisation on the Gaster bump (Gaster, 1965), b) the Gaster slot, the red arrows indicate turbulent flow and the green arrows laminar flow (Alderman et al., 2016).

An application of the same principle of Gaster slot will be shown in Chapter 5. Other active and passive devices have been developed for attachment-line control, such as suction, steps, grooves, etc. A detailed review is reported in Gowree (2014).

2.2.3 Attachment-line instability

The attachment-line contamination clearly explained why the flow was often found to be turbulent already at the attachment-line of the swept back wings, but an open question remains: considering a more general case, with no contamination from the fuselage, as in a swept forward wing, *can the attachment-line flow itself be unstable*? The attachment-line boundary layer is similar to the boundary layer on a flat plate. The disturbances are likely to be amplified in the streamwise direction (spanwise for the attachment-line) and to breakdown into turbulent boundary layer through a transition process.

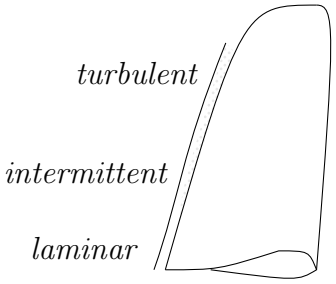


Figure 2.13: Attachment-line instability over a swept wing.

According to Gaster, based on linear stability theory, the attachment-line boundary layer may become unstable due to the propagation of travelling waves similar to the Tollmien-Schlichting ones (TS). Experimentally, Gaster (1967) analysed the growth of TS like waves by inducing a small amplitude sound wave from a tiny hole drilled in the upstream region of the attachment-line. The author concluded that the disturbances did decay up to $Re_\Theta = 170$, which is consistent with the limit for the bump to be effective.

Pfenninger and Bacon (1969) showed the presence of linear instability waves along the attachment-line for similar Re_Θ.

Poll (1978) demonstrated that transition can occur in absence of attachment-line contamination, since disturbances may be amplified travelling along the attachment-line. The author experimentally found that the first turbulent burst can be detected for $\overline{Re} > 550$ in the spanwise direction, and the complete turbulence for $\overline{Re} > 750$. Poll (1978) also investigated the attachment-line instability using the parallel flow approximation, neglecting both the chordwise and the wall-normal velocity components and reducing the problem to the Orr-Sommerfeld equation; he found the critical Reynolds number to be $Re_\Theta = 270$.

Dallmann, in 1980, analysed the global stability problem of an immersed swept cylinder demonstrating that the Görtler-Hämmerlin mode were one of many chordwise modal structures (Obrist and Schmid, 2003a).

The first successful non-parallel stability analysis of swept Hiemenz flow was carried out by Hall, Malik, and Poll (1984). They assumed a disturbance periodic in the direction parallel to the attachment-line and the chordwise perturbation velocity depending linearly on the chordwise coordinate. They obtained the neutral curves to be in good agreement with experiments (figure 2.14) and demonstrated that the attachment-line is unstable to travelling waves, TS like, propagating along the attachment-line for $Re_\Theta > 583.1$.

Spalart (1988) performed a Direct Numerical Simulation (DNS) of the fully non-linear, three-dimensional, time-dependent Navier Stokes equations to study the stability of the attachment-line region as function of the Reynolds number.

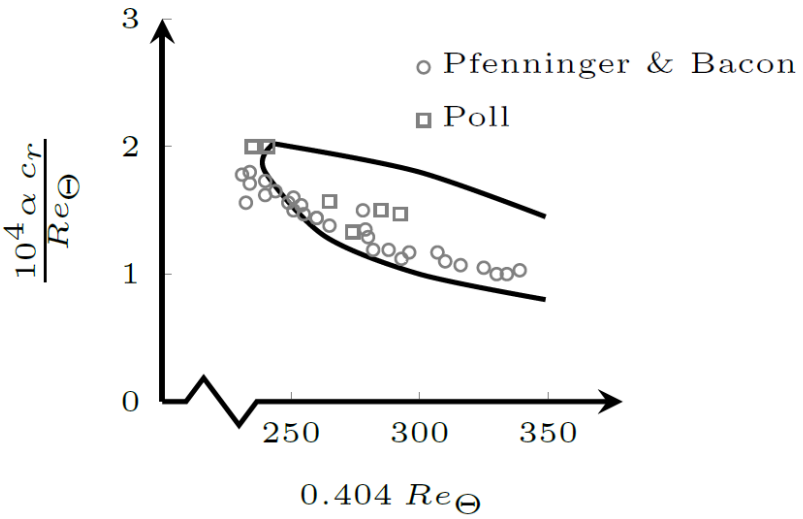


Figure 2.14: Neutral curve for attachment-line flow by Hall et al. (1984), compared to experiments by Pfenninger and Bacon (1969) and Poll (1978).

For the unswept case, $\overline{Re} = 0$, no unstable modes were found. The author explains that his procedure does not allow disturbances from the freestream. He pointed out that studying flows with oncoming vorticity *would be very interesting, but it would be much more difficult*. For the swept case, he focused on instability and on the effect of suction on the re-laminarisation, obtaining results in agreement with Hall et al. (1984); the flow is stable up to $\overline{Re} > 583.1$. No subcritical instability was found, as previously hypothesised by a weakly non-linear study by Hall and Malik (1986)

Lin and Malik (1996) presented a generalised approach to studying the stability of the attachment-line flow by solving a partial differential eigenvalue problem from the linear stability equations. According to the authors, the advantage of their method is that there is no restriction of a parallel flow giving a more general approach with respect to Hall et al. (1984). The authors suggested that the same model can be easily extended to a compressible flow. They only considered travelling modes, assuming real the spatial spanwise number β. Their analysis agrees with Hall et al. (1984) confirming, once more, the lowest critical Reynolds number. Lin and Malik (1997) investigated the effect of the leading edge curvature finding that it has a stabilising effect.

Obrist and Schmid (2003a,b) presented a mathematical model based on adjoint equations for the swept Hiemenz flow. The model was used to study the global

instability and the transient growth showing also how the model can be applied for receptivity problems of the swept Hiemenz flow.

A more broaden review of theoretical works on the attachment-line instability can be found in Arnal and Casalis (2000), Obrist (2000), Obrist and Schmid (2003a,b), Theofilis et al. (2003) and Gowree (2014).

2.2.4 Discussion

The attachment-line flow has been widely studied in literature. Many authors have successfully investigated attachment-line contamination and instability giving answers and solutions to problems commonly experienced on aircraft. Nevertheless, the mechanism by which the oncoming turbulence interacts with the attachment-line flow, and how it eventually is transported downstream, remains an open question. A vorticity amplification approach, similar to that followed by Sutera et al. (1962) seems not to have been carried out for swept flow.

In a recent paper, Gostelow et al. (2013) were interested in studying the attachment-line of turbine blades. The stagnation point/attachment-line is a crucial point for turbomachinery. Since often the leading edge of the turbine blade is a bluff body, similar to a circular cylinder, they have carried out flow visualisation experiments on a swept cylinder at different sweep angles. According to Gostelow et al. (2013), there is a lack of experimental research on attachment-line flow on swept cylinders with low sweep angles. In particular, Poll (1978) has studied a tapered cylinder swept at $55° < \Lambda < 71°$ and Takagi et al. (2006) a swept cylinder at $\Lambda = 50°$. Therefore, their experimental campaign had the aim to cover this gap using a variable sweep cylinder (from $\Lambda = 0°$ to $61°$). The experiments consisted of flow visualisations with the aim of observing how the surface streaks, footprints of the vortices predicted by Kestin and Maeder (1957), evolve with the sweep angle. The paper tries to correlate the wavelength of those vortices with the cross-flow instability vortices (those observed by Poll (1978) and Takagi et al. (2006) at high sweep angles), despite the nature of the two phenomena is completely different. For example,

one main difference is that the cross-flow vortices are co-rotating, while the vortices predicted on the unswept cylinder by Kestin and Maeder (1957) are counter-rotating. Gostelow et al. (2013) have observed that by plotting their own results, together with those of previous experiments, the wavelength of the streaks is a function of the sweep angle (see figure 2.15). They proposed a modified Kestin and Maeder's theoretical wavelength (to be compared with equation 2.11):

$$\lambda = (1.79\,\pi D/\sqrt{Re})\,cos(\Lambda) \tag{2.21}$$

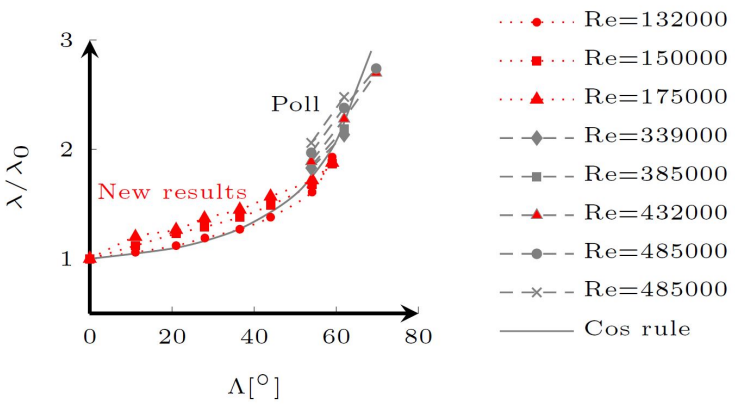


Figure 2.15: Wavelength of streaky pattern as function of sweep angle (Gostelow et al., 2013).

Chapter 3

A first experiment

3.1 Design of the model

The first attempt was to design a model suitable for the experimental investigation of both the distortion of the turbulence approaching a three-dimensional swept wing and the receptivity to freestream turbulence of the cross-flow instability. Therefore, the model had to meet two main requirements: (1) the boundary layer on the attachment-line had to be thick enough to enable measurements to be taken close to the wall; (2) the pressure gradient had to be favourable and optimised at the right sweep angle to promote the cross-flow instability, at least in its primary stage.

The experiment was planned to be carried out in the Gaster wind tunnel at City, University of London (figure 3.1). The facility was chosen since it is characterised by an extremely low level of freestream turbulence ($\leq 0.01\%$ for a wind tunnel speed up to $20\,m/s$), which makes the wind tunnel particularly appealing for laminar to turbulence transition investigations and for experiments where the freestream turbulence is the main control parameter.

The choice of the wind tunnel imposed some technical constraints on the design of the experiment. The dimensions of the wind tunnel test section ($0.91\,m \times 0.91\,m \times 3\,m$) limit the size of the model, in relation to its mounting and to the blockage effects. The wind tunnel motor limits the maximum speed at which the experiment could be carried out. In addition, the choice of the

wind tunnel influences the measurement technique to be used. In particular, instrumentations such as PIV or LDA cannot be used in the Gaster wind tunnel since it would be necessary to introduce the seeding particles which would cause the screen to be blocked. Therefore, hot-wire anemometry was the suitable experimental technique. One of the difficulties in using this measurement technique is the alignment of the sensor to the wall. To reduce the alignment uncertainties, one would prefer to have a flat surface in the measurement region, an advantage that has been considered desirable during the design of the model.

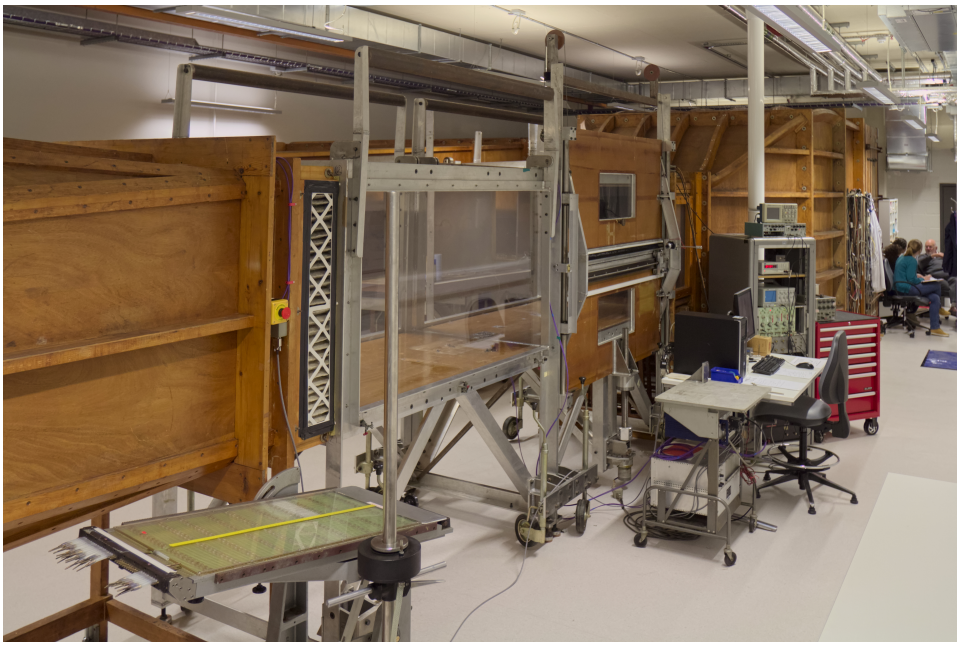


Figure 3.1: Gaster wind tunnel at City, University of London

The first step of the design has been to look at models described by previous works as those capable in promoting cross-flow instability. Among them three models have been considered: (a) swept double wedge, (b) horizontal swept flat plate with displacement bodies, (c) vertical swept flat plate mounted on a wing body. For each of the shapes a parametric study based on the sweep angle, the pressure distribution and the freestream speed has been carried out. To predict the cross-flow instability development both an empirical criteria and an N-factor method have been used.

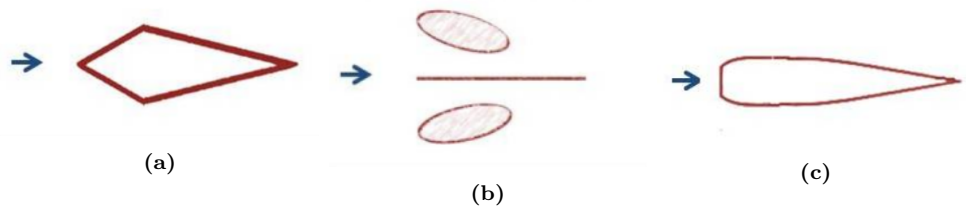


Figure 3.2: Models considered during the design: a) swept double wedge b) horizontal flat plate with displacement bodies c) vertical swept flat plate mounted on a wing body. The arrows indicate the flow direction.

The empirical criteria, initially proposed by Owen and Randall (1952, 1953), was based on the *cross-flow Reynolds number* χ:

$$\chi = \frac{|c_{\epsilon\, max}|\, \delta}{\nu} \tag{3.1}$$

where $c_{\epsilon\, max}$ is the maximum cross-flow velocity, δ the boundary layer thickness and ν the kinematic viscosity. The authors proposed the values for the onset of the cross-flow striation patterns and for the breakdown to turbulence. The criterion was later reviewed by Poll (1978, 1979), who suggested a different expression for the cross-flow Reynolds number:

$$\chi = \frac{|c_{\epsilon\, max}|\, \delta_{1\%\, c_{\epsilon\, max}}}{\nu} \tag{3.2}$$

where $\delta_{1\%\, c_{\epsilon max}}$ is the thickness within the boundary layer where the cross-flow velocity profile (see Chapter 1) assumes the value of 1% of its maximum.
This criterion is not considered very reliable, therefore it has been employed just as an initial test. The most promising configurations (pressure distribution and sweep angle) have then been investigated through an N-factor analysis, for which three different numerical codes have been used. The first code, based on the panel method (Hess and Smith, 1967), had to be developed to calculate the 2D pressure distribution, in particular for the complex model made by the flat plate with the displacement bodies. The pressure distribution, calculated with the previous code, has been used as input for the software BL2D, which is laminar boundary layer software for quasi-two-dimensional flows (i.e. infinite-

swept or swept-tapered wings). The output of the software are the boundary layer profiles at the different chord locations at desired Re, speed and sweep angle. The output of BL2D has been used to carry out a stability analysis based on the N-factor method using the three dimensional stability software CoDS[1].

Among the three models considered, the flat plate with the displacement body was found to be the most suitable design to investigate the cross-flow instability at all its stages, but it was not an ideal model to study the attachment-line boundary layer, since the leading edge radius was particularly small. In addition, the presence of the displacement body limited the available area of investigation in the wind tunnel since the front area of the model was not accessible by the hot-wire traverse. On the other hand, the swept wing with the blunt leading edge allowed one to have a relatively thick boundary layer on the attachment-line ($\delta_{AL} \approx 1\ mm$), but it only provided a limited region for the development of cross-flow instability. Therefore, the first experimental attempt was focused on a swept wing with the blunt leading edge. The flat plate with the displacement body has been realised and tested by colleagues for works on roughness (Placidi et al., 2016; van Bokhorst, 2018).

3.1.1 Vertical flat plate

Previous investigations on attachment-line flows have used mainly four types of models: swept wing with circular leading edge (Gaster, 1967), flat nosed swept wing (Pfenninger and Bacon, 1969), swept cylinder (Poll, 1978) and swept wing with thick leading edge (NACA0050 by Gowree (2014)). On the other hand, two-dimensional experiments on stagnation point flows have used: cylinder (Sadeh and Brauer, 1981), vertical flat plate (Sadeh et al., 1970), aerofoil with blunt leading edge (Bearman, 1972), aerofoil (Sadeh and Sullivan, 1980).

Among them, a cylinder and a flat leading edge have been compared using conformal mapping to demonstrate that an equivalent flow field for the two models has the relation $t = 2R$, where t is half width of the plate and R is the

[1]BL2D and CoDS are respectively a laminar boundary layer software and a stability software, both developed by QinetiQ.

radius of the circular cylinder (Piercy, 1947). In particular, considering that the momentum thickness of the boundary layer at the attachment-line (Θ_{AL})is defined by:

$$\Theta_{AL} = 0.4044 \sqrt{\frac{\nu}{a}} \tag{3.3}$$

it becomes:

$$\Theta_{AL}^{Cyl} = 0.4044 \left(\frac{\nu\, R}{2Q_{\infty} cos(\Lambda)} \right)^{1/2} \tag{3.4}$$

$$\Theta_{AL}^{Plate} = 0.4044 \left(\frac{\nu t}{Q_{\infty} cos(\Lambda)} \right)^{1/2} = 0.4044 \left(\frac{\nu\, 2R}{2Q_{\infty} cos(\Lambda)} \right)^{1/2}. \tag{3.5}$$

Therefore the momentum thickness of the plate at the attachment-line is $\sqrt{2}$ times greater than that for the cylinder:

$$\Theta_{AL}^{Plate} = \sqrt{2}\, \Theta_{AL}^{Cyl}. \tag{3.6}$$

The thick boundary layer at the attachment-line together with the flat surface in the measurement region, are the two main advantages of the model with respect to a swept cylinder.

The design was inspired by Bearman (1972), who mounted a vertical flat plate followed by a fairing body in a wind tunnel to realise a two-dimensional aerofoil with a blunt leading edge. The role of the fairing body was to prevent rear separation. The main difference between the present model and that of Bearman (1972)'s was that the flat plate employed here had to allow the development of the cross-flow instability on the flat leading edge by maximising the flat plate width (t). In particular, the maximum possible width of the model was constrained by the height of the wind tunnel. In order to have a corresponding total blockage around 21% it had to be $t \leq 100\, mm$.

The design then focused on the cross-flow instability with the aim to predict whether it would have been possible to observe the development of such instability on the flat surface of the model.

According to Poll (1978) the cross-flow Reynolds number (χ) can be derived considering the cross-flow velocity profile (c_{ϵ}) and the streamwise velocity pro-

file (s_ϵ) purely aligned with the spanwise and chordwise directions (which corresponds to $\epsilon = 0$, if ϵ is the orientation of the cross-flow respect to the streamline, as shown in figure 1.8). In that case the velocity profiles are simply a projection of the Falkner-Skan-Cooke solution (equations 2.16):

$$c_\epsilon = W_\infty \, cos(\theta - \epsilon) \left(g(\eta) - f'(\eta) \frac{tan(\theta - \epsilon)}{tan(\theta)} \right) \tag{3.7}$$

where θ is the orientation of the streamlines at each x-location.
As reported in appendix A, for a Hiemenz flow, the maximum of c_ϵ is $c_{\epsilon max} = -0.240 \, W_\infty (U_e/Q_e)$ and the corresponding $\delta_{1\% c_{\epsilon max}} = 3.490 \sqrt{\frac{\nu}{a}}$, where W_∞ is the spanwise velocity in the freestream, a is the Hiemenz constant and U_e,Q_e are the chordwise and total velocities at the edge of the boundary layer.
Therefore, the cross-flow Reynolds number is:

$$\chi = \frac{|c_{\epsilon max}| \, \delta_{1\% c_{\epsilon max}}}{\nu} = 0.838 \, \frac{W_\infty}{Q_e} \sqrt{\frac{a x^2}{\nu}}. \tag{3.8}$$

Substituting W_∞ and Q_e, as shown in appendix A,the cross-flow Reynolds number becomes:

$$\chi = 0.838 \sqrt{\frac{Q_\infty cos(\Lambda) \, x^2 t}{(x^2 \, tan(\Lambda)^{-2} + t^2)\nu}}. \tag{3.9}$$

Poll (1978) suggested the value of $\chi = 125$ for the appearance of the vortices and $\chi = 175$ for the transition.
The cross-flow Reynolds number has been used to optimise the sweep angles, in order to promote the cross-flow instability and to verify that the first occurrence of the vortices appears on the flat surface. In particular, figure 3.3a shows the cross-flow Reynolds number, normalised with respect to the speed and the thickness of the flat plate, as function of the sweep angle Λ.
The maximum wind tunnel speed during the design was assumed to be $25 m/s$, which, for $\Lambda = 40°$ and $t = 0.09m$, makes $\chi > 125$ from $x > 0.06m$ reaching a maximum $\chi = 181$. This corresponds to the appearance of cross-flow vortices on the flat surface, according to Poll (1978).

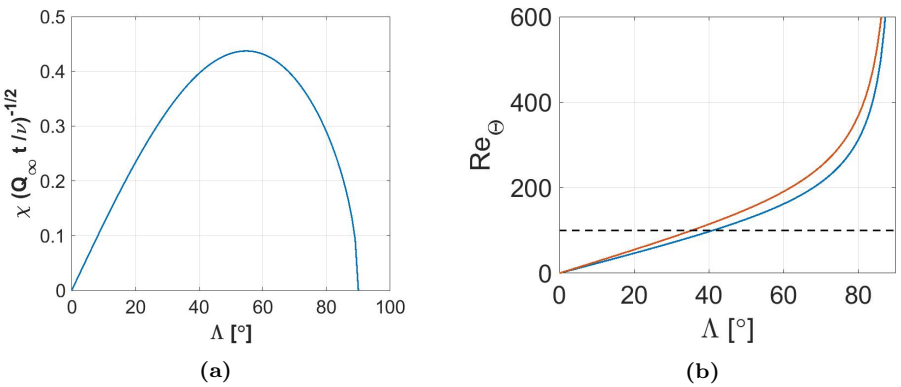


Figure 3.3: a) Cross-flow Reynolds number (χ) at $x = t$ normalised to be function only of the sweep angle (Λ); b) Re_Θ at the attachment-line for $Q_\infty = 25\,m/s$ (red) and for $Q_\infty = 18\,m/s$ (blue) as function of the sweep angle Λ for $t = 0.09m$. The black dashed line represents the limit to avoid attachment-line contamination.

Another issue that had been considered during the design, was that the model could only be mounted horizontally with respect to the wind tunnel in a swept-back configuration. That was due to the traverse system, which moves the hot-wire, that is located on one side wall of the test section. As explained in chapter 2, a swept-back configuration is subjected to attachment-line contamination, which may cause a turbulent flow along the attachment-line. The contamination had to be avoided since the aim of the experiment was to study laminar flows and transition. According to the attachment-line contamination criteria (as reported in chapter 2), the attachment-line Reynolds number (Re_Θ) has to be in the limit of $Re_\Theta \leq 100$. For the flat plate it results:

$$Re_\Theta = 0.404\sqrt{\frac{t\,Q_\infty\,tan(\Lambda)\,sin(\Lambda)}{\nu}} \tag{3.10}$$

Figure 3.3b shows Re_Θ as function of the sweep angle for $Q_\infty = 25\,m/s$ and $Q_\infty = 18\,m/s$. To be below the limit the sweep angle needed to be $\Lambda \leq 40°$. On the other hand, the N-factor analysis with CoDs showed that the cross-flow would not grow enough at $\Lambda = 40°$ (the maximum N-factor was found to be 2 at $Q_\infty = 25\,m/s$), making the onset of the instability extremely difficult to be experimentally observed. It was decided to test the model anyway, since it was an appropriate solution for studying the freestream turbulence distortion approaching the attachment-line boundary layer. The model was realised with

a sweep angle of $\Lambda = 40°$, which should enable measurements on the laminar attachment-line up to $18\,m/s$. The existence of cross-flow instability at that velocity would still be checked and eventually an anti-contamination device could have been employed to run at higher speeds.

Since the study was focused on the receptivity problem, the design had also looked at the location of the neutral stability point, which is the location, along the chordwise direction, after which the disturbances are expected to grow. Thomas et al. (2015) have numerically investigated the cross-flow instability on a swept Hiemenz flow. Considering a sweep angle of 40° and a wind tunnel speed of $18\,m/s$, the simulation of the swept Hiemenz flow, carried out by Thomas, showed that the neutral point is at x/t=0.33 (private communication).

The main parameter of the final design are reported in table 3.1, as sketched in figure 3.4a. The curvature between the flat leading edge and the fairing body ($r = 15\,mm$) has been designed to have a pressure gradient low enough to avoid separation, although it must be considered that a three-dimensional flow over a swept body is less likely to separate than that on an unswept body.

Λ	t	t_{max}	L	Q_∞	Re_θ	χ at $x = t$
40°	$90\,mm$	$100\,mm$	$700\,mm$	$18\,m/s$	97.2	154

Table 3.1: Parameters in the final design of the flat face wing.

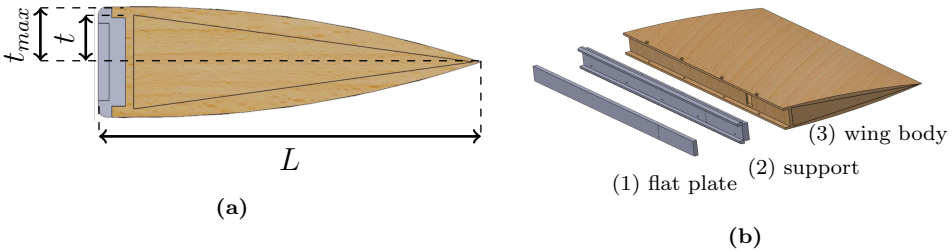


Figure 3.4: Overview of the model design: a) cross section of the model, b) design for manufacturing.

Anyway, during the experiment, the eventual flow separation has been checked using tufts and no clear evidence was found. This cannot completely exclude the presence of a separation, although not strong enough to allow disturbances

propagating upstream up to the measurements area, therefore the flow has been tripped with a roughness strip applied at the end of the plate before the curvature (see figure 3.11).

In terms of manufacturing, the model was designed in three parts (figure 3.4b): (1) flat aluminium plate; (2) aluminium insert for support; (3) wooden wing body. The vertical flat surface at the leading edge was made of aluminium, since it required a high surface finish, using a thick plate (20 mm) to prevent vibrations of the model. In addition, in order to achieve a completely flat and clean surface, with no screws or fasteners disturbing the flow, the aluminium plate was mounted on a second insert through some bolts on the back. The insert was made from aluminium and the gap between the two components was covered by poly filler and smoothed to ensure that the surface was continuous. The aluminium insert together with the flat aluminium plate, were secured to the wing body with bolts on the top of the shoulder. The wing body, simply made of wood, took no part in the experimental investigation and therefore did not require a high surface finish. Some pressure taps were located downstream close to the tip of the flat leading edge.

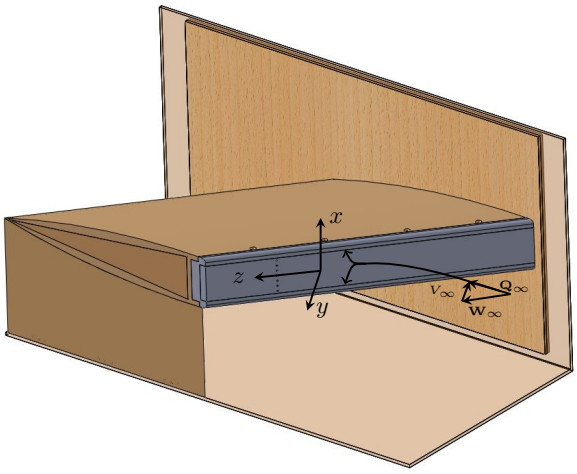


Figure 3.5: The model mounted in the Gaster wind tunnel (flow from right to left).

Figure 3.5 shows the model mounted in the Gaster wind tunnel. On one side it was secured to a thick wooden board, while on the traverse side it rested on a support screwed to the floor of the wind tunnel.

3.2 Wind tunnel facilities

Figure 3.6 shows the experimental facilities. When the project started, the laboratory had been just refurbished; therefore the setup of the wind tunnel instrumentations was part of the project. The wind tunnel was provided with barometric pressure transducer, a Pitot tube to measure the wind tunnel speed, two thermocouples, one to measure the temperature inside the test section and one to measure the ambient temperature. In addition, the system was equipped with a three-axis traverse on which the hot-wire was mounted. The hot-wire was connected to an anemometer and to a filter. Both the unfiltered and filtered signals were acquired, together with the wind tunnel temperature and the atmospheric pressure, using a National Instrument DAQ through LabVIEW software. The code was organised with a main user interface from which different types of acquisition and control modes could be chosen, i.e. simply moving the traverse a certain amount, or turn on the wind tunnel at a desired speed or Reynolds number.

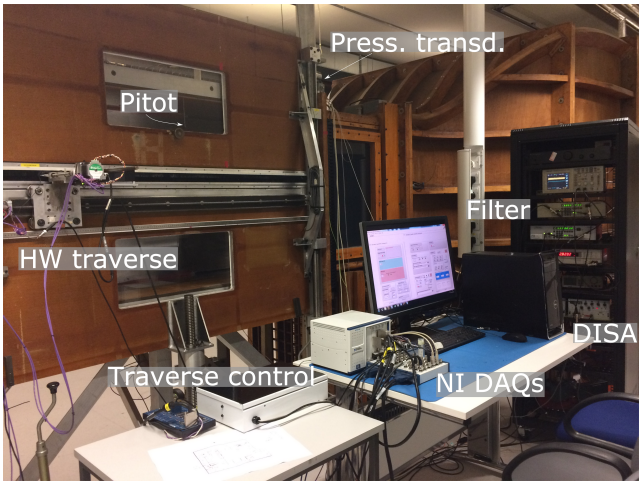


Figure 3.6: Overview of the wind tunnel facilities.

Scan methodology and wall detection

One useful characteristic of the code is the automation of the hot-wire scan coupled together with the wall detection. The code was designed so that one can input a set of xyz-locations at which the velocity has to be acquired, to-

gether with the desired wind tunnel speed or Reynolds number.

The measurements were carried out mainly within the boundary layer, so that one issue was identifying the wall location. The hot-wire is very fragile and it can easily break if it accidentally touches the model surface. The zero, which corresponds to the position closest to the wall, is set at the beginning of each scan. When the scan is automated, the problem is that the surface may present imperfections and the hot-wire in the input locations may be slightly misaligned. To prevent the hot-wire from hitting the surface, the code checks the mean velocity at each location and if it is decreasing below a certain threshold, it skips the point. This together with the high resolution wall normal traverse (1.25 μm for the y-axis) has allowed to carry out detailed boundary layer scan on an extended area.

The coordinate system is defined according to figure 3.7 with y perpendicular to the surface, z spanwise and x on the flat surface in the vertical direction. The origin of the coordinate system is defined along the attachment line at a distance of $300mm$ from the wind tunnel side wall where the traverse is located.

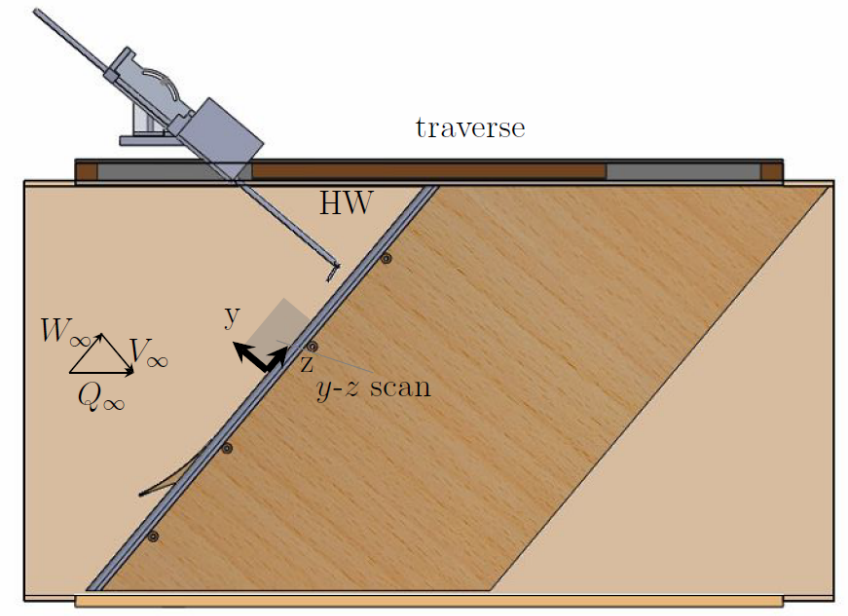


Figure 3.7: Top view of the wind tunnel with the coordinate system adopted. The hot-wire traverse, mounted perpendicular to the leading edge, approaches the model from a side.

Hot-wire anemometer

The measurements were carried out using a single hot-wire anemometer mounted parallel to the attachment-line as shown in figure 3.7.
In this way the hot-wire measures a combination of the velocity perpendicular to the leading edge and parallel to the attachment-line. Since the flow curves as it approaches the leading edge, close to the surface the streamlines are parallel to the flat surface and the velocity is oriented parallel to the attachment-line. The traverse was mounted so that the hot-wire could be moved perpendicular to the leading edge (y-direction).
The goal of the experiment was to measure whether the flow fluctuations are amplified as they approach the attachment-line and whether the disturbances grow downstream over the leading edge. Therefore, the flow was investigated through four types of scan: boundary layer scans along the attachment-line, to check the amplification; z-y scans in planes parallel to the attachment-line to check continuity and at different height to detect cross-flow vortices; x-y scans along the entire surface of the leading edge.
The procedure to setup (gain setting, square wave test) and to calibrate the hot-wire are reported in appendix B, together with the post-process analysis. Briefly, the hot-wire was connected to a band passed filter to remove the frequencies below 2 Hz and above 10 kHz. Both the raw and the filtered signals were acquired simultaneously. The filter signal was used to calculate the Root Mean Squared (RMS) and the Power Spectral Density (PSD), while the Direct Current (DC) part of the signal was used to calculate the mean velocity.

Boundary layer interpolation and wall location

The hot-wire anemometer is not able to locate the wall by itself. As mentioned earlier, the zero is set so that the sensor is aligned close enough to the surface, but always few microns off the surface.
During the experiment the hot-wire was aligned, parallel to the attachment-line, such that the W-velocity component was measured. The solution of the Hiemenz boundary layer is given in chapter 2 via the Falkner-Skan-Cooke

equations. In particular, since the hot-wire measures the velocity parallel to the attachment-line (W), the boundary layer profile is described by:

$$W = W_\infty \quad g(\eta) \tag{3.11}$$

where η is the dimensionless coordinate corresponding to $\eta = \sqrt{\frac{a}{\nu}}y$ (a is determined by the conformal mapping) and $g(\eta)$ is the function defined by the Falkner-Skan-Cooke solution.

The data points correspond to a wall distance y determined by the zero set on the traverse, but the boundary layer must be shifted respect to the real location of the wall. The first step is to transform the dimensional y in the dimensionless η. The boundary layer is shifted by interpolating the first few points with a straight line and checking where the line crosses the η-axis ($\Delta\eta$). The resulting coordinate is $\eta = \eta + |\Delta\eta|$, as shown in figure 3.8.

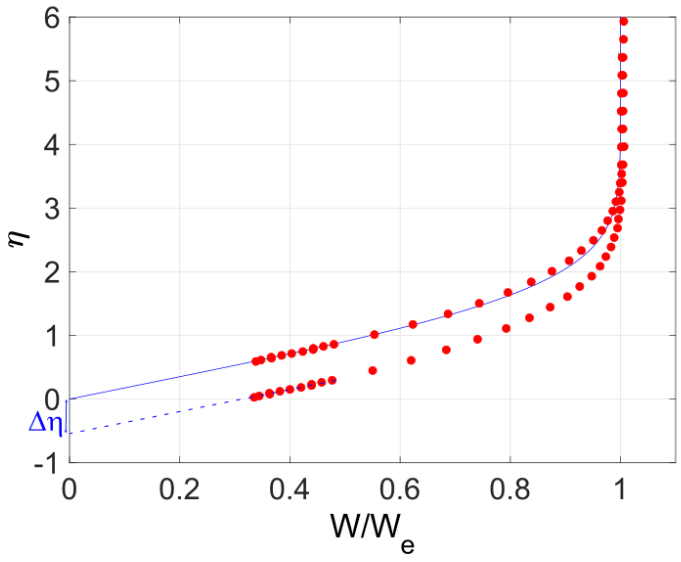


Figure 3.8: Boundary layer at the attachment-line; $\Delta\eta$ is the shift from the wall.

This method works since in a Hiemenz velocity profile the velocity decreases linearly along the points closer to the surface.

In some tests, it was found that not enough data points inside the linear part of the boundary layer were available for interpolation since the total boundary layer thickness was around 1 mm. To enable a better interpolation, the

boundary layer displacement thickness (δ^*) and the momentum thickness (Θ) were calculated by numerically integrating the data point. Their values were compared with the theoretical Falkner-Skan-Cooke solution and the wall shift $\Delta\eta$ iteratively changed until the profile matched the theoretical shape.

3.3 Preliminary experiments

3.3.1 Attachment-line contamination

When a model is mounted for the first time in a wind tunnel, it is good practice to give a general check of the flow state to identify whether the flow is laminar and where, eventually, the transition to turbulence occurs. A qualitative method is to listen to the flow with a stethoscope, technique that allows a rapid interpretation of the flow development over a large area. The stethoscope was connected to a pressure tube placed at the end of a long arm that could be inserted in the wind tunnel and easily moved around. Nothing is heard if the flow is laminar, while a chaotic white noise characterises the turbulent flow.
The analysis has been conducted at different wind tunnel speeds along the flat surface around the attachment-line. The flow was found to be clearly laminar at low velocity, but rapid turbulent spots were detected at $8\,m/s$. By increasing the wind tunnel speed, the frequency of the turbulent spots increased, up to $10\,m/s$ when the flow became completely turbulent.
This observation was unexpected since Re_Θ criteria was respected up to $18m/s$, while turbulent spots were first heard at $8\,m/s$. To solve the issue an anti-contamination device was developed to block the turbulence. Initially, a Gaster device and a splitter plate in different configurations were tested, without success. The reason for that was found by applying tufts on the leading edge and on the wind tunnel wall. At the corner between the thick leading edge and the wind tunnel wall a big recirculation bubble was created, as shown in figure 3.9. Since the size of the bubble was too big to apply the tiny Gaster's device, the same principle was used to create the anti-contamination device shown in the same figure.

The working principle, analogous to the Gaster's device, is explained in figure 3.10a. The turbulent flow coming from the wind tunnel wall flows behind the device to escape at the bottom and top of the wing body. On the leading edge of the device a new laminar attachment-line was created, so that the flow over the device and downstream remained laminar.

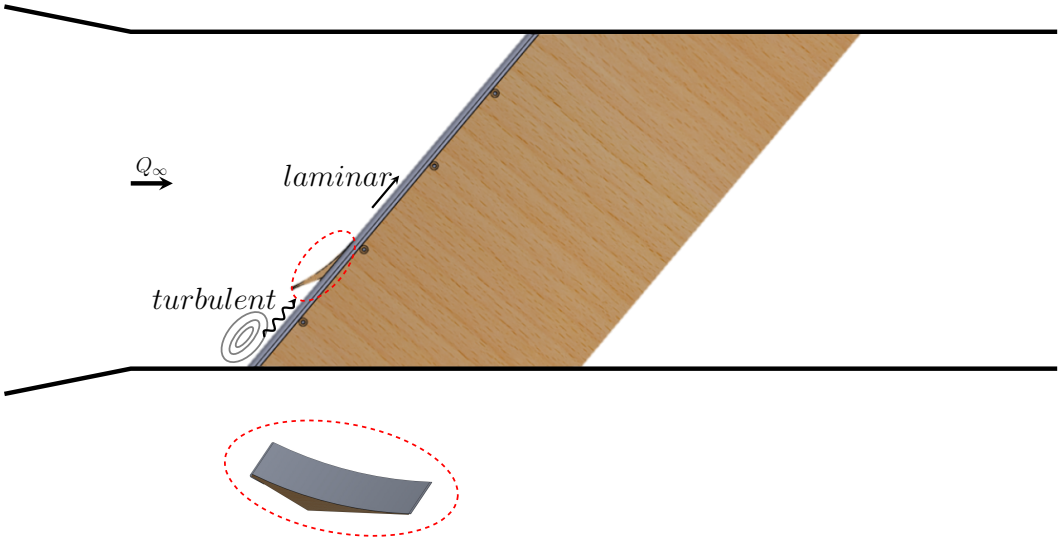


Figure 3.9: Device to prevent the attachment-line contamination from the circulation bubble at the corner between the model's root and the wind tunnel.

The device, in figure 3.9, was built using a wooden structure able to support a thin aluminium foil. Different curvatures of the ramp were tested, but no particular differences were found. Nevertheless, three practical aspects were found to be important in the design of the device:

- the leading edge of the device needs to be rounded to allow the formation of a new attachment-line on the device itself;
- the trailing edge of the device needs to be smoothly joined to the surface with no gaps or steps;
- the flow behind the device has to be free to flow away from the bottom and the top surface.

Figure 3.10b shows a flow visualisation that has been carried out using Surface Oil Flow Visualisation (SOFV). A mixture of a fluorescent pigments (dayglo)

with white spirit and oleic adic was painted on the surface. When the wind tunnel is turned on, part of the paint evaporates while the dye stays on the surface identifying the flow direction. The critical point analysis (Délery, 2001) has been then applied to understand the flow directions, as drawn in figure 3.10b. Two critical points can be identified on the surface, one corresponding to the recirculation bubble and one under the device. The latter, a *saddle point* to which the flow converges, probably is due to the reverse flow underneath the device.

The model in the final configuration installed in the wind tunnel is shown in figure 3.11.

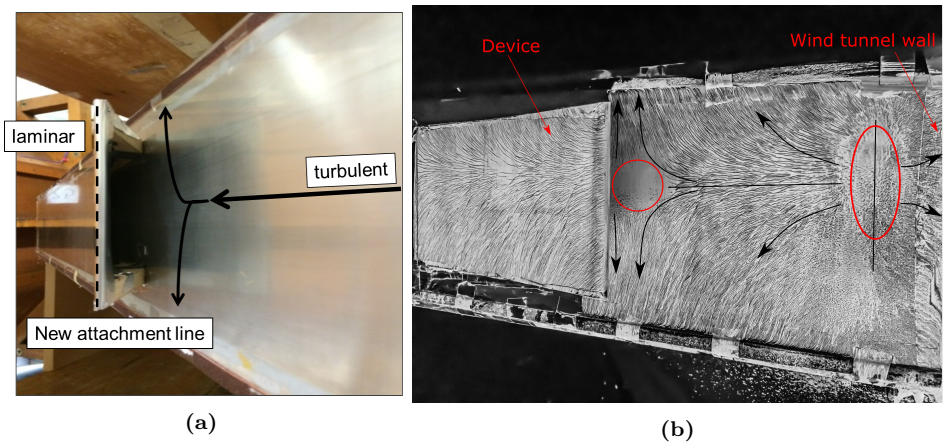


Figure 3.10: a) anti-contamination device installed on the model, b) flow visualisation.



Figure 3.11: Front view of the model mounted in the Gaster wind tunnel with the device to prevent contamination.

Although the device was found to be effective up to 20 m/s, a few turbulent spots appeared randomly in the time signal of the hot-wire inside the boundary layer. Figure 3.12 shows an example of the raw and filtered hot-wire signal at 10 m/s, where around 3 s a big peak can be detected both in the filtered and unfiltered signal. By looking closely at the spikes several frequencies can be detected in the corresponding signal. The origin of the turbulent spots was attributed to some unsteadiness in the recirculation bubble which was able to detach and travel downstream along the attachment-line. The presence of those spots did not change the nature of the flow, but influenced the post-process of the signal.

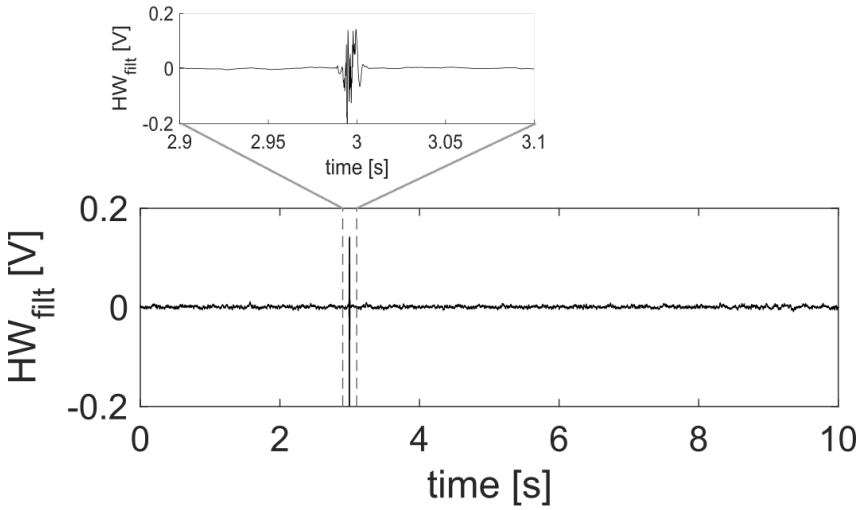


Figure 3.12: Spike appearing in the hot-wire filtered time signal.

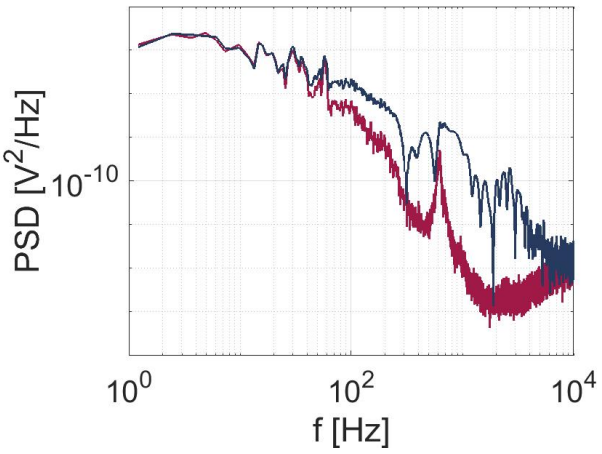


Figure 3.13: Spectra of the hot-wire signal with (blue) and without (red) the spike.

In particular, figure 3.13 shows the spectra of the same time signal with and

without the turbulent spike. The presence of the spike modifies the frequency content over a broad range and therefore those spikes have to be detected and then removed from the signal in the post-processing. The methodology adopted to evaluate the mean, RMS and PSD of the time signal is reported in appendix B. Briefly, when the PSD is carried out the time signal is divided in blocks of equal time length. The PSDs of each block are calculated and averaged to get the PSD of the whole signal. This technique reduces the noise in the spectra. To remove the spikes without modifying the signal, the blocks containing the spike are directly ignored in the final average. This procedure has been carried out for all the data points. The turbulent spots appeared randomly distributed in time. On average one or, more rarely, two appearances in a 10 seconds signal were detected at 18 m/s.

3.3.2 Pressure measurements

The pressure distribution on flat surface was measured by using a pressure transducer connected to a scannivalve. It is usually given in terms of dimensionless pressure coefficient:

$$c_p = \frac{p_s - p_{s\infty}}{\frac{1}{2}\rho Q_\infty^2} \tag{3.12}$$

where p_s is the static pressure at each pressure tap, $p_{s\infty}$ is the static pressure of the Pitot, ρ is the air density.
In figure 3.14, the measured c_p is compared to the numerical one computed by using a potential flow code. The code enables the calculation of the two-dimensional distribution (c_p^{2D}), that is afterwards converted to the three-dimensional distribution by:

$$c_p^{3D} = c_p^{2D} cos^2(\Lambda) \tag{3.13}$$

The geometrical sweep angle Λ is 40°, but due to the blockage and non-uniformity of the flow in the wind tunnel the actual sweep angle could vary. In the present experiment an effective sweep angle of $\Lambda = 36°$ has been estimated

by interpolating the pressure measurements.

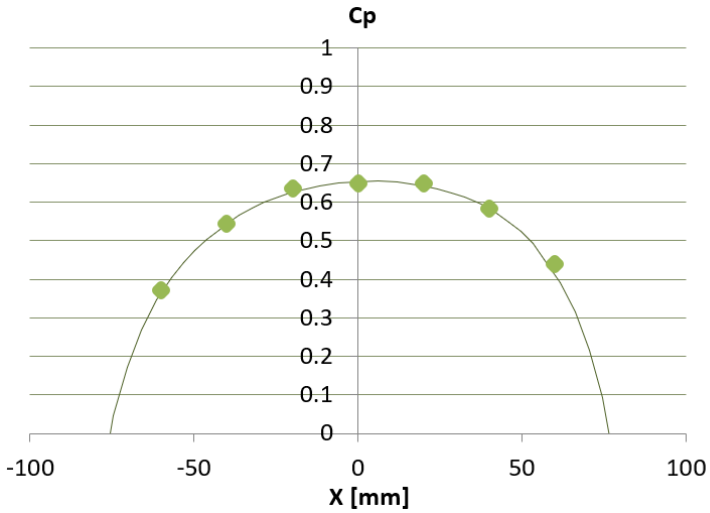


Figure 3.14: Pressure distribution on the flat leading edge: • measured, **-** numerical.

3.4 Flow approaching the leading edge

The first objective of the experiment was to determine whether the flow fluctuations are amplified approaching the attachment-line.

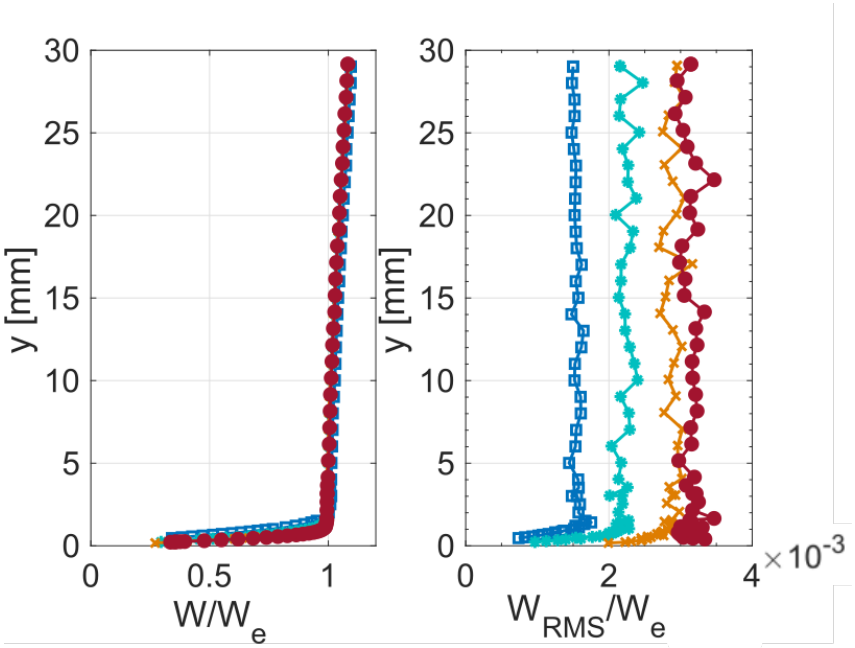
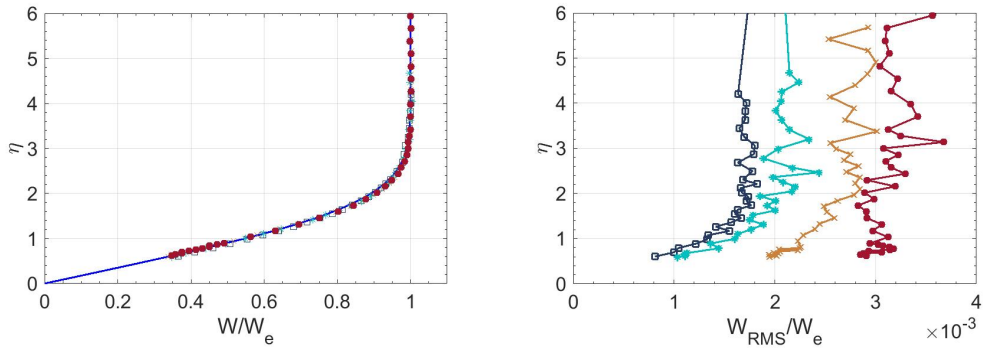


Figure 3.15: Velocity profiles, mean and RMS, approaching the model at different freestream velocities: □ $Q_\infty = 8m/s$, * $Q_\infty = 10m/s$, × $Q_\infty = 15m/s$, • $Q_\infty = 18m/s$.

Figure 3.15 shows the mean and the fluctuations of the velocity approaching the leading edge from a distance of 30 mm at four different freestream speeds (8 m/s, 10 m/s, 15 m/s and 18 m/s). The field of investigation was limited by a small area accessible by the hot-wire traverse. The mean velocity decreases far from the leading edge until it becomes fully spanwise ($W/W_e = 1$) and then decrease inside the boundary layer. The fluctuations are constant throughout the field of measurements decreasing only close to the wall inside the boundary layer. The measurements did not show the increment in the velocity fluctuations at the edge of the boundary layer, as it was observed in the experiments on the two-dimensional stagnation point flow available in literature (discussed in Chapter 2). The reason may be sought in the low level of disturbances naturally presented in the wind tunnel, which is not enough to show the amplification effect.

Figure 3.16a and 3.16b further show the mean and the RMS velocity profiles zoomed inside the boundary layer as a function of the dimensionless coordinate η. All the boundary layer profiles are in good agreement with the Falkner-Skan-Cooke solution (blue line in figure 3.16a).



(a) **(b)**

Figure 3.16: a) Boundary layer velocity profile compared to Falkner-Skan-Cooke solution (blue line) and b) RMS profiles at four freestream velocities: □ $Q_\infty = 8\,m/s$, * $Q_\infty = 10\,m/s$, × $Q_\infty = 15\,m/s$, • $Q_\infty = 18\,m/s$.

To further analyse the data, the Power Spectra Density (PSD) of each data point has been calculated. Figure 3.17 shows an example of spectra at different velocity at the edge of the boundary layer. In that location, the spectra are similar for the four freestream velocity, slightly increasing at low frequencies.

A peak clearly appears at 150 Hz at low velocities, due to the main electric current and not to a particular condition of the flow.

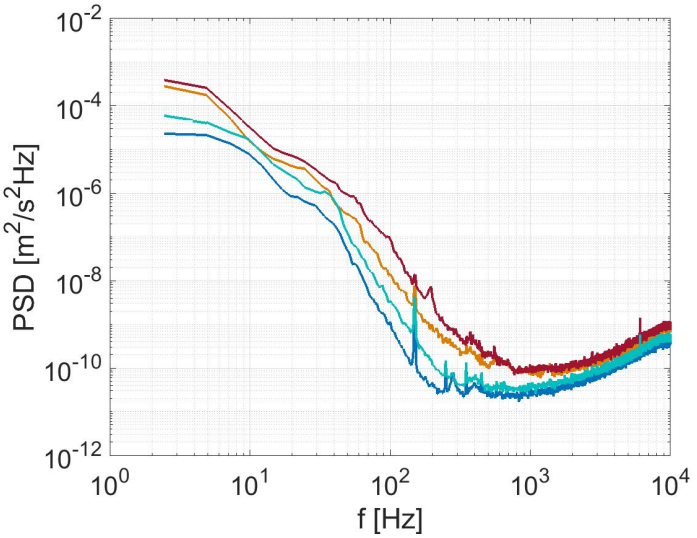


Figure 3.17: Spectra at the edge of the boundary layer at different velocities: $Q_\infty = 8\,m/s$, $Q_\infty = 10\,m/s$, $Q_\infty = 15\,m/s$, $Q_\infty = 18\,m/s$.

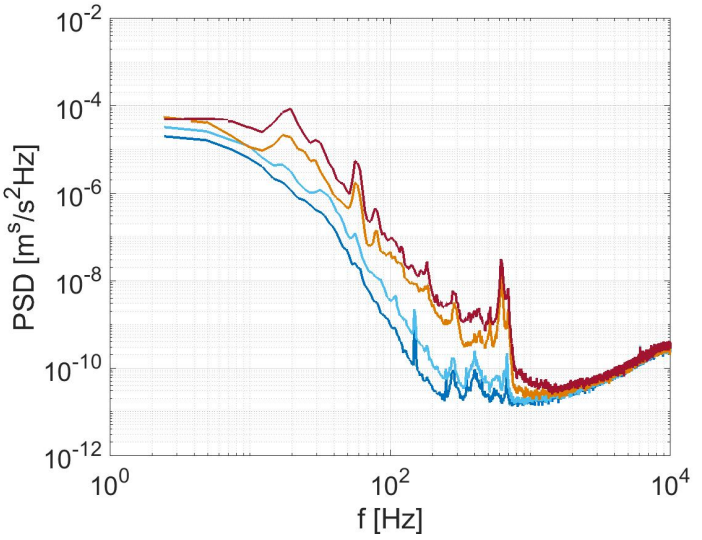


Figure 3.18: Spectra inside the boundary layer (closest point to the wall) at different freestream velocities: $Q_\infty = 8\,m/s$, $Q_\infty = 10\,m/s$, $Q_\infty = 15\,m/s$, $Q_\infty = 18\,m/s$.

The spectra inside the boundary layer do not change between $8m/s$ and $10m/s$, but at 15 m/s and 18 m/s three frequencies appear particularly amplified: 20 Hz, 58 Hz and 600 Hz. The latter will be discussed in section 3.5. Figure 3.19 shows the signal band passed around those two frequencies. The graph

confirms how the frequencies are hightlight going towards the wall only at higher velocities.

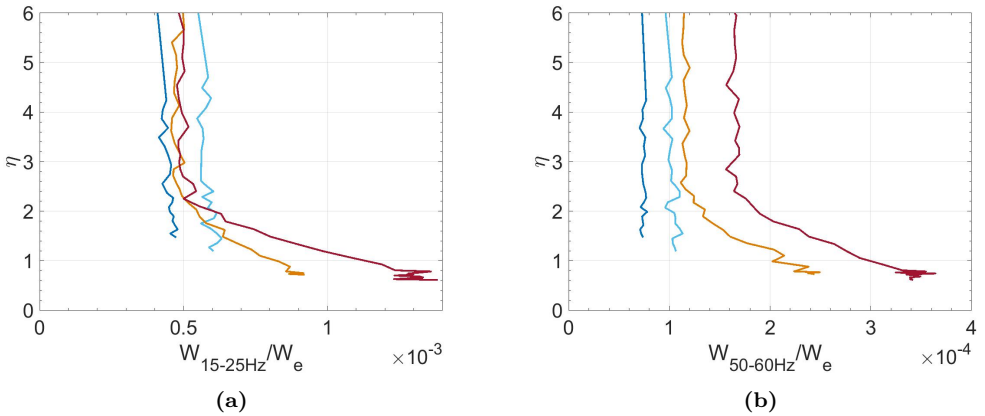


Figure 3.19: Boundary layer profile of the signal band passed respectively in the ranges a) $15\ Hz \leq f \leq 25\ Hz$ and b) $50\ Hz \leq f \leq 60\ Hz$, at different velocities: $Q_\infty = 8\ m/s$, $Q_\infty = 10\ m/s$, $Q_\infty = 15\ m/s$, $Q_\infty = 18\ m/s$.

The origin of those amplifications were not clear, therefore a second hot-wire was employed for the investigation. The second hot-wire was mounted on a manual traverse attached to the surface. A pivot mechanism enabled the distance from the wall to be manually set. By checking the flow within the boundary layer in the same location with the new traverse, the amplified frequencies were not found in the second hot-wire. It was supposed that the frequencies were due to the traverse vibrations.

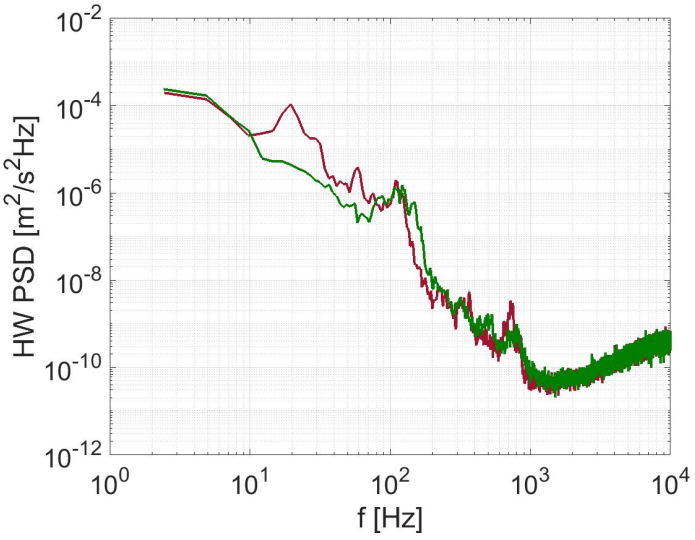
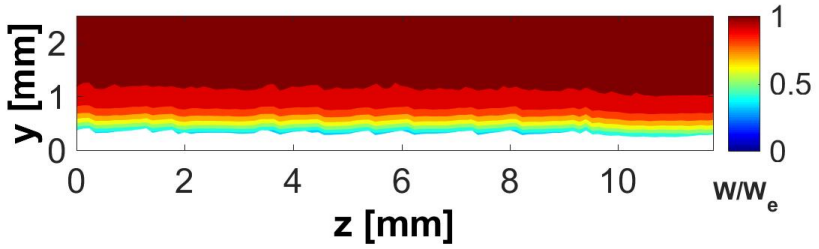


Figure 3.20: PSD of the hot-wire signal at $Q_\infty = 18\ m/s$, $1\ mm$ from the wall (edge of the boundary layer) with (green) and without (red) the tape holding the sensor.

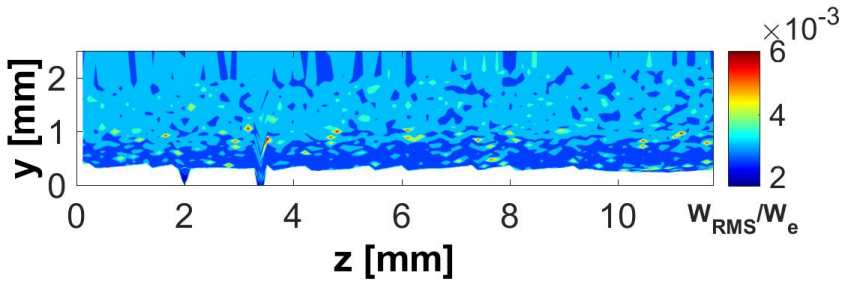
To verify this hypothesis, the hot-wire with the original traverse system was placed quite close to the surface and two consecutive measurements were taken, the first in the original configurations, the second with some tape to hold the probe against the surface. Figure 3.20 shows the comparison of the signals in the two cases at $18\,m/s$ in the same location; the green line is the measurement with the tape and the red without the tape. The plot shows how the frequencies $20\,Hz$ and $58\,Hz$ completely disappear when the hot-wire is kept steady.

3.4.1 Boundary layer along the attachment-line

The boundary layer along the attachment-line ($x = 0$) has been measured over a distance of $12\,mm$, starting from the origin of the coordinate system defined in figure 3.7, with a resolution of $0.2\,mm$. The intention has been to check the uniformity of the flow and to investigate whether flow structures were present along the attachment-line.



(a)



(b)

Figure 3.21: Contour plot inside the boundary layer along the attachment-line (z-direction) at $18\,m/s$: a) mean velocity b) RMS.

The measurements carried out at 18 m/s are shown on figure 3.21, showing both the mean and the RMS of the hot-wire signal along the attachment-line normalised by the edge velocity. The velocity contour shows that the flow is uniform along the z-direction.

3.5 Cross-flow instability and development of the flow along the flat plate

The second objective of the investigation was to observe the cross-flow instability. As explained in Chapter 1 the development of the cross-flow instability appears like co-rotating vortices in the spanwise direction.

The difficulty of measuring the cross-flow instability using a single hot-wire anemometer is that it measures only one velocity component perpendicular to the wire itself. On a swept body, the streamlines are curved making the hot-wire hardly aligned with the streamlines. Therefore, the hot-wire does not measure the cross-flow velocity profile, but usually measures the chordwise or spawise velocity component. Those components may show a distortion and a spanwise modulation in the boundary layer as an effect of the cross-flow instability.

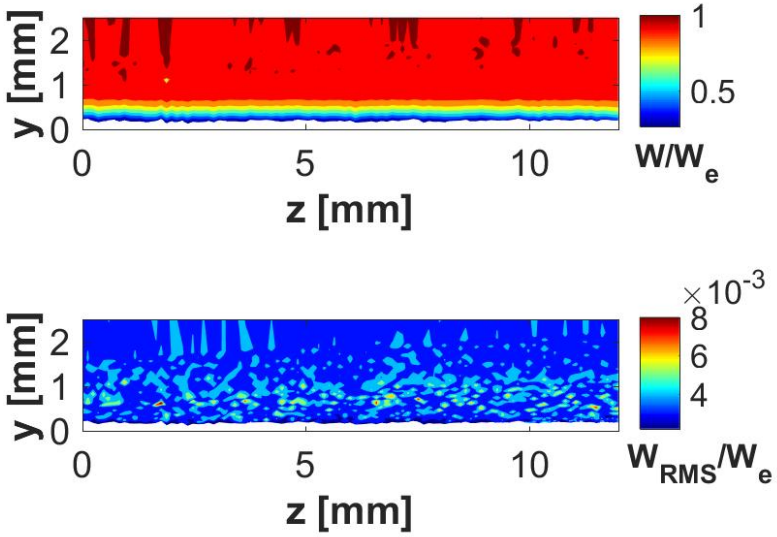


Figure 3.22: YZ scan along the boundary layer at x=60 mm.

According to Thomas et al. (2015) the neutral stability point on the model should be at $x/t = 0.33$, from which the disturbances should start growing. The flow was measured in a plane perpendicular to the leading edge at different heights at 18 m/s.

In particular, figure 3.22 shows the scan at $x = 60\,mm$ which corresponds to $x/t = 0.6$. The flow has been acquired with a spatial resolution of 0.2 mm along a distance of 12 mm.

If stationary cross-flow instability were developing, one would expect to see spanwise modulation in the meanflow developing as shown in figure 3.23. Such modulation does not appear at any chordwise locations along the flat surface. To verify the absence of cross-flow vortices in the spanwise direction, the average spanwise fluctuations from the mean velocity profile (W^*) are quantified as:

$$W^* = \frac{1}{n}\sqrt{\sum_{i=1}^{n}\left(\frac{W(y_i) - \overline{W_z(y_i)}}{W_e}\right)^2} \tag{3.14}$$

where n is the number of velocity profiles along z, $\overline{W_z(y_i)}$ is the mean velocity along the spanwise coordinate z and $W(y_i)$ is the velocity within the boundary layer. If no spanwise modulation is present W^* is zero.

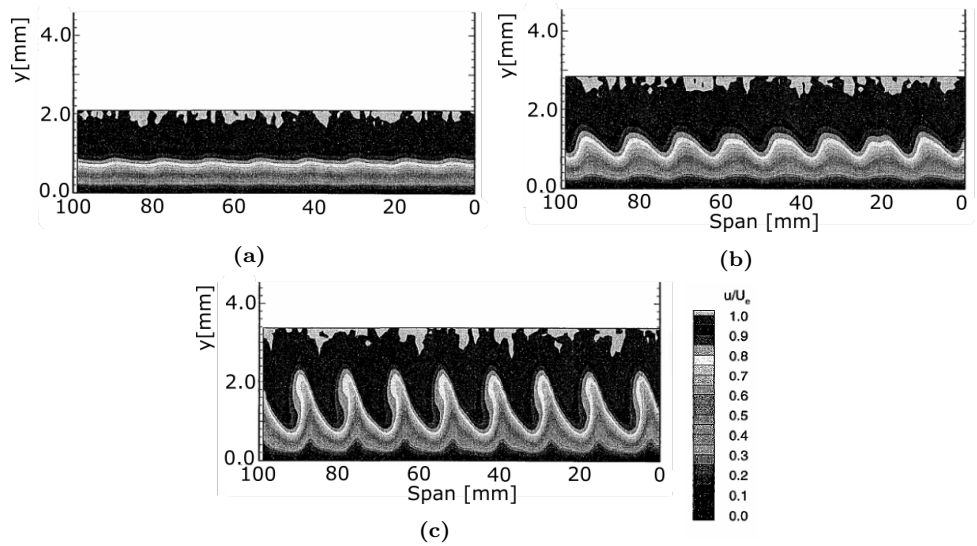


Figure 3.23: Influence of the cross-flow instability on the mean chordwise velocity over a wing at different chordwise location (x/c) from Reibert (1996): a)$x/c = 0.1$ corresponding to the neutral stability point, N-factor=0 b)$x/c = 0.2$, N-factor=1.8 c)$x/c = 0.3$ N-factor=3

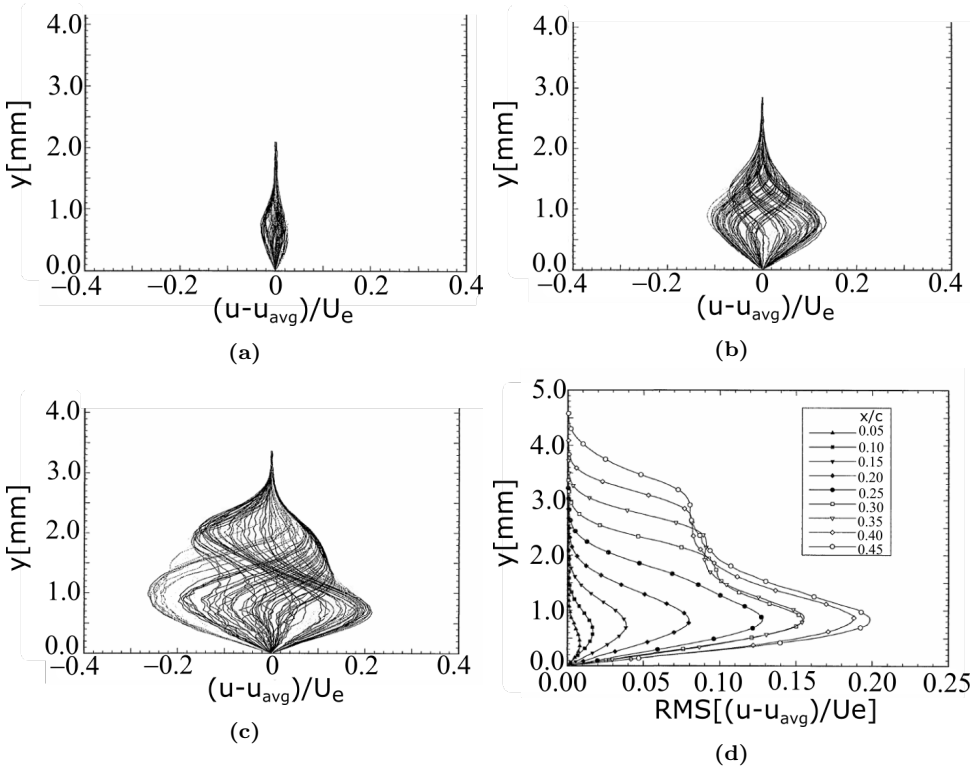


Figure 3.24: The spanwise fluctuation of the mean velocity in the presence of cross-flow instability by Reibert (1996). The plots a), b) and c) correspond to figure 3.23 d) evolution of the mode shape along the chord.

Figure 3.24 shows an example of the mean chordwise velocity fluctuation ($\frac{U(y_i)-\overline{U_z(y_i)}}{U_e}$) for the example of cross-flow development over a swept wing reported in figure 3.23 (Reibert, 1996). The development shows how the cross-flow instability deforms the mean velocity when the vortices are not visible in the mean boundary layer profile (figure 3.24a).

The same procedure has been carried out for the actual experiment and the results are reported in figures 3.25a, 3.25b and 3.25c. The mean velocity profiles in figure 3.25a almost lie on top of each other. In the same figure, the average profile is represented by the black line. Figure 3.25b reveals small differences between the profiles at the edge velocities and a higher deviation inside the boundary layer below $\eta = 2$.

Finally, the average of the spanwise fluctuation (W^*) is represented in figure 3.25c. The plots show a spanwise deviation from the average mean profile as it happens in cross-flow instability, but the discrepancy is quite close to the wall with the maximum of W^* at $\eta = 1$. In Reibert (1996), a small variation

in the spanwise RMS of the boundary layer profile has been measured already at a distance of x/c=0.1 from the attachment-line where the N-factor starts growing (see figure 3.23). Figure 3.25c compares the evolution of W^* at the attachment-line and at $x = 60\,mm$; the spanwise variations grow but remain anyway small. A second analysis has looked at the frequency domain, and at the evolution of the PSD within the boundary layer at $x = 60\,mm$.

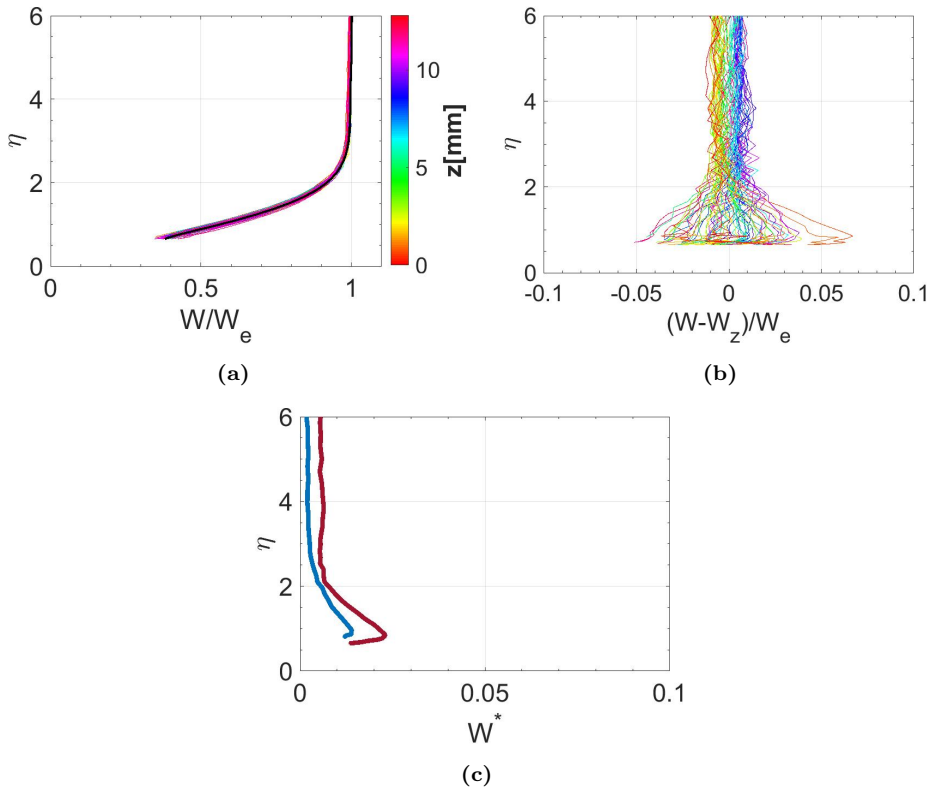


Figure 3.25: (a) Boundary layer profiles across z at $x = 60\,mm$, (b) spanwise variations from the average boundary layer profile at $x = 60\,mm$, (c) average spanwise variations (W^*) at x=0 mm (blue) and x=60 mm (red).

The PSD at different locations approaching the boundary layer is reported in figure 3.26a. For a better clarification the same plot is reported as a contour plot in figure 3.26b. The spectra at all the y-locations appear to be quite regular, except for the power at 600 Hz that seems to be amplified in the boundary layer as it was also observed at the attachment line.

To analyse the contribution of the 600 Hz frequency to the whole signal, from the PSD the RMS band passed between 550 Hz and 650 Hz has been plotted in figure 3.27 for the y-z domain. This frequency band appears homogeneously amplified along the z within the boundary layer.

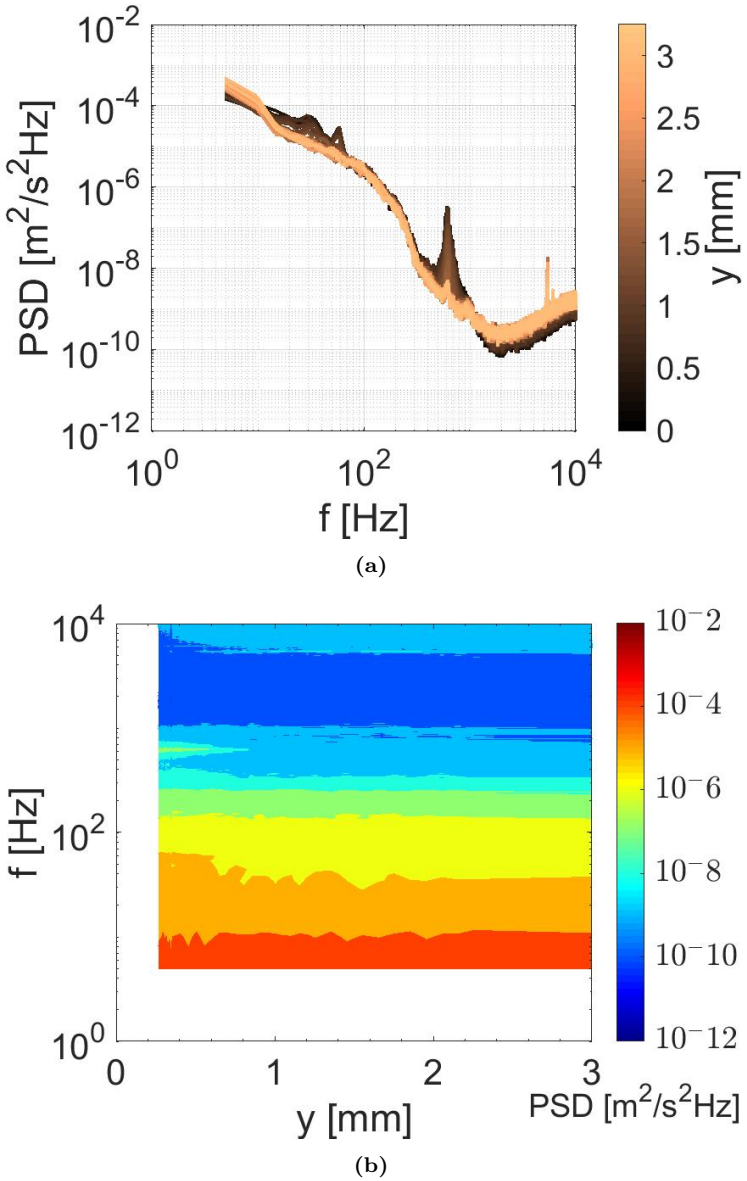


Figure 3.26: Spectra of a single boundary layer profile at $x = 60\,mm$: a) spectra plot at different height in the boundary layer b) corresponding contour plot.

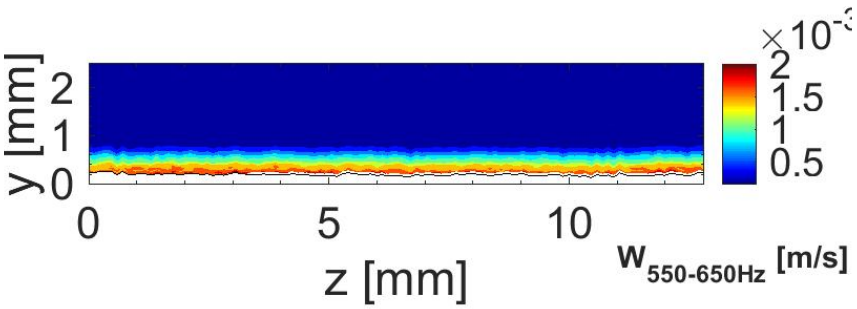


Figure 3.27: Contour plot of the velocity fluctuations band passed between 550 Hz and 650 Hz in a y-z plane.

YX scan

A YZ scan along the entire flat leading edge has confirmed that the band around 600 Hz grows downstream over the plate close to the surface. Figure 3.28 shows the mean and the band passed signal between 550 and 650 Hz which clearly amplifies around $x = 50\,mm$.

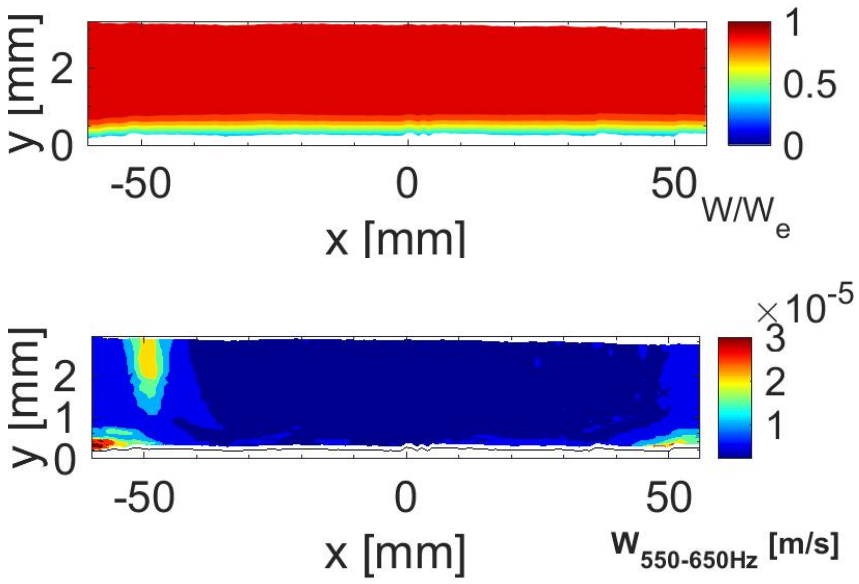


Figure 3.28: YX scan along the entire plate: mean spanwise velocity and signal bandpassed between $550 - 650\,Hz$.

To complete the picture, figure 3.29a and 3.29b compare the spectra inside the boundary layer ($\eta = 1$) and outside the boundary layer ($\eta = 6$) at $x = 0\,mm$ and at $x = 60\,mm$. Again, the 600 Hz frequency is clearly amplified at $x = 60\,mm$. A second difference can be identified in the range around $100\,Hz$, which contains much more energy downstream both in the boundary layer and at the edge of the boundary layer.

Although some frequencies appear to be amplified downstream, from this analysis it can be concluded that stationary cross-flow instability has not been observed on the model at $18\,m/s$. Whether it would appear at higher velocities, as predicted by the N-factor analysis, is difficult to confirm since such velocities cannot be reached in the actual wind tunnel configuration.

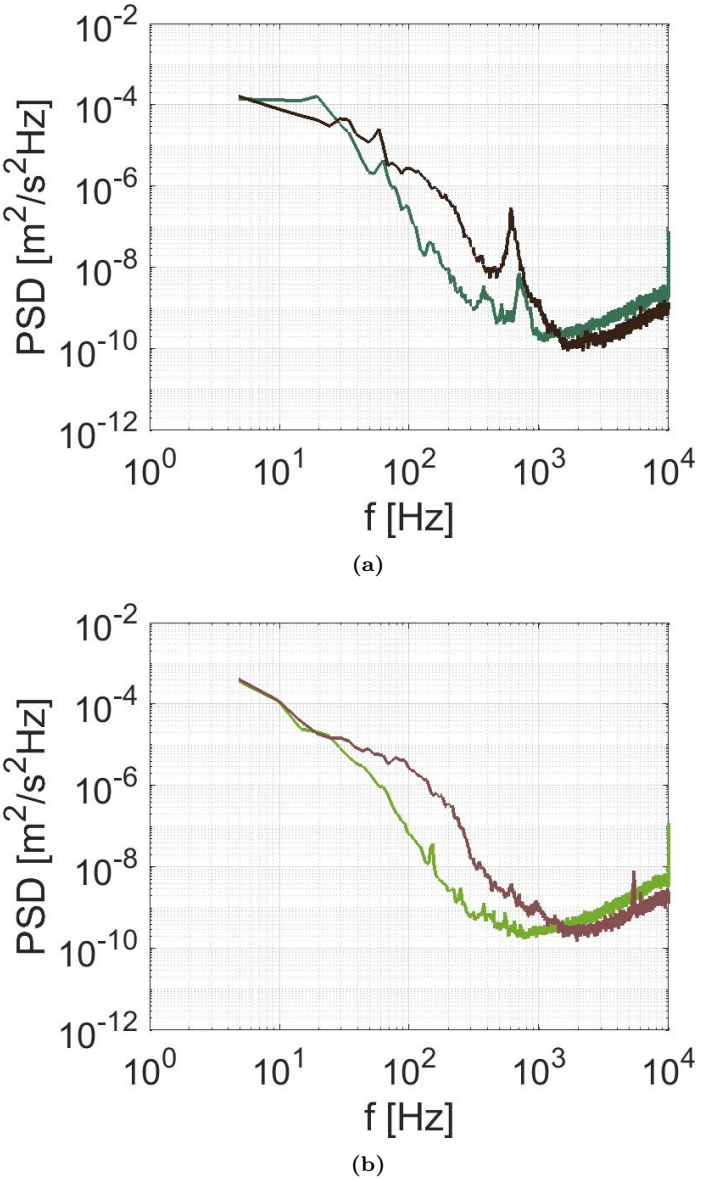


Figure 3.29: Spectra of a single boundary layer profile at $x = 60\,mm$ (brown) and $x = 0\,mm$ (green): a) Inside the boundary layer ($\eta = 1$) b) outside the boundary layer ($\eta = 6$).

3.6 Experiments with freestream disturbances

3.6.1 The string

The aim of the experiment was to study the effect of the freestream turbulence on the flow impinging on a swept blunt leading edge. Since the freestream turbulence level in the wind tunnel was low, the turbulence level has been increased by placing a metallic string ahead of the model. The wake of the

string generates a vortex street which travels towards the model and interacts with the boundary layer. The disturbance so created would be followed downstream observing whether it is amplified or attenuated approaching the boundary layer. Similar technique has been used in vorticity amplification experiments, for instance, by Nagib and Hodson (1978).

In order to mount the string at different locations across the wind tunnel a mechanism to keep the string steady and well tensioned had to be designed. The mechanism had to be outside the wind tunnel to avoid interference and it needed to be easy to install in different locations. For this purpose, the system in figure 3.30 was fabricated.

It consisted of a simple wooden L-shaped base on which a guitar tuning key was mounted. This solution was found to be cheap and simple to realise, guaranteeing an easy and quick way to tension the wire. Two of those systems were mounted at the two ends of the wind tunnel. A tiny hole in the wood was drilled for each position to allow the string to travel across the test section.



Figure 3.30: Mechanism to tension the string.

The string was mounted both horizontally and vertically at different locations as shown in figure 3.31 and in table 3.2. The orientation of the string, which in the table has been specified by the letters H or V, changes the orientation of the vortices generated in the wake. When the string was mounted horizontally with respect to the wind tunnel the wake would generate vortices oriented in the spanwise direction, while when the string was mounted vertically the vortices would be oriented in the chordwise direction. According to the vorticity amplification theory, developed for two-dimensional bodies, the vorticity oriented perpendicular to both the stagnation line and the wall-normal (x-direction in this case) should be mostly amplified. Therefore, if the theory could have been directly extended to the swept configuration, one would expect that the vortices generated by the vertical string would have greater amplification then the horizontal case.

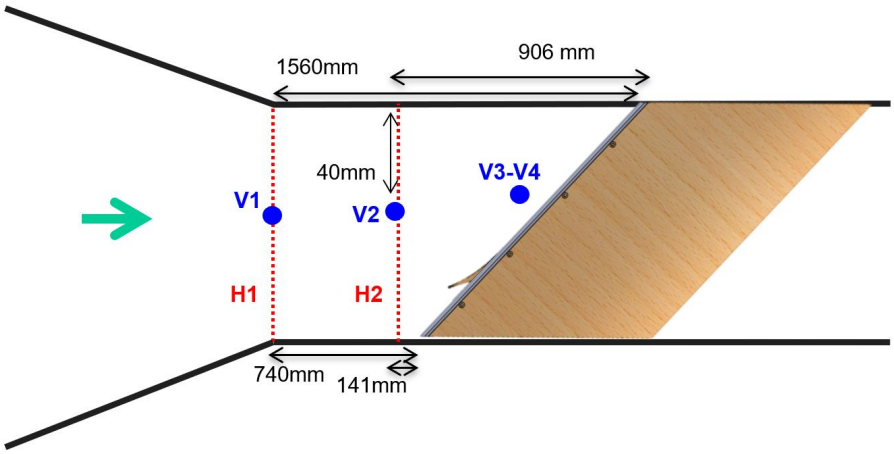


Figure 3.31: String location with respect to the model for each test case.

Location	$d\ [mm]$	$Q_\infty\ [m/s]$	Re_d	Observations
H1	0.53	18	631	Turbulent
H1	$0.23 \leq d \leq 3$	$6 \leq Q_\infty \leq 18$	$91 \leq Re_d \leq 10^3$	Turbulent
H2	0.23	18	274	Laminar
V1	$0.23 \leq d \leq 3$	$6 \leq Q_\infty \leq 18$	$91 \leq Re_d \leq 10^3$	Laminar
V2	0.23	18	274	Laminar
V3 ($y_g = 4\,mm$)	0.23	6	91	Laminar
V4 ($y_g = 6\,mm$)	0.15	18	178	Laminar

Table 3.2: Test cases: H and V indicate the string orientation, respectively horizontal or vertical, d the diameter of the string, Q_∞ the freestream velocity, Re_d the Reynolds number of the string, y_g the distance from the leading edge. For each test case, the nature of the flow at the attachment-line is reported.

Horizontal string

Initially, the string was mounted after the contraction in the positions H1. Different string diameters (d) were tested at this location corresponding to different Reynolds numbers based on the string diameter (Re_d). The string diameter was chosen so that the wake was in laminar state, $Re_d < 10^3$ (Zdravkovich, 1997). In position H1, the boundary along the attachment-line on the model was found to be turbulent at all the Reynolds numbers tested.

A second attempt was carried out moving the string closer to the model, in position H2. The boundary layer was found to be laminar with the fluctuations, in the outer region, three times higher with respect to the case without the

string ($W/W_e = 0.8\%$ respect to $W/W_e = 0.3\%$). The RMS profile approaching the wall was constant in the outer region decreasing inside the boundary layer as for the case without a string. The main issue with the string in location H2 was that the wire was aligned horizontally to the wind tunnel test section and not parallel to the model. Therefore, since the streamlines were curved, the disturbance generated by the string was non-homogeneous in the spanwise direction and probably highly three-dimensional. On the other hand, the available space in the test section in front of the model did not allow one to mount the string parallel to the attachment-line, in order to be equidistant from the leading edge. In addition, if the string was placed far from the attachment-line, the wake would dissipate and increase its width approaching the wall. This makes the wake near the wall too wide to experimentally follow its evolution downstream.

The fact that the flow was laminar in H2 and turbulent in H1 was unforeseen. A possible explanation, as sketch in figure 3.32, is that the wake of the string reaches the root of the wing interacting with the recirculation bubble still present and making the attachment-line of the device itself turbulent. This effect enhances the importance of the wing root in a swept-back configuration.

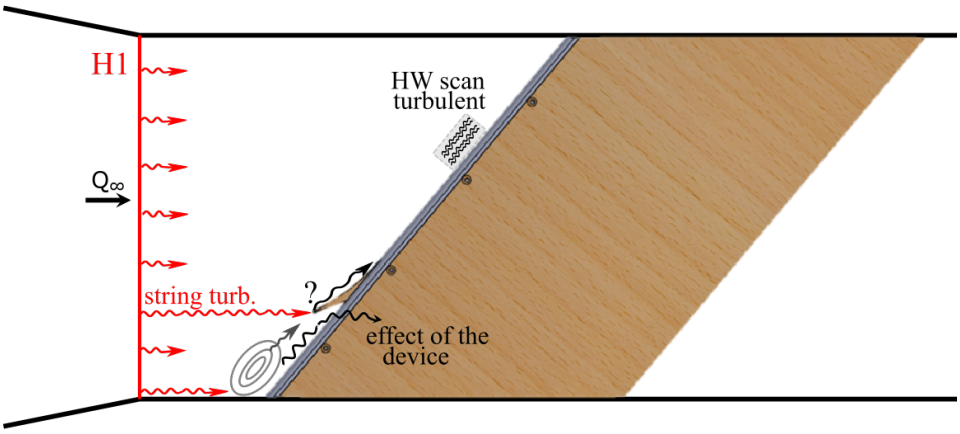


Figure 3.32: Interaction of the horizontal string with the model. The turbulence coming from the string (red) may interact with the anti-contamination device and make the flow turbulent on the attachment-line of the device itself.

Vertical string

The string with the vertical orientation was installed in the locations defined in figure 3.31 and table 3.2. The boundary layer was found to be laminar for all those locations.

The problem with the vertical string was that the wake moves along the streamlines, therefore if the string is placed far from the leading edge, the vortex would never reach the boundary layer. Figure 3.33 shows an example with the string placed in position V1 at different velocities. On top of the boundary layer a typical wake profile can be observed with the minimum velocity within the wake at x=15 mm from the surface. The RMS velocity fluctuations, in figure 3.33, shows as well the typical profile with the double hump of the wake.

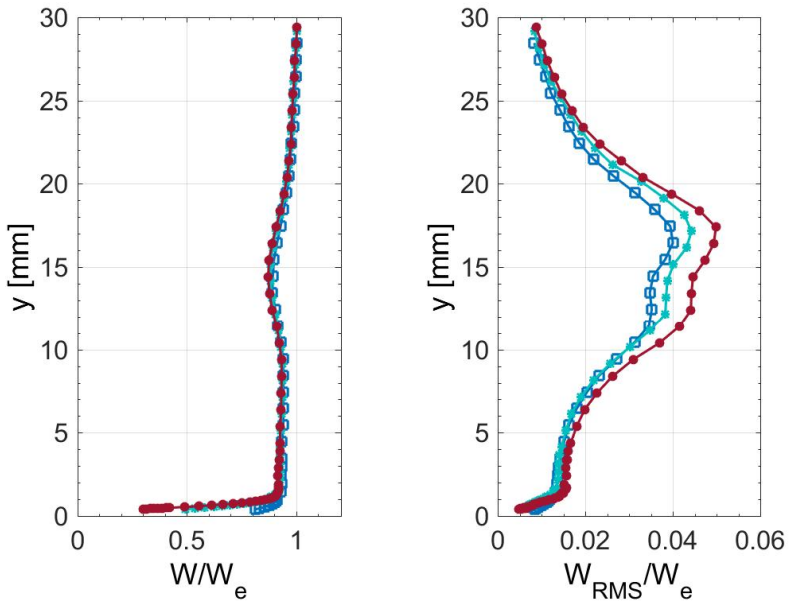


Figure 3.33: Mean and RMS velocity profile, approaching the model with the vertical wire in position V1 at different velocities: □ $Q_\infty = 8\,m/s$, ∗ $Q_\infty = 10\,m/s$, • $Q_\infty = 18m/$.

The absence of symmetry between the humps is due to the wake being not completely aligned with respect to the flow scan, since the streamlines are curved. The variation in the freestream velocity changes the wake appearance in all its characteristics (velocity deficit, RMS level, wake width), but overall

it does not change too much and more interestingly the effect on the boundary layer is somewhat similar. Only the tail of the wake reaches the boundary layer.

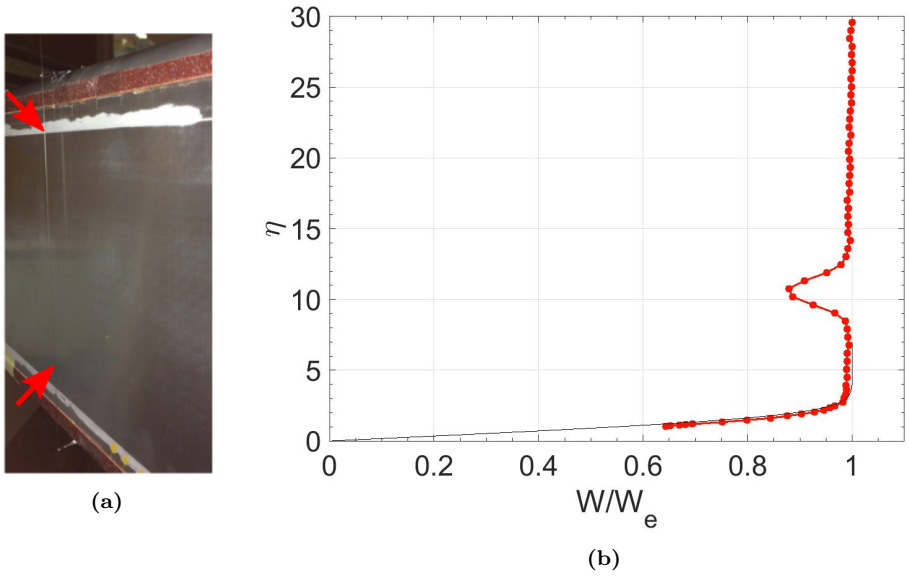
Two issues had to be solved, the wake was too wide with respect to the boundary layer and it was travelling far from the boundary layer edge. To solve these issues it appeared necessary to mount the string closer to the surface and reduce the string diameter (positions V3 and V4).

Figure 3.34 shows the string in position V4 and the corresponding boundary layer profile.

Since the string in this case was 0.15 mm the wake was less wide, but the velocity deficit on the boundary layer increases to 20% of the edge velocity. The boundary layer is still laminar and comparable with the Falkner-Skan-Cooke solution.

Figure 3.35 shows the velocity and RMS contour along z with the wake of the string travelling, with the streamlines, parallel to the attachment-line.

Nevertheless, this makes the nature of the disturbance different compared to the desired one. In fact, in the resulting configuration the experiment represents a wake-boundary layer interaction rather than a freestream disturbance impinging on a surface.



(a) (b)

Figure 3.34: a) Vertical string in the position V4 and b) an example of the corresponding velocity profile along the attachment-line downstream of the string ($Q_\infty = 18\,m/s$).

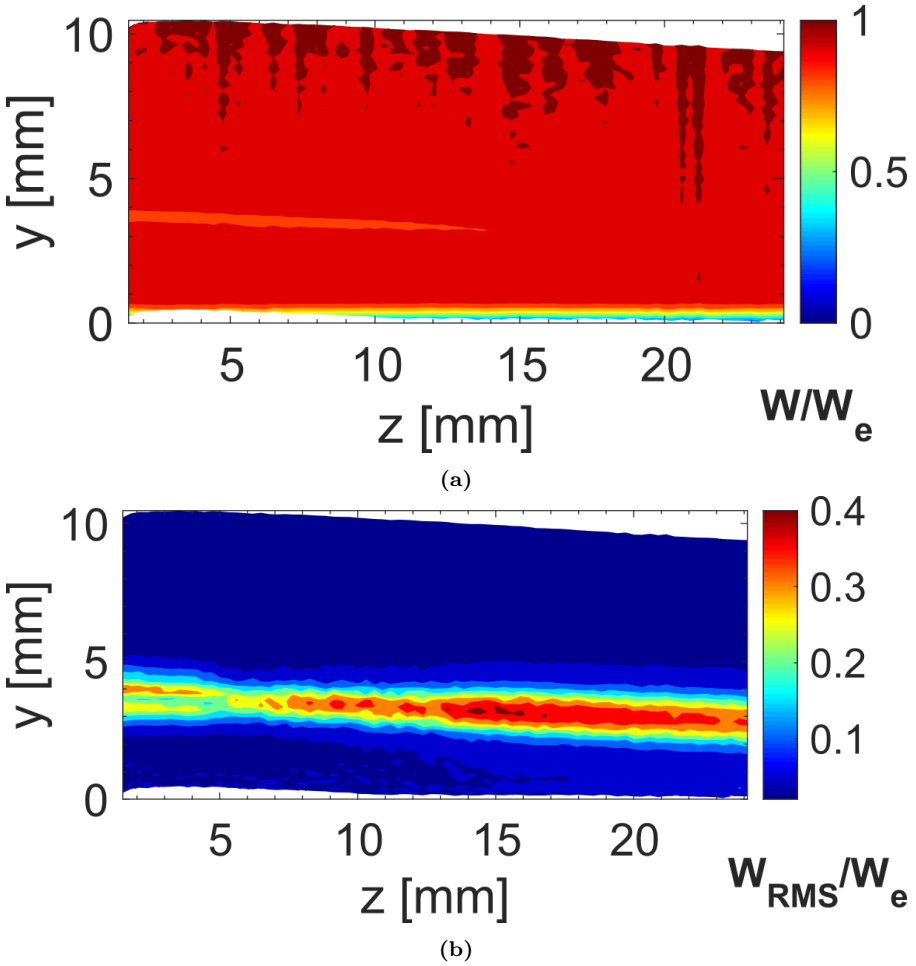


Figure 3.35: Contour plot of the mean and rms velocity along the attachment-line with the vertical string in position V4.

Results

The idea of having a simple string to observe the evolution of an artificially generated disturbance was found to be unsuitable for a swept-back configuration. Summarising, the horizontal configuration has the following issues: (1) the wake generated by the string may interact with the recirculation bubble at the root of the model making the flow completely turbulent already at the attachment-line; (2) the string should be installed equidistant from the leading edge in order to have an homogeneous disturbance along the attachment-lime; (3) the wake produced by the string increases its width approaching the model so that its size becomes incommensurate with respect to the attachment-line boundary layer. The vertical configuration has revealed other issues: (1) the wake generated by the string follows the streamlines and does not reach the

attachment-line; (2) if the string is too far from the leading edge the wake becomes too wide when it reaches the attachment-line; (3) if the string is placed close to the leading edge, so that its width is small and comparable with the boundary layer, the wake velocity deficit is still quite big changing the nature of the experiment in a wake-boundary layer interaction; (4) in addition, very close to the leading edge the streamlines are fully spanwise and the wake travels parallel to the leading edge, which is not representative of a disturbance approaching from the freestream.

Overall, the experiments have revealed that a disturbance localised in the spanwise direction, as the one generated by the vertical string, is convected so that it aligns the vortex parallel to the streamlines without reaching the boundary layer, while a disturbance which is homogeneous in the spanwise direction reaches the boundary layer and eventually triggers transition.

3.6.2 The grid

The technique of mounting the string ahead of the model to create a small vortical disturbance approaching the leading edge from the freestream was found not applicable. On the other hand, the results of the experiments without the freestream turbulence have not shown as amplification in the fluctuations at the edge of the boundary layer, as it would predict by the vorticity amplification theory.

In the literature, other techniques commonly used to generate a freestream turbulence disturbance in the wind tunnel are: vibrating ribbon, turbulence generating grids and jets. Among them, a second attempt has been carried out following the vorticity amplification experiments by Sadeh et al. (1970). The authors created a turbulent generating grid with parallel rods (see figure 3.36). This configuration, respect to the square-mesh grid, enable on to generate anisotropic turbulence with eddies oriented in a preferential direction. In particular, by mounting the grid alternatively horizontally and then vertically, the freestream disturbance would be changed. Sadeh et al. (1970) found out that on a two-dimensional stagnation point flow the disturbances generated

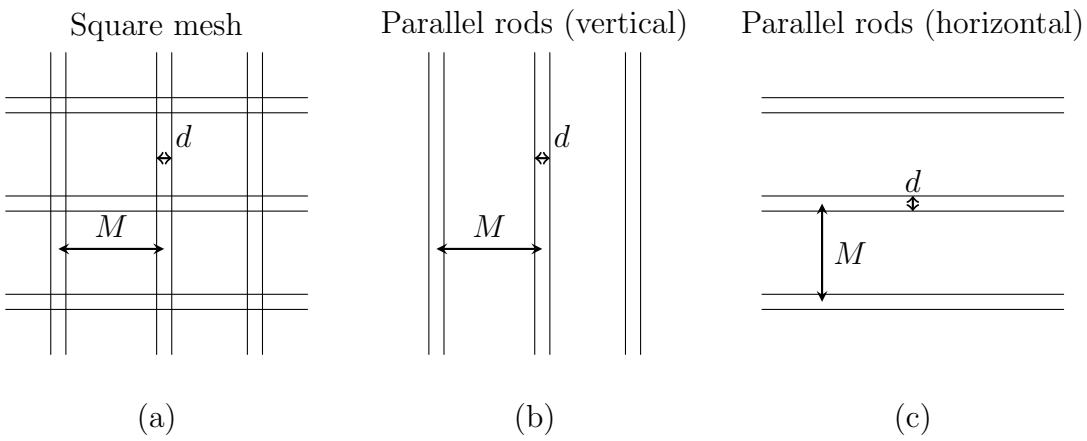


Figure 3.36: Overview of different types of grids: (a) square mesh, (b) parallel vertically rods, (c) parallel horizontal rods.

by the grid parallel to the x-direction of the model are more amplified than the disturbances generated by a grid parallel to the spanwise direction, as predicted by the vorticity amplification theory. The aim of the investigation was to observe the behaviour on a swept leading edge flow.

In this configuration, the design of the grid involves the choice of the rods diameter (d) and the rods distance (M) based on the desired characteristics of the turbulence. Guidelines on how to design the turbulence generating grids can be found in Roach (1986) and in Kurian and Fransson (2009).

Design of the turbulence grid

According to the two-dimensional vorticity amplification theory the wavelength of the oncoming vorticity must be greater than a natural wavelength λ_0 (Sadeh et al., 1970), which for the Hiemenz flow is:

$$\lambda_0 = 2\pi \sqrt{\frac{\nu}{a}} = 2\pi \sqrt{\frac{t\nu}{V_\infty}} \tag{3.15}$$

The freestream velocity in the experiment has been in the range of $6 \div 18\, m/s$, corresponding to a natural wavelength $\lambda_0 = 3.3 \div 1.9\, mm$.

Consequently, the turbulence grid must generate an integral length scale (Λ_x) greater than λ_0.

Following Roach (1986), the integral turbulent scale due to a turbulence-generating grid depends on the diameter of the rod (d) and the distance of

the grid from the model (x_g):

$$\Lambda_x = 0.20\, d\, \sqrt{x_g/d}.$$

Calling $N_{\Lambda x}$ the ratio between the integral scale and the neutral scale ($N_{\Lambda x} = \Lambda_x/\lambda_0$) the rod diameter is defined by:

$$d = \left(\frac{\Lambda_x}{0.20 x_g^{1/2}}\right)^2 = \left(\frac{N_{\Lambda x}\,\lambda_0}{0.20 x_g^{1/2}}\right)^2. \tag{3.16}$$

The wind tunnel was already equipped with a slot at the end of the contraction to insert a turbulence generated grid. The slot is distant 741 mm from the root of the swept blunt wing and 1506 mm from the tip. The average distance $x_g = 1000$ has been used for the design.

Figure 3.37 gives the rod diameters as function of $N_{\Lambda x}$, from which the diameter can be chosen.

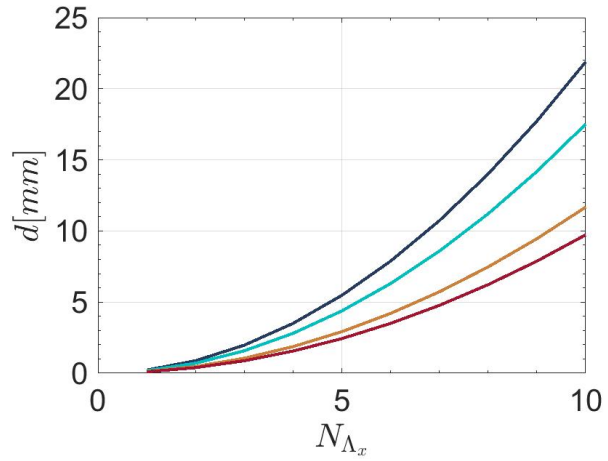


Figure 3.37: Rod diameter of the grid (d) as function of the amplification (Λ/λ_0) at different velocities: $Q_\infty = 8\ m/s$, $Q_\infty = 10\ m/s$, $Q_\infty = 15\ m/s$, $Q_\infty = 18\ m/s$.

To decide the rod distance M, one has to consider the porosity β^*. Roach (1986) has defined the porosity for parallel rods as: $\beta^* = (1 - d/M)$. Alternatively, Kurian and Fransson (2009) define the solidity σ, which is $\sigma = 1 - \beta^*$. In particular, Kurian and Fransson (2009) suggest a porosity greater than 0.55, which corresponds to $M > \frac{d}{0.45}$. Roach (1986) suggested a ratio between the

mesh width and the wind tunnel height smaller than 0.1.

The turbulence intensity generated by the grid depends on the distance from the grid to the measurement region and can be roughly estimated by:

$$Tu = C(x_g/d)^{-5/7} \quad Tv = DTu \quad Tw = ETu,$$

where (u, v, w) are referred to the three velocity components and the constants depend on the Re number and the grid geometry. For a parallel rod grid at high Re the constant given by Roach (1986) are $C = 0.8$, $D = E = 0.89$.

It was decided to use parallel circular rods of diameter $3\,mm$ placed at a distance $M = 20\,mm$ which corresponds to $N_{\Lambda x}$ between 0.87 and 1.97 in the freestream velocity range of $[8 \div 18]\,m/s$. The corresponding Reynolds number is in the range of $[1.2 \div 2.7] \cdot 10^4$.

The grid in the vertical configuration is showed in figure 3.38. It was made by carbon fibre rods which were inserted in a perforated aluminium plate screwed to the wooden frame. The perforated plate presented holes at the required distance M. To keep the rods in tension collars at the two ends of each rod were used.

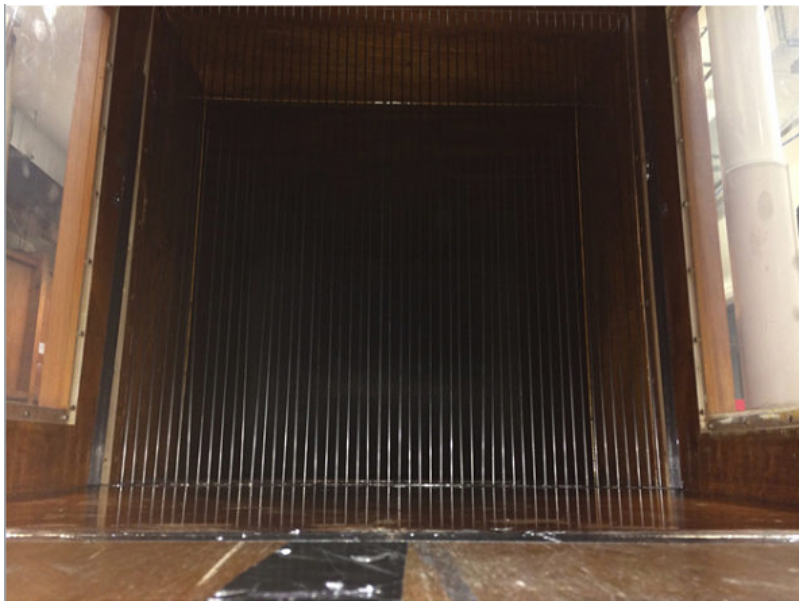
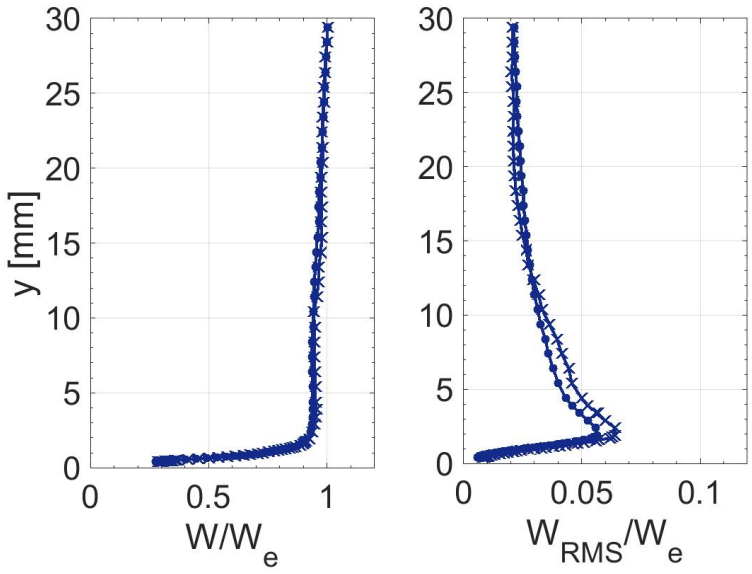


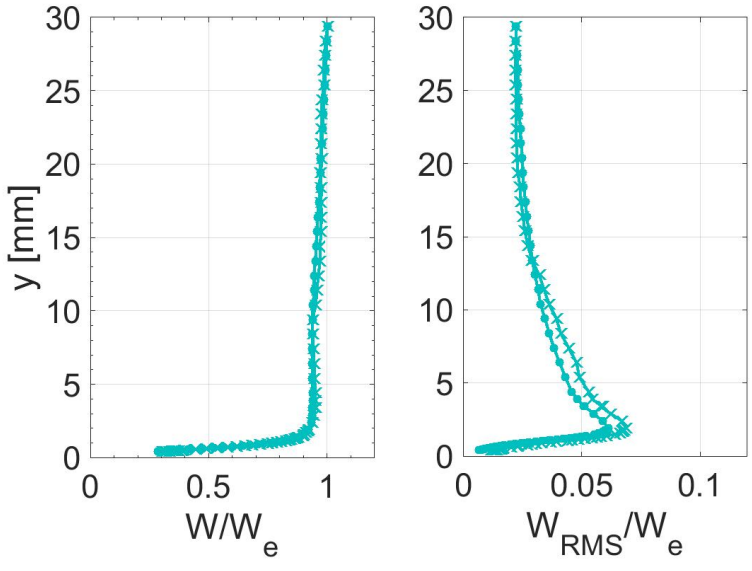
Figure 3.38: Turbulence generating grid mounted vertically in the wind tunnel.

Results

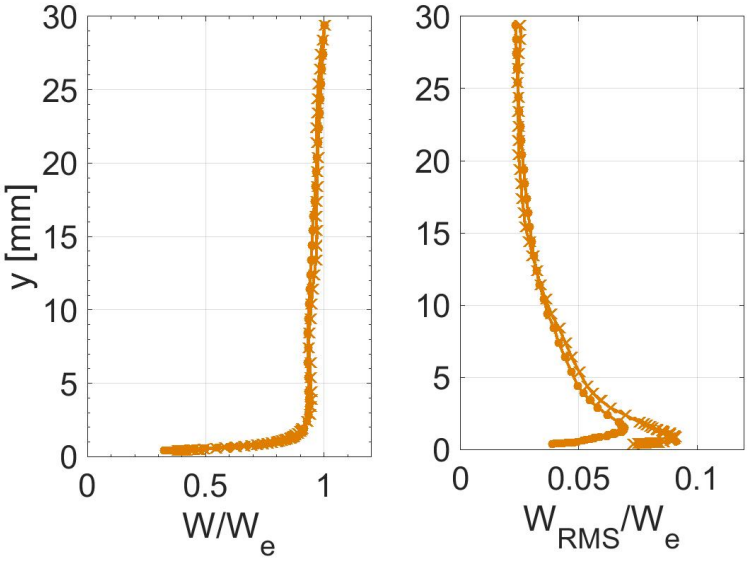
Two different tests were carried out, in the vertical and in the horizontal configuration. Figure 3.39 shows the results by comparing the effects with the horizontal and the vertical grid at different velocities.



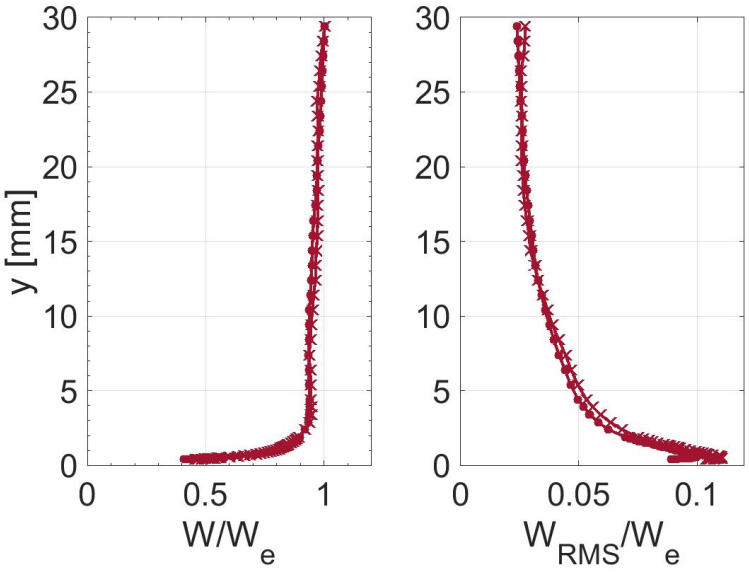
(a) $Q_\infty = 8\,m/s$



(b) $Q_\infty = 10\,m/s$



(c) $Q_\infty = 15\,m/s$



(d) $Q_\infty = 18\,m/s$

Figure 3.39: Boundary layer velocity profiles on the attachment-line at different velocities with turbulence generating grid installed horizontally (•) and vertically (×).

The figures can be compared to figure 3.15, which shows the results without the disturbances upstream, considering that in that case the velocity fluctuations are two order of magnitude lower. In both the horizontal and vertical case, the turbulent boundary layer at the attachment-line is thicker (i.e. $\delta = 3.5\,mm$ at $18\,m/s$) and fuller with respect to the laminar cases presented in the previous

sections. The RMS level far from the leading edge is similar for all the configurations and for all the freestream velocities, but approaching the wall the RMS increases with a maximum within the boundary layer. The height of the maximum level of fluctuations decreases when the velocity increases.
Table 3.3 reports the turbulence intensity at 30 mm from the plate with and without the grid.

Q_∞	Tu		
	No grid	Vertical	Horizontal
18 m/s	0.31%	1.8%	1.6%
15 m/s	0.29%	1.7%	1.6%
10 m/s	0.21%	1.52%	1.53%
8 m/s	0.09%	1.48%	1.49%

Table 3.3: Turbulence intensity at $y = 30\,mm$ from the leading edge with the turbulence generating grid in the horizontal and vertical configuration compared to the turbulence intensity without the grid.

The maximum level of the RMS is always higher in the vertical configuration, as it should be according to the two-dimensional theory, although the difference is not enough to confirm Sadeh et al. (1970) observations for a swept case. Figure 3.40 shows the PSD of the hot-wire signal at the maximum RMS location. With a broad band of exited frequency the PSD appears that typical of a turbulent boundary layer.

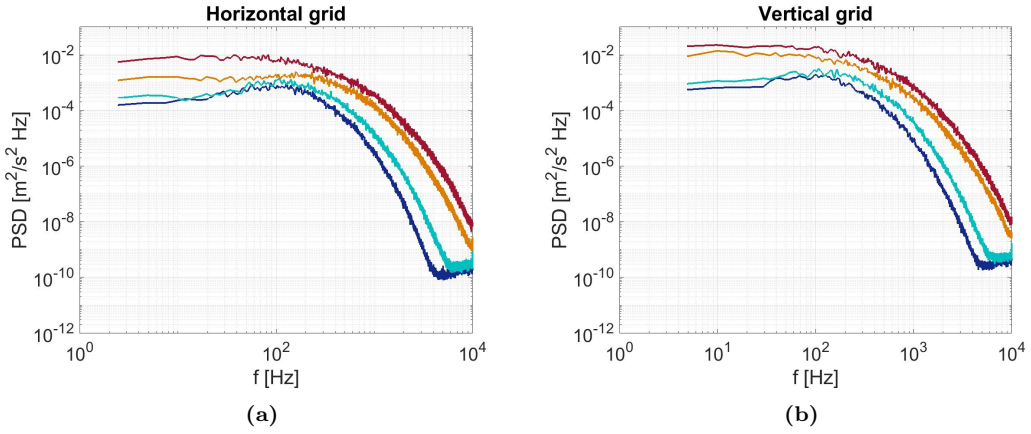


Figure 3.40: PSD inside the boundary layer at the maximum of the RMS with (a) an horizontal grid and (b) a vertical grid for each freestream speed: $Q_\infty = 8\,m/s$, $Q_\infty = 10\,m/s$, $Q_\infty = 15\,m/s$, $Q_\infty = 18\,m/s$.

Finally, in figure 3.41 the results at $Q_\infty = 18\,m/s$ are compared to the results with the horizontal string installed in H1 (same location of the grid) with a diameter of $0.23mm$ and of $3mm$. In particular, in the latter case the diameter of the string was the same as for the grid rods.

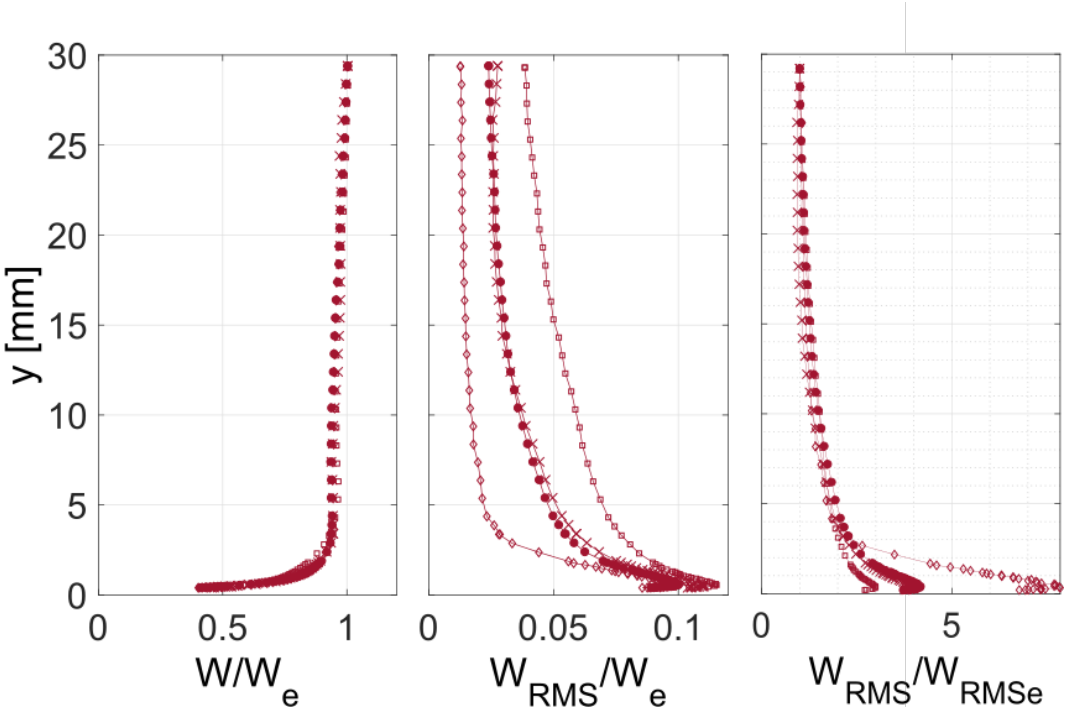


Figure 3.41: Comparison of the effect of the grid with respect to the effect of the horizontal string in H1 at $Q_\infty = 18\,m/$: • grid horizontally oriented,× grid vertically oriented, □ string $d = 3\,mm$ in H1, ◊ string $d = 0.23\,mm$ in H1.

In all the cases, the boundary layer on the attachment-line was fully turbulent, the fluctuations increase close to the wall reaching a maximum at $0.56\,mm$. The locations of the maximum in the fluctuation profiles are the same for all the environments. This suggests that the location depends on the boundary layer properties and, therefore, freestream speed; while the maximum intensity of fluctuations depends on the level of external disturbances. In figure 3.41 the RMS profiles have also been plotted normalised with respect to their value far from the wall at $y = 30\ mm$. The rate of amplification outside the boundary layer is constant for all the cases, but the boundary layer response depends on the disturbances levels.

3.7 Summary

In this chapter, the design and the experiments of a vertical flat plate with a fairing body have been presented. The idea of the model was to study the vorticity amplification theory and the cross-flow instability. Although the wind tunnel configuration did not enable a high enough velocity to observe clearly the cross-flow instability, it was decided to adopt the model to study the vorticity amplification theory on a swept configuration, which has not been reported in literature.

It was found that in the low turbulence wind tunnel, the velocity fluctuations approaching the attachment-line did not increase, as observed in two-dimensional experiments. This was attributed to the level of disturbances naturally presented in the wind tunnel which were not large enough. With the purpose of creating a localised disturbance, a string was placed ahead of the model at several locations with different orientations. Many issues have been reported regarding the applicability of this technique on a swept model. Nevertheless, it can be concluded that the string in the horizontal configuration generated disturbances spread in the spanwise direction, able to reach the attachment-line boundary layer and eventually trigger transition; while the vertical string generated a disturbance which was localised in the spanwise direction, this would travel parallel to the streamlines without reaching the boundary layer. For the vertical case, it was observed that even if the string was placed at the edge of the boundary layer the flow was found to be laminar, but in that case the problem would become more a wake/boundary layer interaction.

Finally, the flow was investigated using a turbulence generating grid. The turbulence generated by the grid was greater than 1% and the boundary layer was found to be fully turbulent in all the test cases, even at low velocity. It was found that the fluctuations amplify approaching the attachment-line reaching a maximum within the turbulent boundary layer, similarly to those reported in the experiments on two-dimensional bodies. In contrast, no particular difference was found in the amplification of the disturbances generated by

the horizontally oriented grid with respect to those generated by the vertical case; further experiments would be necessary to confirm the observation on the unswept model were the vertical orientation is more amplified Sadeh et al. (1970).

The question whether this increment in the fluctuation can be possible also in a laminar boundary layer remained an open question. It has been, therefore, decided to move to an experiment in a different wind tunnel where the level of turbulence intensity, naturally present, is already around 1%. The experiment looked at the flow in front of a cylinder at different sweep angles with the aim of investigating the effect of sweep angle on the velocity fluctuations approaching the model. The advantage in changing the wind tunnel was that the investigation could employ multi-component laser Doppler anemometry, which enabled simultaneous measurements of the three velocity components in the same location. The results are presented in the next chapter.

Chapter 4

Experiments on a circular cylinder

4.1 The model and the wind tunnel

The influence of sweep angles on the vorticity amplification around the stagnation region of a circular cylinder has been experimentally investigated in the T2 wind tunnel in the Handley Page laboratory at City, University of London. Four low sweep configurations were studied and the measurements compared to those on the unswept cylinder.

As reported in chapter 2, the experiments on the vorticity amplification theory, available in literature, have been carried out mainly through flow visualisation or single hot-wire measurements. Here, a multi-component Laser Doppler Anemometry (LDA) system has been used to measure the three velocity components ahead the leading edge of the cylinder.

The model was a straight Perspex cylinder mounted vertically from the bottom to the top of the wind tunnel (figure 4.1).

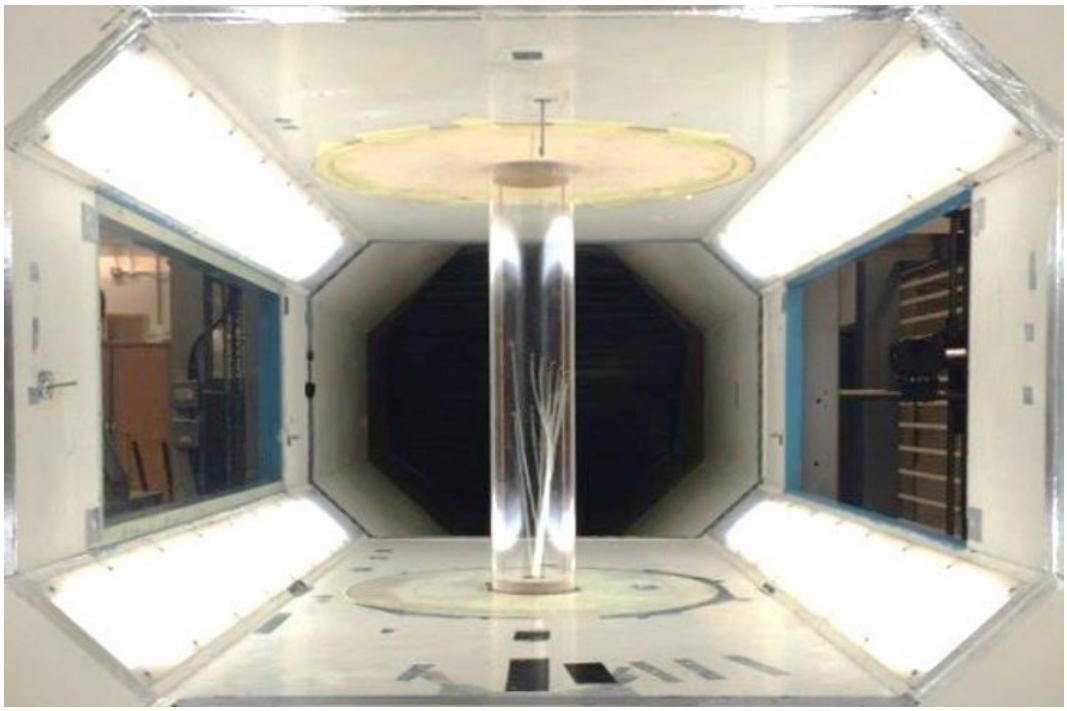


Figure 4.1: Unswept Perspex cylinder mounted in the wind tunnel.

Two removable inserts enable the model to be fixed to the roof and floor of the wind tunnel. The cylinder was screwed to those inserts through two circular wooden disks, mounted inside the Perspex cylinder itself.

To mount the cylinder at a sweep angle, two wedges were inserted under the wooden disks (figure 4.2). The wedges were made to mount the cylinder swept-back in four configurations (Λ): 5°, 10°, 20°, 30°. For each case a different groove was created and properly sealed.

The cylinder had a radius (R) of 75 mm and 15 pressure taps were installed along its perimeter at different heights.

The T2 closed loop wind tunnel has a test section of $1.80 \times 1.12 \times 0.81$ m and can run from $4\,m/s$ to $55\,m/s$ with a turbulence intensity less than 1.0% and a flow uniformity around 0.4%, in an empty test section. The blockage ratio of the cylinder was 13%. The effect of the cylinder on the turbulence intensity is reported in section 4.5.1.

To investigate the flow ahead of the leading edge, a three-component Laser Doppler Anemometer (LDA), provided by Dantec Dynamics, was used. Figure 4.3 shows the two optic groups, in back scatter configuration, installed outside the wind tunnel on a three-axes traverse, as explained in more details

in appendix C.

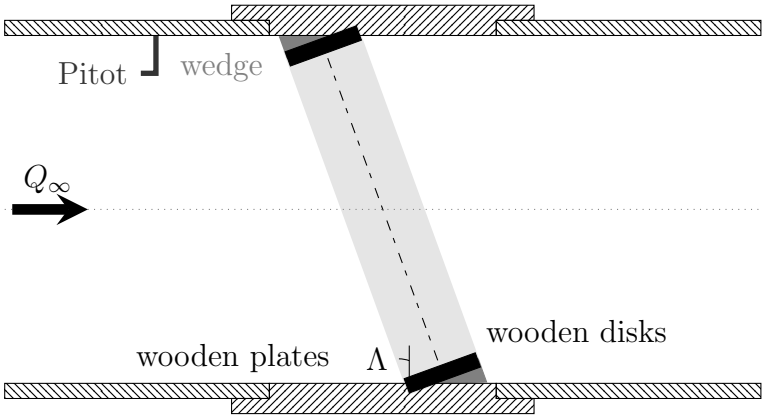


Figure 4.2: Cylinder mounted on a sweep angle inside the wind tunnel.

The flow in the wind tunnel was seeded with olive oil particles generated by an atomiser and injected in the wind tunnel through a pipe at the end of the test section. The oil particles had a diameter of approximately 1 μm.
The LDA instrumentation was brand-new, and needed to be commissioned. Certain issues arose that need to be mentioned. The first issue is related to the optical access to the wind tunnel. A thick Perspex window, that was transparent to the laser wavelengths, was installed, but the window was found to be non-uniform. This may cause differences in the data rate between measurement points, but it can be monitored in advance.
The second issue is related to the seeding particles losses. Some leakages in the wind tunnel were identified during the experiment and sealed, while some others were more difficult to find. Furthermore, at low velocities the concentration of the particles in the wind tunnel fell with time quite quickly due to their deposition. Both the leakages and the depositions contribute to particles losses during the experiment. The particles losses would not affect the measurements in the freestream, where the data rate usually is greater than 10 kHz, but it can influence the measurements within the thin stagnation point boundary layer where the deceleration rate is high and velocities are extremely low, and the low date rate keeps dropping further during the acquisition time. The wind tunnel is not equipped with an automatic system to control the particle

concentration; therefore the seeding of particles was manually adjusted during the experiments in order to maintain a reasonable data rate.

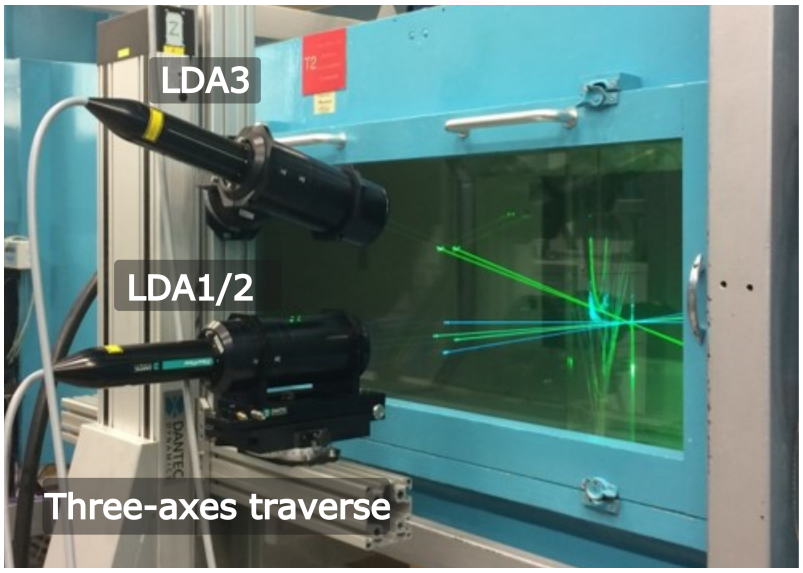


Figure 4.3: LDA setup outside the wind tunnel.

4.2 Methodology

The experiments was carried out always following the same procedure. The two wooden plates, on which the cylinder was mounted at the desired sweep angle, enabled the model to be aligned with respect to the test section. The alignment and the sweep angle were verified with an electronic inclinometer.
Then, one of the pressure taps on the cylinder was aligned with the centre of the wind tunnel, in order to measure the pressure around the cylinder with a manometer (see sections 4.3.1 and 4.4.1). The pressure tap was then used as reference for the centre of the cylinder.
After the alignment of the model, the LDA was oriented so that laser LDA1 and LDA2, coming from the first optic group, were respectively perpendicular and parallel to the leading edge, while the laser LDA3, from the second optic group, was perpendicular to the leading edge (see figure 4.3). Details concerning the alignment procedure are reported in appendix C.
In order to set the origin of the traverse coordinate system, the leading edge of the cylinder was identified by placing a few millimetres L-shaped metallic

foil at an height of approximately 300 mm from the wind tunnel floor (figure 4.4) and traversing the LDA until it interferences with the beam.

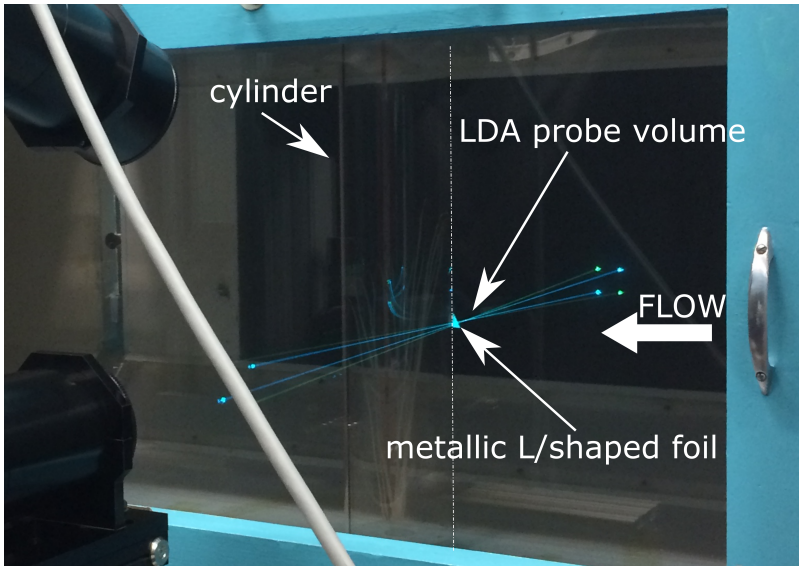


Figure 4.4: LDA during the alignemnt procedure usign the L-shaped metallic foil.

To ensure that this is exactly at the stagnation point, the velocities were measured across the span at three chordwise distances in front of the leading edge (figure 4.5).

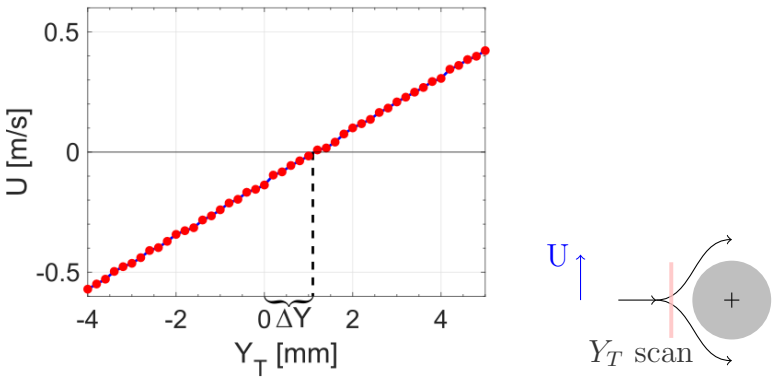


Figure 4.5: Example of the flow in front of the cylinder to align the laser with the stagnation point

Scans were then carried out with the three-component LDA. The results enabled one to find where the flow diverged symmetrically, corresponding to the change of sign of the U-velocity component, perpendicular to the freestream. From this position ($Y_T = 0$) it was possible to find the stagnation point. The

LDA was traversed along the freestream direction until the signal interfered with the wall at the stagnation point, which was then set as zero on the acquisition software. Then the coordinate system of the traverse is defined by the software as: X_T in the direction of the freestream velocity, Z_T parallel to the cylinder axis and Y_T perpendicular to both X_T and Z_T (figure 4.6).

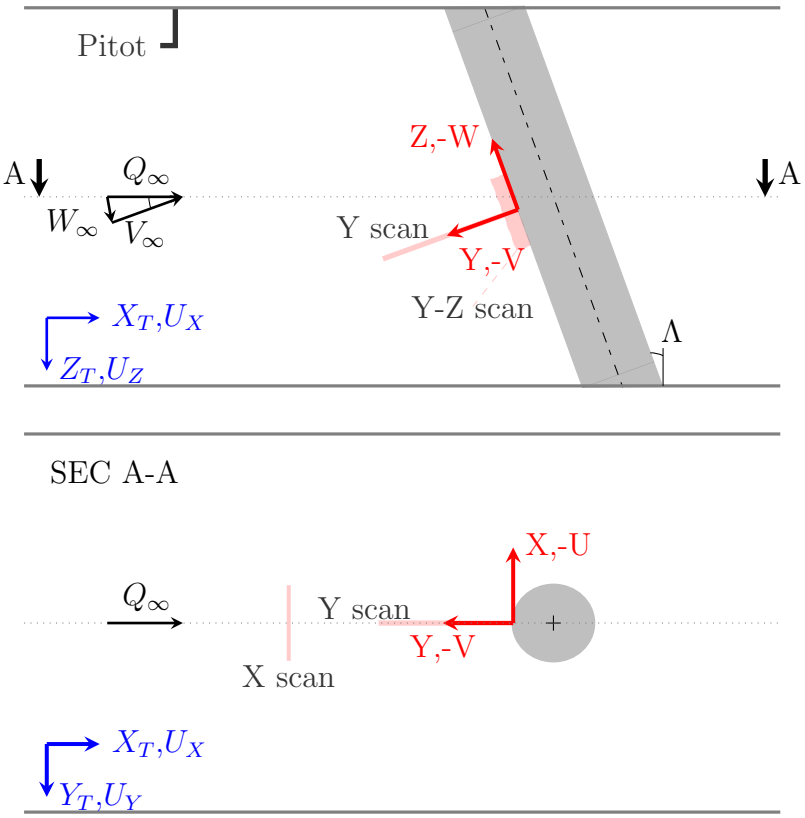


Figure 4.6: Coordinate systems for the cylinder experiments: (X_T, Y_T, Z_T) is the coordinate system defined by the LDA traverse, (X, Y, Z) is the coordinate system adopted in the data analysis.

The experiments for each sweep angle were carried out in the region in front of the leading edge. As sketched in figure 4.6, four types of measurement were carried out: X-scan to align the laser, as explained earlier, Y-scan in the potential flow region and Y-scan in the boundary layer region and on a Y-Z plane. For each scan the value at a distance of 220 mm from the stagnation point has been used as reference. The freestream velocity (6 m/s), corresponding to a Reynolds number $Re_D \tilde{=} 6 \cdot 10^4$, was monitored with the Pitot tube.

4.3 Results on the unswept cylinder

4.3.1 Pressure distribution

The static pressure distribution around the cylinder was measured through the 15 pressure ports built on the model using an inclined multi tube manometer. Figure 4.7 shows the experimental distribution of the pressure coefficient (c_p) compared to the theoretical pressure derived from the potential flow theory as a function of the circumferential angle θ:

$$c_p^{cyl} = (2cos(2\theta) - 1) \tag{4.1}$$

At the stagnation point the flow is at rest and c_p is 1 as predicted by the potential flow theory. That theory does not consider the viscous effect and therefore differences exist between the experimental and the theoretical profiles. Actually, the pressure coefficient decreases up to 75°, reaching a minimum of -1 to the point where the flow separates and the pressure coefficient oscillates around a constant value. This experimental behaviour is in agreement with previous investigations at the same Reynolds number, widely reported in literature, as reviewed by(Zdravkovich, 1997).

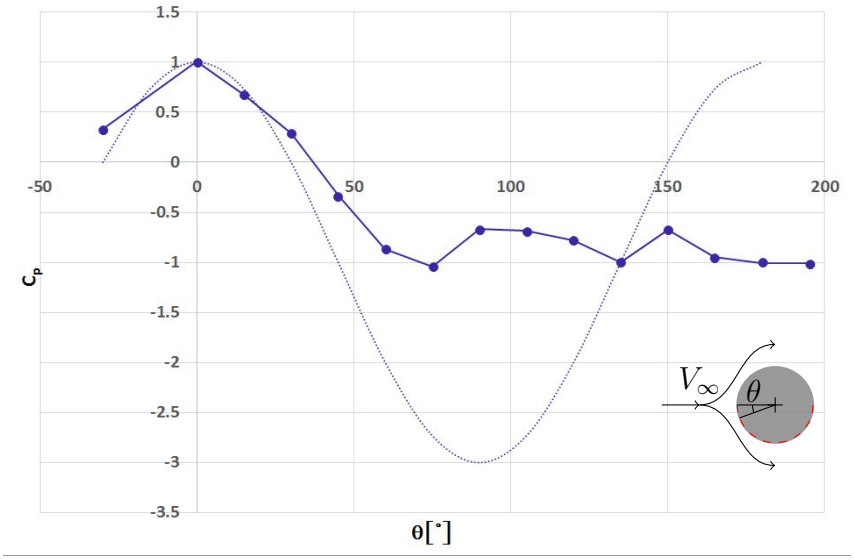


Figure 4.7: Pressure distribution on the unswept cylinder.

4.3.2 Potential flow

To investigate the flow approaching the leading edge of the cylinder, three-component LDA measurements were made. The three measured non-orthogonal velocity components (U_1, U_2, U_3) were converted to the wind tunnel orthogonal coordinate system (U_X, U_Y, U_Z) by applying the transformation matrix as explained in appendix C.

The velocity (U_X, U_Y, U_Z) were then converted to the cylinder coordinate system (U, V, W) (figure 4.6). In particular, the chordwise velocity was assumed to be positive in the freestream direction, in opposite direction with respect to the Y coordinate.

Figure 4.8 shows the mean and the fluctuations for the three velocity components, approaching the cylinder, measured in coincidence mode.

The mean of the chordwise velocity V decreases towards the model, while the spanwise mean velocity, W, and the third component U are almost zero. Actually, the small offset of the U from the zero, close to the wall, is due to the laser beams being slightly off the centre-line in the set of measurements plot in the figure.

In the same figure, the fluctuations for each component of the velocity are shown; further details on the procedure are explained in appendix C. The fluctuations, almost constant far from the model, start to be influenced by the presence of the model itself from a distance approximately of $1.3R$. Actually, the major effect can be observed very close to the wall where the viscous effect starts to dominate ($Y \leq 0.05R$). This aspect will be discussed in the next section.

Going back to the mean flow chordwise velocity, it has to be underlined that its behaviour approaching the cylindrical model, far from the boundary layer, is predicted by the potential flow theory:

$$V(Y) = V_\infty \Big(1 - \frac{R^2}{(Y+R)^2}\Big) \tag{4.2}$$

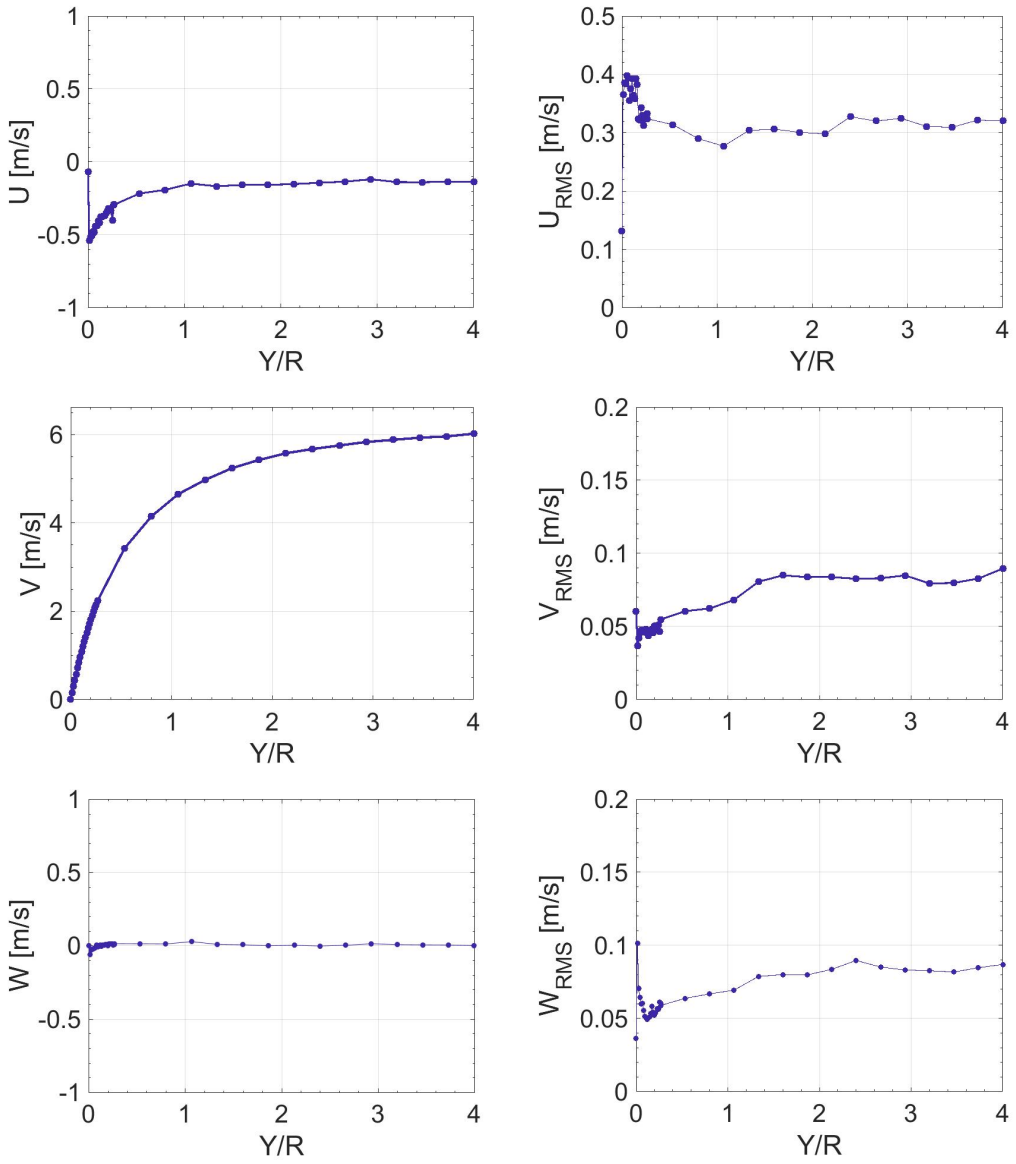


Figure 4.8: Mean and RMS of the three velocity components approaching the straight cylinder.

In the proximity of the model, outside the boundary layer, the V-component of the velocity can be approximated by a straight line, as described by Hiemenz solution:

$$V(Y) = -aY \tag{4.3}$$

where $a = 4V_\infty/D$. Figure 4.9 shows the agreement between the experimental data and both the potential flow theory and the Hiemenz linear solution starting at $Y \leq 0.1R$. The constant a in the equation 4.3, calculated by interpolating the experimental data was found to be smaller by 10% of the

theoretical prediction.

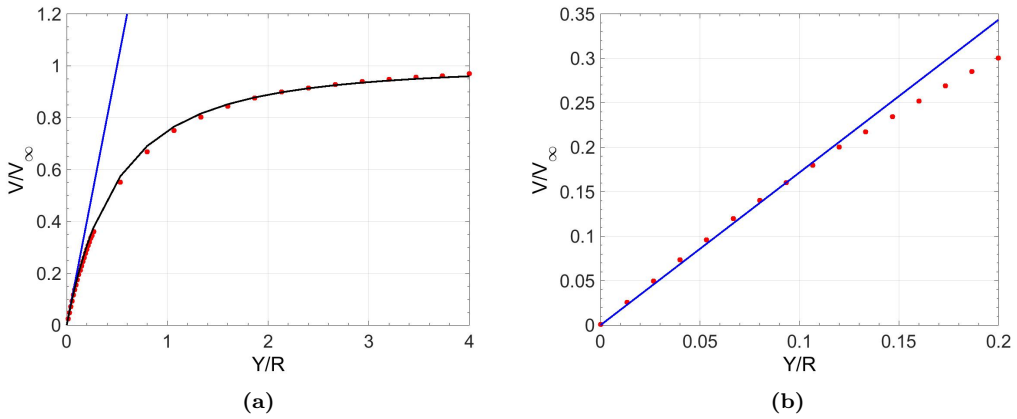


Figure 4.9: Potential flow approaching the cylinder: data points •, potential flow theory —, Hiemenz theory—.

4.3.3 Viscous effect

Figure 4.10 shows the mean and the RMS of the three velocity components approaching the leading edge of the cylinder. The Y-axis is given with the dimensionless variable $\eta = Y\sqrt{a/\nu}$, where ν is the kinematic viscosity and a is the constant of the Hiemenz flow.

As explained in the previous section, the zero for the acquisition system is set where the laser start interfering with the cylinder, but since the beam itself is around $0.2\,mm$ in diameter the exact location of the wall ($\eta = 0$) has to be estimated from the experimental data. According to the viscous theory, reported in Chapter 2, the viscosity close to the wall acts on the mean velocity profile as a *shift* from the wall.

The inviscid Hiemenz straight line, extrapolated from the theoretical viscous Falkner-Skan solution, crosses the $\eta - axis$ at $\eta = 0.65$ (see figure 4.11). Therefore, also the interpolation line of the experimental data has to cross the η-axis at 0.65.

Going back to figure 4.10 the V-velocity component shows a linear deceleration away from the wall and non-linear behaviour where the viscous effects become significant.

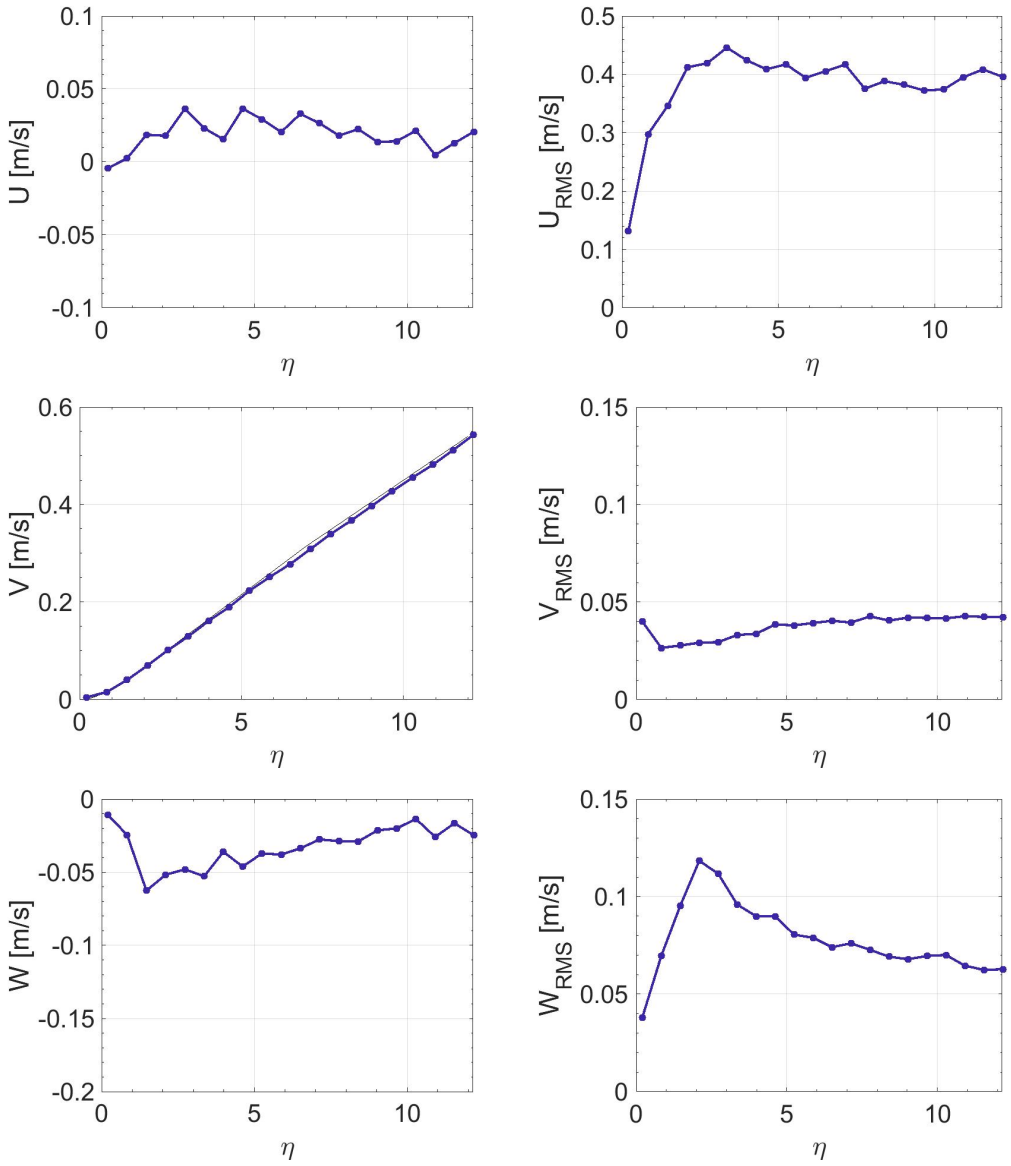


Figure 4.10: Mean and RMS (•) of the velocity components in the boundary layer at the stagnation point. The V-component is compared to the Falkner-Skan (-) solution.

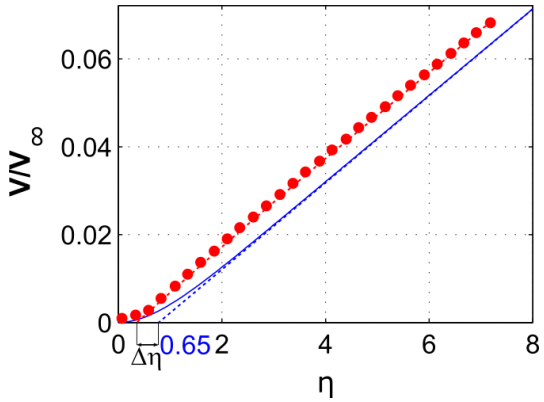


Figure 4.11: Method used to find the distance from the wall: • experiment — theory.

The velocity does not show a typical boundary layer profile, i.e.for a Blasius flow, with a constant edge velocity. Therefore, at the stagnation point the boundary layer thickness is assumed to be the distance at which the velocity deviates from the linear Hiemenz solution that is $\eta = 2.4$. In the experiment this point corresponds to $\delta = 0.72\,mm$. The other two velocity components are approximately constant and very close to zero, as they must be at the stagnation point. Although, the intensity of the W-velocity component increases slightly, up to $\eta = 1.9$, remaining quite small. In this region the absolute value of the mean W-velocity component is greater than that of the V-velocity component, indicating that the flow assumes a three-dimensional behaviour as hypothesised by Sutera (1965).

Regarding the fluctuation components, the most interesting behaviour is that the V_{RMS} and the W_{RMS} show an opposite behaviour: the chordwise component decreases and the spanwise increases reaching respectively a minimum at $\eta = 0.97$ and a maximum at $\eta = 2.23$, close to the theoretical boundary layer thickness.

As reported in Chapter 2, previous investigations on the stagnation point vorticity amplification have regarded mainly flow visualisation and hot-wire measurements. In particular, the hot-wire experiments were carried out with a single hot-wire measuring the mean and the fluctuating component of the velocity in the direction perpendicular to the wire itself. Some results by Sadeh and Brauer (1981) for a straight cylinder of radius similar to that used in the present experiment, and at similar Reynolds number, are shown in figure 4.12. The mean square of the velocity normalised with respect to its minimum value (at about 2.5 times the cylinder radius) is plotted versus the ratio between the distance from the leading edge and the cylinder radius. The maximum amplification is at the edge of the boundary layer.

To compare the two experiments, the three velocity RMS have been squared and normalised with respect to their values at $200\,mm$ away from the leading edge, which corresponds to $Y = 2.6R$ (figure 4.13). The spanwise velocity fluctuations present the most interesting behaviour, quite similar to the hot-wire measurements by Sadeh and Brauer (1981). In fact, both the curves (figures

4.12 and 4.13c) increase, with respect to their freestream value, reaching a maximum around the boundary layer edge.

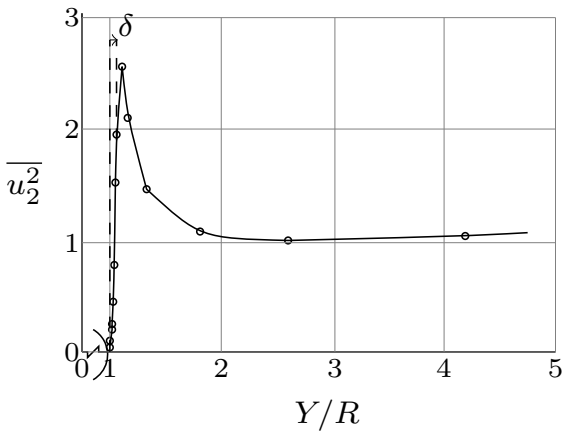


Figure 4.12: Velocity fluctuations ($\overline{u_2^2}$) from hot-wire measurements by Sadeh and Brauer (1981) on a straight cylinder: $Re_D = 12 \times 10^4$, $R = 80\,mm$.

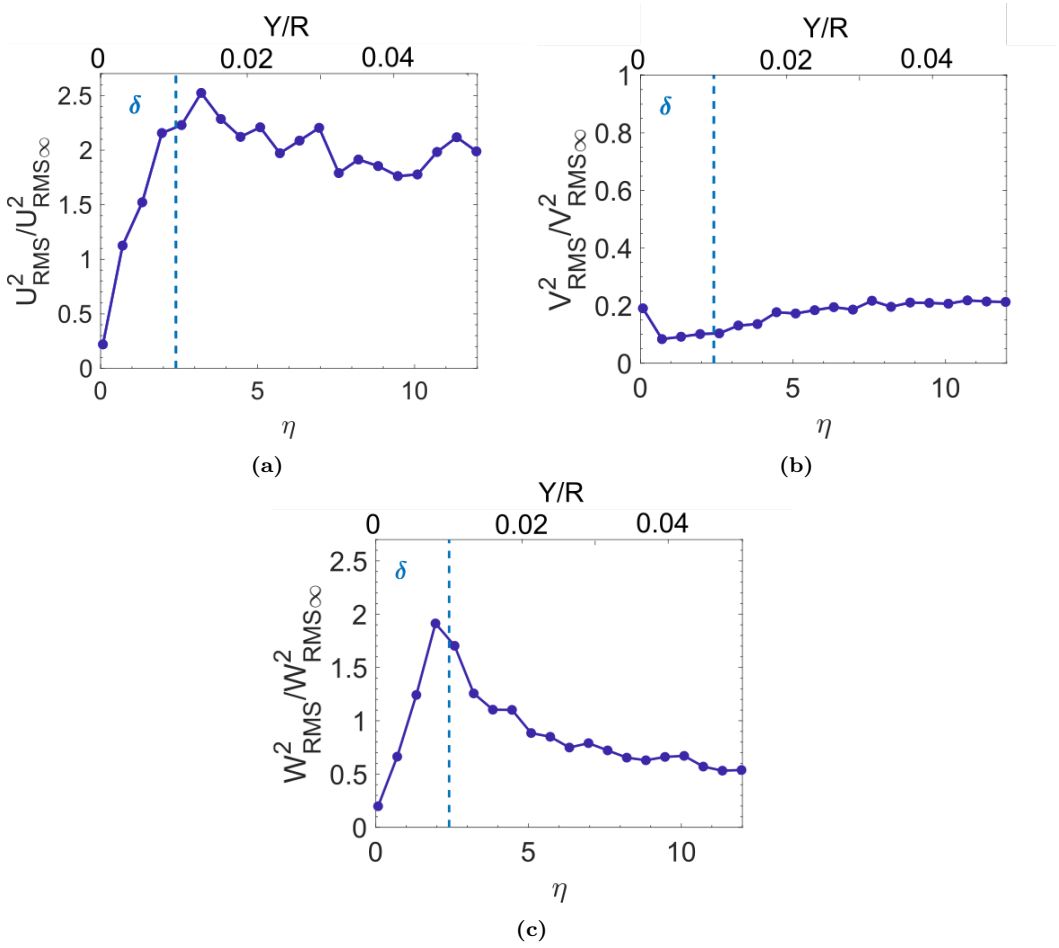


Figure 4.13: Normalised RMS for the three velocity components.

4.3.4 Frequency domain

To further analyse the phenomenon, a frequency domain analysis has been carried out. The algorithm used to find the Power Spectral Density (PSD) for the LDA measurements is explained in appendix C, but it is important to note that the maximum resolvable frequency in the PSD depends on the data rate and on the acquisition time.

In the case of the coincident measurements reported in the previous section, the PSD (for a signal of 90 seconds with data rate 500 Hz inside the boundary layer) could be resolved only up to frequencies below 100 Hz. To have a more complete and reliable PSD up to higher frequencies, the data has to be acquired in semi-coincidence mode, where the data rate is greater. This was possible since the phenomenon under investigation only influences the V and W velocity components, lying on the plane identified by LDA1 and LDA2. In the semi-coincident mode the signals from LDA1/LDA2 are acquired simultaneously, but independently from that of LDA3. In this way, the whole mean velocity field can still be measured, but the fluctuations can be resolved only on the plane defined by LDA1/LDA2, the YZ plane on which the two velocity components V and W lie.

The measurements were in agreement with those in coincidence mode showing also the reliability and repeatability of both the mean and RMS.

The data rate for LDA1 and LDA2 was increased up to 2.5 kHz, with the acquisition time kept at 90 s. Consequently, the frequency domain achieved in semi coincidence mode is more than an order of magnitude higher than the one in coincidence mode. Figures 4.14a and 4.14b show the PSD for the two velocity components at difference distances from the wall according to the colour bar in figure.

The PSDs of the V-velocity is an order of magnitude lower compared to the W-velocity according to their RMS values. The PSDs of V and W components do not show a particular frequency of amplification, but the phenomenon seems to be related to a wide range of low frequencies, at which the energy of the V-component decreases towards the wall, while the energy of W-component

increases.

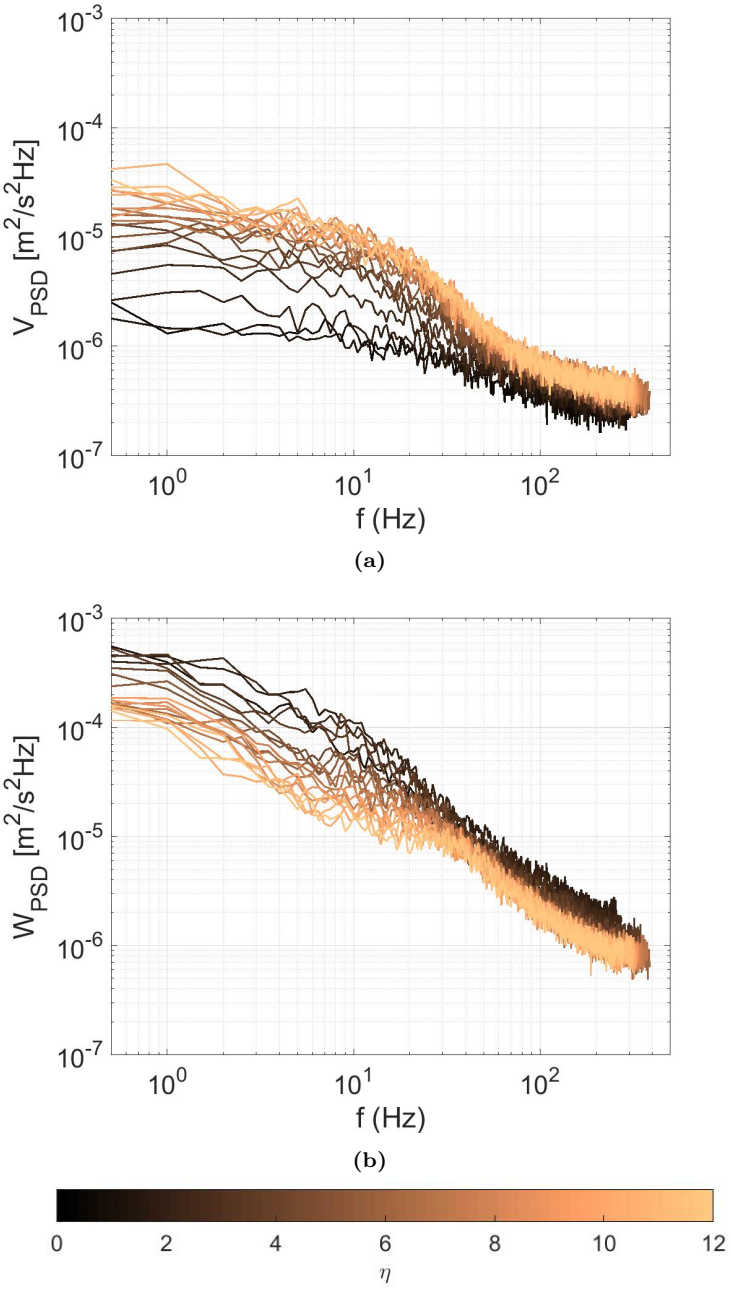


Figure 4.14: Spectra at various η for a) V component and b) W component.

To better visualise the frequency contributions, the PSD is plotted in a contour graph showing the energy content, contour levels, of each frequency at different distances from the wall (figure 4.15).

The figure shows that the low frequencies of the V-PSD attenuates rapidly inside the boundary layer ($\eta < 2.4$), while the W-PSD increases its energy

content at low frequencies (up to 30 Hz) gradually up to a maximum inside the boundary layer.

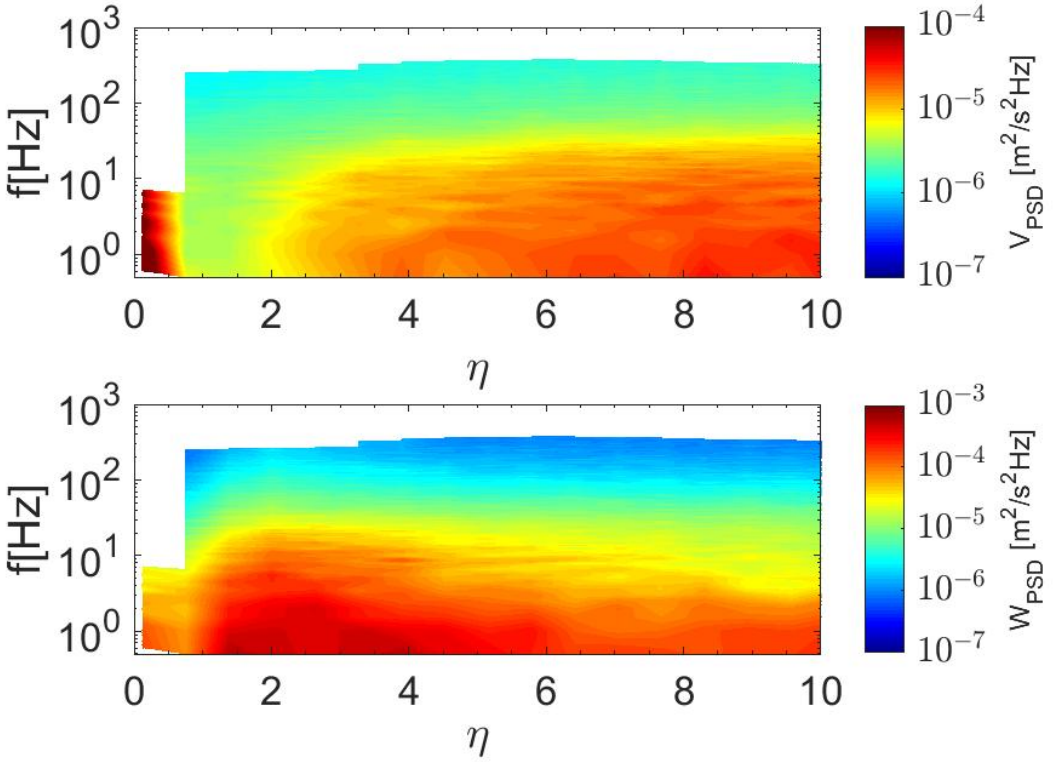


Figure 4.15: Contour plot of the PSD for the V and the W velocity components in the boundary layer

Sadeh et al. (1970) investigated the vorticity amplification at the stagnation point flow on a vertical flat plate using a single hot-wire anemometry with different types of turbulence-generating grids. The authors found an amplification in the fluctuating velocity around the boundary layer edge. The rate of the amplification depended on the orientation and on the wavelength of the turbulence generated by the grid. The energy spectrum showed that the amplification was associated with signals of frequencies below 25 Hz, for all the grids, similar to that observed in figure 4.15.

The vorticity amplification theory demonstrates that the frequency below a natural wavelength becomes amplified. To analyse the amplified wavelengths in the experiment, the methodology followed by Sadeh et al. (1970), based on the Taylor's hypothesis of frozen pattern, has been adopted. The time spectrum and the spatial spectrum are connected, and therefore the eddy size can

be calculated as the ratio between the mean local velocity and the frequency:

$$\lambda_y = \frac{V}{f} \tag{4.4}$$

and analogous

$$\lambda_z = \frac{W}{f}. \tag{4.5}$$

According to Sutera (1965) the neutral wavelength for the Hiemenz flow is $\lambda_0 = \frac{2\pi R}{\sqrt{Re_D}}$. Kestin and Maeder (1957) further analysed the instability of a cylinder stagnation point finding that when the curvature is included the flow is unstable for disturbances only for $\lambda = 1.79\lambda_0$. In both the papers the imposed perturbation was parallel to the cylinder axis, therefore λ_0 must be considered in the λ_z. In figure 4.16 the value of λ_0 has been marked with a black dashed line.

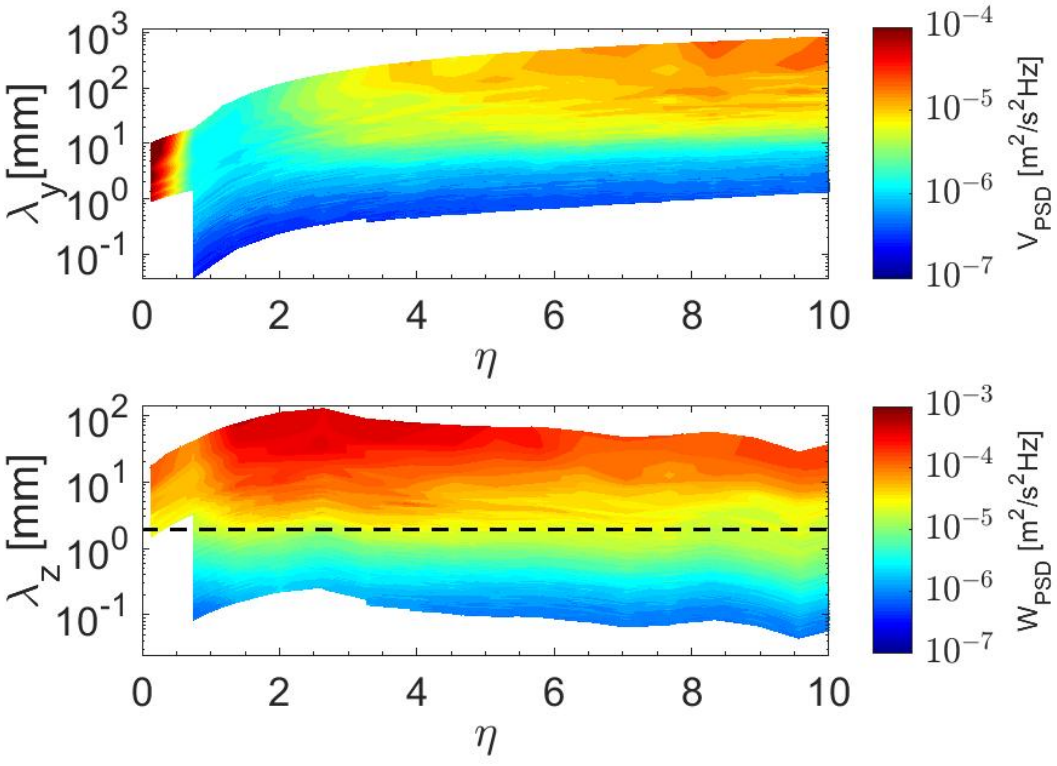


Figure 4.16: Contour plot of the PSD for the V and the W velocity components in the boundary layer as function of the length scale. The dashed line represents **- -** is the neutral wavelength (λ_0) for Hiemenz flow.

The plot shows that the wavelengths under amplification are those greater

than the black dashed line. The maximum λ_y decreases approaching the wall together with the energy content, showing that the eddies are becoming smaller with less energy content while the flow is decelerating. On the other hand, the maximum value of λ_z increases slightly, around the boundary layer edge. The energy content of λ_z increases greater for wavelengths than λ_0, while remains almost constant for smaller wavelengths. This means that the bigger scale eddies are amplified. According to Sutera (1965) the vorticity with scale smaller than the natural scale dissipates into thermal effects, while that with bigger scale amplifies more rapidly than it is dissipated as the boundary layer is approached.

4.3.5 YZ Scan

The flow has been scanned in a 4x3 mm^2 YZ-plane with a resolution of $0.2mm$ to analyse whether there is any periodicity or difference along the Z-axis. Figure 4.17 shows a contour plot of the results in dimensional units.

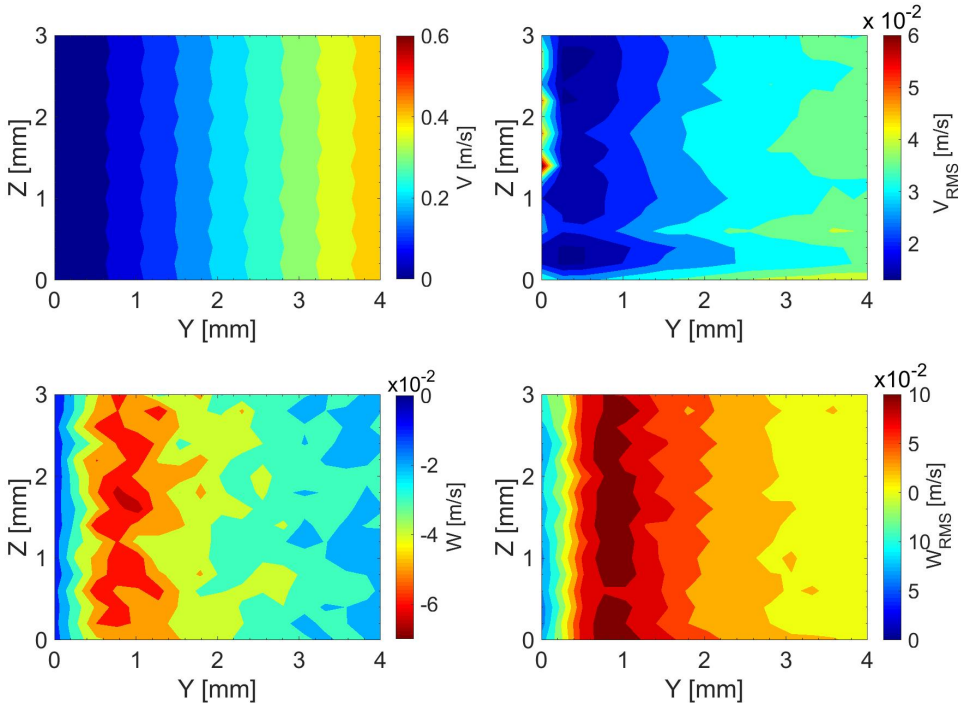


Figure 4.17: Velocities and fluctuation on a YZ plane.

The plots do not show any clear structure either in the mean or the RMS. A small undulation can be observed, in particular in the mean V velocity, but its wavelength corresponds to the measurement resolution.

As for the single boundary layer scan presented in the previous section, for all the Z locations the minimum for the V_{RMS} is around 0.5 mm, while the maximum of the W_{RMS}, around 1 mm.

It is not immediately observable from the figure, but the absolute value of the mean streamwise velocity V is higher with respect to the absolute of spanwise mean velocity W, as one would expect, only up to $Y = 0.6\,mm$ ($\eta = 2$), after which the behaviour is the opposite up to the wall where both are zero. This suggest a three-dimensionality of the flow in the boundary at the stagnation point, as stated by Sutera (1965).

To check for the periodicity, firstly the average values of RMS across Z for each Y location ($\overline{V_{RMS}}$ and $\overline{W_{RMS}}$) have been calculated and then subtracted to the RMS of each corresponding location. The results are shown in figure 4.18: the V is homogeneous through the measured area, while the W shows small patches comparable to the resolution.

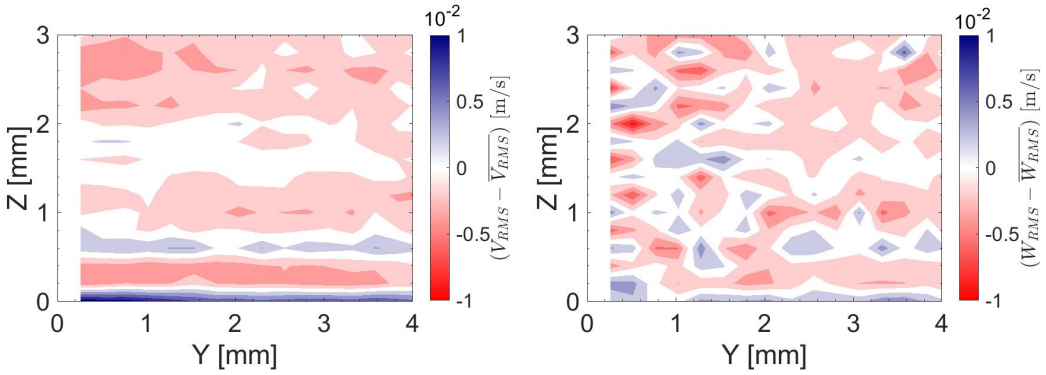


Figure 4.18: Velocity fluctuation after having subtracted the mean of RMS along Z.

A spatial PSD was carried out within the range of the YZ scan, but no significant periodicities were found. In addition, the frequency spectra along the Z at each Y-location were found to be similar.

4.4 Results on the swept cylinders

The experiments on the straight cylinder have shown an increment in the spanwise velocity fluctuations at the edge of the stagnation point boundary layer and a reduction in the chordwise velocity fluctuations. To investigate the effect of a sweep angle on that phenomenon, experiments were carried out on four different sweep configurations and the results compared to the unswept case.

4.4.1 Pressure distribution

The theoretical pressure coefficient for a body with a sweep angle ($c_{p_{3D}}$) can be deduced from the unswept pressure coefficient ($c_{p_{2D}}$) according to:

$$c_{p_{3D}} = c_{p_{2D}} cos(\Lambda)^2 \tag{4.6}$$

where Λ is the sweep angle as shown in figure 4.6. Therefore, in the case of a swept cylinder equation 4.1 becomes:

$$c_{p_{3D}}^{cyl} = [2cos(2\theta) - 1]cos(\Lambda)^2 \tag{4.7}$$

In figure 4.19 the theoretical potential pressure distributions are shown together with the experimental measurements for each sweep angle.
The effect of the sweep angle at the leading edge, $\theta = 0°$, is to decrease the two-dimensional pressure coefficient by $cos(\Lambda)^2$. The corresponding experimental values can be used to calculate the effective sweep angle (Λ_{eff}), that is the angle at which the streamlines approach the model, that may differ from the geometrical sweep (Λ_{geom}) measured on the model. From the pressure distribution, the effective sweep angle was found approximately less than 10% compared to the geometrical one. The system holding the cylinder in the wind tunnel did not allow fine rotation of the model and therefore did not allow fine adjust of the pressure taps corresponding to $\theta = 0°$ with the symmetry of the flow field. For this reason, more precise effective sweep angles have been

obtained from the multi-component LDA measurements: 5.28°, 10.7°, 21.08°, 32°.

In figure 4.19 the curves corresponding to different sweep angles present a similar behaviour following the theoretical $c_{p_{3D}}^{cyl}$ for small θ and a constant zero slope after the flow separates.

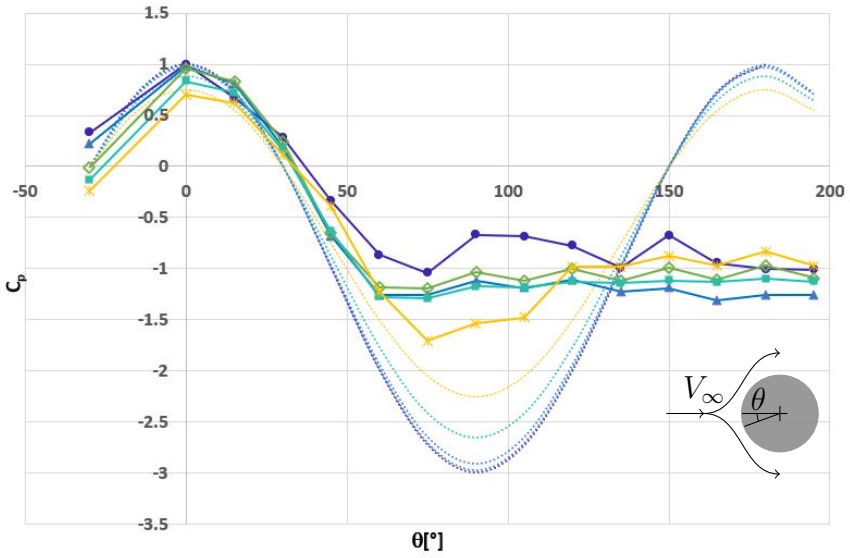


Figure 4.19: Pressure distribution at different sweep angle: theoretical laminar (dashed line) and experimental data (dots). The colours indicate the sweep angles:● $\Lambda = 0°$, ▲ $\Lambda = 5°$, ◇ $\Lambda = 10°$, ■ $\Lambda = 20°$, ∗$\Lambda = 30°$

The different behaviour of $\Lambda = 30°$ is due to the boundary layer being, only in that case, tripped by a strip of roughness applied over the shoulder of the cylinder. The strip of roughness should make the boundary layer turbulent and modify the pressure distribution accordingly. The boundary layer was tripped to reduce the influence of the wake shedding frequency observed on the V spectra in front of the leading edge. Usually, the shedding frequency influences only the U spectra at the stagnation point, since that is due to the shedding of the wake vortices, which induces a movement of the whole flow field in the X-direction (see section 4.5.4). When the cylinder was swept the wake became three-dimensional. Probably, for that reason, at the highest sweep, the effect of the wake was also observed on the V-PSD at the stagnation point. The presence of the trip has still diminished the shedding frequency energy in the spectra, although the flow separation was delayed only up to $\theta = 75°$.

4.4.2 Potential flow

The potential flow approaching the attachment-line of a swept cylinder (at $X = 0$) can be calculated in the coordinate system of figure 4.6 considering the *independence principle*:

$$\overrightarrow{Q(Y)} = \left(0, V_\infty\left(1 - \frac{R^2}{(Y+R)^2}\right), W_\infty\right) \tag{4.8}$$

The main difference from the unswept case is the spanwise velocity, W_∞. Two examples at $\Lambda = 30°$ and $\Lambda = 20°$ are presented in figure 4.20.

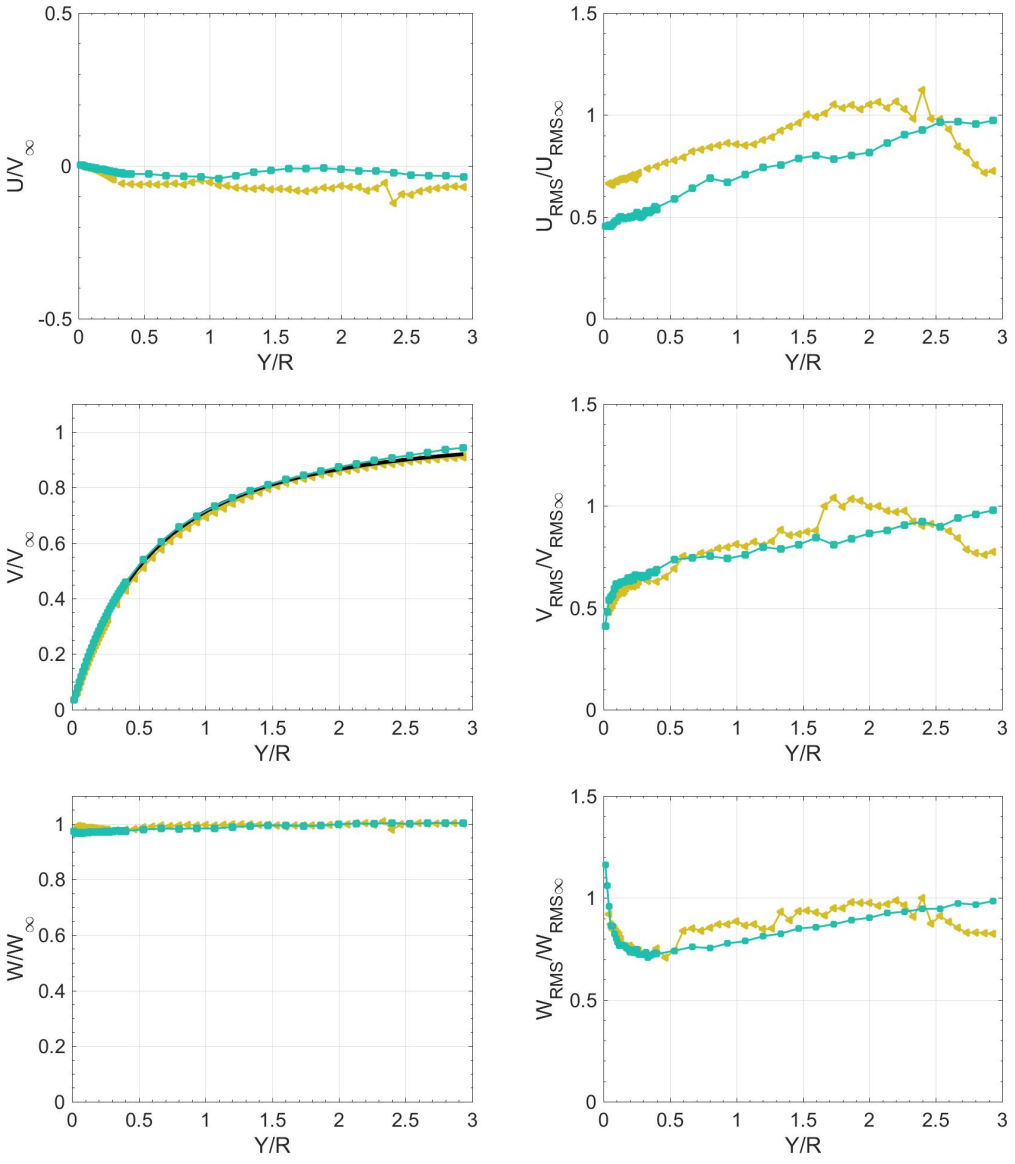


Figure 4.20: Potential flow approaching the sweep cylinder in two configurations, ■ $\Lambda = 20°$, ◀ $\Lambda = 30°$, compared to potential flow theory (black line).

The flow was measured in a direction X_T not perpendicular to the leading edge, and then projected on the perpendicular direction to allow the comparison with the potential flow theory. Figure 4.20 shows the mean and the RMS of the three velocity components from a distance of three times the radius up to the leading edge. The mean velocity components are in agreement with the potential flow theory, shown in the figure by a black line. The fluctuating velocities decrease linearly with a similar slope approximately up to $Y = 0.5R$, where V_{RMS} keeps decreasing and the W_{RMS} increases rapidly both not linearly . The slope of the attenuation in the first part is quite low in dimensional units and may be considered almost constant. It comes out that the region of major interest is closer to the leading edge within $Y/R = 0.05$, which will be analysed in the next section.

4.4.3 Viscous effect

When the flow is close enough to a swept leading edge the effect of viscosity creates a boundary layer in the spanwise direction as predicted by the Falkner-Skan-Cooke numerical solutions (see Chapter 2).

Figure 4.21 shows the same plot in dimensionless units: V with respect to V_∞, while W, W_{RMS} and V_{RMS} with respect to their own value outside the boundary layer at $\eta = 10$. The mean velocities show an agreement with the Falkner-Skan-Cooke numerical solution. The W/W_e for the unswept case is not plotted since W_e would be zero. The V-fluctuations, in this normalisation, show a higher attenuation with the sweep angle, up to 0.4 times the outer V_{RMS} value, although the case $\Lambda = 30°$ the attenuation is less. The W-fluctuation increases approaching the wall in all the cases, up to an average maximum value of 1.4 times for Λ from 0° to 20°. However, a clear trend was not easily identified by the mean RMS. The intensities of the fluctuations, for the different sweep angles, are of the same order of magnitude, with the W_{RMS} more than double the intensity of the V_{RMS}. For the unswept case it was pointed out that the mean V velocity component was higher than W up to $\eta = 2$, indicating the existence of a three-dimensional effect in the boundary layer.

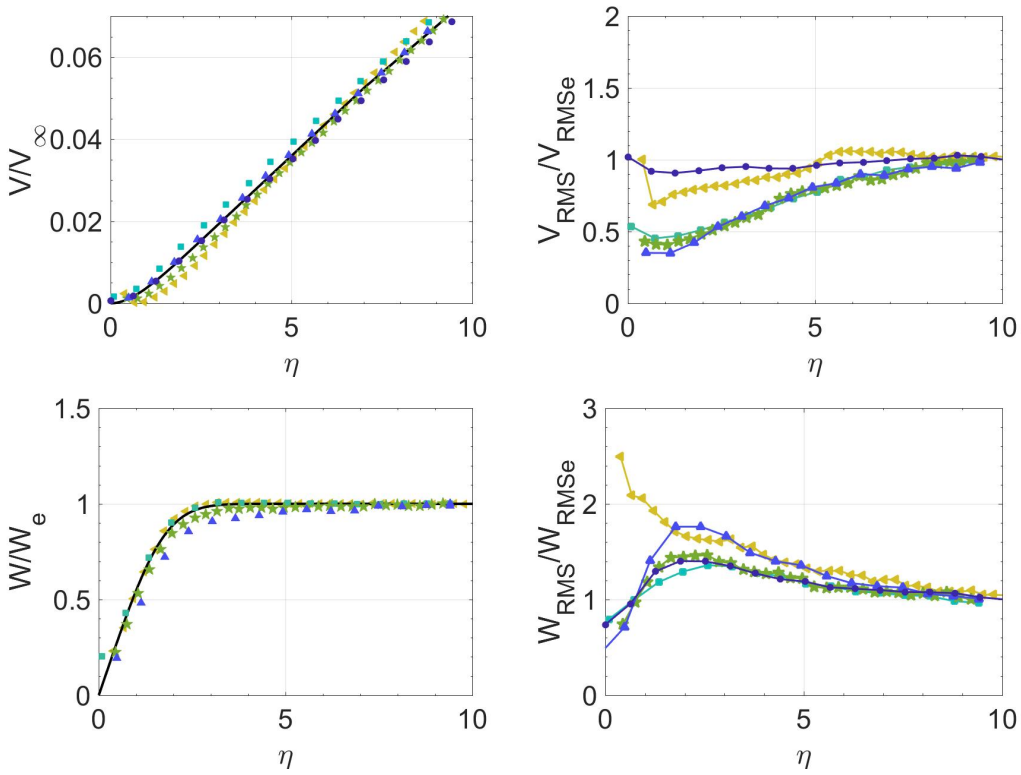


Figure 4.21: Mean and fluctuating velocity for different sweep angle: • $\Lambda = 0°$, ▲ $\Lambda = 5°$, ⋆ $\Lambda = 10°$, ■ $\Lambda = 20°$, ◀ $\Lambda = 30°$. W/W_e for $\Lambda = 0°$ is not plotted. The mean velocity are compared to Falkner-Skan-Cooke solution -.

Reynolds stress

The cross product $\overline{vw}$ has been calculated as reported in appendix C and normalised with respect to the RMS velocities components. The results, for all the sweep angles, are reported in figure 4.22. The cross product gives an indication of the correlation between two quantities; physically, it corresponds to the Reynolds stresses, giving the transfer of momentum from the mean flow to the fluctuations.

For the straight cylinder the product is zero at any distance from the wall, while it becomes negative for any swept configuration and reaches the minimum, that is the maximum correlation between the two velocity fluctuation components, at a distance from the wall around $2 \leq \eta \leq 5$.

This behaviour is due to the presence of a spanwise boundary layer in the swept cases, which causes the production of vortices close to the wall.

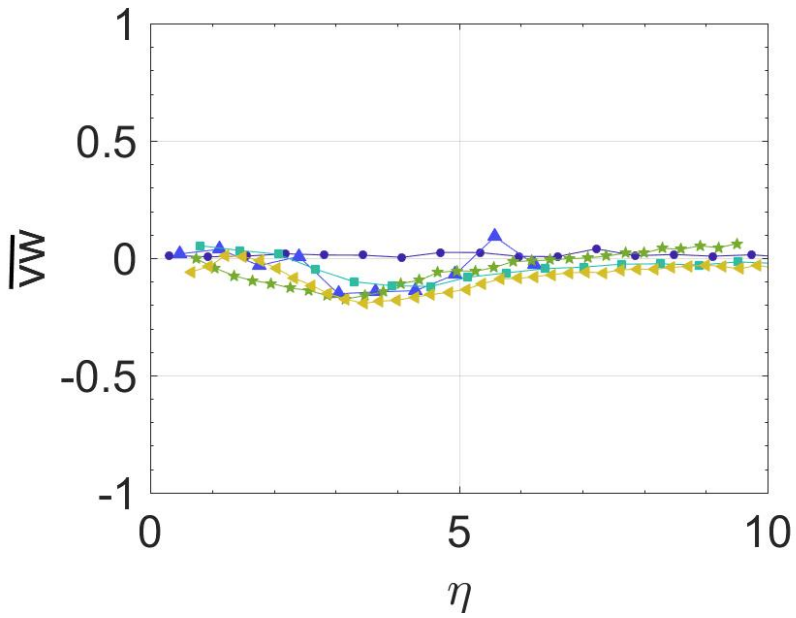
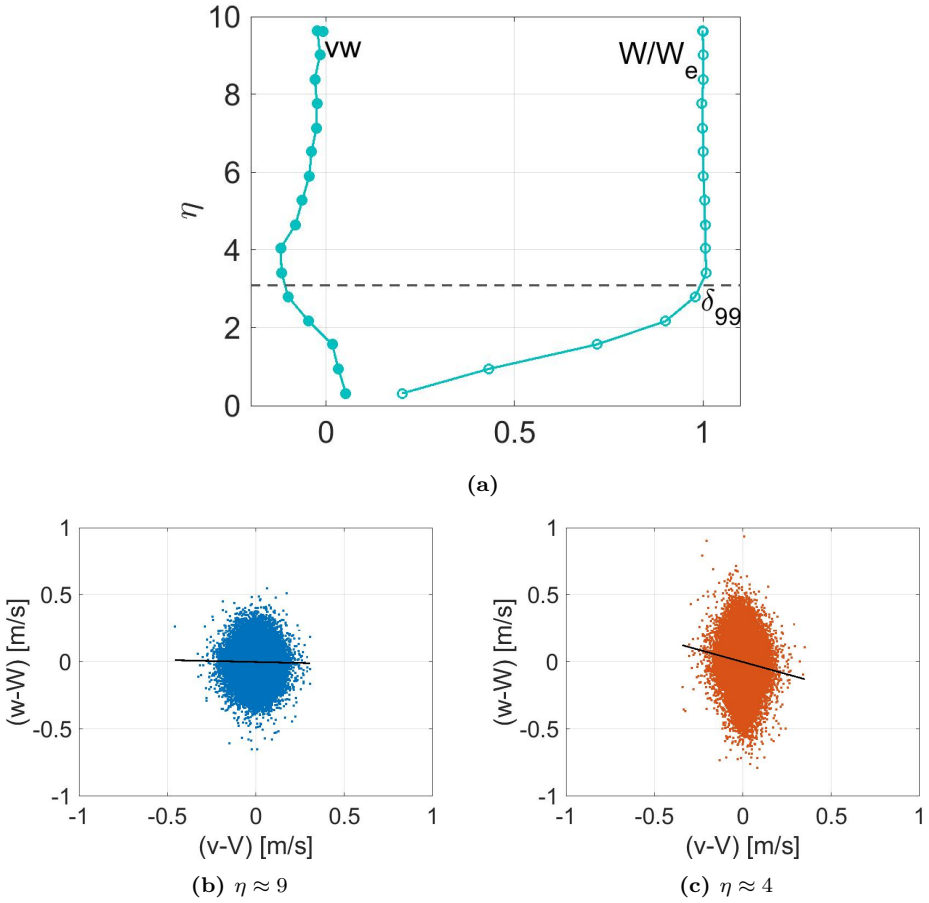


Figure 4.22: Normalised coviariance for different sweep angles: • $\Lambda = 0°$, ▲ $\Lambda = 10°$, ⋆ $\Lambda = 10°$, ■ $\Lambda = 20°$, ▶ $\Lambda = 30°$.



(a)

(b) $\eta \approx 9$

(c) $\eta \approx 4$

Figure 4.23: a) Normalised coviariance for $\Lambda = 20°$ and the w versus v scatter plots for the corresponding data at b) $\eta \approx 9$ and c) $\eta \approx 4$. The black lines indicate the linear regression.

To better explain the phenomenon, figure 4.23a shows the cross product for the sweep angle $\Lambda = 20°$. In particular, the maximum correlation can be observed to be roughly around the boundary layer edge.

In addition, figures 4.23c and 4.23b show the distribution of the data points respectively at $\eta \approx 9$ and at $\eta \approx 4$. In the first case, the cross product is zero showing a cloud of points well rounded and symmetrical. In contrast, the case at $\eta \approx 4$ shows an elliptical cloud with higher fluctuations in the spanwise direction. The plots report also the regression lines (black in the figures), which has a zero slope for $\eta \approx 9$ and a negative slope for $\eta \approx 4$. The negative slope indicates that at the wall the fluctuations of v and w have statistically an opposite sign (with two possible situations $v > 0$ and $w < 0$ or $v < 0$ and $w > 0$), that explains also the negative sign in the cross correlation.

Finally, figure 4.24 further shows the cross-products for the case $\Lambda = 20°$ at different Z locations along the attachment-line. The behaviour with the maximum correlation at the edge of the boundary layer appears to be homogeneous in the spanwise direction.

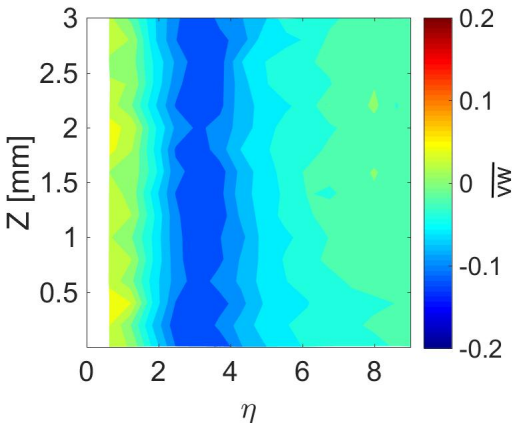


Figure 4.24: Contour plot of the cross-product along the spanwise direction for $\Lambda = 20°$

4.4.4 Frequency domain

A better insight to the phenomenon is obtained by comparing the spectra. Figures from 4.25 to 4.28 show the contour plot of the PSD for one boundary layer profile on the attachment-line for the V and W velocity components at different sweep angles. They can be compared to the unswept case in figure

4.15.

The unswept contour of the PSDs, already discussed in the previous section, show: an attenuation of the low frequencies (below 30 Hz) for the V-velocity component associated to a growth in energy in the same frequency range for the W velocity component.

The following observations can be listed by comparing the contour of the PSDs with the different swept angles:

- the attenuation of the V_{PSD} at the low frequencies happens farther from the wall as the sweep angle of the cylinder is increased;

- when the sweep angle is greater than 10°, the spectra of the V-component in the range frequency $[20 \div 100]\, Hz$ decreases, approaching the wall, at a different rate with respect to the spectra in the range below 20 Hz;

- W_{PSD} at frequencies below 30 Hz, clearly amplify on the unswept model and at $\Lambda = 5° \div 10°$, but remains constant at higher sweep;

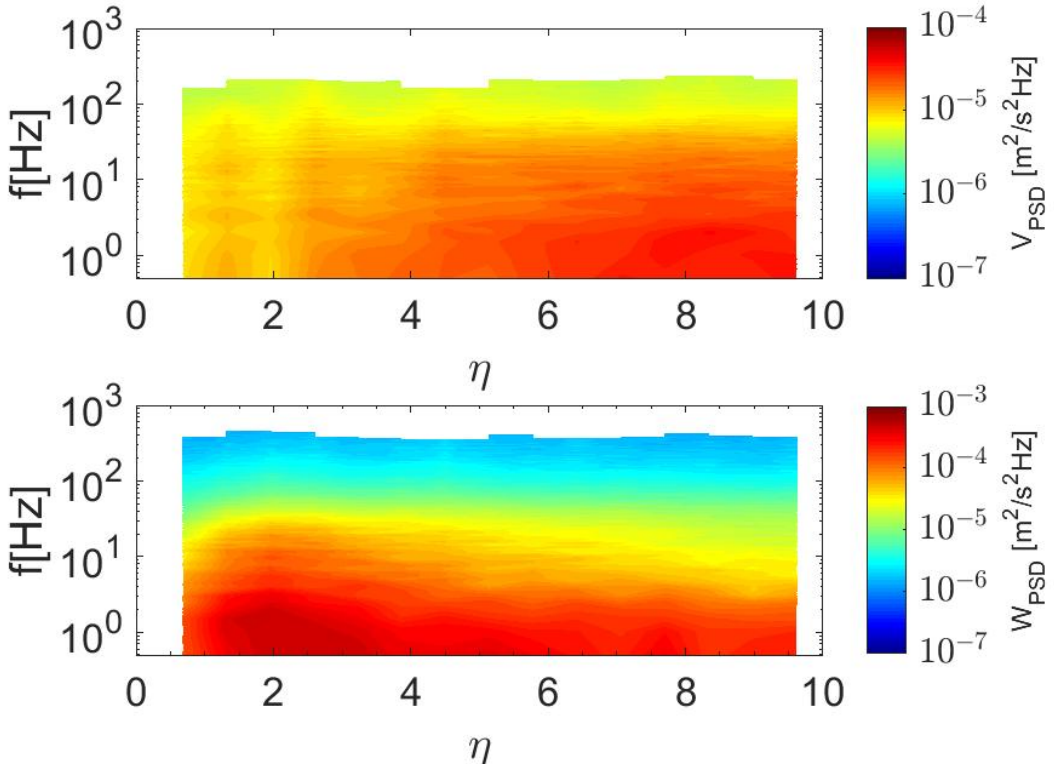


Figure 4.25: PSD contour plot $\Lambda = 5°$.

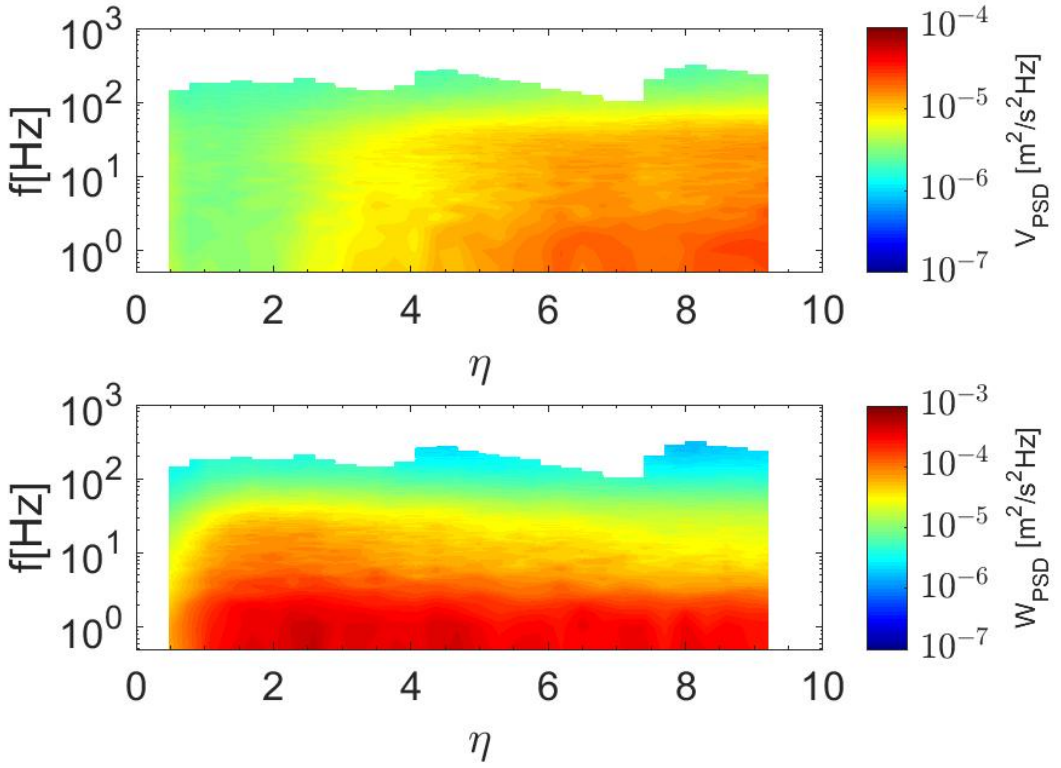


Figure 4.26: PSD contour plot $\Lambda = 10°$.

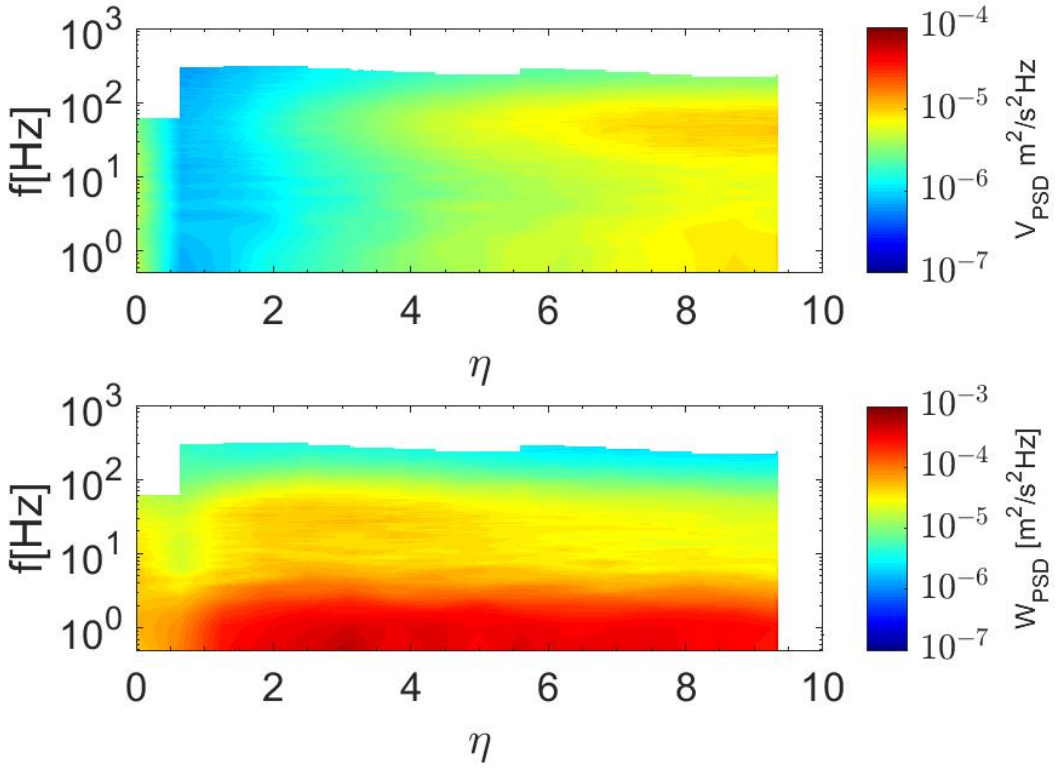


Figure 4.27: PSD contour plot $\Lambda = 20°$.

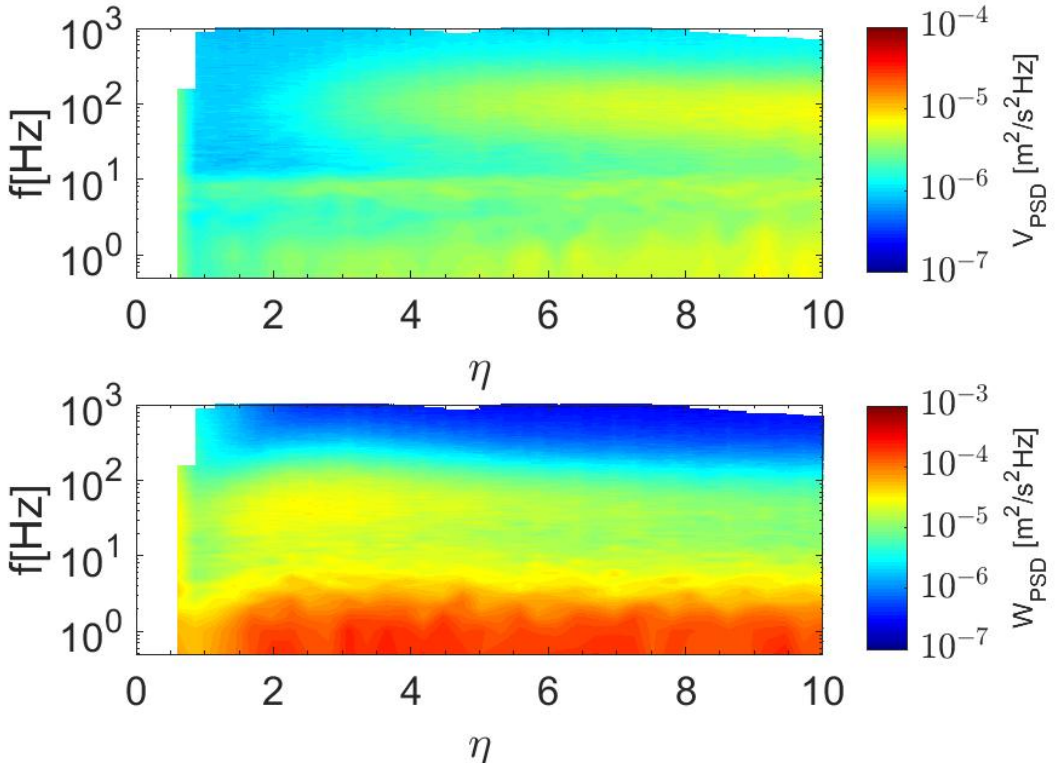


Figure 4.28: PSD contour plot $\Lambda = 30°$.

- in contrast, at higher sweep a second region of amplification on the W_{PSD} can be identified at frequencies between 20 and 80 Hz, moving to higher frequencies when the sweep increases.

The vorticity amplification theory focuses on the amplified wavelengths. Therefore, to highlight the differences with respect to the unswept case, predicted by the theory, the procedure based on the frozen pattern assumption has been applied also to the swept cases. The frequencies have been converted to wavelengths and the correspondent associated energy content is shown in the contour plots in figures 4.29 to 4.32.

For all the cases, the maximum λ_y clearly decreases approaching the wall since the eddies become smaller. On the other hand, the largest eddy scale contained in the λ_z direction remains constant up to $\eta = 2.5$ for all the sweep angles. The increment in maximum λ_z wavelength approaching the boundary layer edge was observed only in the unswept case (see figure 4.16).

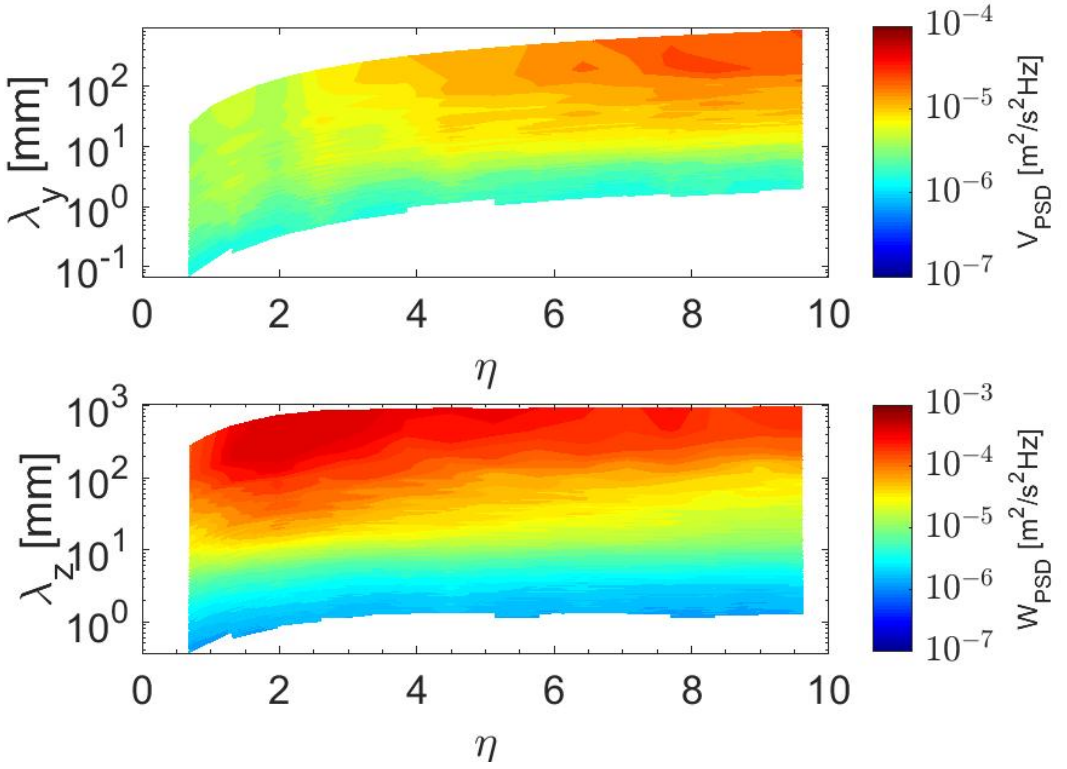


Figure 4.29: Contour plot $\Lambda = 5°$.

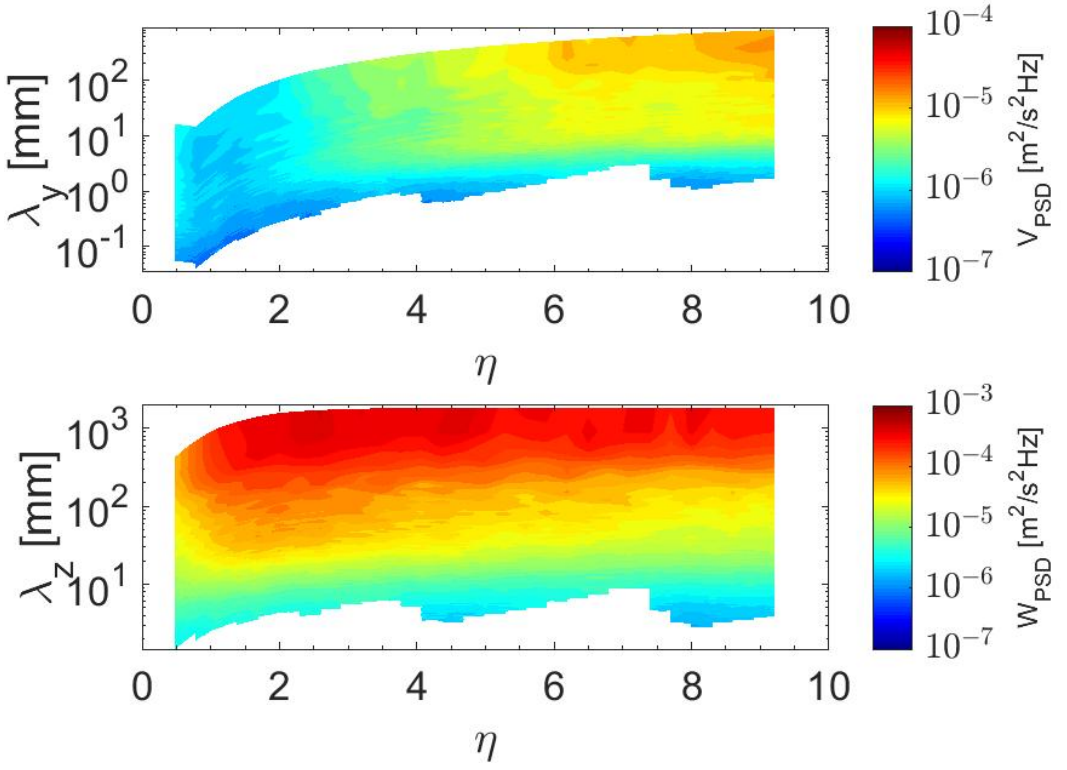


Figure 4.30: Contour plot $\Lambda = 10°$.

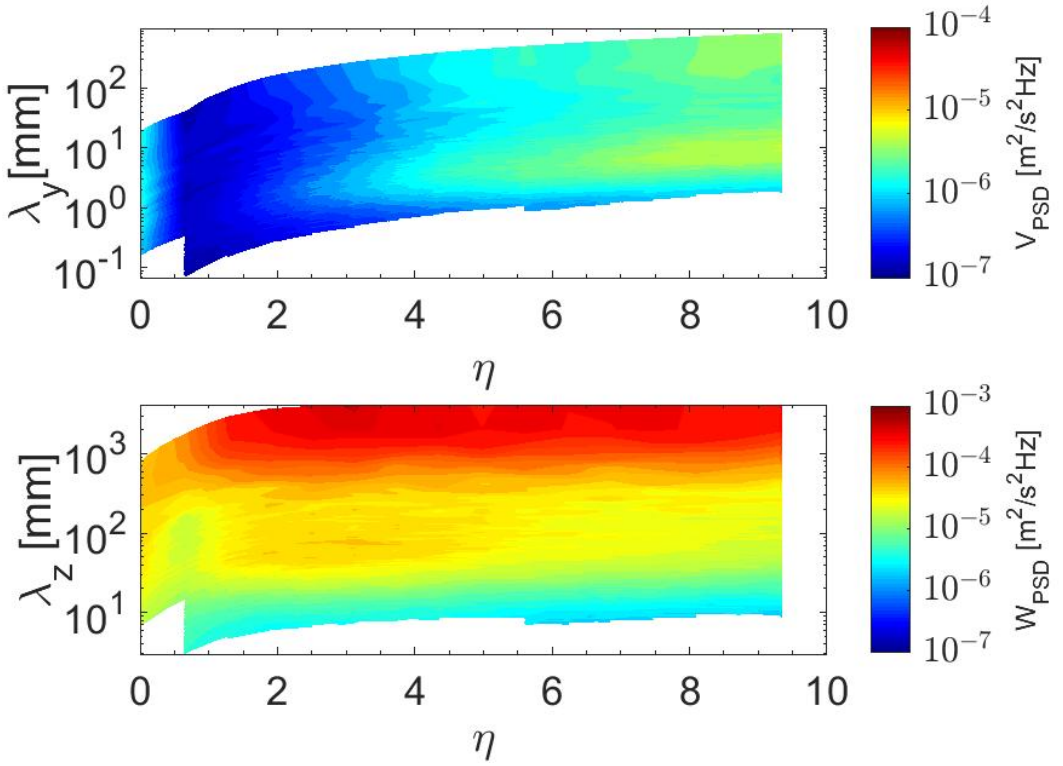


Figure 4.31: Contour plot $\Lambda = 20°$.

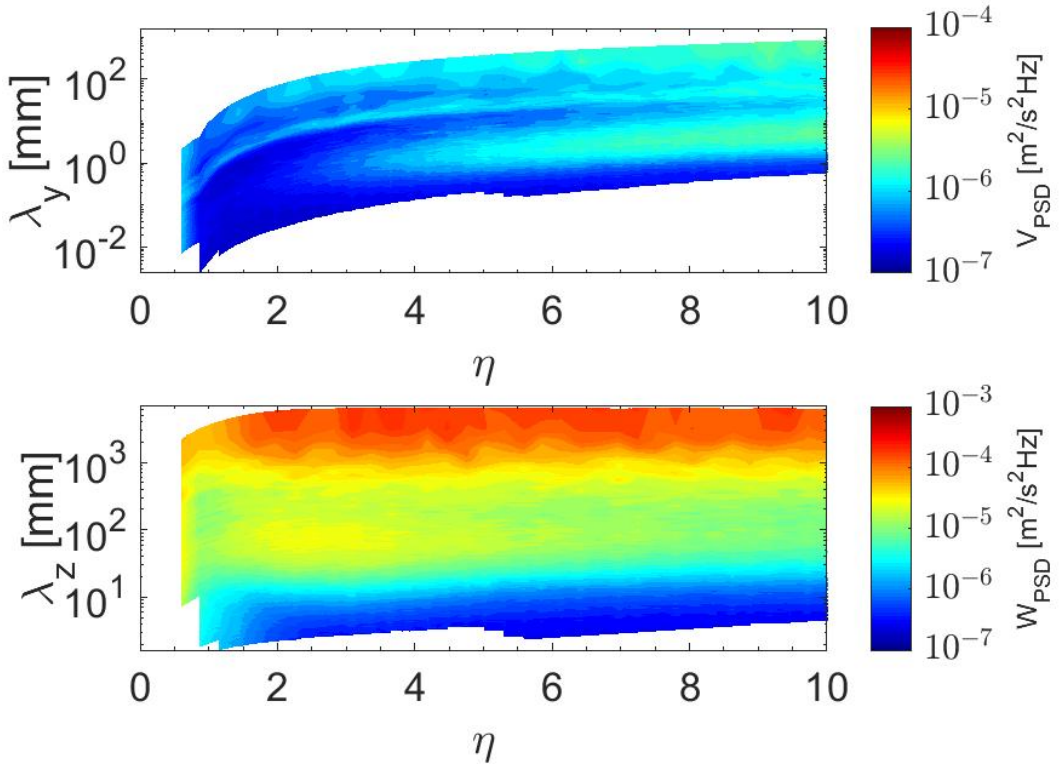


Figure 4.32: Contour plot $\Lambda = 30°$.

4.4.5 YZ scan

For each sweep angle the YZ scan, as for the unswept cylinder, was carried out in a $3 \times 3\,mm^2$ area with a resolution of $0.2\,mm$. Also for swept cases the flow appears quite homogeneous at all the Z locations and at all the sweep angles.

4.5 Other results and observations

In addition to the investigations discussed in the previous sections, some analysis and specific tests have been carried out concerning: the characterisation of the freestream condition for all the sweep angles, in order to compare the disturbances approaching the wall in the different cases; the influence of the freestream velocity influences the observed phenomenon; the influence of the vortex shedding of the wake on the stagnation point/attachment-line flow.

4.5.1 Characterisation of freestream disturbances

The presence of the cylinder at different sweep angle changes the flow field in the wind tunnel. Furthermore, the distance between the Pitot tube and the model varies when the model is swept-back as shown in figure 4.2. The Pitot has been used to set the wind tunnel at the desired speed ($6m/s$), but to record a reference condition for all the cases, the flow field at $200\,mm$ from the model has been measured for each sweep condition in semi-coincidence mode (table 4.1). The turbulence intensity (Tu) has been calculated using the chordwise and spanwise velocity fluctuations, the results are in figure 4.33.

Λ [°]	V_∞ [m/s]	$V_{\infty RMS}$ [m/s]	W_∞ [m/s]	$W_{\infty RMS}$ [m/s]	Q_∞ [m/s]	Re_D	Re_Θ
0	6.05	0.081	0.061	0.073	6.05	6.810^4	0
5	5.91	0.078	0.55	0.095	5.92	$5.8\ 10^4$	6.2
10	5.90	0.0789	0.59	0.0944	5.93	$5.8\ 10^4$	9.23
20	5.72	0.0764	1.76	0.0748	5.98	$5.6\ 10^4$	22.8
30	5.14	0.0894	2.12	0.0664	5.59	$5.1\ 10^4$	31.54

Table 4.1: Freestream conditions for experiments at different sweep angles.

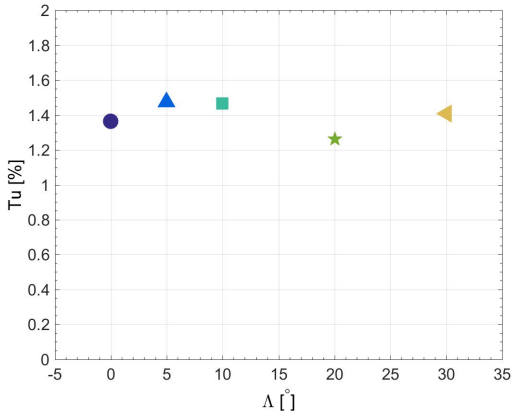


Figure 4.33: Freestream turbulence intensity at 200 mm from the leading edge of the cylinder for various sweep angle. Legend as in figure 4.34.

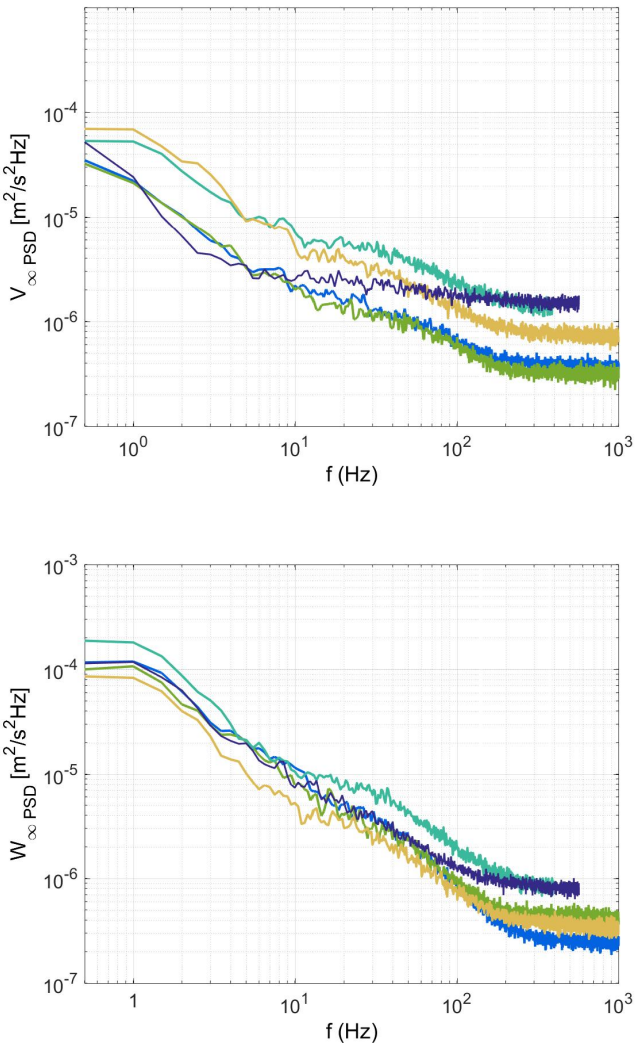


Figure 4.34: Freestream spectra for different sweep cylinder: $\Lambda = 0°$, $\Lambda = 5°$, $\Lambda = 10°$, $\Lambda = 20°$, $\Lambda = 30°$.

In addition, figure 4.34 shows the frequency distribution of the velocity components for each sweep angle experiment expressed in the cylinder coordinate system. This comparison is to show that the characteristic of the freestream disturbances was similar for all the experiments.

4.5.2 Velocity dependence

A set of measurements taken at $\Lambda = 20°$ at different freestream velocities were carried out to investigate how the observed phenomenon changes with the velocity.

The flow in the boundary layer at the attachment-line was measured at four wind tunnel speeds ($6\,m/s, 8\,m/s, 10\,m/s, 15\,m/s$ as reported in table 4.2), the results are shown in figure 4.35.

Λ [°]	V_∞ [m/s]	$V_{\infty RMS}$ [m/s]	W_∞ [m/s]	$W_{\infty RMS}$ [m/s]	Q_∞ [m/s]	Re_D	Re_Θ
20	5.72	0.0764	1.76	0.0748	5.98	5.6 10^4	22.8
20	7.52	0.111	2.32	0.11	7.87	7.4 10^4	26.1
20	9.40	0.118	2.87	0.118	9.84	9.3 10^4	29.1
20	14.07	0.178	4.30	0.154	14.71	13 10^4	35.6

Table 4.2: Freestream condition for experiments at different speeds and $\Lambda = 20°$.

The V mean velocity component shows different slopes for each case in agreement with the Hiemenz theory (the coefficient a is, in fact, function of the velocity); the W component shows the typical Falkner-Skan-Cooke boundary layer with the edge velocity increasing with the speed; the V_{RMS} and the W_{RMS} have similar trend for all the freestream velocities.

In particular, although the absolute values of V_{RMS} and W_{RMS} increase with the freestream velocity, the minimum of the V_{RMS} reaches always the same absolute value around $\eta = 1$. In addition, the spectra for each freestram velocity within the boundary layer was compared; the energy distribution was found to be similar to that at $Q_\infty = 6\,m/s$.

In addition, fiugre 4.36 shows the cross-correlation for $\Lambda = 20°$ at different freestream speeds. The absolute maximum value of the cross product increases

as the freestream speed increases, remaining constantly negative, in accordance with the RMS values. It can be observed that the point where $\overline{vw} \to 0$ in the outer region moves farther as the velocity increases.

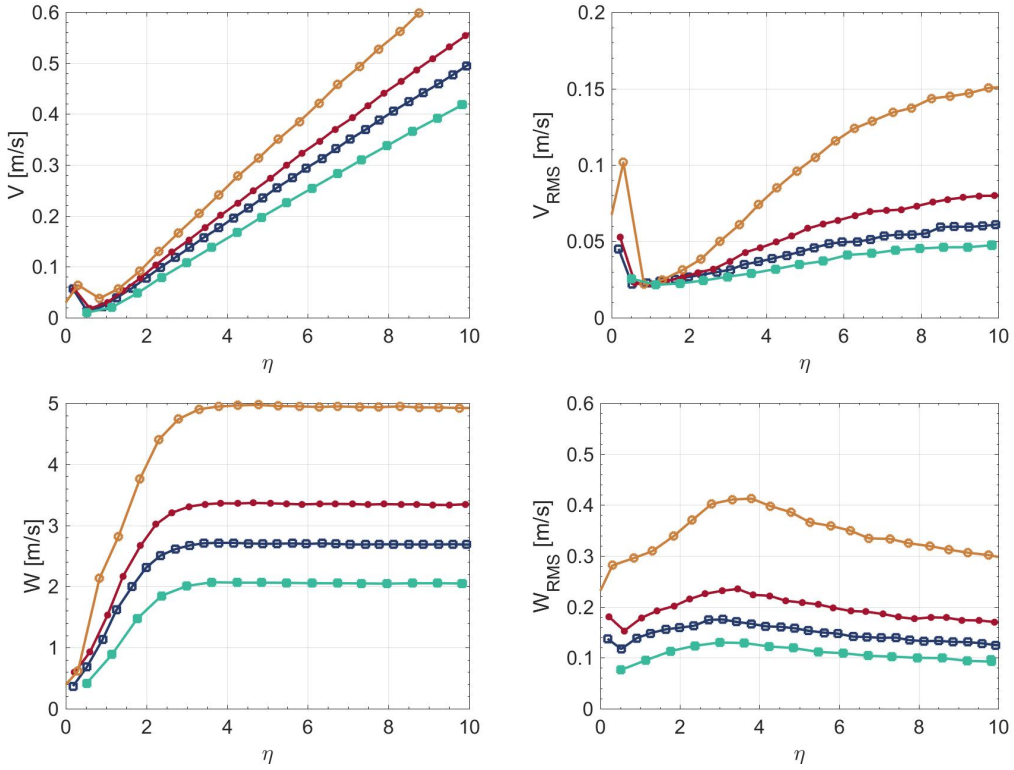


Figure 4.35: Mean and fluctuation of the velocity at different freestream Reynolds number:$\Lambda = 20°$ ■ $Q_\infty = 6\,m/s$, □ $Q_\infty = 8\,m/s$, • $Q_\infty = 10\,m/s$, ○ $Q_\infty = 15\,m/s$.

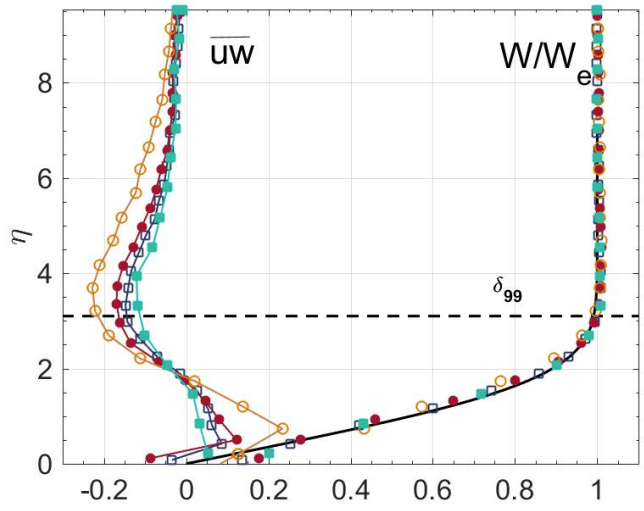


Figure 4.36: Mean and shear stress of the velocity at different freestream velocities:$\Lambda = 20°$ ■ $Q_\infty = 6\,m/s$, □ $Q_\infty = 8\,m/s$, • $Q_\infty = 10\,m/s$, ○ $Q_\infty = 15\,m/s$.

4.5.3 Re_Θ dependence

When studying the attachment-line it is good practice to refer to the Re_Θ, the Reynolds number based on the attachment-line momentum thickness and spanwise velocity. This is obviously zero in the unswept case since there is no spanwise velocity at the stagnation point.

The previous experiments have been run at the same Re_D, but different Re_Θ as shown in table 4.1. The results of the experiments at 30° show a different behaviour of the RMS compared to the other sweep angles, that asks the question whether the phenomenon observed in that case would also be observed at same Re_Θ. The measurements on the cylinder at $\Lambda = 30°$ at $6\,m/s$ correspond to a Re_Θ of 31.5, which is in between the Re_Θ of the cases for $\Lambda = 20°$ at $10\,m/s$ and at $15\,m/s$, as shown in table 4.2. Therefore, the profiles have been compared in figure 4.37.

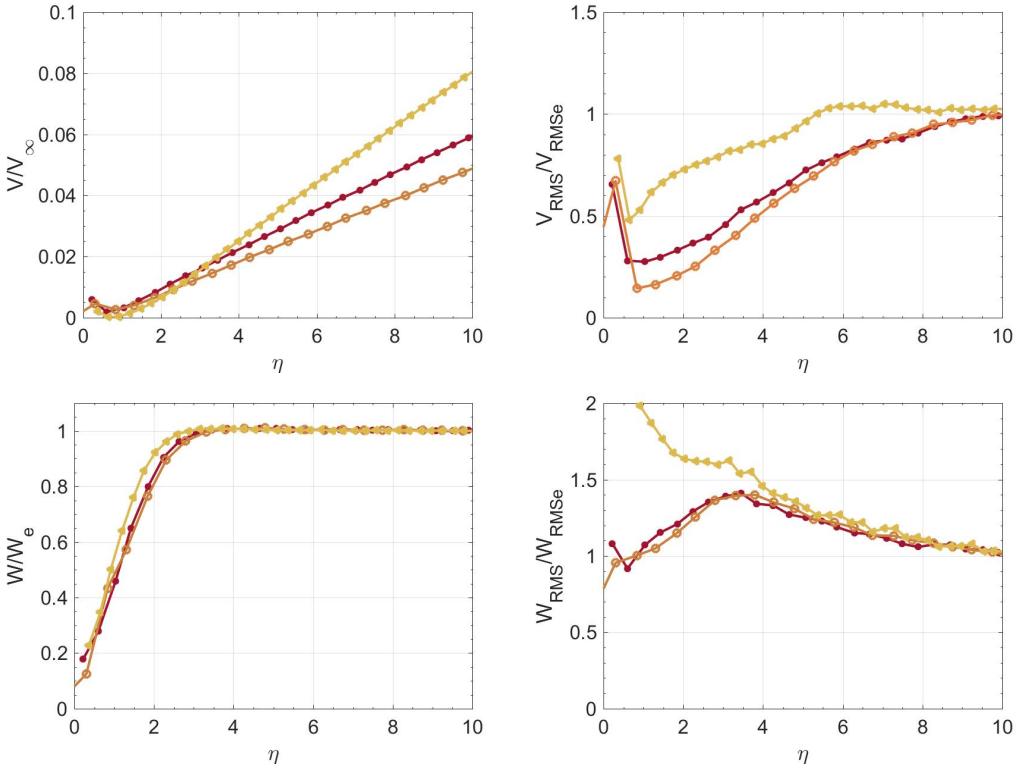


Figure 4.37: Mean and fluctuation of the velocity at different Re_Θ and two sweep angles: $\Lambda = 20°$ • $Re_\Theta = 29.1$, ○ $Re_\Theta = 35.6$ and ◀ $\Lambda = 30°$ $Re_\Theta = 31.5$.

It is shown that the trend of the W_{RMS} is identical for $\Lambda = 20°$ at the different velocities with a maximum always appearing in the profiles. This behaviour

differs from that of $\Lambda = 30°$, in which the curve keeps increasing close to the wall.

This results suggest that the observed phenomenon is effectively related to the sweep angle rather than to Re_Θ.

4.5.4 Effect of separation on the observed phenomenon

The vortex shedding due to laminar separation in the rear part of the cylinder influences the U velocity component at the stagnation point. In fact, usually the shedding frequency appears amplified only in the PSD of the U velocity. To verify that the laminar separation does not influence the phenomenon under investigation, which involves only the V and W velocity components, the flow, in the $\Lambda = 10°$ configuration, has been analysed with and without two strips of roughness, applied symmetrically on the shoulder of the cylinder. The role of the roughness was to trip the laminar boundary layer to a turbulent one, so that also the separation becomes turbulent. Figure 4.38 shows the spectra of the signal recorded by the third laser during semi-coincidence mode measurements.

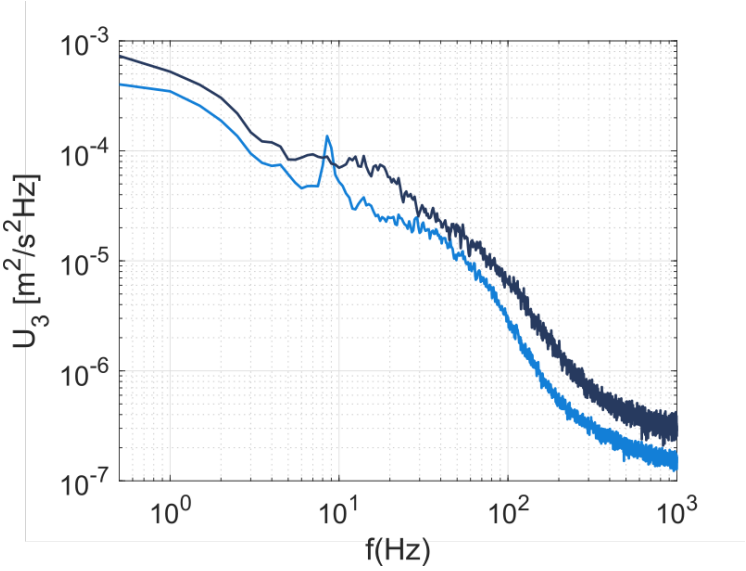


Figure 4.38: PSD of LDA3 signal at $\eta = 7.5$ on the cylinder at $\Lambda = 10°$ with - and without - the roughness strips to trip the boundary layer.

In that configuration, the third laser measures a combination of the W and the U velocity components (U_3 in the figure). The PSD shows a clear peak at 8.5 Hz, corresponding to the shedding frequency, only without the trip. The results of mean and the fluctuations of the velocity, for the V and W velocity components, at attachment-line flow, with and without the roughness are reported in figure 4.39.

The mean flow velocity is compared with the Falkner Skan Cooke solution and the RMS values are normalised with respect to their value at $\eta = 6$ and plotted as function of the boundary layer dimensionless coordinate η. The two cases have the same trend for both the mean and the RMS of the velocity profile. This means that the vortex shedding on the back of the cylinder does not have a significant effect on the observed phenomenon.

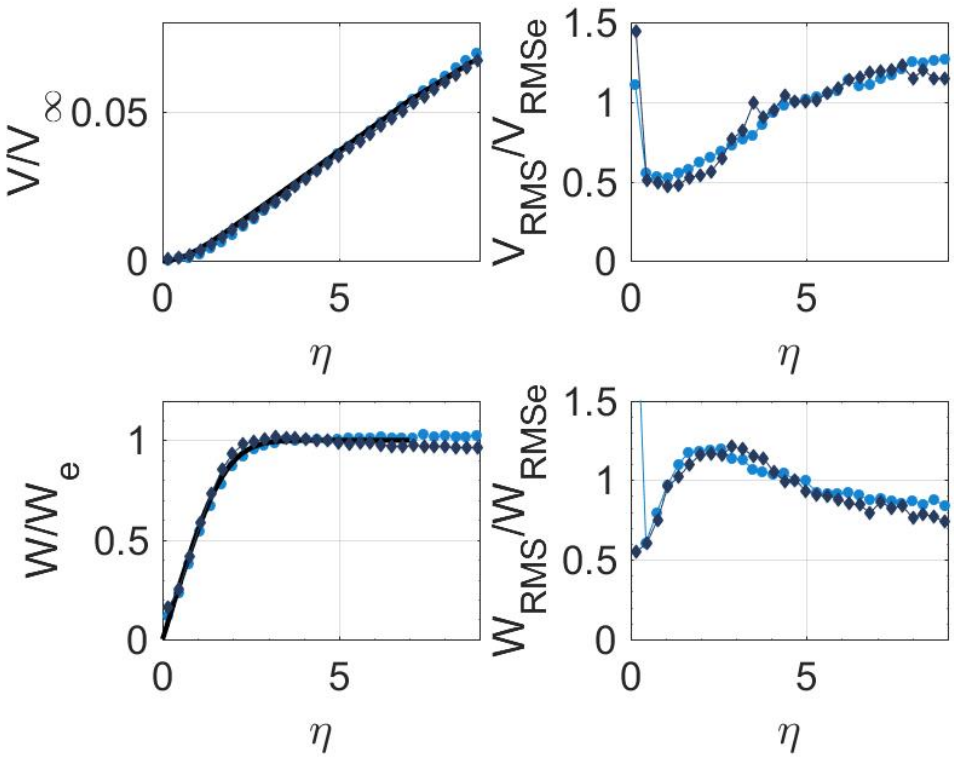


Figure 4.39: Flow at the stagnation point on a cylinder at $\Lambda = 10°$ with ♦ and without • the roughness strips to trip the boundary layer. The mean velocity profiles are compared to Falkner Skan Cooke (black line).

4.6 Summary

The experimental investigation on the cylinder focused on two main aspects: the vorticity amplification at the stagnation point for an unswept model and the effect of the sweep angle on the same phenomenon. The results can be respectively summarised as follow.

Unswept Cylinder

- The multi-component LDA allowed the whole three-dimensional flow field to be measured including the very narrow area close to the leading edge.

- The mean flow has been found to be in agreement with the potential flow theory far from the leading edge, with the Hiemenz theory closer to the stagnation point and with the Falkner-Skan theory in the boundary layer. In particular, the high spatial resolution has enabled one to observe the small non-linear region of the V-velocity component close to the wall.

- The velocity fluctuations decrease from the freestream approaching the stagnation point, up to the boundary layer where the spanwise fluctuations were found to increase up to almost twice the freestream value.

- The phenomenon, analysed in more details in the frequency domain, shows that the amplification is associated with low frequencies below 30 Hz. This result is agreement with the experiment by Sadeh et al. (1970).

Swept Cylinder

- The effect on the vorticity amplification at the leading edge with a sweep angle has been investigated with four configurations. In all the cases the mean flow was found to be in agreement with the potential flow theory far from the leading edge, with Hiemenz theory closer to the attachment-line and with the Falkner-Skan-Cooke theory in the boundary layer.

- The velocity fluctuations were found to behave similarly to those observed for the straight cylinder far from the leading edge, where the three velocity components decrease. Close to the stagnation point, the wall-normal velocity fluctuation decrease, while the spanwise fluctuations increase. A maximum was found, as in the unswept case, for all the sweep angles except $\Lambda = 30°$ for which the fluctuations increase farther towards the wall. The anomalous behaviour of the $\Lambda = 30°$ does not depend on Re_Θ, as observed by comparing the fluctuation profiles to those at $\Lambda = 20°$ at higher velocities.

- The analysis in the frequency domain has revealed that the increment of the spanwise fluctuations for the $\Lambda = 30°$ is associated with a frequency range around 100 Hz, higher than the low frequencies observed in the unswept case. Actually, the higher frequencies appear amplified also at the lower sweep angles (10° and 20°). It can be concluded that with a swept cylinder the fluctuations profiles look quite similar to those of the unswept case, but where the excited frequencies are higher.

- The experiments at constant sweep angle ($\Lambda = 20°$) with increasing freestream speeds show the spanwise velocity fluctuations always increasing approaching the attachment-line boundary layer reaching a maximum.

- In order to check if the separation on the cylinder influences the spanwise fluctuation at the stagnation point, experiments were carried out with and without a roughness strip applied on the cylinder. The results in the case of a laminar separation compared to the case of a turbulent separation did not show substantial differences.

Chapter 5

Some theoretical considerations

This experimental investigation revealed that the flow at the stagnation point of a two-dimensional body presents an increase in the spanwise velocity flucuations, but the experiments have also revealed that an increase of the spanwise fluctuations is also present on the three-dimensional attachment-line and, actually, the fluctuations seem to increase within the boundary layer at higher sweep angles. To thoroughly understand the observations, though, a theoretical model is necessary. During the PhD, an attempt to solve the equations was carried out. Although the attempt was found not to be successful, some theoretical considerations are here presented which may be of help in developing a comprehensive theory.

5.1 The vorticity amplification theory

In the vorticity amplification theory the time-independent vorticity transport equation, the continuity equation and time-independent energy transport equation were solved for a flow impinging on a flat vertical plate:

$$\left(\overrightarrow{u^*} \cdot \nabla\right) \overrightarrow{\omega^*} = \left(\overrightarrow{\omega^*} \cdot \nabla\right) \overrightarrow{u^*} + \nu \, \nabla^2 \overrightarrow{\omega}^* \tag{5.1a}$$

$$\nabla \cdot \overrightarrow{u^*} = 0 \tag{5.1b}$$

$$\left(\overrightarrow{u^*} \cdot \nabla\right) T^* = (\nu/Pr)\nabla^2 T^* \tag{5.1c}$$

where the $\overrightarrow{u^*}$, $\overrightarrow{\omega^*}, T^*$ are respectively the velocity, the vorticity and the temperature in dimensional quantities. By introducing the dimensionless quantity:

$$(\xi, \eta, \zeta) = (\sqrt{a/\nu}x, \sqrt{a/\nu}\, y, \sqrt{a/\nu}\, z)$$

$$\overrightarrow{u} = (a\nu)^{-1/2}\overrightarrow{u^*} \qquad \overrightarrow{\omega} = (a)^{-1}\overrightarrow{\omega^*}, \qquad T = (T_w - T^*)/(T_w - T_\infty)$$

where a is the Himenz flow constant, T_w the temperature at the wall and T_∞ the freestream temperature and the coordinate system is defined so that ξ the direction of the divergent flow, η is the direction perpendicular to the wall, ζ is the axis of flow symmetry.

It results:

$$(\overrightarrow{u} \cdot \nabla)\, \overrightarrow{\omega} = (\overrightarrow{\omega} \cdot \nabla)\, \overrightarrow{u} + \nabla^2 \overrightarrow{\omega} \tag{5.2a}$$

$$\nabla \cdot \overrightarrow{u} = 0 \tag{5.2b}$$

$$(\overrightarrow{u} \cdot \nabla)\, T = (1/Pr)\nabla^2 T \tag{5.2c}$$

where the vorticity is defined by $\overrightarrow{\omega} = \frac{1}{2}\nabla \times \overrightarrow{u}$, T is a temperature function and Pr the Prandtl number. For brevity, here only the solution of the vorticity will be discussed.

The theory assumed solutions of the type:

$$\begin{cases} U = (U_0(\eta) + u(\eta, \zeta))\, \xi \\ V = V_0(\eta) + v(\eta, \zeta) \\ W = w(\eta, \zeta) \end{cases} \tag{5.3}$$

where $U_0\, \xi, V_0$ are the mean flow velocity, and the $(u(\eta, \zeta)\, \xi, v(\eta, \zeta), w(\eta, \zeta))$ the perturbation.

The perturbation was assumed to describe a vorticity oriented in the ξ-direction. It was assumed to be sinusoidal along the ζ-axis, so that far from the wall $(\eta \to \infty)$ it would be characterised by only one harmonic component $V = V_0(\eta) + V_1(\eta)cos(k\zeta)$.

Nevertheless, the equations are non-linear and the solution had to contain all

the Fourier components. It turns to be:

$$U = (U_0(\eta) + A\sum_{n=1}^{\infty} u_n(\eta)cos(k_n\zeta))\,\xi \tag{5.4a}$$

$$V = V_0(\eta) + A\sum_{n=1}^{\infty} v_n(\eta)cos(k_n\zeta) \tag{5.4b}$$

$$W = A\sum_{n=1}^{\infty} k_n^{-1} w_n(\eta)cos(k_n\zeta) \tag{5.4c}$$

$$\Omega = A\sum_{n=1}^{\infty} \omega_n(\eta)sin(k_n\zeta) \tag{5.4d}$$

By substituting the perturbation in the equations 5.2, after some trigonometric manipulations, a system of six ordinary differential equations, five of which are linear, was found. Since the equations in the system were coupled they must be solved simultaneously considering the appropriate boundary conditions to get the solution for each individual harmonic component.

All the details are contained in the original papers (Sutera et al. (1962) and Sutera (1965)). Let's focus on the *natural wavelength* of the disturbance λ_0, which determines the threshold for the disturbances which are supposed to be amplified. To find this parameter, Sutera et al. (1962) considered the asymptotic solution where the flow far from the wall is described by the Hiemenz inviscid solution:

$$\begin{cases} V_0(\eta) \to \eta, & \text{if } \eta \to \infty \\ V_0'(\eta) \to 1, & \text{if } \eta \to \infty. \end{cases} \tag{5.5}$$

Ignoring the non-linear terms, which describe the interaction between the harmonics, the vorticity equation becomes:

$$\omega_1'' + \eta\omega_1' + (1 - k_1^2)\omega_1 = 0, \tag{5.6}$$

where the subscript 1 means that only the first harmonic is considered and the apex indicates the derivative respect to η. The solutions of this equation are:

$$\omega_{1a} \sim \frac{e^{-(1/2)\,\eta^2}}{\eta^{k_1^2}} \left(1 - \frac{k_1^2(k_1^2+1)}{2\eta^2} + ...\right) \tag{5.7a}$$

$$\omega_{1b} \sim \eta^{k_1^2-1} \left(1 + \frac{(1-k_1^2)(2-k_1^2)}{2\eta^2} + ...\right) \tag{5.7b}$$

The first solution vanishes approaching the wall, while the second increases approaching the wall if $k_1^2 < 1$. Therefore it is only the vorticity larger than the neutral scale (which in dimensional units corresponds to $\lambda_0 = 2\pi(a/\nu)^{-1/2}$) which can be amplified in the stagnation point flow ($k_1 < 1$, $\lambda < \lambda_0$).

If one wants to apply exactly the same procedure to the swept case, the mean flow has to be modified by introducing the spanwise velocity, so that 5.4d would become:

$$W = W_0 + A\sum_{n=1}^{\infty} k_n^{-1} w_n(\eta) cos(k_n \zeta) \tag{5.8}$$

This modification would add one term to the equations, but the dependence from ζ could not be easily removed. Since the aim here is to only discuss the influence of the sweep angle, a different approach is presented in the next section.

5.2 Influence of the sweep angle on the vorticity transport (far field)

Let's consider again the vorticity transport equation and the continuity, assuming a mean flow ($\overrightarrow{\Omega}$, $\overrightarrow{U}$) on which is superimposed a perturbation ($\overrightarrow{u}$, $\overrightarrow{\omega}$) following the same dimensionless used in the vorticity amplification theory, as shown in the previous section. Considering the perturbation smaller than the mean flow, the vorticity transport equation would become:

$$\begin{cases} (\overrightarrow{U}\cdot\nabla)\overrightarrow{\omega} + (\overrightarrow{u}\cdot\nabla)\overrightarrow{\Omega} = (\overrightarrow{\Omega}\cdot\nabla)\overrightarrow{u} + (\overrightarrow{\omega}\cdot\nabla)\overrightarrow{U} + \nabla^2\overrightarrow{\omega} \\ (\overrightarrow{u}\cdot\nabla)\overrightarrow{\omega} = (\overrightarrow{\omega}\cdot\nabla)\overrightarrow{u} \end{cases} \tag{5.9}$$

where the terms of second order have been written separately. The aim is to study the behaviour of the flow at $\eta \to \infty$ to verify that, if the flow is swept, the far field solution would still amplify approaching the wall, and eventually at which rate. To do so, let consider the irrotational mean flow ($\overrightarrow{\Omega} = 0$) as the inviscid Hiemenz solution: (U, V, W)=$(\xi, -\eta, W_\infty)$ and the vorticity perturbation defined by (ω^ξ, ω^η, ω^ζ). The equations, projected on the three coordinate, become:

$$\xi\,\omega^\xi_\xi - \eta\,\omega^\xi_\eta + W_\infty\,\omega^\xi_\zeta = \omega^\xi + \omega^\xi_{\xi\xi} + \omega^\xi_{\eta\eta} + \omega^\xi_{\zeta\zeta} \tag{5.10a}$$

$$\xi\,\omega^\eta_\xi - \eta\,\omega^\eta_\eta + W_\infty\,\omega^\eta_\zeta = -\omega^\eta + \omega^\eta_{\xi\xi} + \omega^\eta_{\eta\eta} + \omega^\eta_{\zeta\zeta} \tag{5.10b}$$

$$\xi\,\omega^\zeta_\xi - \eta\,\omega^\zeta_\eta + W_\infty\,\omega^\zeta_\zeta = \omega^\zeta_{\xi\xi} + \omega^\zeta_{\eta\eta} + \omega^\zeta_{\zeta\zeta} \tag{5.10c}$$

where the subscripts indicate the derivatives and the superscript the components. So far, the only assumption made is that the mean flow is potential. The equations are identical to those derived by Sutera et al. (1962), except for the W_∞ which would be zero in the two-dimensional case.

Some observations can be carried out already at this stage. The first terms on the right hand side of the first two equations are the stretching terms. In particular, that on the first equation (ω^ξ) is the one which causes the amplification of the vorticity. This is not modified by the sweep angle, therefore a stretching behaviour can be expected similar to the two-dimensional case. On the other hand, the extra term with respect to the two-dimensional case is the last term the left hand side of all the three equations. This describes that the vorticity is transported by the spanwise velocity component. It was experimentally observed in Chapter 5, that the vortices generated by the wake of the string, placed ahead of the swept body, were transported parallel to the attachment-line; which is what that term describes.

To look at the evolution of a vorticity perturbation oriented in the ξ-direction, let consider only the first equation of the system 5.10 and let assume the

perturbation of $\omega^{\xi}(\eta,\zeta)$ as:

$$\omega^{\xi}(\eta,\zeta) = \omega(\eta)\, e^{ik\zeta} \tag{5.11a}$$

where the i indicates the complex number. By substituting in the first equation of 5.10 it results:

$$\omega'' + \eta\,\omega' - (i\,k\,W_{\infty} + k^2 - 1)\omega = 0. \tag{5.12}$$

Let's assume the solution of the type $\omega(\eta) = B\eta^{\beta}$. By substituting it is obtained:

$$\beta(\beta-1)\eta^{\beta-2} + \eta^{\beta} - (i\,k\,W_{\infty} + k^2 - 1)\eta^{\beta} = 0 \tag{5.13}$$

since $\eta^{\beta-2} << \eta^{\beta}$ for $\eta \to \infty$ the equation leads to:

$$\beta = (k^2 - 1) + i(W_{\infty}k). \tag{5.14}$$

It should be noticed that for the two-dimensional case ($W_{\infty} = 0$) this solution has the same form of that of the vorticity amplification theory (equation 5.7b). The final solution for the far field becomes:

$$\omega^{\xi}(\eta,\zeta) = B\eta^{(k^2-1)+i(W_{\infty}k)}\, e^{ik\zeta} \tag{5.15}$$

which corresponds to

$$\omega^{\xi}(\eta,\zeta) = B\,\eta^{(k^2-1)}\ (cos((W_{\infty}k)ln(\eta)) + i\,sin((W_{\infty}k)ln(\eta)))\ e^{ik\zeta}.$$

Mathematically, the solution describes a function that increases or decreases approaching the wall while it oscillates with a wavelength that increases with logarithm of the wall distance. The function would increase approaching the wall if $k > 1$ and decrease if $k < 1$, as shown in figure 5.1. The amplification threshold (given by $\mathbb{R}(\beta)$) does not change with respect to the unswept case, but the complex exponent introduces periodical oscillations, with increasing period, approaching the wall. The period of these oscillations in-

creases with the sweep angle since, in dimensional units, it corresponds to $\mathbb{I}(\beta^*) = W^*_\infty k(a/\nu)^{1/2}$.

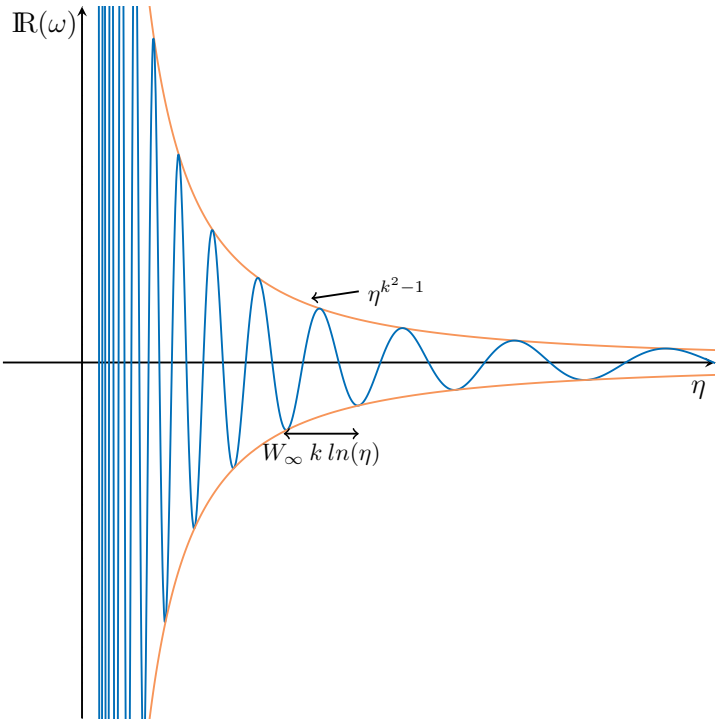


Figure 5.1: Logarithmic oscillations.

5.2.1 The full solutions

The solution just described is only a partial one of the vorticity transport equation in the far field. It is useful to observe the differences between the swept and unswept cases and to highlight that an amplification of the vorticity would be expected also in the swept case.
To find a comprehensive solution of the problem, the full Navier-Stokes equations with the perturbation would need to be considered.

An attempt was carried out during the PhD, using the same approach followed by Kerr and Dold (1994). The equations were derived considering the perturbation on the velocity and vorticity field as function only of η and ζ, as in the previous section. The projections of the Navier-Stokes on the three coordinate axis were combined together to remove the pressure and, by introducing the streamfunction of the perturbation, the equations were conducted to one

second order non-linear ordinary differential equation in terms of streamfunction of the perturbation and vorticity. The boundary conditions at the wall imposed the velocity, both of the mean and of the perturbation field, to be zero; while at infinity the mean flow had to behave like the potential flow solution. The far field solution was used as shooting condition for the vorticity. With this method, the solutions could be found by applying a 4^{th}-order Runge Kutta integration algorithm. Nevertheless, by introducing the sweep angle the code struggled to converge. It was concluded that the streamfunction for the perturbation cannot be used in the case of the three-dimensional swept flow.

A different approach needs, therefore, to be found. In particular, the main difficulty of this problem is that the disturbances do not go to zero at infinity, but an appropriate shooting condition has to be found for the vorticity. It must also specify that for the swept case it is important to use the viscous mean flow, since it would introduce a vorticity at the wall oriented in the same direction of the perturbation.

In addition, it would be interesting to look at the eventual change also on the thermal boundary layer and probably, since the experiment has observed an influence of the spectra in the frequency domain, the equations should be solved considering the time-dependent part.

Chapter 6

Discussion and conclusion

6.1 Main objective

The objective of the research was to examine the behaviour of the flow on the attachment-line of a swept body and to observe whether the oncoming freestream turbulence increases approaching the boundary layer on the attachment-line. The motivation was that an eventual amplification may have a role in the receptivity of the cross-flow instability to the freestream turbulence.

An extensive review of the literature on the freestream turbulence interacting with a stagnation point flow, and on the swept attachment-line flow, revealed that an approach similar to the vorticity amplification theory had not been developed for swept flows yet. In addition, it was found that experiments looking at the increase of the velocity fluctuations approaching a swept attachment-line were not available.

6.2 Experimental methods and apparatus

Two experimental investigations were carried out on two different models in two different wind tunnels using two different experimental techniques. The first investigation was carried out on a swept vertical flat plate in the Gaster wind tunnel employing a single hot-wire anemometer, the second investigation

on a circular cylinder in the T2 wind tunnel using a multi-component laser Doppler anemometer.

A major task was the setup of the Gaster wind tunnel. It involved the development of an acquisition system capable of controlling the wind tunnel speed, while recording simultaneously a large amount of data from different sensors (Pitot, thermocouple, hot-wire), and of carrying out automated measurements over a large area. This was realised with some colleagues using the LabVIEW software.

The multi-component LDA system, used in the T2 wind tunnel, was brand new and therefore required setting up so as to obtain reliable three-component measurements. Briefly, the process involved: the development of a methodology for the alignment of the laser, the choice of the data acquisition criteria for the specific flow under investigation and for the specific post-process analysis (i.e. frequency domain), the interpretation of the signal from each laser and the transformation into the desired coordinate system and, lastly, the different aspects of safety during the experiments.

For both the wind tunnel experiments, a specific post-processing of the data was accomplished through MATLAB. Each experimental technique required a different post-process analysis.

6.3 Experiments on a vertical swept flat plate

The design

The design of the model had to make it suitable for investigating the vorticity amplification near the attachment-line and, possibly, also the cross-flow excitation.

Models referred to in the literature, used to study these two phenomena, were analysed. A vertical flat plate with a faring body was chosen. The design entailed the use of different software taking into account the constraint due to the wind tunnel and to the adopted experimental technique.

Attachment-line contamination

In the swept-back configuration the model was unexpectedly found to suffer from attachment-line contamination even at low speed. The issue was overcome by designing an anti-contamination device, which made the attachment-line laminar up to the highest speed that could be achieved in the wind tunnel.

Experiments in a low turbulence environment

The flow on the attachment-line was measured using a single hot-wire anemometer placed parallel to the leading edge surface. The mean flow on the attachment-line was found to be in agreement with the Falkner-Skan-Cooke solution. In the low turbulence Gaster wind tunnel, without introducing external disturbances, the velocity fluctuations did not amplify from the freestream approaching the boundary layer at the attachment-line and were attenuated within the boundary layer.

Experiments with external disturbances

External disturbances were introduced by placing a string ahead of the model in various configurations. The experiments demonstrated that the technique generated a localised disturbance when the string was vertically oriented and a spanwise distributed disturbance when it was horizontally oriented. It was shown that the localised disturbance (vertical string) does not interact with the boundary layer at the attachment-line, since it travels along the streamlines. The horizontal string was able to trigger the turbulent boundary layer on the attachment-line.

A further attempt to increase the freestream turbulence level was carried out by introducing a turbulence generating grid. The grid was made of parallel rods and it was mounted either horizontally or vertically to induce freestream disturbances with different preferential directions. In both cases, the boundary layer was found to be turbulent at the attachment-line. The fluctuations amplify approaching the attachment-line reaching a maximum within the turbulent boundary layer. No substantial differences were observed between the

two orientations of the grid.

Cross-flow instability

The model was also tested to check the presence of the cross-flow instability modes. They were not observed, as had predicted by the design, probably because the oncoming stream was very low turbulent.

6.4 Experiments on the circular cylinder

The second experiment was carried out to analyse the effect of the sweep angle on the vorticity amplification theory. This was achieved with a cylinder mounted at different sweep angles.

Unswept cylinder

The results found on the unswept cylinder were compared to those of similar experiments referred in the literature. In addition, the adopted measurement technique, the multi-component LDA, allowed information in the time domain and hence in the frequency domain of the three velocity components simultaneously revealing new details of the phenomenon. In particular, the mean flow was found to be in agreement with the theoretical models of the flow approaching a stagnation point (potential flow, Hiemenz flow, Falkner-Skan boundary layer). In addition, an increase of the spanwise velocity fluctuations at the stagnation point boundary layer was observed, while the streamwise velocity fluctuations decreased. The phenomenon was found to be related to frequencies below 30 Hz in agreement with previous hot-wire investigations.

Swept cylinder

Four configurations of sweep angles were studied: 5°, 10°, 20°, 30°. The comparison of the results of flow at the attachment-line at different sweep angle with the flow at the stagnation point of the unswept cylinder addresses the answer to the main question of the thesis.

For all the sweep configurations the mean flow was found to be in agreement with the theories, as for the unswept configuration. The velocity fluctuations showed analogies with the unswept case for all the sweep configurations. The spanwise velocity fluctuations increased from the freestream towards the attachment-line boundary layer, at the same rate, up to a maximum. Inside the boundary layer, the spanwise fluctuations decreased for all the sweep angles except for the case at 30°, for which the spanwise fluctuations kept increasing approaching the wall. That increment was related to frequencies in the range around 80 Hz, while the amplification in the unswept case was related to frequencies below 30 Hz. The range of frequencies around 80 Hz appeared to be slightly amplified at lower sweep angles.

6.5 Conclusion

The research has identified that the freestream turbulence amplification approaching the swept attachment-line flow is a topic which has not been widely investigated. The first set of experiments has looked at a model with fixed sweep angle and variable freestream disturbances; while the second set of experiments has focused on the effect of the sweep angle with an unchanged, higher-Tu environment. Both investigations represent a new contribution to the body of knowledge since comparable research was not found in the literature.

Overall, this study has shown that in a low turbulence environment the velocity fluctuations remain constant up to the boundary layer edge, but then decrease approaching the wall. Whereas, in an environment with a higher level of turbulence, the velocity fluctuations increase as the boundary layer is approached both for the laminar and turbulent case. This indicates that nonlinear processes are involved. It was found, as well, that the attachment-line flow behaves differently if subjected to a localised or a distributed turbulence, suggesting that two-dimensional theory is not easily applicable to the swept case.

In addition, the flow at the stagnation point of a straight cylinder, which

was used as a reference case, has been investigated adopting multi-component LDA. The use of this technique has showed new details of the phenomenon. Overall, the study has revealed the much greater complexity of the phenomenon both for the swept flow and for the basic behaviour of the impinging turbulence. The large number of new or unexpected results has made it difficult to formulate a conceptual model to explain these phenomena, and simple numerical analogies have also proven difficult to apply to the swept flow.

6.5.1 Suggestions for further work

The phenomena needs further experimental and numerical investigations. They are necessary to deeply understand the effect of the turbulence on the attachment-line flow.

Experimental investigations

With reference to the model, it would be convenient to have a model with variable sweep angle. In particular, it would be interesting to investigate the trend between 20° and 30° for a cylinder and to observe the effect of higher sweep angles.
In order to change the turbulence level in the flow different grids should be used, with parallel rods in different orientations to create turbulence with a preferential direction. In addition, the grids should have different distances between the rods and different rod diameters to compare the effect of different levels of turbulence intensity-scale.
With reference to the measurement technique, the LDA was found to be a valuable tool for the investigation of the flow in a narrow region with high resolution obtaining the three velocity components simultaneously.
The LDA could be accompanied by PIV (Particles Imagine Velocimetry), with a resolution compatible to the boundary layer thickness on the attachment-line, to reveal information on the vorticity. This would help our understanding of whether the increment in the velocity fluctuations is due to the vorticity amplification mechanism.

Theoretical investigations

The literature review revealed that an approach similar to the vorticity amplification theory on a swept model has not been developed yet. Some theoretical considerations have been presented highlighting the difficulties of applying the vorticity amplification theory to a swept model. An alternative method has been used to show the differences between the swept and unswept case in the far field. Nevertheless, the experimental findings presented here open an interesting perspective for mathematical modelling.

Appendices

Appendix A

Cross-flow Reynolds number

Let consider the viscous swept Hiemenz flow as solution of the Falkner-Skan-Cooke equations reported in Chapter 2:

$$\begin{cases} u = af'(\eta)x \\ v = -\sqrt{a\nu}f(\eta) \\ w = W_\infty g(\eta) \end{cases} \tag{A.1}$$

According to Poll (1978), the cross-flow velocity profile (c_ϵ) and the streamwise velocity profile (s_ϵ) at each chordwise location are:

$$\begin{cases} s_\epsilon = w\, cos(\theta - \epsilon) + u\, sin(\theta - \epsilon) \\ c_\epsilon = w\, cos(\theta - \epsilon) - u\, sin(\theta - \epsilon) \end{cases} \tag{A.2}$$

where θ is the streamlines angle and ϵ the cross-flow direction. By substituting the Falkner-Skan-Cooke solution, and considering θ being defined by the potential velocity components ($tan(\theta) = W_\infty/U_e$), it is obtained:

$$c_\epsilon = W_\infty\, cos(\theta - \epsilon)\left(g(\eta) - f'(\eta)\frac{tan(\theta - \epsilon)}{tan(\theta)}\right) \tag{A.3}$$

The cross-flow velocity has been derived to be substituted in the definition of the cross-flow Reynolds number (Poll, 1978), which has been used in Chap-

ter 5:

$$\chi = \frac{|c_{\epsilon max}|\, \delta_{1\% c_{\epsilon max}}}{\nu} \tag{A.4}$$

According to Poll (1978), $|c_{\epsilon max}|$ is the maximum of the cross-flow velocity profile and $\delta_{1\% c_{\epsilon max}}$ is the minimum height at which the velocity assumes 1% of its value for $\epsilon = 0$. Figure A.1 shows the cross-flow velocity profile for $\epsilon = 0$, where $c_{\epsilon max} = -0.240 W_\infty (U_e/Q_e)$ and $\delta_{1\% c_{\epsilon max}} = 3.490\sqrt{\frac{\nu}{a}}$. It results that:

$$\chi = 0.838\, \frac{W_\infty}{Q_e} \sqrt{\frac{U_e\, x}{\nu}}. \tag{A.5}$$

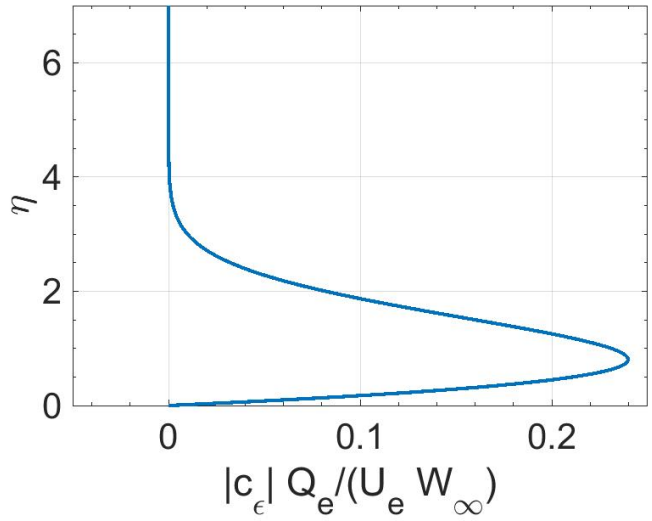


Figure A.1: Cross-flow velocity profile for $\epsilon = 0$.

At an height along x, far from the attachment-line, it can be considered $Q_e = \sqrt{U_e^2 + W_e^2}$, where $U_e = ax$ and $W_e = W_\infty$. By substituting in the equation A.5, after some manipulations, it is obtained:

$$\chi = 0.838 \sqrt{\frac{Q_\infty cos(\Lambda)\, x^2 t}{(x^2\, tan(\Lambda)^{-2} + t^2)\nu}} \tag{A.6}$$

Appendix B

Hot-wire anemometer

B.1 Working principle

The hot-wire anemometer is a widely used instrument for flow velocity measurements, relatively cheap and easy to setup and use. In particular, it provides a high spatial and temporal resolution with a high frequency response. On the other hand, it is an intrusive technique since the sensor has to be placed in the flow field.

The sensor consists of an thin conductive wire, usually made of Tugsten or Nickel. The wire is soldered or welded on two metallic prongs connected to an electronic circuit.

The hot-wire measurements are based on convective heat transfer. When a current is induced through the wire (I_w), the latter increases its temperature by the Joule effect of an amount ($I_w^2 R_w$) proportional to the current and to the wire resistance (R_w). The hot-wire transfers heat by convection, conductivity and radiation, but it can be shown that when the sensor is in the stream, the heat transfer due to conductivity and radiation is much less than that due to convection (Bruun, 1996). Therefore, it can be concluded that:

$$I_w^2 \, R_w = Q_{conv} \tag{B.1}$$

where Q_{conv} is the heat released to the fluid by convection. To convert the measured voltage (E) to flow velocity the King's law can be derived (Jørgensen,

2005):

$$E^2 = A + B\,U^n \tag{B.2}$$

that is used to convert the measured voltage to the velocity of the flow itself. The coefficients A and B depend on the properties of the hot-wire and of the fluid.

King's law is also used to convert the voltage fluctuations (e') into velocity fluctuations (u'). In particular, if the measured voltage signal is $e = \overline{E} + e'$ and the velocity signal is $u = \overline{U} + u'$:

$$u' = \frac{2\bar{E}}{B\,n\overline{U}^{n-1}}\,e' \tag{B.3}$$

The hot-wire can operate in two modes, Constant Current (CCA) or Constant Temperature (CTA). In the first mode the current through the sensor is maintained constant, while in the second mode the sensor temperature is kept constant. In the experiments in Chapter 5 the hot-wire has been used always in the CTA mode since it is easier to setup, while maintaining a high frequency response and a low noise.

B.2 Hot-wire setup

The sensor is connected to the Dantec DISA 55M01 unit, which contains the Wheastone bridge. The output of the DISA, which is the hot-wire raw voltage signal, is sent to the National Instrument Data Acquisition (NI DAQ) through which it is stored in the computer. The raw hot-wire signal is also sent to a band-passed filter. The filtered hot-wire signal is then sent to the NI DAQ and stored as well. Both the filtered and unfiltered signals are displayed on an oscilloscope during the experiment.

In the experiments in Chapter 5 a Tungsten single wire has been used with a diameter of $5\mu m$ and length of 1.25mm.

At the beginning of each experiment, the following procedures to setup the instrumentation have to be carried out.

Resistance setting

Considering that the resistance of the wire is function of its temperature, it is important to define the working temperature of the sensor T_0, corresponding to the reference resistance R_0. When the wire is warmed up to a generic temperature T_w, the resulting resistance R_w is:

$$R_w = R_0 \left[1 + \alpha_0 \left(T_w - T_0\right)\right] \tag{B.4}$$

where α_0 is the sensor temperature coefficient at T_0. The ratio between the resistance of the wire at T_w and the resistance at the reference temperature defines the overheat ratio OHR:

$$OHR = \frac{R_w}{R_0} = 1 + \alpha_0 (T_w - T_0) \tag{B.5}$$

The OHR is a non-dimensional parameter that quantifies how much the wire resistance would rise. The overheat ratio was usually set at 1.5.

Gain setting

The gain of the amplifier in the Wheatstone bridge circuit is set by carrying out a frequency response test, commonly called *square wave test*. The test has to be carried out at the maximum velocity of the planned experiment. From the DISA unit a square wave is sent to the bridge, which simulates an instantaneous change in velocity. The CTA output is connected to an oscilloscope, which allows analysing the shape of the output. The aim of the test is to optimize the bandwidth of the circuit, by setting a gain to the amplifier such that it operates stable with sufficiently high bandwidth for the specific application. The gain can be changed by turning a knob on the DISA, until an output signal as shown in figure B.1 is obtained.

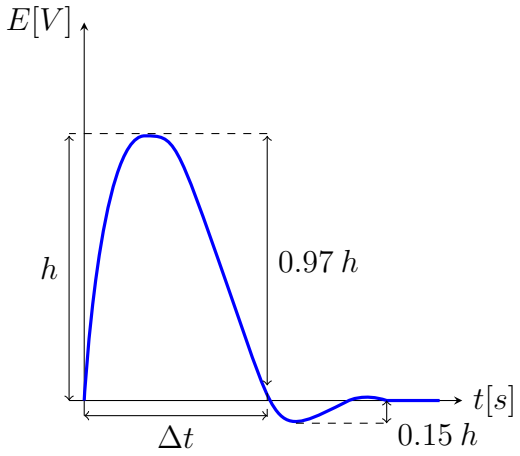


Figure B.1: Desired hot-wire voltage (E), as function of time (t), during the square wave test(Jørgensen, 2005).

The response has to be smooth without "ringing" either at the top or at the zero line. The gain is changed until the response curve gets a 15% undershoot (Jørgensen, 2005). Then Δt can be read on the oscilloscope and the bandwidth of the probe/anemometer system, which is defined as the frequency at which the fluctuation amplitude is damped by a factor 2 (-3 dB limit), can be calculated:

$$f_c = \frac{1}{1.3\Delta t} \tag{B.6}$$

that is also called the cut-off frequency.

B.3 Calibration

The aim of the calibration is to determine the coefficient A, B and n in the King's law (see equation B.2).

The hot-wire is positioned close to the Pitot tube in the freestream so that the two sensors measure a similar velocity without interfering. The software to carry out the calibration, developed in LabVIEW, changes the speed of the wind tunnel from $2\,m/s$ up to $18m/s$ in steps of $2\,m/s$. Every time the speed is changed, the code allows $30\,s$ to the flow to set steadily, before acquiring the hot-wire voltage (E) and the Pitot velocity (U) simultaneously. The calibration coefficients are found looking for the best linear interpolation of $\overline{E}^2$ as function of $\overline{U}^n$ by varying the n coefficient between 0.2 and 1.12 by an incre-

ment of 0.01 (where the overline indicates the mean values, averaged from the time signal). The best value for n was chosen such that it minimises the error $R = \sqrt{\sum_{i=1}^{N}(\overline{E_i} - E_i)^2}$. Once n is chosen, the corresponding coefficient A and B were defined by the linear fitting. The values of n during the experiments have been found to be always between 0.3 and 0.45.

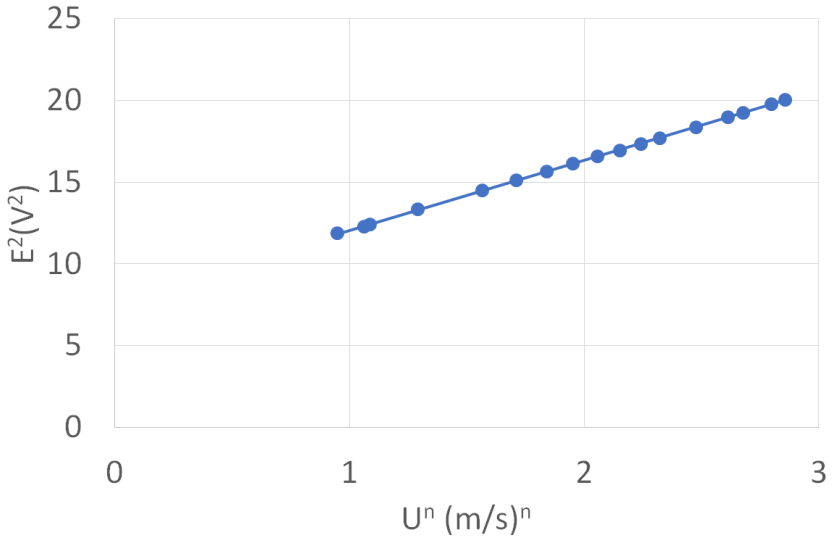


Figure B.2: Hot-wire calibration, example of King's law.

B.4 Data acquisition

The sampling frequency (f_s) is chosen depending on the higher frequency (f_{max}) in the flow, according to the *Shannon theorem*:

$$f_s = 2\, f_{max}.$$

The hot-wire is also connected to a band passed filter, so that both the raw and the filtered signals are acquired. The low-pass filtering is used to remove noise, but also as anti-aliasing filter preventing higher frequencies from folding back into lower ones. The high pass filter cuts off the low frequencies and, in particular, the DC part of the signal (corresponding to the 0 Hz). The low pass frequency is chosen based on the maximum f_{MAX}.

In the experiment in Chapter 3, a band pass filter between 2 Hz and 10 kHz

has been used. The filtered signal has also been amplified with a gain of $20\,dB$.

B.5 Data analysis

Temperature corrections

The room temperature was found to vary around $\pm 1°$ during the experiments, in same extreme cases up to $\pm 3°$. These temperature fluctuations create an error to the voltage-velocity conversion. In fact, the latter conversion is based on the calibration coefficients which are defined from data at a specific temperature (T_{cal}). To minimise this error, the ambient temperature was measured simultaneously with the hot-wire for the whole duration of the experiment. The hot-wire voltage has been corrected considering the recorded ambient temperature (T_A) according to:

$$E_{corr} = E \sqrt{\frac{T_w - T_{cal}}{T_w - T_a}} \tag{B.7}$$

where E_{corr} is the voltage after the correction, E is the measured voltage, T_{cal} is the calibration temperature, T_a is the ambient temperature and T_w is the wire temperature, which has been calculated by combine equations B.4 and B.5.

Time domain

After having applied the temperature corrections the unfiltered and filtered data are converted into velocity by applying equations B.2 and B.3. The unfiltered data are used to calculate the mean velocity (U), while the filtered data are used to calculate the Root Mean Square (RMS) of the fluctuating velocity.

Frequency domain

To analyse the signal in the frequency domain, the filtered signal, of sampling period T, is divided in B blocks of equal time Δt_B. For each block a Fast Fourier Transform (FFT) algorithm is applied to calculate the Power Spectra Density (PSD) of each block ($S_b^*(f)$). The number of samples per block determines the frequency resolution Δf.

To prevent leakage errors the signal in each block is firstly multiplied by the

Hann window:

$$H_w(t) = \begin{cases} \frac{1}{2}\left(1 - cos\frac{2\pi t}{T}\right) & for \quad 0 \leq t \leq T \\ 0 & otherwise. \end{cases} \tag{B.8}$$

Therefore the PSD for each block is:

$$S_b^*(f) = \left[2\, FFT(H_w(t)\, u(t))\right]^2. \tag{B.9}$$

The PSDs $S_b^*(f)$ of each block are averaged to get a clean PSD of the whole signal ($S^*(f)$):

$$S^*(f) = \frac{1}{B} \sum_1^B S_b^*(f)$$

The PSD has been normalised to be directly related to the RMS. Therefore, the PSD has to verify the Parseval theorem for each block:

$$\sum_{i=0}^{N} u'^2(t_i) = \sum_{f=0}^{f_{max}} S^*(f) \frac{\gamma_H\, B}{N_B},$$

where γ_H is the window factor equal to 8/3 for the Hann window (Bendat and Piersol, 2011), N_B is the number of the sample in each of the B blocks. Finally, the relation between the RMS and the PSD is:

$$u' = \sqrt{\frac{1}{N} \sum_i (u_i - U)^2} = \sqrt{\sum_j S^*(f_j) \frac{\gamma_H\, B}{N_B\, N}},$$

where N is the total number of samples.

Appendix C

Laser Doppler anemometer

C.1 Working principle

The Laser Doppler Anemometer (LDA), also called Laser Doppler Velocimetry (LDV), is a non-contact optical instrument for fluid flow investigations. The system, developed in the early sixties, measures the flow velocity based on light scattered from small inhomogeneities in the flow or from seeding tracer particles.

The system has some practical advantages, i.e. does not need calibration, but overall it is quite complicated; in particular, it needs a careful alignment of the beams to get reliable data and particles to be seeded in the flow for experimental investigation in wind tunnels (Tropea and Yarin, 2007).

The technique is based on the Doppler effect, which describes the change in frequency or wavelength for an observer who is moving relatively to the wave source. The wave source is the laser which is reflected by the intercepted moving particle.

An overview of the LDA system is shown in figure C.1. The laser beams travel through a Bragg cell, a component that splits the laser in two beams giving a small frequency shift to one of the beam. That shift causes the interference fringes to move, thus define the flow direction (Albrecht et al., 2013).

The two laser beams go to the transmitting optics and passing through the focal lens cross inside the wind tunnel intersecting each other to create a mea-

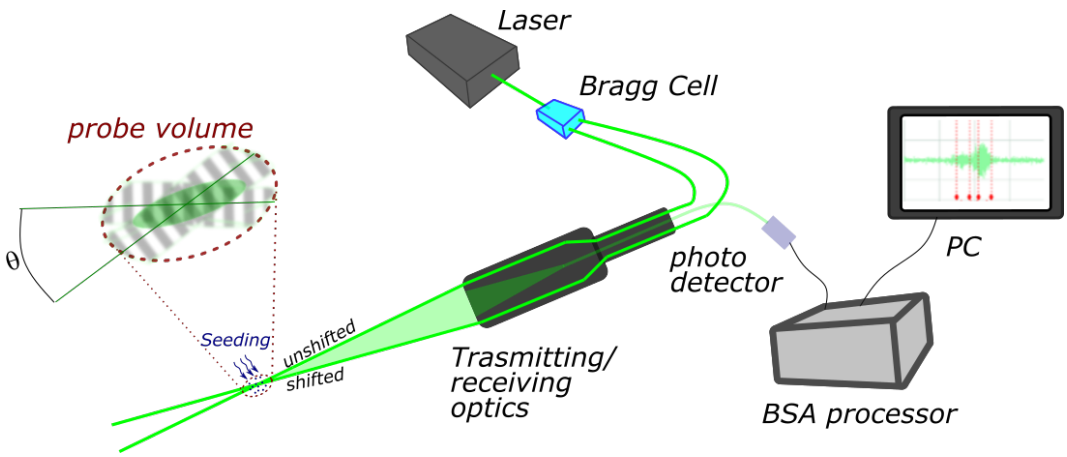


Figure C.1: Overview of LDA setup in back scatter configuration.

surement region. When the seeding particle passes through the probe volume the light is reflected to the receiver.

The system can work in two configurations, forward or back scatter, depending on the position of the receiver with respect to the transmitting optics. The wind tunnel, adopted for the experimental investigations refereed in Chapter 4, allows only the back scatter configuration since its width is too large respect to the focal length. In this configuration the transmitting and the receiving optics are in the same component (figure C.1).

From the receiving optics the laser goes to a photo detector. The output of the photo detector is a current signal, which appears like a burst when a particle passing through the probe volume scatters a light. The signal is filtered and analysed by the BSA processor and sent to a pc, acquired by the BSA flow software. The whole LDA system used at City, University of London, including the optic components, the BSA processor and the software are provided by the Dantec Dynamic.

C.2 Multi-component velocity measurements

The LDA system does not interfere with the flow, since only the laser beams enter in the wind tunnel. This advantage makes the system suitable for multi-component measurements using more than one laser. Depending on the aim

of the experimental investigation, multiple laser can be employed with different setups. To obtain three spatial velocity components in each measurement point, three laser have to be used.

The system used for the experiments, reported in Chapter 4, consists of two optics groups: the first is connected to two laser, the second to a single laser (figure C.3). The first emits two pair of laser beams of different wavelength (one green $\lambda_{LDA1} = 514.2nm$ and one blue $\lambda_{LDA2} = 488nm$) enabling the instrument to measure two perpendicular velocity components, the second emits one pair with a still different wavelength (green $\lambda_{LDA3} = 532.3nm$) and provide the third velocity component.

Each optic is connected to one photo detector with filters to select the different wavelengths. Each pair of laser beams measures a velocity component lying on the same plane of the two laser beams themselves. The planes defined by the three different couple of laser beams are defined during the alignment procedure. Actually, the three planes are not orthogonal, but a transformation matrix allows one to derive the orthogonal velocity components referenced to the wind tunnel coordinate system, as explained below.

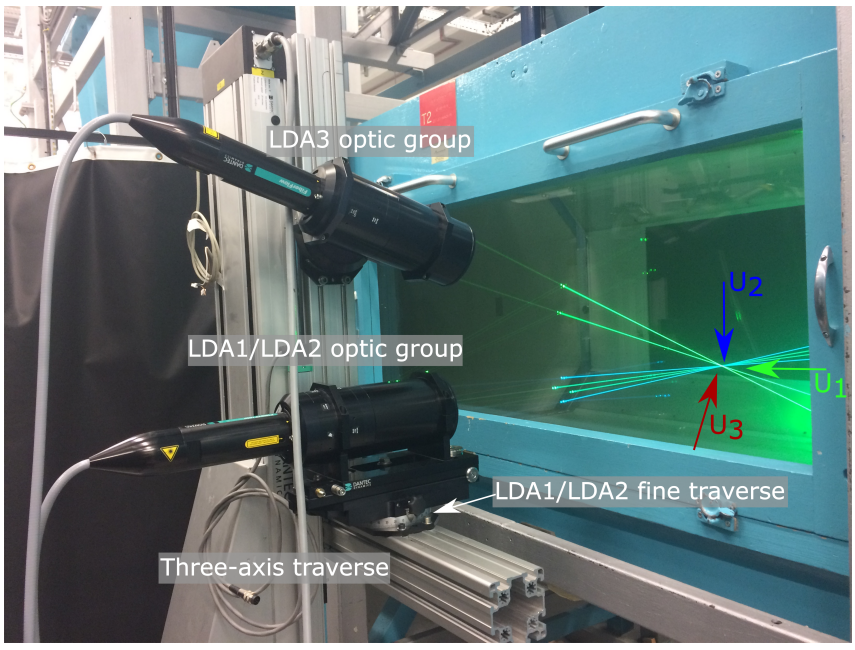


Figure C.2: Three-component LDA optic groups mounted on the three-axis traverse.

Information regarding the beam dimensions, the probe volume, the frequency

shift and other characteristic of the optical LDA systems are reported in table C.1.

Property		**LDA1**	**LDA2**	**LDA3**
Wavelength	$[nm]$	514.5	488	532
Focal length	$[mm]$	800	800	800
Beam diameter	$[mm]$	2.2	2.2	2.2
Beam expander ratio		1.95	1.95	1.95
Beam spacing	$[mm]$	37	37	38
Frequency shift	$[MHz]$	40	40	40
Number of fringes		21	21	21
Beam angle	$[^\circ]$	2.78	2.78	2.78
Probe volume d_x	[mm]	0.12	0.12	0.13
Probe volume d_y	[mm]	0.12	0.12	0.13
Probe volume d_z	[mm]	2.60	2.39	2.60

Table C.1: Three-component LDA characteristics.

C.3 Laser beams setup

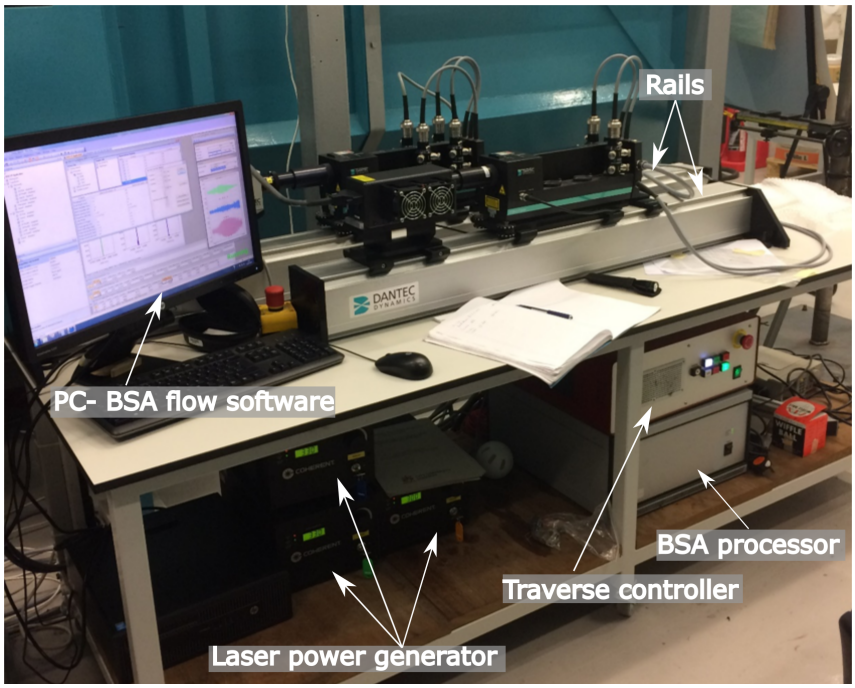
The LDA does not require calibration, but the alignment of the laser beams must be carefully carried out. It is usually done only once, before starting the experiment, however in same cases it may be necessary to repeat the alignment procedure since the system is subjected to thermal effect, which may cause misalignment.

In the following, the beams alignment procedure is explained for the case of three-component LDA in back scatter configuration.

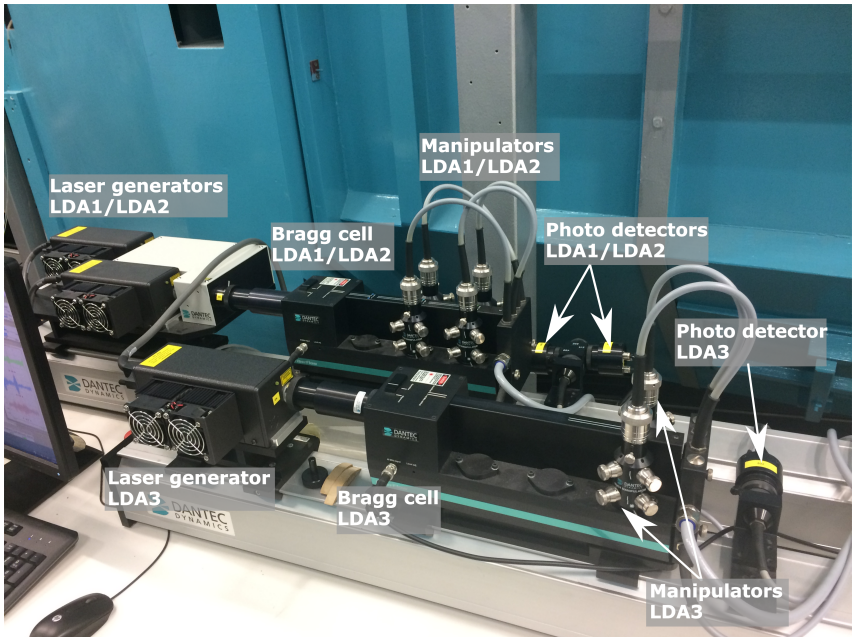
The optics groups in figure C.1are connected to the apparatus shown in figure C.3. In particular, the figure shows the three laser power generators on bottom left, the traverse controller on the bottom right, on top of the BSA processor, the two rail systems and a pc.

The laser power generators regulate the laser intensity. The rail system supports the photo detector, the laser generator and the Bragg cell together with the manipulators. The role of the manipulators is to centre and direct the laser beams to the fibre optics cable which are connected to the optics groups.

The components on the rails must be aligned to allow the laser beams flowing freely through them, procedure normally done once with the installation of the system.



(a)



(b)

Figure C.3: Three-component LDA optic groups mounted on the three-axis traverse: a) overall view, b) rails.

Power losses

During the alignment procedure of the laser beams it is important to minimise the power losses.

The routine procedure uses a sensor, placed at the focal point of the laser beams, connected to a power meter. The power meter displays the power measured at the focal point, which differs from the power set on the power generator. The difference between the two values corresponds to the global power losses of the system. Once the laser power is set at a specific value, the losses can be reduced by regulating the five knobs located on the manipulators. This has to be done for each laser beam individually. In the multi-component measurements the power losses at the focal point should be approximately the same for each laser beam.

Normally, the losses through the whole system are around 80%, including those due to the wind tunnel window. For example, for one laser beam powered with 200 mW on the power generator, a power measured at the focal point is about 35 mW. The higher the power is at the focal point the better is the reflection and the data rate, which will be discussed in the following section, so that the reduction of the power losses is an extremely important procedure.

Alignment procedure

Once the power losses are minimised, each pair of laser beams must be focused in the same point.

A high resolution camera is placed at a distance equivalent to the focal length and connected to the computer. To find the focal point, a light is shone through the receiving fibre cable (Step1 figure C.4). The optics mounted on the traverse are moved towards the wind tunnel until the light source, captured by the camera and visualised on the screen of the pc, becomes a clear white rounded dot. The position of the focal point is marked on the screen; from this moment the camera, the optics and the traverse must not be moved. Once the light has been removed; each individual beam, one at a time, is shone through the optics, captured on the camera and displayed on the pc. To bring each beam

on the focal point, the prisms inside the optics have to be adjusted through tiny screws on the optic group (Step2 figure C.4).

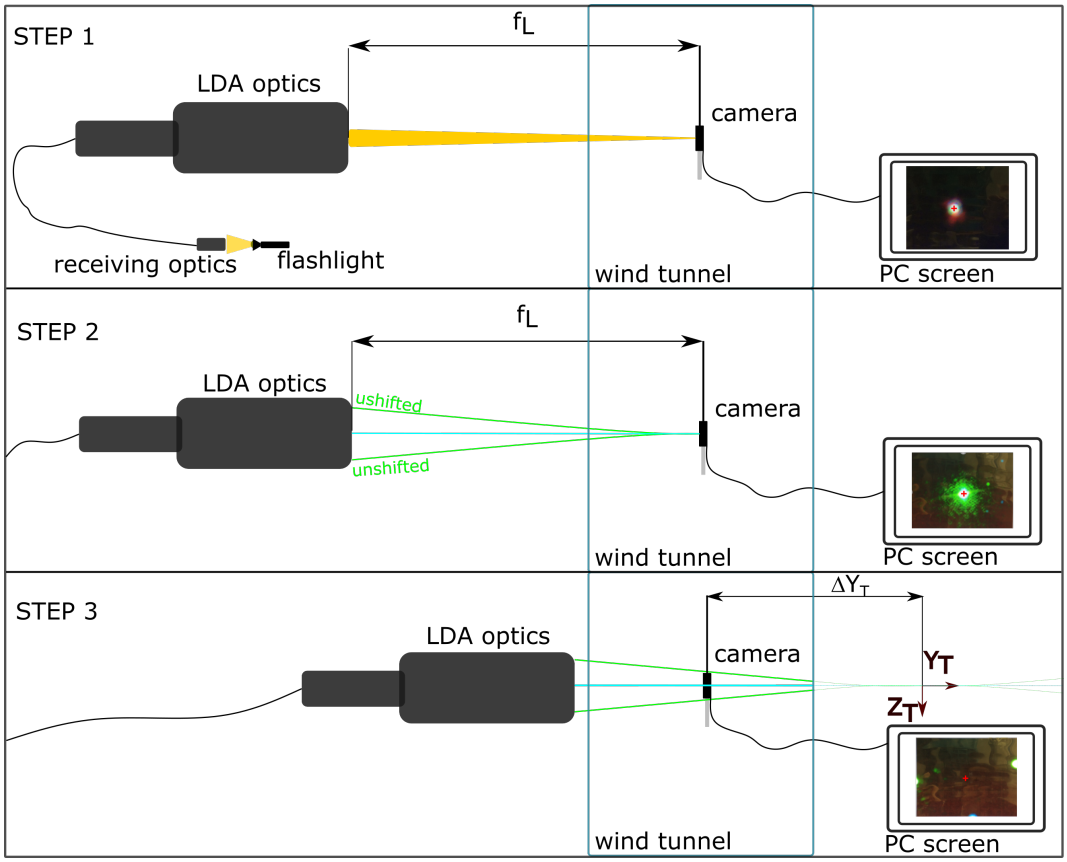


Figure C.4: Sketch of LDA Alignment procedure, components not in scale.

The alignment procedures for one optic group in back scatter configuration ends here, also if it is connected to multi laser. In case of two optic groups working together, i.e. when the three velocity components are measured at the same point, the alignment procedure continues to align the six laser beams to the same focal point. This is done through a manual traverse for fine adjustment, installed on one of the two optics group (see figure C.3).

Measure of the orientation

Coming back to the case of multi-component measurements, it is important to determine the direction of the velocity component measured by each laser, that can be derived from the exact orientation of each beam.

Each pair of beams measures the velocity component on which they are lying

with positive direction from the not-shifted beam to the shifted one. Here, an indirect method has been used to identify the orientations and to derive the *transformation matrix* which transforms the not-orthogonal velocity components in the orthogonal coordinate system.

The high resolution camera, already used for the alignment procedure, is placed at the focal point, where the six beams cross together (Step 2 figure C.4). This point is set as the origin of the coordinate and it is marked on the screen of the computer.

Moving the traverse perpendicularly to the camera by a fixed distance, ΔY_T, the laser beams are not crossing in the origin any more (Step 3 figure C.4). By moving again the traverse, this time in the $X_T - Z_T$ plane, parallel to the camera, the new position of each beam may be visualised on the screen and its distance (X_T,Y_T,Z_T) from the origin of the coordinate may be measured. This distance for each beam identifies its position in the space. An example is reported in table C.2, for three laser LDA_1, LDA_2, LDA_3, identified respectively as G, B, V both for the shifted or unshifted laser beam.

Laser	Beam	X_T [mm]	Y_T [mm]	Z_T [mm]
G	shifted	+10.80	-220.00	-3.85
	unshifted	-7.00	-220.00	6.75
B	shifted	+7.15	-220.00	10.05
	unshifted	-3.10	-220.00	-7.35
V	shifted	-5.80	-220.00	-84.41
	unshifted	-6.00	-220.00	-64.81

Table C.2: Example of wind tunnel coordinate to find the laser beams orientation

Each pair of laser beams identify a vector, that for the case of $\overrightarrow{G}$ is:

$$\overrightarrow{G} = \frac{\vec{G}_{sh}}{|G|_{sh}} - \frac{\vec{G}_{unsh}}{|G|_{unsh}}$$

and the corresponding unity vector is:

$$\widehat{G} = \frac{\overrightarrow{G}}{|G|} \tag{C.1}$$

where $\widehat{\ }$ indicates the unity vector and $|\ \ |$ the intensity of the vector. The

same procedure has to be done for the laser $\overrightarrow{B}$ and $\overrightarrow{V}$, in order to get the transformation matrix:

$$T = inv \begin{bmatrix} \widehat{G} \\ \widehat{B} \\ \widehat{V} \end{bmatrix} \tag{C.2}$$

Being U_1, U_2, U_3 the velocity components, measured by the three laser beams pairs, the corresponding components refereed to the wind tunnel coordinate system (U_x, U_y, U_z) are (figure C.5):

$$\begin{bmatrix} U_x \\ U_y \\ U_z \end{bmatrix} = T \begin{bmatrix} U_1 \\ U_2 \\ U_3 \end{bmatrix} \tag{C.3}$$

Similar procedure is followed for the two-components measurements.

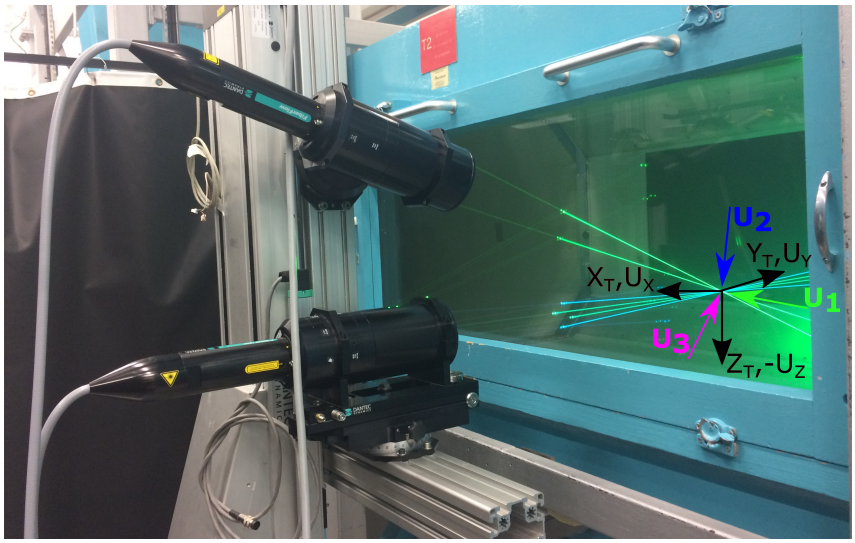


Figure C.5: LDA velocity coordinate systems. Flow right to left.

C.3.1 Data acquisition

For the acquisition of the data the maximum acquisition time and the maximum number of samples has to be set. Then, the software acquires data until either the maximum time or the maximum number of samples is obtained.

The *data rate* is defined as the number of particles acquired per second.
The user sets also the expected velocity and the span velocity based on the maximum fluctuations. A bar chart plotted through the software displays the distribution of the velocities of the intercepted particles. Ideally, the best would be one single bar, which would correspond to a regular flow in absence of noise or other disturbance sources.
The aim is to have data rate as high as possible combined with good validation. This would correspond to a clear burst in the signal with low noise.Further reading on the LDA settings can be found in Albrecht et al. (2013).
For the multi-component measurements, three different modes of acquisition are possible: coincidence, non-coincidence or semi-coincidence. In the first mode the velocity is recorded only if the particle is detected simultaneously by all the photo detectors. In this case, the three velocity signals contain the same number of samples at the same acquisition time. Whereas, the non-coincidence mode records the particles velocity independently for each laser beam. In this case, each signal has a different number of samples and different acquisition time. Finally, in the semi-coincidence mode, one signal is recorded independently, while the other two pair of laser beams is acquired in coincidence mode.
To obtain a good data rate in the coincidence mode the laser beams must be very well aligned; but even with an almost perfect alignment the probe volume created by the six laser beams is reduced with respect to the case of one-component measurement. Therefore in the coincidence mode the data rate is always lower.
The three acquired velocity signals can be transformed in perpendicular velocity components only if they are acquired simultaneously in coincidence mode.

C.4 Data analysis

The Dantec BSA Flow Software provides the data in velocity (m/s) for each laser beam pair. In this section the post-processing analysis followed for each

experimental case is shortly explained. The codes have been implemented in Matlab.

The LDA technique acquires the signal whenever the photo detector identifies a burst, which corresponds to a particle passing through the probe volume. The time between two appearances of the burst is random and therefore the LDA signal is randomly distributed in time, as shown in figure C.6. This intrinsic character influences the way the statistic moments and the spectra of the signal are evaluated.

Before proceeding with the temporal and spectral analysis, the code checks that all the data are within a tolerance of acceptance, defined as a multiple of the RMS. The check is necessary since sometimes big droplet of oil cross the probe volume, i.e. oil coalesced on the grid or on the wind tunnel walls may suddenly detach and be convected with the flow in the probe volume. Usually, in a 90 seconds signal only few points may be outside the range. An example is marked with a red circle in figure C.6. In those cases the code automatically ignores the data points during the analysis.

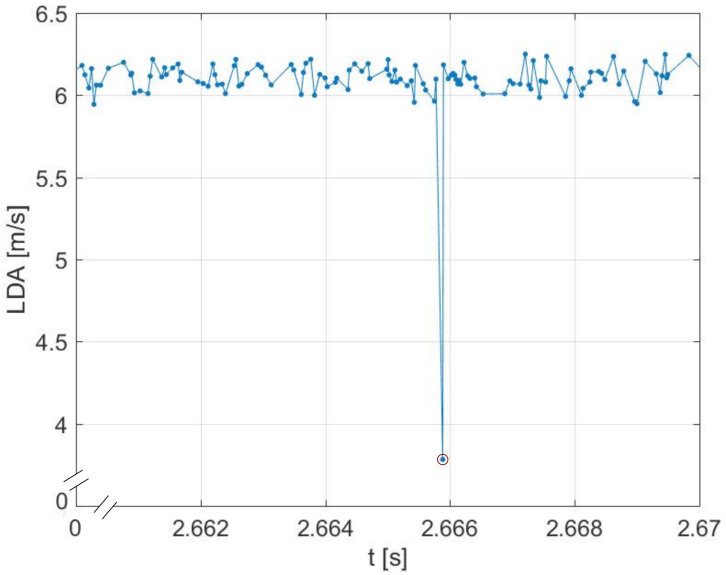


Figure C.6: Example of a LDA signal randomly distributed in time.

C.4.1 Time domain analysis

The time domain analysis is done through the statistic momentum:

- the mean representing the average value of the signal

$$U = \sum_{i=0}^{N} f_{w,i} \cdot u(t_i) \tag{C.4}$$

- the root mean square (RMS), the average distance of the fluctuations from the mean

$$U_{RMS} = \sqrt{\sum_{i=0}^{N} f_{w,i} \cdot (u(t_i) - U)^2} \tag{C.5}$$

- the skewness, describing if the distribution is skewed respect to the mean (i.e., it is 0 for Gaussian distribution, symmetrical about the mean)

$$U_{sk} = \frac{1}{U_{RMS}^3} \sum_{i=1}^{N} f_{w,i}(u(t_i) - U)^3 \tag{C.6}$$

- the kurtosis or flatness, describing if the distribution is wide and flat, or narrow and heigh (it would be 3 for a Gaussian distribution):

$$U_{ku} = \frac{1}{U_{RMS}^4} \sum_{i=1}^{N} f_{w,i}(u(t_i) - U)^4 \tag{C.7}$$

- a last estimator for the joint momentum is the covariance, that is related to two orthogonal velocities, it can be defined only if the particles are taken in coincidence mode:

$$\overline{u'w'} = \sum_{i=1}^{N} f_{w,i}(u(t_i) - U)(w(t_i) - W) \tag{C.8}$$

where $f_{w,i} = 1/N$ is the inverse of the number of points in the signal, if the arithmetical momentum are considered.

Generally, the seeded particles do not have the same diameter (around 1 μm), as well as their velocity may vary from particle to particle, especially in turbulent flows. Furthermore, the particles cross the laser probe volume with different orientations, some of them may cross the probe volume at its edge,

covering a shorter distance, while others cross the whole diameter (figure C.7). These, among others, lead to an error (called *velocity bias*) in the arithmetical statistic momentum not being representing of the flow characteristic since the velocity distribution of the particles is biased.

To ensure statistically independent samples, a weighting factor can be used. Among the different weighting factors suggested in the literature (Albrecht et al., 2013), a common one is the transit time (TT), defined as the time that a particle takes to cross the probe volume:

$$f_{w,i} = \frac{TT_i}{\sum_{i=0}^{N} TT_i} \tag{C.9}$$

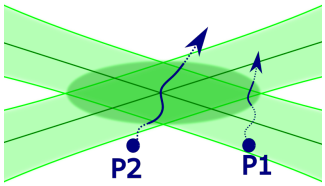


Figure C.7: Two particles crossing the probe volume with different trajectory.

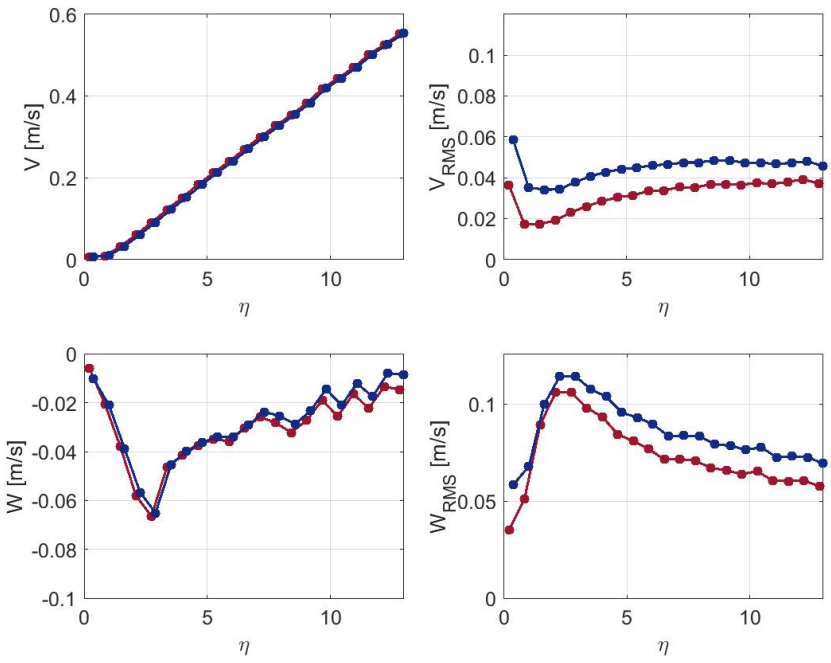


Figure C.8: Example of mean and RMS of the stagnation point flow on the unswept Cylinder: • arithmetical momentum, • weighted momentum (coordinate system according to figure 4.6).

As explained, the bias error is related more to the flow rather than to the optics, therefore, to verify the need of using the weighting factor for the ex-

periments reported in Chapter 4, the following analysis has been carried out. Figure C.8 shows the mean and RMS of the two velocity components (V, W according to the coordinate system in figure 4.6) for a typical boundary layer scan at the edge of the unswept cylinder, as reported in Chapter 4.

The measurements have been carried out in semi-coincidence mode, therefore the velocity measured at each time from LDA1 and LDA2 should correspond to the same particle crossing the probe volume at that time.

The two curves correspond to, respectively, the arithmetical statistic momentum and the weighted momentum according to equation C.9. The effect on the mean is practically irrelevant, while the differences on the RMS are quite heigh, overestimated by the arithmetical moment.

To further understand this error, the distributions of the two velocity components, for the fourth point, counting from $\eta = 0$ in the boundary layer scan of figure C.8, have been plotted as function of the number of particles (N) and as function of the transit time (TT) in figure C.9. For the same point the static momentum, with and without weighting factor, are also reported in table C.3. The same procedure has been carried out for one point in the freestream, 200 mm in front of the stagnation point of the cylinder. Table C.4 shows that for the last case the statistic momentum calculated with and without the weighting factor do not differ. The difference between the two signals is immediately clear comparing the data points distributions, as function of N and TT (figure C.10 and C.9).

Boundary layer fourth point							
V $[m/s]$	V_{RMS} $[m/s]$	V_{sk}	V_{ku}	W $[m/s]$	W_{RMS} $[m/s]$	W_{sk}	W_{ku}
0.0610	0.0343	-0.0460	7.5077	-0.0567	0.1143	-0.0483	3.5088
V_w $[m/s]$	$V_{RMS,w}$ $[m/s]$	$V_{sk,w}$	$V_{ku,w}$	W_w $[m/s]$	$W_{RMS,w}$ $[m/s]$	$W_{sk,w}$	$W_{ku,w}$
0.0602	0.0190	-0.0128	14.8849	-0.0573	0.1060	-0.0722	3.4478

Table C.3: Arithmetical and weighted momentum for the fourth point of the scan in figure C.8.

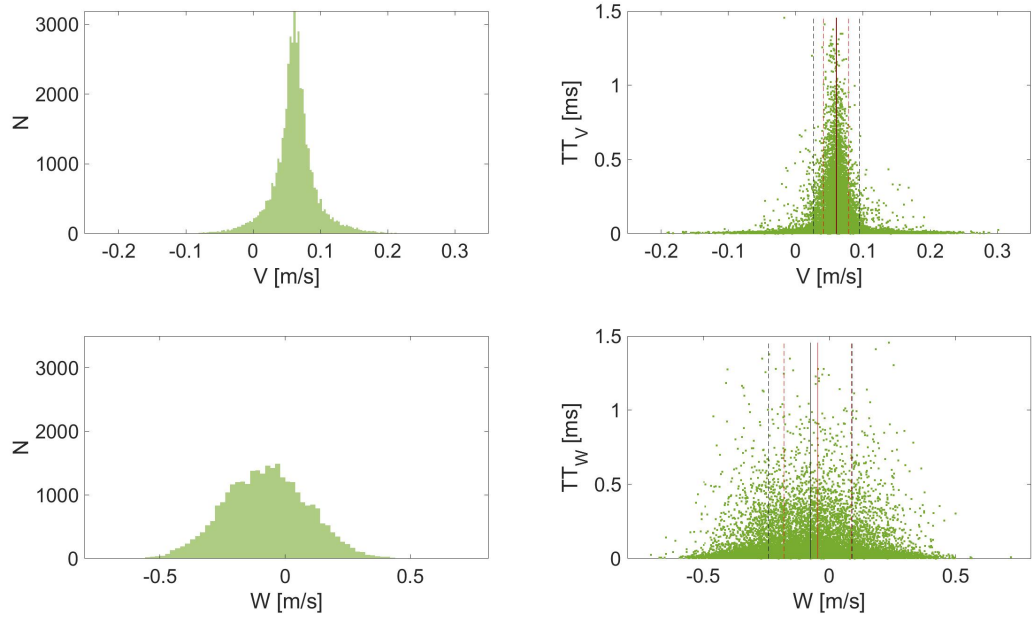


Figure C.9: Velocity distribution as function of the number of particles (N) and the transit time (TT) for the point in the boundary layer in table C.3. - weighted mean, - - weighted RMS, - arithmetical mean and - - atihmetical RMS.

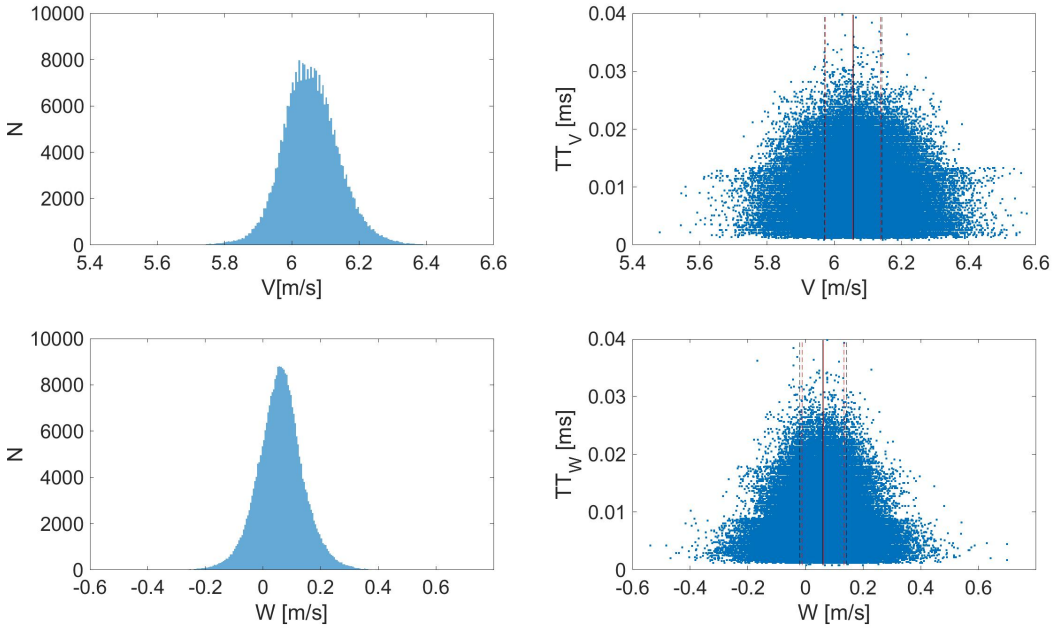


Figure C.10: Velocity distribution as function of the number of particles (N) and the transit time (TT) in the freestream. - weighted mean, - - weighted RMS, - arithmetical mean and - - atihmetical RMS.

Freestream measurements							
V $[m/s]$	V_{RMS} $[m/s]$	V_{sk}	V_{ku}	W $[m/s]$	W_{RMS} $[m/s]$	W_{sk}	W_{ku}
6.0566	0.0848	0.1852	3.9408	0.0607	0.0805	0.0159	4.1990
V_w $[m/s]$	$V_{RMS,w}$ $[m/s]$	$V_{sk,w}$	$V_{ku,w}$	W_w $[m/s]$	$W_{RMS,w}$ $[m/s]$	$W_{sk,w}$	$W_{ku,w}$
6.0566	0.0815	0.1848	3.9830	0.0611	0.0729	-0.0052	4.2283

Table C.4: Arithmetical and weighted momentum for a point at 200 mm from the cylinder stagnation point.

The freestream signal appears homogeneously distributed in the whole velocity range with narrow tales; while, the signal inside the boundary layer, and in particular the V-velocity component, shows a distribution gathered around the mean with long and disperse tales, whose influence the RMS, the Skewness and the Kurtosis.

The reason of this difference is to be sought in the type of flow under investigation, which quickly decelerates while approaching a wall at low velocity. Therefore, the data rate inside the boundary layer is intricately less respect to the freestream; the relative turbulence intensity ($T_V = V_{RMS}/V$, $T_W = W_{RMS}/W$) close to the wall is much higher respect to the freestream; the maximum time that particles take to cross the probe volume is obviously much longer compared to the freestream signal, since the flow is almost at rest and the velocity distribution is spread over a higher TT range, as shown in the figures.

From this study it can be concluded that, since the flow under investigation has a high level of turbulence and is quite slow, it is necessary to use the TT as weighting factor to correct for bias error. This has been adopted for the measurements discussed in Chapter 4.

C.4.2 Spectral analysis

The spectral analysis for the LDA signal cannot be evaluated applying directly a Fourier algorithm due to the random character of the signal itself, unless some manipulations are done beforehand.

Several methods have been proposed in literature, among which the slotting technique, developed by Gaster and Roberts (1975; 1977), has been chosen.

The slotting technique is based on the autocorrelation function $R_u(t,\tau)$, defined to study the periodicity of a random process:

$$R_u(t,\tau) = E[u(t) \cdot u(t+\tau)]$$

where $E[\ \ ]$ is an operator to indicate the expected or mean value. For a stationary process the autocorrelation is independent on the acquisition time (t) but depends only on the lag time (τ); furthermore $R_u(\tau) = R_u(-\tau)$. According to the Wiener-Khinchine relationship, the Fourier transform of the autocorrelation function is the Power Spectral Density (PDS):

$$S_u(f) = \int_{-\infty}^{+\infty} R_X(\tau) e^{-j2\pi f\tau} d\omega \tag{C.10}$$

where f is the frequency.

The slotting technique (see figure C.12) divides the autocorrelation function in K slots equally spaced in time ($\Delta\tau$) and for each of them calculates the average weighted on the number of cross-products ($[u(t_i) \cdot u(t_i + t_j)]$). For each slot:

$$R_u(k\Delta\tau) = \frac{1}{\sum_{i=1}^{N-1}\sum_{j=i+1}^{N} b_k(t_j - t_i)} \sum_{i=1}^{N-1}\sum_{j=i+1}^{N} u(t_i)u(t_j)b_k(t_j - t_i) \tag{C.11}$$

where $k = 1, 2, ...K$ indicates the slot and b_k is defined as:

$$b_k(t_j - t_i) = \begin{cases} 1 & for |\frac{t_j - t_i}{\Delta\tau} - k| < 0.5 \\ 0 & otherwise \end{cases} \tag{C.12}$$

Before applying the slotting technique and to obtain a low noise spectra, the signal is divided in blocks of equal time and the PSD of each block is calculated. In addition, it is important to remove the first point in the autocorrelation.

For the same reasons discussed in the previous section, the weight factor can be used also when evaluating the autocorrelation function. In this case, con-

sidering also the TT as weight, b_k in the equation C.11 becomes:

$$b_k(t_j - t_i) = \begin{cases} TT_k(t_j - t_i) & for|\frac{t_j - t_i}{\Delta\tau} - k| < 0.5 \\ 0 & otherwise \end{cases} \tag{C.13}$$

Figure C.11 compares the PSD for the V and the W velocity component with and without weighting factor for the same signal discussed in the previous section (see figure C.9), corresponding to the fourth point of the boundary layer profile in figure C.8.

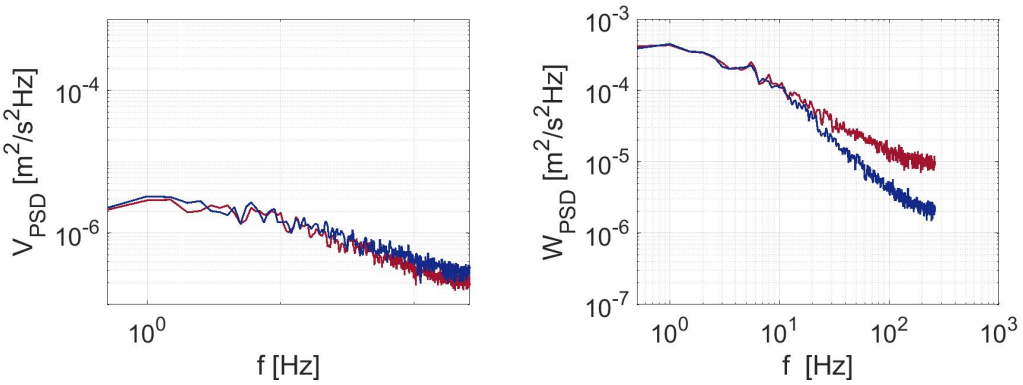


Figure C.11: Example of PSD for the V and W velocities: - with and - without the weighting factor.

The difference on the V component is almost not detectable since the signal has already a quite low energy; while the spectra for the W velocity component shows a different only in the high frequencies with the PSD being underestimated if the weighting factor is not used. This can be understood by looking at the distribution of the W data points as function of the TT in figure C.9. The W-TT distribution of the signal is highly dispersed at high transit time. Considering two ideal particles travelling at the same velocity and crossing the probe volume with the same trajectory, the particle fluctuating at higher frequencies has a higher transit time and vice versa. The weighted spectra accounts for this type of effects. For this reason the weight has been considered also for the evaluation of the PSD.

Overall, the analysis can be summarised in the following steps:

1. each signal, having a number of samples N, acquired in a sampling period

T, is divided in B blocks of equal time period ΔT_b. Each individual block has a different number of samples still randomly distributed;

2. for each block the mean is removed from the block signal and then the autocorrelation is calculated, which will be still randomly spaced,

3. each block is divided in slots. It is desirable to have a high number of slots, but on average at least few points per slot are necessary. If one slot does not have any data point the code takes the value of the autocorrelation function of the previous slot. The period of each slot Δt_s, depending on the number of slots chosen per block, is:

$$\Delta t_s = \frac{avarage \quad n^\circ \quad points \quad in \quad slot}{datarate}$$

It must be constant within the blocks of each signal.
From Δt_s the resolution in the frequency spectra, in order to avoid aliasing, must be:

$$\Delta f = \frac{1}{2\Delta t_s}$$

Δf corresponds also to the minimum frequency f_{MIN} of the spectra. On its turn, the maximum resolvable frequency in the spectra is given by:

$$f_{MAX} = \left(\frac{N_{slots}}{2} + 1\right)\frac{1}{2\Delta t_s}$$

4. at this stage the autocorrelation function for each block has the same time resolution and it is not random any more; the number of points per block is constant. Therefore, a Fast Fourier Transform (FFT) algorithm can be applied to calculate the PSD for each block ($S_b^*(f)$). To prevent leakage errors the signal is firstly multiplied by the Hann window:

$$H_w(t) = \begin{cases} \frac{1}{2}\left(1 - cos\frac{2\pi t}{\Delta T_B}\right) & for \quad 0 \leq t \leq \Delta T_B \\ 0 & otherwise \end{cases} \tag{C.14}$$

5. the PSD $S_b^*(f)$ of each block are averaged to get a clean PSD of the whole signal:

$$S^*(f) = \frac{1}{B}\sum_1^B S_b^*(f)$$

The code for the spectra for the random data is validated with randomly samples taking from simulated sine waves.

6. the spectra is normalised ($S(f)$) so that the Parseval theorem is verified for each block and the RMS level can be directly calculated.

$$\sum_{i=0}^{N} u'^2(t_i) = \sum_{f=0}^{f_{max}} S^*(f)\sqrt{\gamma_H}\frac{B}{N_B}$$

where γ_H is the window factor equal to 8/3 for Hann Window (Bendat and Piersol, 2011), N_B is the number of the sample in each of the B blocks.

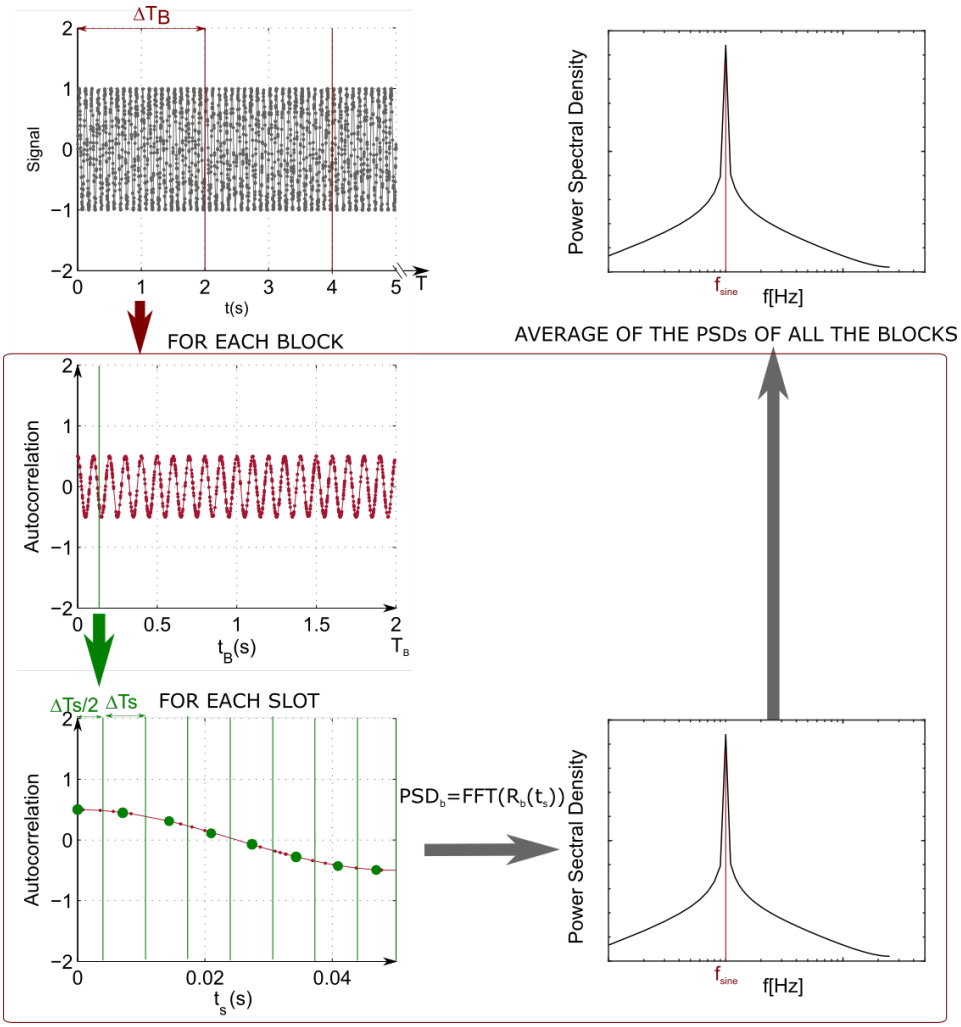


Figure C.12: LDA data analysis: the slotting technique.

Appendix D

Uncertainty analysis

D.1 Experimental errors

The experimental measurements are influenced by different types of errors that have to be identified, possibly removed or otherwise quantified.
The first type regards errors in a strict sense, for example due to miscalculations or to mistakes in the procedure. These, commonly called *human errors*, can be identified and prevented.
Nevertheless, even if the procedure has been carefully followed without mistakes, the measurements are indeed affected by other two types of errors: *random* and *systematic*. The appearance of random errors in the measurement is unpredictable and their sources are not always identifiable. However they can be reduced by repeating the measurement or refining the measurement methodology or technique.
Systematic errors, associated with accuracy of tools or instruments, cannot be completely eliminated. Nevertheless, their contribution to the final result can be quantified through the *uncertainty analysis*.
In the descriptions of the experiments some human and random errors have already been discussed, while the contributions to the final results of the systematic errors are quantified in this appendix through the uncertainty analysis.

D.2 Uncertainty analysis

Let Y be a quantity measured not directly but derived from measurements of other quantities (x_i), to which it is related to through a function f:

$$Y = f(x_1, x_2, ...x_n). \tag{D.1}$$

The uncertainty of Y will be affected by a combination of the uncertainties of the measured x_i quantities ($\Delta x_1, \Delta x_2, ...\Delta x_n$).
If f is a linear function of the variables x_i, i.e $f = x_1 + x_2 + ...x_n$, the uncertainties can be calculated as the sum of the absolute errors Δx_i:

$$\Delta Y = \sum_{i=1}^{N} \Delta x_i \tag{D.2}$$

or, in term of standard deviations as:

$$\Delta Y = \sqrt{\sum_{i=1}^{N} \Delta x_i^2}. \tag{D.3}$$

In case of a non linear relation, i.e. $f = x_1^{p_1} x_2^{p_2} ... x_2^{p_n}$, the combined uncertainty is the sum of the relative errors:

$$\frac{\Delta Y}{Y} = \sum_{i=1}^{N} \left(\frac{p_i \Delta x_i}{x_i} \right) \tag{D.4}$$

or in term of standard deviation:

$$\frac{\Delta Y}{Y} = \sqrt{\sum_{i=1}^{N} \left(\frac{p_i \Delta x_i}{x_i} \right)^2}. \tag{D.5}$$

Following the JMG 100:2008 guide for the error analysis (BIPM, 2008), the standard uncertainty has been adopted. The uncertainty of a quantity Y expressed by a generic function f is defined as:

$$\Delta Y = \sqrt{\sum_{i=1}^{N} \left(\frac{\partial f}{\partial x_i} \right)^2 \Delta x_i^2}. \tag{D.6}$$

For a more precise evaluation of the propagation of the errors, often the expanded uncertainty is adopted. This can be obtained by multiplying the combined standard uncertainty by a coverage factor (k_c):

$$\Delta Y = k_c \Delta f. \tag{D.7}$$

The value of k_c depends on the probability distribution of the measured variable and the desired confidence level. It is typically in the range of $2 \div 3$. For a normal distribution $k_c = 1.96$ corresponds to a confidence level of 95% and $k_c = 3$ to a confidence level of 99%. In the following the combined uncertainties have been calculated.

In the current thesis, two experimental investigations have been presented. One on a vertical flat plate and one on cylinders carried out in two different wind tunnels equipped with different instrumentations. The general procedure to calculate the uncertainties is reported hereafter. The results are listed in tables D.1 and D.2.

D.3 Density of the air

The density of the air is calculated from the ideal gas law:

$$\rho_{air} = \frac{P_{ATM}}{RT} \tag{D.8}$$

where T is the air temperature, P_{ATM} the barometric pressure and R the Boltzman constant for dry air.
Based on the uncertainties of the measured quantities (P_{ATM}, T) the corresponding relative error is:

$$\frac{\Delta\rho}{\rho} = \sqrt{\left(\frac{\Delta P_{ATM}}{P_{ATM}}\right)^2 + \left(\frac{\Delta T}{T}\right)^2} \tag{D.9}$$

D.4 Freestream velocity

The freestream velocity is derived by the differential pressure measured with a Pitot tube, according to:

$$U_\infty = \sqrt{\frac{2(p_\infty - p_{s\infty})}{\rho_{air}}} \tag{D.10}$$

The combined uncertainty is given by:

$$\frac{\Delta U_\infty}{U_\infty} = \sqrt{\left(\frac{1/2\Delta P_{Pitot}}{P_{Pitot}}\right)^2 + \left(\frac{1/2\Delta\rho_{air}}{\rho_{air}}\right)^2} \tag{D.11}$$

D.5 Pressure distribution

D.5.1 Gaster wind tunnel

The pressure distribution on the model, in the Gaster wind tunnel, is measured by connecting the pressure tubes to a scani-valve which is connected to a pressure transducer. The pressure transducer acquires the static and the total pressure from the Pitot. Therefore the differential pressure P_{diff} is directly obtained from the transducer output.
The pressure distribution on the model has been reported through the dimensionless coefficient:

$$c_P = \frac{P_{diff}}{1/2\rho_{air}U_\infty^2} \tag{D.12}$$

In this case, the error on this parameter results:

$$\frac{\Delta c_P}{c_P} = \sqrt{\left(\frac{\Delta P_{diff}}{P_{diff}}\right)^2 + \left(\frac{\Delta\rho_{air}}{\rho_{air}}\right)^2 + \left(\frac{2\Delta U_\infty}{U_\infty}\right)^2} \tag{D.13}$$

D.5.2 T2 wind tunnel

The pressure distribution in the T2 wind tunnel on the model is measured using an inclined manometer:

$$P_s = hsin(\phi_m)g\rho_m \tag{D.14}$$

where h is the differential height of the column of fluid in the manometer, ρ_m is the density of the alcohol, g the gravity acceleration and ϕ_m the angle of inclination of the manometer, which is measured using an inclinometer. Considering the ρ_m as a known quantity, the resulting combined uncertainty for the pressure is:

$$\frac{\Delta P_s}{P_s} = \sqrt{\left(\frac{\Delta h}{h}\right)^2 + \left(\frac{\Delta \phi_m}{tan(\phi_m)}\right)^2}. \tag{D.15}$$

The pressure distribution has been represented with the pressure dimensionless coefficient:

$$c_P = \frac{P_s - P_{s\infty}}{1/2\rho_{air}U_\infty^2} \tag{D.16}$$

The error on this parameter is:

$$\frac{\Delta c_P}{c_P} = \sqrt{\left(\frac{\Delta P_s}{P_s}\right)^2 + \left(\frac{\Delta P_{s\infty}}{P_{s\infty}}\right)^2 + \left(\frac{\Delta \rho_{air}}{\rho_{air}}\right)^2 + \left(\frac{2\Delta U_\infty}{U_\infty}\right)^2} \tag{D.17}$$

Since the Pitot is connected to the manometer during the pressure measurements, the uncertainty on $P_{s\infty}$ is the same of P_s.

GASTER WIND TUNNEL

Transducers	Quantity	x	Δx	$\Delta x/x$
Thermocouple NI	T	20°	0.1°	0.5%
Setra 239	P_{ATM}	$101325Pa$	$55Pa$	0.05%
Setra 264	P_{Pitot}	$154Pa$	$0.2Pa$	0.12%
Furness FCO56	P_{diff}	$31Pa$	$0.2Pa$	0.6%

Derived quantities	$\Delta Y/Y$
ρ_{air}	0.5%
U_∞	0.25%
c_P	0.6%

Table D.1: Uncertainties on measurements carried out in the Gaster wind tunnel.

T2 WIND TUNNEL

Transducers	Quantity	x	Δx	$\Delta x/x$
Thermocouple NI	T	$20°C$	$0.1°C$	0.5%
Barometer B740	P_{ATM}	769mmHg	0.1mmHg	0.013%
Furness F318	P_{Pitot}	$21Pa$	$1Pa$	4.76%
Inclined manometer	h	3 in	0.1 in	3.33%
Inclinometer	ϕ_m	10.64°	0.01°	0.094%

Derived quantities	$\Delta Y/Y$
ρ_{air}	0.5%
U_∞	2.39%
P_s	6.58%
c_P	9.91%

Table D.2: Uncertainties on measurements carried out in T2 wind tunnel.

D.6 Hot-wire measurements

Hot-wire measurements are velocity measurements based on heat transfer. The output of the anemometer is a voltage signal (E), which has to be converted in velocity through a calibration law (Jørgensen, 2005). The uncertainties of the hot-wire measurements can be calculated considering three stages: (1) calibration procedure, (2) data acquisition, (3) experimental and environmental conditions. The three uncertainties are here discussed and quantified, and their values are reported in table D.3. The final uncertainty is:

$$\Delta U_{HW} = \sqrt{\sum_{i=0}^{N} \Delta U_i^2} \tag{D.18}$$

Calibration

The calibration procedure, as reported in appendix B, has been carried out by placing the hot-wire close to the Pitot. The velocity from the Pitot (U_∞) is used to find the constants in the relationship with the hot-wire voltage (E). Therefore, part of the uncertainty during the calibration is due to uncertain on the Pitot velocity (ΔU_∞), which has been calculated in the previous section. At the reference velocity $10m/s$, the absolute error of the Pitot is $0.025m/s$.

Another source of the uncertainty is due to the curve fit that is carried out to determine the constants A, B, n in the King's law. Taking the data from the calibration shown in figure B.2, the difference between the U_∞ and U_{est} from the hot-wire voltage, using the corresponding calibration factors, leads to an uncertainty of $\Delta U_{lin} = (U_{est} - U_\infty) = 0.007 m/s$ for the reference velocity $U_\infty = 10 m/s$.

Data acquisition

The hot-wire voltage signal is converted from an analogue to a digital signal using an A/D board. As described by Jørgensen (2005), the resolution is:

$$\Delta U_{AD} = \frac{1}{U} \frac{E_{AD}}{2^n} \frac{\partial U}{\partial E} \tag{D.19}$$

where U is the reference velocity, E_{AD} is the input velocity range($10V$), n is the resolution of the A/D board (16 for a 16-bit A/D) and $\frac{\partial U}{\partial E}$ is the sensitivity ($27 m/s/V$).

Experimental and environmental conditions

The experimental and the environmental conditions may influence the uncertainty of the hot-wire measurements.
The probe may be misaligned of an angle γ_{HW}:

$$\Delta U_{pos} = (1 - cos(\gamma_{HW})) \tag{D.20}$$

According to Jørgensen (2005), to quantify the misalignment an uncertainty of $\Delta\gamma_{HW} = 1°$ must be considered.
Another systematic error is introduced by the temperature during the measurements, which may differ from the calibration temperature. This has been prevented by applying temperature corrections in the post-process procedure.

Summering, the uncertainties of the hot-wire are reported in the following table and the final uncertainty results 0.08%.

Error source	$\Delta U_i[m/s]$
ΔU_∞	$0.025m/s$
ΔU_{lin}	$0.007m/s$
ΔU_{AD}	$0.004m/s$
ΔU_{pos}	$0.00015m/s$
ΔU_{HW}	$0.008m/s$ (0.08%)

Table D.3: Hot-wire uncertainties for a reference velocity of $10m/s$, corresponding to $E = 4.16V$ and calibration coefficients $A = 4.29$, $B = 7.74$ and $n = 0.35$.

D.7 LDA measurements

The LDA system is an absolute flow measurement method that does not need calibration. The data are converted to velocity by the Fiber Flow software. To estimate the uncertainty of the velocity computed by the software, the guidelines published in the 25th International Towing Tank Conference (2008) have been followed.

The equation used by the FiberFlow software to calculate the velocity is:

$$U_{LDA} = \frac{\lambda_{LDA}}{2sin(\theta/2)} f_D \tag{D.21}$$

where λ_{LDA} is the wavelength of the laser light, θ the angle between the laser beams and f_D the doppler frequency.

The uncertainty on the doppler frequency and on the laser wavelength are negligible, while the beam intersection angle is derived from:

$$\theta = 2atan\left(\frac{B_s}{2f_L}\right) \tag{D.22}$$

where B_s is the beam spacing and f_L the focal length as shown in figure D.1.

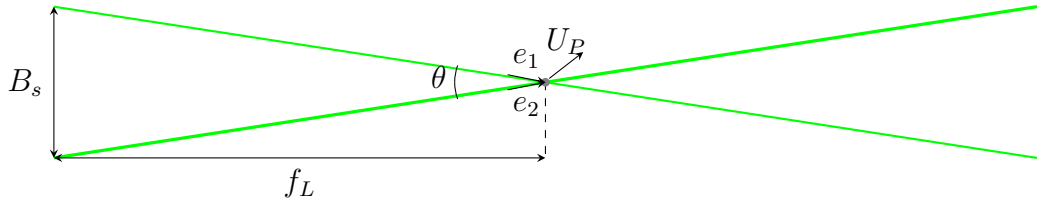


Figure D.1: Two laser beam and a particle crossing the probe volume with velocity U_P.

The reference beam spacing is provided by the assembly test and inspection certificate provided by the Dantec Dynamics during the system installation and corresponds to $38.84mm \pm 0.02mm$. While, the error on the focal length, $f_L = 800mm$, is considered negligible. Therefore the beam intersection reference value is $\theta = 2.78°$ and the relative error is:

$$\Delta\theta = \left(\frac{1}{1 + (B_s/2f_L)^2}\right)\frac{2f_L}{B_s^2}\Delta B_s \tag{D.23}$$

that results 0.03°.

Knowing the relative error on the intersection angle, the combined uncertainty for the velocity is:

$$\frac{\Delta U_{LDA}}{U_{LDA}} = \sqrt{\left(\frac{1}{2}tan^{-1}\left(\frac{\theta}{2}\right)\right)^2\Delta\theta^2} \tag{D.24}$$

which corresponds to $5.4 \cdot 10^{-5}\%$ considering $\Delta\theta$ in radians.

Transformation matrix

In the case of two- and three- dimensional measurements, the acquired velocity components, $\overrightarrow{LDA_1}$, $\overrightarrow{LDA_2}$ and $\overrightarrow{LDA_3}$, are in a non-orthogonal coordinate system and are then transformed to the wind tunnel orthogonal coordinate system. This transformation is carried out through the so called *transformation matrix*. The procedure to obtain the matrix has been explained in appendix C, here the analysis of the uncertainties on the matrix itself is reported.

The procedure consists of calculating the individual LDA laser orientation by indirectly measuring the beam positions on a high resolution camera. The pro-

cedure consists of three main steps (see figure C.4): the camera is positioned at the focal point of the laser; each laser is moved such that they all cross on the focal point, which location is marked on the screen; the laser optics groups are traversed perpendicular to the camera and the new positions (X_T, Y_T, Z_T) of the laser beams on the screen, respect the point previously marked, are recorded (see table C.2).

The first step may cause errors due to the beams that do not cross precisely at the focal point. This situation would affect the signal itself by reducing the data rate up to the worst scenario in which it would not even be possible to take measurements in coincidence mode. Therefore, it be would a human error and not an uncertainty of the velocity measurements. In these circumstances, the alignment procedure must be repeated.

For the other two steps of the procedure, the systematic errors are related to the localisation of the laser beam on the camera view. To calculate those uncertainties the beam dimension of each laser beam on the camera view at each step of the procedure has to be calculated. However, since the diameter of the laser beam is not constant, first of all it is necessary to explain how it varies.

The beam coming from the LDA is a *gaussian beam*, which means that at all the cross sections the light intensity has as a Gaussian distribution and the width of the beam is defined by the edge-intensity (Zhang, 2010). Figure D.2 shows a sketch of two crossing beams with variable width, exaggerated for clarity.

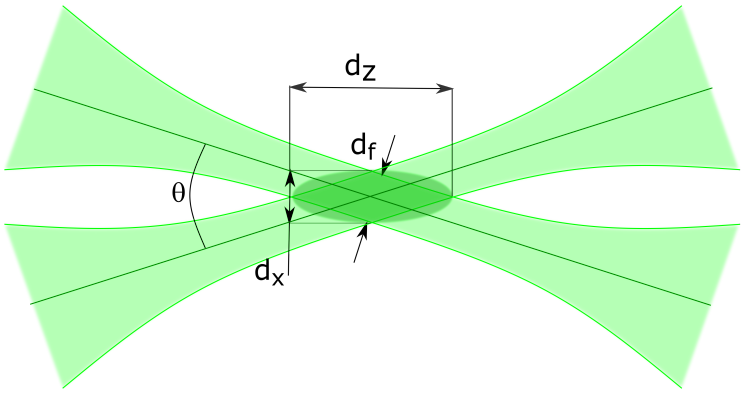


Figure D.2: Two laser beam crossing in the probe volume.

The smallest width is at the focal point where the beams cross. At this point each laser beam is described by the so called beam waist. Knowing some characteristics of the optical system the diameter d_f is uniquely defined as followed:

$$d_f = \frac{4 f_L \lambda_{LDA}}{\pi E D} \tag{D.25}$$

where f_L is the focal length, λ_{LDA} the laser wavelength, D the waist diameter of the laser beam before passing through the front lens and E is the beam expander ratio. The value of D has been measured during the installation by Dantec Dynamics and it has been certificated as equal to $2.2mm \pm 0.02mm$. The beam expander is a combination of lenses in front, or replacing the front lens, of the LDA system, used to reduce the size of the measuring volume at the measuring distance, allows one to reach greater measuring distances without sacrificing the signal-to-noise ratio,(Dynamics, 2011). The beam expander ratio represents the reduction of the probe volume after the beam has passed across the beam expander; for the system used it corresponds to $E = 1.95$. The focal length is the same for each LDA group, while the wavelength changes as shown in table D.4.
Therefore the waist beam diameters with the associated uncertainty for each LDA group are:

$$d_{f1} = 0.12mm \qquad d_{f2} = 0.11mm \qquad d_{f3} = 0.13mm\%.$$

The probe volume, as shown in figure D.2, is identified by:

$$d_x = \frac{d_f}{cos(\theta/2)}, \qquad d_y = d_f, \qquad d_z = \frac{d_f}{sin(\theta/2)}.$$

The resulting probe volume dimensions are reported in table D.4.

Coming back to the indirect procedure to calculate the laser beams orientation, when the camera is placed at the focal point, each beam on the screen of the pc appears as a bright circle (see figure D.3). The diameter of the circle depends on the diameter of the beam and the orientation of the optics. Since the camera has a high resolution and the inclination of the optics group is usu-

		LDA1	LDA2	LDA3
λ_{LDA}	[nm]	514.5	488	532
f_L	[mm]	800	800	800
θ	[°]	$2.78° \pm 0.03°$	$2.78° \pm 0.03°$	$2.78° \pm 0.03°$
d_f	[mm]	0.12	0.11	0.13
d_x	[mm]	0.12	0.12	0.13
d_y	[mm]	0.12	0.12	0.13
d_z	[mm]	2.60	2.39	2.60

Table D.4: LDA parameters

ally small, the diameter of the circle on the screen is approximately d_x. The uncertainty on the location of the focal point on the screen is half of the beam diameter ($d_x/2$), that is also the uncertainty on the origin of the coordinate system for the axes X_T and Z_T, plane captured by the camera.

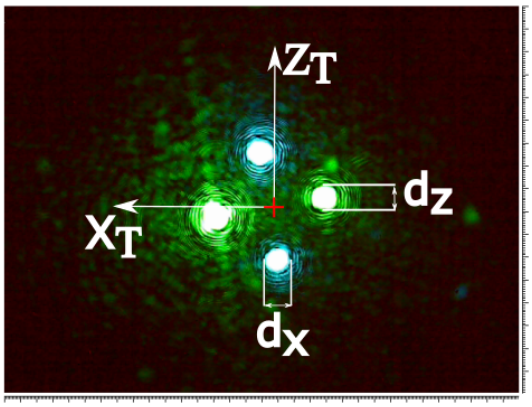


Figure D.3: Four laser beams captured by the camera during alignment procedure.

In the second step of the procedure, the optics are traversed along Y_T by a fixed distance and the traverse is then moved along X_T and Z_T to record the new position of the beams with respect to the previous point. The uncertainties on the X_T and Z_T are related to the beam diameter. As shown in figure D.2 the diameter of the Gaussian beam varies with the distance. Considering the angle between the beams small enough the diameter ($d(Y_T)$) at the Y_T location can be calculated according to (Dynamics, 2011):

$$d(Y_T) = d_f \sqrt{1 + \left(\frac{4\lambda_{LDA} Y_T}{\pi d_f^2}\right)^2}. \tag{D.26}$$

For $Y_T = 200mm$ it corresponds, for all the six beams, to $d(200) = 1.07mm$. The laser beam positions at $Y_T = 200mm$ are calculated as the difference between the (0,0,0) and the new (X_T, Y_T, Z_T), therefore the error is the sum of the absolute uncertainties of the two positions:

$$\Delta X_T = \Delta Z_T = d(Y_T)/2 + d_f/2$$

The uncertainty regarding Y_T is only due to the traverse, which has an absolute error of 0.01 mm. An example of transformation matrix, together with the relative error is reported in table D.5.

Laser	Beam	X_T [mm]	Y_T [mm]	Z_T [mm]
G	shifted □	$+10.80 \pm 0.24$	-220.00 ± 0.01	-3.85 ± 0.24
	unshifted	-7.00 ± 0.24	-220.00 ± 0.01	6.75 ± 0.24
B	shifted •	$+7.15 \pm 0.25$	-220.00 ± 0.01	10.05 ± 0.23
	unshifted ∘	-3.10 ± 0.25	-220.00 ± 0.01	-7.35 ± 0.25
V	shifted □	-5.80 ± 0.25	-220.00 ± 0.01	-84.41 ± 0.25
	unshifted	-6.00 ± 0.25	-220.00 ± 0.01	-64.81 ± 0.25

Table D.5: Example of wind tunnel coordinate to find the laser beams orientations with their absolute uncertainties.

Bibliography

ITTC 25th International Towing Tank Conference. Recommended Procedures and Guidelines. Uncertainty Analysis Laser Doppler Velocimetry Calibration. Technical report, 2008.

H. E. Albrecht, N. Damaschke, M. Borys, and C. Tropea. *Laser Doppler and Phase Doppler Measurement Techniques*. Springer Science & Business Media, 2013.

J. E. Alderman, S. Rolston, M. Gaster, and C. J. Atkin. A method of reducing the drag of transport wings. In *34th AIAA Applied Aerodynamics Conference*, page 3115, 2016.

J. D. Anderson Jr. *A history of aerodynamics and its impact on flying machines*. Cambridge University Press, 1999.

A. Anscombe and L. N. Illingworth. Wind-tunnel observations of boundary layer transition on a wing at various angles of sweepback. Technical report, Aeronautical Research Council Great Britain, HM Stationery Office, 1956.

D. Arnal and G. Casalis. Laminar-turbulent transition prediction in three-dimensional flows. *Progress in Aerospace Sciences*, 36(2):173–191, 2000.

P. W. Bearman. Some measurements of the distortion of turbulence approaching a two-dimensional bluff body. *Journal of Fluid Mechanics*, 53(3):451–467, 1972.

J. S. Bendat and A. G. Piersol. *Random Data. Analysis and Measurement Procedures*. John Wiley & Sons, 2011.

F. P. Bertolotti. On the connection between cross-flow vortices and attachment-line instabilities. In *Laminar-Turbulent Transition*, pages 625–630. Springer, 2000.

BIPM. Evaluation of measurement data–guide to the expression of uncertainty in measurement. *JCGM*, 2008.

H. Bippes. Basic experiments on transition in three-dimensional boundary layers dominated by crossflow instability. *Progress in Aerospace Sciences*, 35(4):363–412, 1999.

H. Bippes and B. Mueller. Experiments on the laminar-turbulent transition on swept wings. *NASA STI/Recon Technical Report N*, 90:3–16, 1988.

V. I. Borodulin, A. V. Ivanov, and Y. S. Kachanov. Swept-wing boundary-layer transition at various external perturbations: scenarios, criteria, and problems of prediction. *Physics of Fluids*, 29(9):094101, 2017.

J. Böttcher and E. Wedemeyer. The flow downstream of screens and its influence on the flow in the stagnation region of cylindrical bodies. *Journal of Fluid Mechanics*, 204:501–522, 1989.

R. E. Britter, J. C. R. Hunt, and J. C. Mumford. The distortion of turbulence by a circular cylinder. *Journal of Fluid Mechanics*, 92(2):269–301, 1979.

H. H. Bruun. *Hot-wire Anemometry: Principles and Signal Analysis*. IOP Publishing, 1996.

M. Choudhari. Roughness-induced generation of crossflow vortices in three-dimensional boundary layers. *Theoretical and Computational Fluid Dynamics*, 6(1):1–30, 1994.

J. C. Cooke. The boundary layer of a class of infinite yawed cylinders. In *Mathematical Proceedings of the Cambridge Philosophical Society*, volume 46, pages 645–648. Cambridge University Press, 1950.

J. D. Crouch. Localized receptivity of boundary layers. *Physics of Fluids A: Fluid Dynamics*, 4(7):1408–1414, 1992.

J. M. Délery. Robert Legendre and Henri Werlé: Toward the Elucidation of Three-Dimensional Separation. *Annual review of fluid mechanics*, 33(1): 129–154, 2001.

H. Deyhle, G. Höhler, and H. Bippes. Experimental investigation of instability wave propagation in a three-dimensional boundary-layer flow. *AIAA Journal*, 31(4):637–645, 1993.

R. S. Downs and E. B. White. Free-stream turbulence and the development of cross-flow disturbances. *Journal of Fluid Mechanics*, 735:347–380, 2013.

P. G. Drazin and W. H. Reid. *Hydrodynamic Stability*. Cambridge University Press, 1981.

Dantec Dynamics. *LDA and PDA - Reference Manual*. Dantec Dyanamics A/S, 2011.

V. M. Falkner and S. W. Skan. LXXXV. Solutions of the boundary-layer equations. *The London, Edinburgh, and Dublin Philosophical Magazine and Journal of Science*, 12(80):865–896, 1931.

J. H. M. Fransson, L. Brandt, A. Talamelli, and C. Cossu. Experimental and theoretical investigation of the nonmodal growth of steady streaks in a flat plate boundary layer. *Physics of Fluids*, 16(10):3627–3638, 2004.

M. Gaster. A note on the relation between temporally-increasing and spatially-increasing disturbances in hydrodynamic stability. *Journal of Fluid Mechanics*, 14(2):222–224, 1962.

M. Gaster. On the flow along swept leading edges. Technical report, The college of aeronautics Cranfield, 1965.

M. Gaster. On the flow along swept leading edges. *The Aeronautical Quarterly*, 18(2):165–184, 1967.

M. Gaster. Establishment of laminar boundary layer flow on an aerofoil body, May 8 2012. US Patent 8,172,185.

M. Gaster and J. B. Roberts. Spectral analysis of randomly sampled signals. *IMA Journal of Applied Mathematics*, 15(2):195–216, 1975.

M. Gaster and J. B. Roberts. The spectral analysis of randomly sampled records by a direct transform. *Proceedings of the Royal Society of London A: Mathematical, Physical and Engineering Sciences*, 354(1676):27–58, 1977. ISSN 0080-4630.

M. I. Goldhammer and B. R. Plendl. Surface coating and drag reduction. *AERO*, pages 14–20, 2014.

M. E. Goldstein. The evolution of Tollmien–Sclichting waves near a leading edge. *Journal of Fluid Mechanics*, 127:59–81, 1983.

M. E. Goldstein. Scattering of acoustic waves into Tollmien-Schlichting waves by small streamwise variations in surface geometry. *Journal of Fluid Mechanics*, 154:509–529, 1985.

H. Görtler. Instabilität laminarer Grenzschichten an konkaven Wänden gegenüber gewissen dreidimensionalen Störungen. *ZAMM-Journal of Applied Mathematics and Mechanics/Zeitschrift für Angewandte Mathematik und Mechanik*, 21(4):250–252, 1941.

H. Görtler. Dreidimensionale instabilität der ebenen Staupunktströmung gegenüber wirbelartigen Störungen. *50 Jahre Grenzschichtforschung*, 304: 304–314, 1955.

J. P. Gostelow, A. Rona, M. De Saint Jean, S. J. Garrett, and W. A. McMullan. Investigation of Streamwise and Transverse Instabilities on Swept Cylinders and Implications for Turbine Blading. *Journal of Turbomachinery*, 135(5): 051018, 2013.

E. R. Gowree. *Influence of Attachment Line Flow on Form Drag*. PhD thesis, City University London, 2014.

W. E. Gray. The effect of wing sweep on laminar flow. *Royal Aircraft Establishment*, 1952.

J. Green. Laminar flow control-back to the future? In *38th Fluid Dynamics Conference and Exhibit*, page 3738, 2008.

N. Gregory and W. S. Walker. Brief wind tunnel tests on the effect of sweep in laminar flow. *Technical Report ARC*, 14,928, 1952.

P. Hall. The Görtler vortex instability mechanism in three-dimensional boundary layers. *Proc. R. Soc. Lond. A*, 399(1816):135–152, 1985.

P. Hall and M. R. Malik. On the instability of a three-dimensional attachment-line boundary layer: weakly nonlinear theory and a numerical approach. *Journal of Fluid Mechanics*, 163:257–282, 1986.

P. Hall, M. R. Malik, and D. I. A. Poll. On the stability of an infinite swept attachment line boundary layer. In *Proc. R. Soc. Lond. A, 1809*, volume 395, pages 229–245. The Royal Society, 1984.

G. Hämmerlin. Zur instabilitätstheorie der ebenen Staupunktströmung. *50 Jahre Grenzschichtforschung*, pages 315–327, 1955.

R. E. Hanson, H. P. Buckley, and P. Lavoie. Aerodynamic optimization of the flat-plate leading edge for experimental studies of laminar and transitional boundary layers. *Experiments in fluids*, 53(4):863–871, 2012.

J. L. Hess and A. M. O. Smith. Calculation of potential flow about arbitrary bodies. *Progress in Aerospace Sciences*, 8:1–138, 1967.

K. Hiemenz. Die Grenzschicht an einem in den gleichformigen Flussigkeitsstrom eingetauchten geraden kreiszylinder. Gottingen dissertation. *Dingler's Polytech. J*, 326:311, 1911.

ICAO. Long-term traffic forecasts, July 2016.

F. E. Jørgensen. *How to measure turbulence with hot-wire anemometers: a practical guide*. Dantec dynamics, 2005.

O. S. Kerr and J. W. Dold. Periodic steady vortices in a stagnation-point flow. *Journal of Fluid Mechanics*, 276:307–325, 1994.

J. Kestin and P. F. Maeder. Influence of turbulence on transfer of heat from cylinders. Technical report, National Advisory Comitee for Aeronautics, 1957.

J. Kestin and R. T. Wood. Enhancement of stagnation-line heat transfer by turbulence. *Prog. Heat Mass Transfer*, 2:249–253, 1969.

J. Kestin and R. T. Wood. On the stability of two-dimensional stagnation flow. *Journal of Fluid Mechanics*, 44(3):461–479, 1970.

A. M. Kuethe, W. W. Willmarth, and G. H. Crocker. Stagnation point fluctuations on a body of revolution. *The Physics of Fluids*, 2(6):714–716, 1959.

T. Kurian and J. H. M. Fransson. Grid-generated turbulence revisited. *Fluid dynamics research*, 41(2):021403, 2009.

T. Kurian, J. H. M. Fransson, and P. H. Alfredsson. Boundary layer receptivity to free-stream turbulence and surface roughness over a swept flat plate. *Physics of fluids*, 23(3):034107, 2011.

R. S. Lin and M. R. Malik. On the stability of attachment-line boundary layers. Part 1. The incompressible swept Hiemenz flow. *Journal of Fluid Mechanics*, 311:239–255, 1996.

R. S. Lin and M. R. Malik. On the stability of attachment-line boundary layers. Part 2. The effect of leading-edge curvature. *Journal of Fluid Mechanics*, 333:125–137, 1997.

M. J. Lyell and P. Huerre. Linear and nonlinear stability of plane stagnation flow. *Journal of Fluid Mechanics*, 161:295–312, 1985.

L. M. Mack. Boundary-layer linear stability theory. *AGARD Report n.709*, 1984.

M. V. Morkovin. Transition in open flow systems-a reassessment. *Bull. Am. Phys. Soc.*, 39:1882, 1994.

M. V. Morkovin, E. Reshotko, and T. Hebert. On the question of instabilities upstream of cylindrical bodies. Technical report.

H. M. Nagib and P. R. Hodson. Vortices induced in a stagnation region by wakes. *Aerodynamic heating and thermal protection systems*, page 66, 1978.

D. Obrist. *On the stability of the swept leading-edge boundary layer*. Phd thesis, University of Washington, 2000.

D. Obrist and P. J. Schmid. On the linear stability of swept attachment-line boundary layer flow. Part 1. Spectrum and asymptotic behaviour. *Journal of Fluid Mechanics*, 493:1–29, 2003a.

D. Obrist and P. J. Schmid. On the linear stability of swept attachment-line boundary layer flow. Part 2. Non-modal effects and receptivity. *Journal of Fluid Mechanics*, 493:31–58, 2003b.

P. R. Owen and D. G. Randall. *Boundary layer transition on a sweptback wing*. Royal Aircraft Establishment, 1952.

P. R. Owen and D. G. Randall. Boundary layer transition on a sweptback wing: Effect of incidence. *RAE Unpublished Paper*, 1953.

W. Pfenninger and J. W. Bacon. Amplified laminar boundary layer oscillations and transition at the front attachment line of a 45 swept flat-nosed wing with and without boundary layer suction. In *Viscous Drag Reduction proceedings*, pages 85–105. Plenum Press, 1969.

N. A. V. Piercy. *Aerodynamics*. English Universities Press, 1947.

N. A. V. Piercy and E. G. Richardson. XCVI. The variation of velocity amplitude close to the surface of a cylinder moving through a viscous fluid. *The London, Edinburgh, and Dublin Philosophical Magazine and Journal of Science*, 6(39):970–977, 1928.

N. A. V. Piercy and E. G. Richardson. XCIV. The turbulence in front of a body moving through a viscous fluid. *The London, Edinburgh, and Dublin Philosophical Magazine and Journal of Science*, 9(60):1038–1041, 1930.

M. Placidi, E. van Bokhorst, and C. J. Atkin. On the effect of discrete roughness on crossflow instability in very low turbulence environment. In *8th AIAA Flow Control Conference*, page 3470, 2016.

D. I. A. Poll. *Some aspects of the flow near a swept attachment line with particular reference to boundary layer transition*. Phd thesis, Cranfield Institute of Technology, College of Aeronautics, 1978.

D. I. A. Poll. Transition in the infinite swept attachment line boundary layer. *The Aeronautical Quarterly*, 30(4):607–629, 1979.

L. Prandtl. On fluids motions with very small friction. In *Verhandlungen des Dritten Internationalen Mathematiker-Kongressess, Hidelberg*, 1904.

R. H. Radeztsky, M. S. Reibert, and W. S. Saric. Effect of isolated micron-sized roughness on transition in swept-wing flows. *AIAA Journal*, 37(11): 1370–1377, 1999.

M. S. Reibert. *Nonlinear Stability, Saturation, and Transition in Crossflow-Dominated Boundary Layers*. PhD thesis, Arizona State University, 1996.

O. Reynolds. XXIX. An experimental investigation of the circumstances which determine whether the motion of water shall be direct or sinuous, and of the law of resistance in parallel channels. *Philosophical Transactions of the Royal Society of London*, 174:935–982, 1883.

H. Riedel and M. Sitzmann. In-flight investigations of atmospheric turbulence. *Aerospace Science and Technology*, 2(5):301–319, 1998.

P. E. Roach. The generation of nearly isotropic turbulence downstream of streamwise tube bundles. *International Journal of Heat and Fluid Flow*, 7 (2):117–125, 1986.

L. Rosehead. *Laminar Boundary Layers*. Oxford University Press, Oxford, 1963.

W. Z. Sadeh and H. J. Brauer. Coherent substructure of turbulence near the stagnation zone of a bluff body. In *Fourth Colloquium on Industrial Aerodynamics*, 1980.

W. Z. Sadeh and H. J. Brauer. Coherent substructure of turbulence near the stagnation zone of a bluff body. *Journal of Wind Engineering and Industrial Aerodynamics*, 8(1):59–72, 1981.

W. Z. Sadeh and P. P. Sullivan. Turbulence amplification in flow about an airfoil. In *ASME 1980 International Gas Turbine Conference and Products Show*, pages V01BT02A017–V01BT02A017. American Society of Mechanical Engineers, 1980.

W. Z. Sadeh, S. P. Sutera, and P. F. Maeder. An investigation of vorticity amplification in stagnation flow. *Zeitschrift für angewandte Mathematik und Physik ZAMP*, 21(5):717–742, 1970.

W. Z. Sadeh, H. J. Brauer, and J. A. Garrison. Visualization study of vorticity amplification in stagnation flow. Technical report, PURDUE UNIV LAFAYETTE IND PROJECT SQUID HEADQUARTERS, 1977.

W. S. Saric. Görtler vortices. *Annual Review of Fluid Mechanics*, 26(1):379–409, 1994.

W. S. Saric. Introduction to linear stability theory. In *Advances in Laminar-Turbulent Transition Modelling*, number RTO-EN-AVT-151 in Educational Notes RDP. S& T Organization, 2008. Open Access.

W. S. Saric, H. L. Reed, and E. B. White. Stability and transition of three-dimensional boundary layers. *Annual Review of Fluid Mechanics*, 35(1): 413–440, 2003.

H. Schlichting. Berechnung der Anfachung kleiner Störungen bei der Plattenströmung. *ZAMM*, 13:171–174, 1933.

H. Schlichting. *Boundary Layer Theory; Trans. J. Kestin.* McGraw-Hill New York etc, 1960.

P. J. Schmid and D. S. Henningson. *Stability and Transition in Shear Flows*, volume 142. Springer Science & Business Media, 2012.

L. U. Schrader. *Receptivity of boundary layers under pressure gradient.* PhD thesis, KTH, 2008.

G. B. Schubauer and H. K. Skramstad. Laminar-boundary-layer oscillations and transition on a flat plate. Technical report, NACA Rep. 909, 1947.

A. M. Smith and N. Gamberoni. Transition, pressure gradient and stability theory. *Douglas Aircraft Company Report ES26388*, 1956.

M. C. Smith and A. M. Kuethe. Effects of turbulence on laminar skin friction and heat transfer. *The Physics of Fluids*, 9(12):2337–2344, 1966.

P. R. Spalart. Direct numerical study of leading edge contamination. *AGARD-CP*, 438(5.15), 1988.

J. T. Stuart. Instability of laminar flows, nonlinear growth of fluctuations and transition to turbulence. In *Turbulence and Chaotic Phenomena in Fluids*, pages 17–26, 1984.

S. P. Sutera. Vorticity amplification in stagnation-point flow and its effect on heat transfer. *Journal of Fluid Mechanics*, 21(03):513–534, 1965.

S. P. Sutera, P. F. Maeder, and J. Kestin. *On the sensitivity of heat transfer in the stagnation point boundary layer to free stream vorticity.* Cambridge Univ Press, 1962.

S. Takagi, N. Tokugawa, and N. Itoh. Characteristics of unsteady disturbances due to streamline curvature instability in a three-dimensional boundary layer. In *IUTAM Symposium on Laminar-Turbulent Transition*, pages 369–374. Springer, 2006.

V. Theofilis, A. Fedorov, D. Obrist, and U. C. Dallmann. The extended Görtler–Hämmerlin model for linear instability of three-dimensional incompressible swept attachment-line boundary layer flow. *Journal of Fluid Mechanics*, 487:271–313, 2003.

C. Thomas, P. Hall, and C. Davies. Nonlinear effects on the receptivity of cross-flow in the swept Hiemenz flow. *Journal of Fluid Mechanics*, 763: 433–459, 2015.

W. Tollmien. Über die Entstehung der Turbulenz. Nachr. *English translation NACA TM*, 609:1931, 1929.

C. Tropea and A. L. Yarin. *Springer handbook of experimental fluid mechanics*, volume 1. Springer Science and Business Media, 2007.

E. van Bokhorst. *Forcing of the primary and secondary cross flow instability.* PhD thesis, City, University of London, 2018.

J. L. Van Ingen. A suggested semi-empirical method for the calculation of the boundary layer transition region. *Delft University of Technology*, 1956.

E. White, W. Saric, R. Gladden, and P. Gabet. Stages of swept-wing transition. In *39th Aerospace Sciences Meeting and Exhibit*, page 271, 2001.

S. D. R. Wilson and I. Gladwell. The stability of a two-dimensional stagnation flow to three-dimensional disturbances. *Journal of Fluid Mechanics*, 84(3): 517–527, 1978.

Z. Xiong and S. K. Lele. Distortion of upstream disturbances in a Hiemenz boundary layer. *Journal of Fluid Mechanics*, 519:201–232, 2004.

Z. Xiong and S. K. Lele. Stagnation-point flow under free-stream turbulence. *Journal of fluid mechanics*, 590:1–33, 2007.

M. M. Zdravkovich. *Flow around Circular Cylinders: Volume 1: Fundamentals.* Oxford University Press, 1997.

Z. Zhang. *LDA application methods: laser Doppler anemometry for fluid dynamics.* Springer Science & Business Media, 2010.